TESIS DE LA UNIVERSIDAD
DE ZARAGOZA

2014

20

Carlos Herce Fuente

A Novel Method for Pre-combustion CO2 Capture in Fluidized Bed

Departamento

Instituto Universitario de Investigación Mixto CIRCE

Director/es

Cumo, Maurizio
Cortés Gracia, Cristóbal

ISSN 2254-7606

Prensas de la Universidad
Universidad Zaragoza

Tesis Doctoral

A NOVEL METHOD FOR PRE-COMBUSTION CO2 CAPTURE IN FLUIDIZED BED

Autor

Carlos Herce Fuente

Director/es

Cumo, Maurizio
Cortés Gracia, Cristóbal

UNIVERSIDAD DE ZARAGOZA
Instituto Universitario de Investigación Mixto CIRCE

2014

SAPIENZA
UNIVERSITÀ DI ROMA

Universidad
Zaragoza
1542

Doctoral School on Energetics
XXV Cycle

Instituto Universitario de Investigación Mixto
circe
UniversidadZaragoza

A NOVEL METHOD FOR PRE-COMBUSTION CO$_2$ CAPTURE IN FLUIDIZED BED

Carlos Herce Fuente

Ph.D. Thesis

January 2014

Advisors:

Cristóbal Cortés Gracia

Maurizio Cumo

A NOVEL METHOD FOR PRE-COMBUSTION CO_2 CAPTURE IN FLUIDIZED BED

Carlos Herce Fuente

Thesis submitted in partial fulfillment of the requirements for the degree of
Doctor of Philosophy

Sapienza University of Rome, Italy

University of Zaragoza, Spain

ABSTRACT

Enormous efforts have been realized by the international community in order to mitigate the effects of greenhouse gas (GHG) emissions in climate change. Approximately the 25% of global GHG (mainly CO_2) are generated by the combustion of fossil fuels in the energy sector. Carbon capture and storage has been proposed to reduce CO_2 emissions from large-scale fossil fuel power plants. Several technologies for the capture of CO_2 have been developed in the last years, in three main lines: post-combustion, oxy-fuel combustion and pre-combustion. This thesis presents a novel method for pre-combustion CO_2 capture in order to obtain hydrogen from coal, without GHG emissions. The main aim of this work is to develop a computational fluid dynamic (CFD) model of the steam reforming of a rich-methane syngas combined with CO_2 capture by means of solids sorbents. This process is known as Sorption-Enhanced Steam Methane Reforming (SE-SMR).

SE-SMR represents a novel, energy-efficient hydrogen production route with in situ CO_2 capture. This process has been studied in bubbling fluidized bed using CaO-based solid sorbents as CO_2 acceptor. Two solid sorbent have been tested in laboratory, a natural sorbent (Dolomite) and synthetic sorbent (CaO- $Ca_{12}Al_{14}O_{33}$). Moreover, some treatments have been developed in order to increase the carrying capacity of these sorbents.

A comprehensive CFD model of the SE-SMR has been implemented. An Eulerian-Eulerian approach, combined with the Kinetic Theory of Granular Flow, has been adopted in order to simulate the hydrodynamic behavior of the bubbling fluidized bed. Kinetic models for steam methane reforming and CO_2 capture have been developed, in order to include different sorbents and pre-treatments. In addition, a particle drag model has been developed in order to reduce the computational cost of the simulations at semi-industrial scale.

An extensive simulation campaign has been carried out in order to validate the model at laboratory and semi-industrial scales. CFD simulations have been combined with a Taguchi Robust Design of Experiments, in order to evaluate the effect of several operational factors in the SE-SMR response.

A NOVEL METHOD FOR PRE-COMBUSTION CO_2 CAPTURE IN FLUIDIZED BED

Carlos Herce Fuente

Tesis realizada para cumplir con los requisitos del grado de Doctor

Universidad de Roma “La Sapienza”, Italia

Universidad de Zaragoza, España

RESUMEN

La comunidad internacional está realizando enormes esfuerzos para mitigar los efectos de las emisiones de gases de efecto invernadero (GEI) en el cambio climático. Aproximadamente le 25% de las emisiones globales de GEI (fundamentalmente CO_2) son generados por la combustión de combustibles fósiles en el sector eléctrico. La captura y almacenamiento de CO_2 se ha propuesto como una alternativa para reducir las emisiones de GEI en centrales térmicas. Numerosas tecnologías para la captura de CO_2 se han desarrollado en los últimos años, fundamentalmente en tres líneas tecnológicas: postcombustión, oxicombustión y precombustión. Esta tesis presenta un nuevo método para la captura de CO_2 en precombustión, produciendo hidrógeno a partir de carbón, sin emisiones de GEI. El objetivo principal de este trabajo ha sido desarrollar un modelo completo, mediante herramientas de fluido dinámica computacional (CFD), del proceso de reformado de un gas de síntesis con alto contenido en metano combinado con la captura de CO_2 mediante adsorción con sorbentes sólidos regenerables. Este proceso es conocido como reformado de metano mejorado por adsorción (o SE-SMR, su acrónimo en inglés).

SE-SMR representa una novedosa y eficiente energéticamente ruta para la producción de hidrógeno con captura in situ de CO_2. Este proceso ha sido estudiado en un lecho fluido burbujeante, usando sorbentes sólidos de óxido de calcio como captores de CO_2. Dos sorbentes sólidos han sido estudiados en laboratorio: uno natural (Dolomita) y uno sintético (CaO-$Ca_{12}Al_{14}O_{33}$). Además, varios tratamientos han sido desarrollados para mejorar la capacidad de captura de estos sorbentes.

Un completo modelo CFD del proceso de SE-SMR ha sido desarrollado. Una aproximación Euleriana-Euleriana ha sido combinada con la Teoría Cinética de Flujos Granulares para simular la fluidodinámica del lecho fluido burbujeante. Los reacciones químicas de reformado y carbonatación han sido implementadas en el modelo CFD. Se ha incluido un modelo detallado de captura de CO_2 para simular el comportamiento de los diferentes sorbentes sometidos a diferentes pretratamientos para mejorar su rendimiento. Asimismo, un modelo de arrastre de partículas ha sido desarrollado para reducir el coste computacional de las simulaciones a escala semi-industrial.

Se ha llevado a cabo una extensa campaña de simulaciones para validar el modelo a escala de laboratorio y semi-industrial. Las simulaciones CFD han sido combinadas con un Diseño de Experimentos Robusto, con el objetivo predecir y evaluar la sensibilidad del proceso SE-SMR a diversos factores operativos.

A NOVEL METHOD FOR PRE-COMBUSTION CO_2 CAPTURE IN FLUIDIZED BED

Carlos Herce Fuente

Tesi realizzata in accordo con requisiti necessari per l'ottenimento del titolo di
Dottore di Ricerca

Università degli Studi di Roma “La Sapienza”, Italia

Università di Saragozza, Spagna

SINTESI

La comunità internazionale ha compiuto notevoli sforzi per ridurre gli effetti dell’emissione di gas serra sui cambiamenti climatici. Approssimativamente il 25% delle emissioni globali di gas serra (prevalentemente CO_2) è prodotta dall’utilizzo di combustibili fossili nel settore energetico. La cattura e stocaggio del carbonio è stata proposta per ridurre le emissioni di CO_2 di impianti di grande scala per produzione di energia da combustibili fossili. Negli ultimi anni sono state sviluppate diverse tecnologie di cattura del CO_2, principalmente lungo tre tipologhie: post-combustione, ossicombustione, e pre-combustione. Questa Tesi illustra un metodo innovativo per la cattura di CO_2 in pre-combustione, al fine di ottenere idrogeno da carbone senza emissioni di anidride carbonica. L’obiettivo principale di questo lavoro è sviluppare un modello computazionale fluidodinamico (CFD) del processo di steam reforming di un gas di sintesi ricco in metano combinato con la cattura di CO_2 per mezzo di sorbenti solidi. Questo processo è noto come Sorption-Enhanced Steam Methane Reforming (SE-SMR).

SE-SMR rappresenta una innovativa ed energeticamente efficiente via di produzione di idrogeno, con cattura in situ di CO_2 . Questo processo è stato studiato in un letto fluidizzato bollente utilizzando sorbenti solidi a base ossido di calcio come captatore di CO_2. Sono stati testati in laboratorio due differenti sorbenti, un sorbente naturale (Dolomite) ed uno sintetico (CaO- $Ca_{12}Al_{14}O_{33}$). Inoltre sono stati sviluppati alcuni trattamenti con il fine di accrescere la capacità di carico di tali sorbenti.

É stato implementato un modello dettagliato CFD del reattore SE-SMR. E’ stato adottato un approccio Euleriano-Euleriano, combinato con la Teoria Cinetica del Flusso Granulare, al fine di simulare il comportamento del letto fluidizzato bollente. I modelli cinetici per steam methane reforming e cattura di CO_2 sono stati sviluppati in maniera tale da includere differenti tipi di sorbenti e pre-trattamenti. In aggiunta è stato sviluppato un modello di trascinamento di particelle, per ridurre il costo computazionale delle simulazioni a scala semi-industriale.

É stata portata avanti un’estesa campagna di simulazioni al fine di validare il modello alle scale sia di laboratorio che semi–industriale. Le simulazioni CFD sono state combinate con un Robust Design of Experiments in modo da poter valutare gli effetti di differenti fattori operanti nella riposta dell’ SE-SMR.

ACKNOWLEDGEMENTS

During this last five years divided between Spain and Italy there are a lot of people with whom I am debt. It would have been impossible to walk this road alone. Thank you very much to all the people who have help me selflessly during the development of this work.

First of all, I want to express my truthful gratitude to my advisors: Cristóbal Cortés and Maurizio Cumo. I would like express my deep thanks Cristóbal for trusting in me to do part of his research group in CIRCE and for his interest in help to me to develop a career as researcher. I’m deeply grateful for his guidance, his valuable suggestions and comments, and, particularly in the last months, for his invaluable help in the continuous corrections and improvements of this thesis, very often in his days off and in odd hours. I thank to Maurizio Cumo, for encouraging to me to continue with the thesis when I was ready to leave it. His enthusiasm since he accepted to be my advisor has been a great motivation to develop this work.

I would thank to CIRCE for the financial support during the last two years, and for provide to me the infrastructure to develop this research. I wish to express my warmest thanks to all the colleagues at Thermal Systems Area of CIRCE. It is difficult to find a group of people with more compromise with research. Since I started to work with them in my final degree project, they made easier the work with its companionship and friendship. I am particular grateful with the co-workers of CFD/UTA group, Mauricio and Juanan, with whom I shared the same feelings (good and bad) generated during a CFD thesis development. It is impossible to thank in these lines all the personal and professional support during these years of Isa and Susana.

I am very grateful to UTTEI-COMSO department of ENEA at C.R.Casaccia at Rome. This work really started in the form of its International Fellowship. During the years I passed here, several material and economic means were made available to me in order to develop this work. I had the pleasure of work with very experienced and professional researchers and technicians, and to do some good friends. I would particularly thank two people. Antonio Calabrò was the director of ZECOMIX project during the time I work under his supervision. I think that I would never return his confidence in my work and his efforts in develop my professional career. I want to express my thruthful gratitude to Stefano Stendardo for his generosity, his interest in teaching, the endless discussions (I still keep the sketches of a paper done on a bar napkin, and his enthusiasm for research. The best ideas of this thesis undoubtedly emerged from the collaborative work with him.

I want to express my gratitude to Benedetta. Working with her has been a pleasure since the first day, at Rome and at Zaragoza. I am thankful for her enthusiasm in the research, and, above all for her friendship.

I would like express my deep thanks to some people who contribute with very useful key contributions to develop this thesis. Pier Ugo Foscolo, for his support during my work under a contract between University of L'Aquila and ENEA, and his readiness for several discussions on fluidization. And thanks to Hans Kuipers and Andrea Di Carlos for their comments on CFD modeling.

I am very thankful to my friends. Your support during these years is a treasure for me. Thank you to share with me music, theater, football, quimica, studies, trips, and lots of laughs, at Zaragoza, Rome or Turin: Ludovico, Livia, Isabelle, David, Luis, Fer, Rubén, Fran, Ana G., Carlos A. Hector, Carlos O. Chus. Ana C…The list of names would be endless; thus, please feel all of you included.

More important, I wish express my eternal gratitude to my parents, Victoriano and María Eugenia. They have always been an example and an unbreakable support. I deeply thank them for their comprehension and support during the good and bad times that we passed separated. They are responsible that all the best on me. I wish to thank my brothers, Alejandro and Ignacio, and Laura for their unconditional support and confidence.

Finally, I can't express with words my gratitude to Lina. For her patience, her comprehension, her enthusiasm, her encouragement and her unending smile. Without her endless support this work would not have any sense.

Once again many thanks to all of you,

Carlos.

A mis padres

A Lina

SCOPE, AIMS AND OUTLINE OF THIS THESIS

This thesis describes the computational fluid dynamic (CFD) study of the Sorption Enhanced Steam Methane Reforming (SE-SMR) of the ZECOMIX pilot plant. This project is leaded by ENEA (Italian National Agency for New Technologies, Energy, and the Sustainable Economic Development). ZECOMIX cycle is a novel method for pre-combustion CO_2 capture, for producing hydrogen and electricity from coal. The first step of the process consists in the gasification with hydrogen of coal. The methane-rich syngas generated is sent to the carbonator reactor. In the carbonator reactor, SE-SMR takes place in a bubbling fluidized bed, composed by reforming catalyst and a CO_2 solid sorbent. The addition of a solid sorbent for the selective removal of CO_2 has a double aim. On one hand, the equilibrium of the reforming reaction is shifted beyond their conventional thermodynamic limits, increasing hydrogen production and removing the carbon on the syngas. On the other hand reaction reforming and capture are energy-balanced at lower temperature than conventional process, with an important reduction of energy demand. The hydrogen-rich syngas produced is sent to a hydrogen modified micro-turbine with a nominal power of 100 kWe.

This thesis proposes a comprehensive low-computational cost CFD model for the simulation of the semi-industrial SE-SMR reactor of the ZECOMIX plant. Several topics related this main scope (as sorbent performance, fluidized bed simulation or scale-up of BFB) are discussed in this thesis.

In Chapter 1 an introduction to carbon capture and storage (CCS) technologies is presented. Taking as starting point the effect of anthropogenic greenhouse gas (GHG) emission in climate change; and recognizing the role of fossil fuels (mainly coal) in the power supply sector; CCS plays a crucial role in the medium-term energy generation. A brief introduction to the role of coal in Italian and Spanish electrical systems is presented, with particular emphasis in the most important projects related with CCS in both countries. A review of different technologies for capture, transport and storage of CO_2 is also summarized. Finally, this chapter explains in detail the ZECOMIX project, and the preliminary results to model the coal hydrogasification (more detailed about Italian Sulcis coal can be found in Appendix A).

Chapter 2 gives an overview about the use solids sorbents for high temperature CO_2 capture. In this work we studied two sorbents, by means of thermogravimetric (TGA) experiments, a natural sorbent (Dolomite) and a synthetic ($CaO\text{-}Ca_{12}Al_{14}O_{33}$, mayenite) sorbent. Dolomite presents a natural decay on the CO_2 carrying capacity with cycling of carbonation/calcination.

In order to improve the performance of dolomite, a novel “triggered calcination” method has been developed, with very promising results. The manufactured sorbent (mayenite) has been synthetized by means of a modification to the classical synthesis route, increasing its capacity. Some thermal treatments have been tested successfully in order to increase the performance of this sorbent. Moreover, a method for estimate from TGA data kinetic parameters and specific surface area has been developed.

The characterization of solids sorbents serves to model CO_2 capture reaction. In chapter 3 is presented a comprehensive model for CFD simulations of the SE-SMR process in a BFB. An Eulerian-Eulerian approach, combined with the Kinetic Theory of Granular Flow, has been adopted in order to simulate the hydrodynamic behavior of the bubbling fluidized bed. Chemical behavior includes the CO_2 capture reaction (for both sorbents, treated and untreated) and steam methane reforming heterogeneous catalytic kinetics. In addition a modified drag submodel has been implemented in order to reduce the computational cost of the simulations. An extensive CFD campaign has been carried out in order to characterize the BFB hydrodynamics. The global model has been validated at laboratory scale with a good agreement compared with literature data.

This model has been scale-up to the semi-industrial scale of ZECOMIX plant. In order to reduce the computational cost of this simulation, a coarse-grid simulation study has been carried out in. The studies of grid and time-step independence, as well as, a sensitive study of the model are presented in Chapter 4. CFD simulations have been combined with a Taguchi Robust Design of Experiments, in order to evaluate the effect of several operational factors in the ZECOMIX reactor response.

Finally, Chapter 5 presents a summary and a general discussion on the major results. New contributions and recommendations for continuing research are also included.

LIST OF PUBLICATIONS

A list of international JCR journal papers published during the development of this work is presented below:

a) C. Herce, B. de Caprariis, S. Stendardo, N. Verdone, P. De Filippis. Comparison of global models of sub-bituminous coal devolatilization by means of thermogravimetric analysis.Journal of Thermal Analysis and Calorimetry, (2014), in press.

b) S. Stendardo, L.K. Andersen, C. Herce. Self–activation and effect of regeneration conditions in CO2 – carbonate looping with CaO - $Ca_{12}Al_{14}O_{33}$ sorbent. Chemical Engineering Journal, 220, (2013), 383-394.

c) B. de Caprariis, P. De Filippis, C. Herce, N. Verdone. Double-Gaussian Distributed Activation Energy Model for Coal Devolatilization. Energy & Fuels, 26 (2012),6153 – 6159.

A list of international JCR journal papers submitted or under preparation derived of the development of this work is presented below:

a) C. Herce, S. Stendardo. Parametric study of CO2 capture capacity of dolomite stabilised by a novel two step calcination method. Submitted.

b) C. Herce, C. Cortés, S. Stendardo. A CFD-Taguchi combined method for the design of an industrial Sorption Enhanced Steam Methane Reforming reactor. Under preparation.

c) B. de Caprariis, M. Scarsella, C.Herce, N. Verdone, P. De Filippis. Double Gaussian distributed activation energy model for biomass pyrolysis. Submitted.

The contributions to international conferences done during the development of the Ph.D. Thesis are presented below:

a) S. Stendardo, A. Calabrò, G. Girardi, P.U. Foscolo, C. Herce A study of a chemical looping carbon capture for high-hydrogen content syngas. In Proceedings of "1st International Conference in Chemical Looping". Lyon, March, 17-19, 2010

b) C. Herce, A. Calabrò, S. Stendardo Numerical simulation of a high temperature CO2 capture fluidized bed. In Proceedings of "Processes and Technologies for a Sustainable Energy". Ischia,June, 27-30,2010

c) C. Herce, R. Mecozzi, A. Calabrò. Kinetics of Sulcis coal devolatilization. In Proceedings of “5th International Conference on Clean Coal Technologies 2011”. Zaragoza, May, 8-12, 2011

d) C. Herce, S. Stendardo, R. Mecozzi, A. Calabrò, A. Di Annunzio. Experimental study of sintering on Dolomite CO2 capture efficiency. In Proceedings of “5th International Conference on Clean Coal Technologies 2011”. Zaragoza, May, 8-12, 2011

e) A. Calabrò, S. Attanasi, A. Dedola, S. Cassani, L. Pagliari, S. Stendardo C. Herce. Commissioning of ZECOMIX Pilot Plant. In Proceedings of “5th International Conference on Clean Coal Technologies 2011”. Zaragoza, May, 8-12, 2011

f) S. Stendardo, L.K. Andersen, C. Herce, A. Calabrò. Experimental investigation of synthetic solid sorbents for multi-cycling CO2 uptake. In Proceedings of “5th International Conference on Clean Coal Technologies 2011”. Zaragoza, May, 8-12, 2011.

g) S. Stendardo, C. Herce, A. Calabrò. Pretreatment of synthetic sorbent for sequentially carbon dioxide capture. In Proceedings of “2nd International Conference on Energy Process Engineering” Frankfurt, June 20-22,2011

h) S. Stendardo, C. Herce, A. Calabrò. Effect of calcination temperature on cyclic CO2 capture using pretreated dispersed CaO as regenerable sorbent. “3rd IEA High Temperature Solid Looping Network Meeting” Vienna (Austria), August 30-31, 2011

i) C.Herce, Y. Li, Q. Wang, I. Guedea, L.I. Díez, C.Cortés CFD simulation of a 90 kWth oxy-fuel combustion bubbling fluidized bed reactor. In Proceedings of “International Conference on Power Engineering-13 (ICOPE 2013)” Wuhan (China), October, 24-27, 2013.

Several ENEA reports on CCS have been compiled in:

a) Fossil Fuels and Carbon Capture and Storage. Chapter in: Joint Research Program MSE/ENEA – Research on National Electric System. Antonino Dattola (Ed.) A. Calabrò, S. Stendardo, C. Herce, P.U. Foscolo, E. Sciubba, A. Cavaliere, M. de Joannon, S. Giammartini, G. Girardi, T. Faravelli, E. Ranzi, G. Cau, et al.ENEA Unità Communicazione. Frascati, Italy, November 2011.

Previously to this work an international JCR journal paper was published, derived from the final degree project:

a) J. Pallarés, A. Gil, C. Cortés, C. Herce. Numerical study of co-firing coal and Cynara Cardunculus in a 350 MWe utility boiler. Fuel Processing Technology, 90 (2009),1207-1213.

INDEX

LIST OF FIGURES

LIST OF TABLES

1 INTRODUCTION

1.1 Background on climate change mitigation

In 1992, international concern about climate change led to the United Nations Framework Convention on Climate Change (UNFCCC). The ultimate objective of that Convention is the "stabilization of greenhouse gas concentrations in the atmosphere at a level that prevents dangerous anthropogenic interference with the climate system".

According with the Intergovernmental Panel on Climate Chang (IPCC) Fourth Assessment Report: "Warming of the climate system is unequivocal, as is now evident from observations of increases in global average air and ocean temperatures, widespread melting of snow and ice and rising global average sea level. […] Most of the observed increase in global average temperatures since the mid-20th century is very likely due to the observed increase in anthropogenic greenhouse gas concentrations" [1].

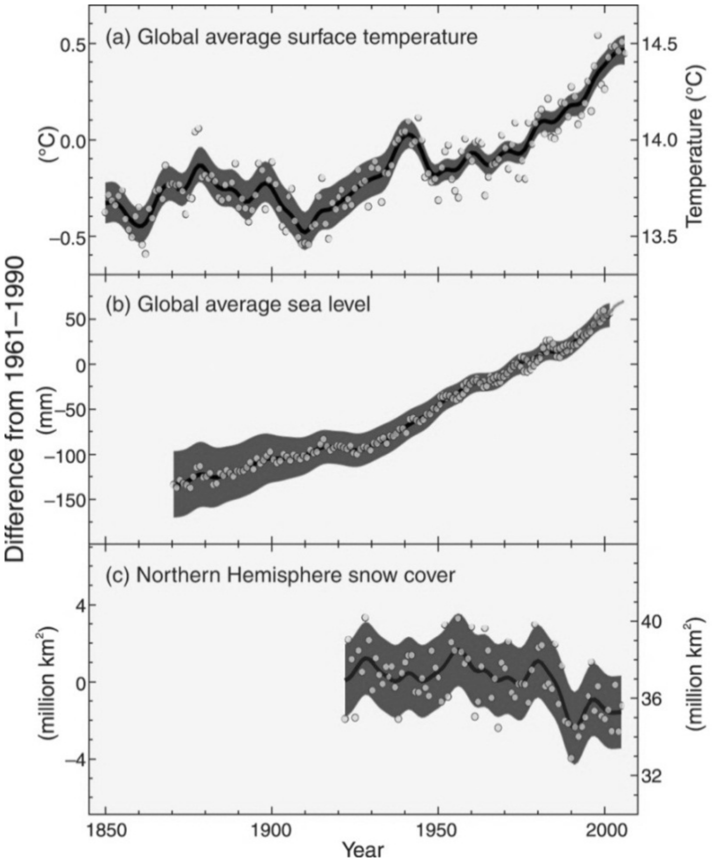

Figure 1. 1 - Global average surface temperature(a), sea level (b) and Northern Hemisphere snow cover(c) variations [1]

Since Arrhenius demonstrated in the end of XIX century the correlation between CO_2 concentration and temperature in the atmosphere [2], the anthropogenic effect on climate has been a very controversial topic. However, nowadays, it seems to be globally accepted that there is a direct relation between greenhouse gas (GHG) emissions and climate change. As shown in Figure 1. 2 the CO_2 concentration in the last 400,000 years, changed periodically between 180 and 300 ppm. However, since the Industrial Revolution, the rise of concentration has been very fast, arriving in a century to 380 ppm.

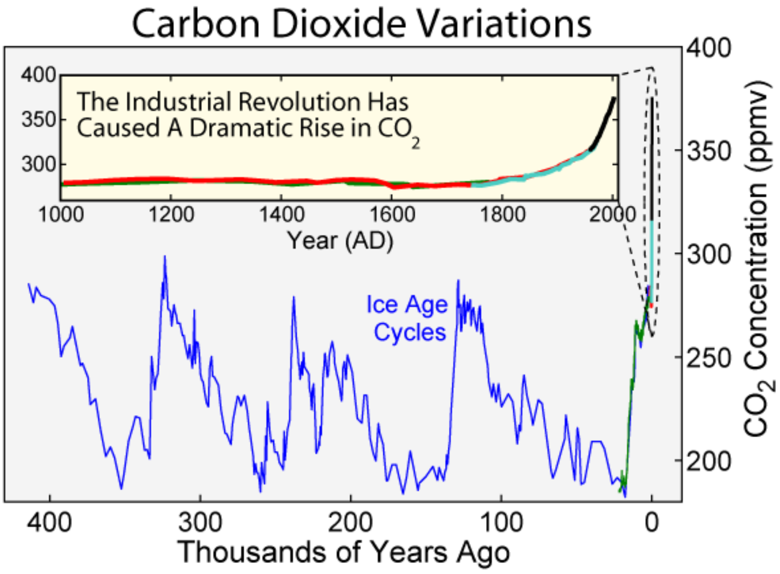

Figure 1. 2 – Carbon dioxide concentration variations [3-7]

This increase of temperatures is mainly associated to the GHG emissions, and in particular due to CO_2 emissions from fossil fuels combustion (56.6%). Other anthropogenic emission sources must be considered as CO_2 increase due to deforestation and decay of biomass, and emission of GHG in a lower concentration but more active in terms of GHG potential as methane (1 ton of CH_4 corresponds to 21 ton of CO_2) and nitrogen oxides (1 to 310 equivalent ton of CO_2). As shown in Figure 1. 3, the CO_2 emissions are due to several sectors as transport, residential and commercial buildings, industry (mainly cement, steel and iron, and refining processes), agriculture, forestry, and, mainly to energy supply.

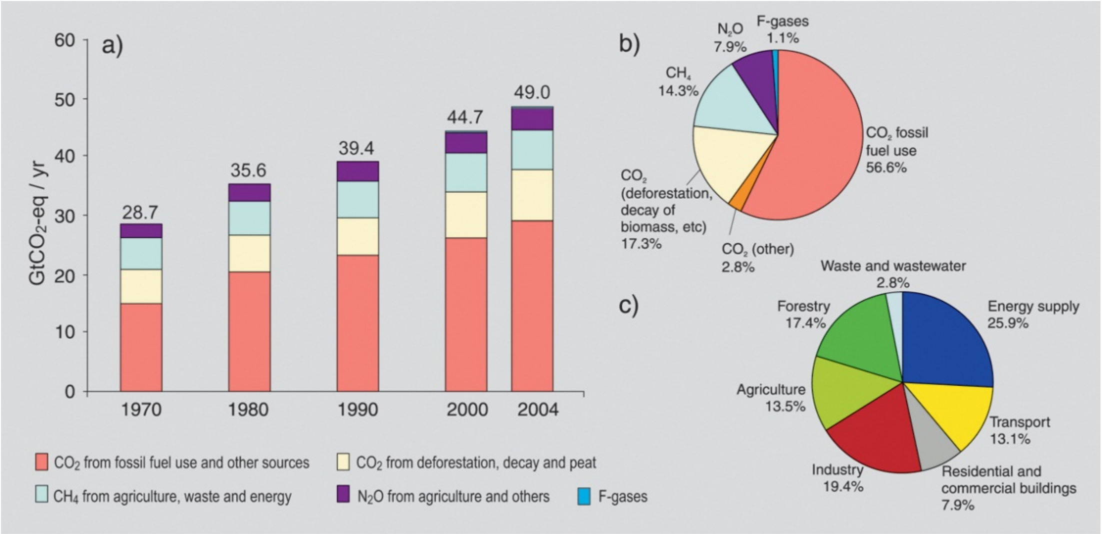

Figure 1. 3 – Carbon dioxide emission inventories (a) as function of sources (b) and sectors (c) [1]

Particularly, the estimation of temperature increase for the XXI century varies from 1.1 to 2.9ºC in the more optimistic scenarios, to 2.4 to 6.4 ºC in the most pessimistic scenario (Figure 1. 4). The UNFCC estimated that an increase higher than 2ºC (corresponding to a CO_2 concentration of 450 ppm), respect to 1980-1999 period, should have dramatic and irreversible impacts on systems and sectors as water (increased water availability in moist tropics and high latitudes; decreasing water availability and increasing drought in mid-latitudes and semi-arid low latitudes; hundreds of millions of people exposed to increased water stress), ecosystems (Increasing species range shifts and wildfire risk; ecosystem changes due to weakening of the meridional overturning circulation; significant (more than 40%) extinctions around the globe), food (complex, localized negative impacts on small holders, subsistence farmers and fishers; productivity of all cereals decreases), coasts (Increased damage from floods and storms; about 30% of global coastal wetlands lost; millions more people could experience coastal flooding each year), and health (increasing burden from malnutrition, diarrheal, cardio-respiratory and infectious diseases; increased morbidity and mortality from heat waves, floods and droughts; changed distribution of some disease vectors; substantial burden on health services).

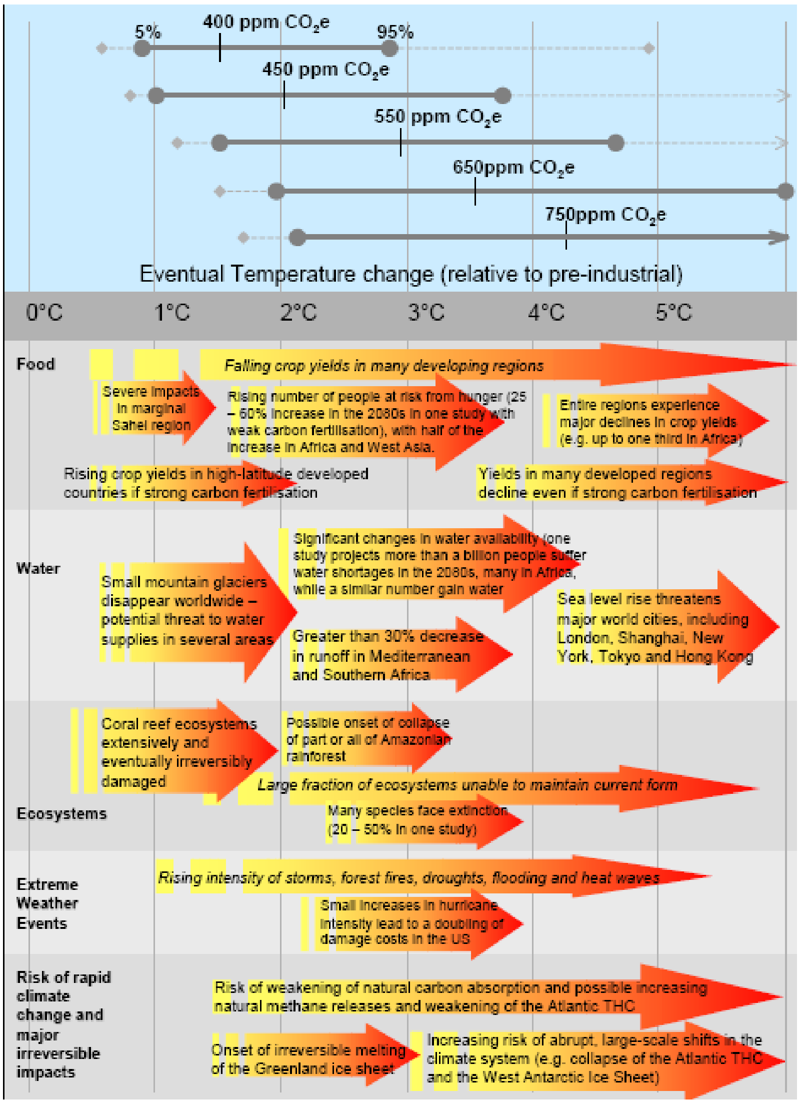

Figure 1. 4 – Stabilization levels and probability ranges of impacts that could be experienced as the world comes into equilibrium with more greenhouse gases for temperature increases [8]

In order to mitigate the effects of GHG in climate changes, the UNFCC promoted the Kyoto Protocol, which commits its Parties by setting internationally binding emission reduction targets [9]. Recognizing that developed countries are principally responsible for the current high levels of GHG emissions in the atmosphere as a result of more than 150 years of industrial activity, the Protocol places a heavier burden on developed nations under the principle of "common but differentiated responsibilities."

The Kyoto Protocol was adopted in Kyoto, Japan, on 11 December 1997 and entered into force on 16 February 2005. The detailed rules for the implementation of the Protocol were adopted in Marrakesh, Morocco, in 2001. Its first commitment period started in 2008 and ended in 2012. Its second commitment period was adopted (but not still accepted) on 21 December 2012 in Doha, Qatar.

Under the Protocol, countries must meet their targets primarily through national measures. However, the Protocol also offers them an additional means to meet their targets by way of three market-based mechanisms. The Kyoto mechanisms are:

- International Emissions Trading: In which Parties have assigned a number of “assigned amount units” (AAUs) corresponding to CO_2 emission rights. Emissions trading allows countries that have emission units to spare - emissions permitted to them but not "used" - to sell this excess capacity to countries that are over their targets.
- Clean Development Mechanism (CDM): allows a country with an emission-reduction or emission-limitation commitment under the Kyoto Protocol to implement an emission-reduction project in developing countries. Such projects can earn saleable certified emission reduction (CERs) credits, each equivalent to one ton of CO_2, which can be counted towards meeting Kyoto targets.
- Joint implementation mechanism (JI): allows a country with an emission reduction or limitation commitment to earn emission reduction units (ERUs) from an emission-reduction or emission removal project in another non-under-development country, each equivalent to one ton of CO_2, which can be counted towards meeting its Kyoto target.

Notable achievements of the UNFCCC and its Kyoto Protocol are the establishment of a global response to the climate change problem, stimulation of an array of national policies, the creation of an international carbon market and the establishment of new institutional mechanisms that may provide the foundation for future mitigation efforts (as shows Figure 1. 5). However, it has been a very controversial project for some reasons. On the one hand, U.S., which made up 16% of global GHG emissions, has no ratified the Kyoto Protocol. On the other hand, other countries as China (17% of global GHG emissions), and India (5%) have no obligations to plan a reduction of emissions. More reasons as volatile prices of emission trade or over-estimations in the assignations plan have been criticized. For all these reasons, some of the most active countries in the development of renewable energies and in the implementation of Kyoto protocol as Canada, New Zealand or Japan, as well as Russia have no accepted second phase Kyoto commitments. In fact, in 31 December 2011, Canada became the first signatory to announce its withdrawal from the Kyoto Protocol.

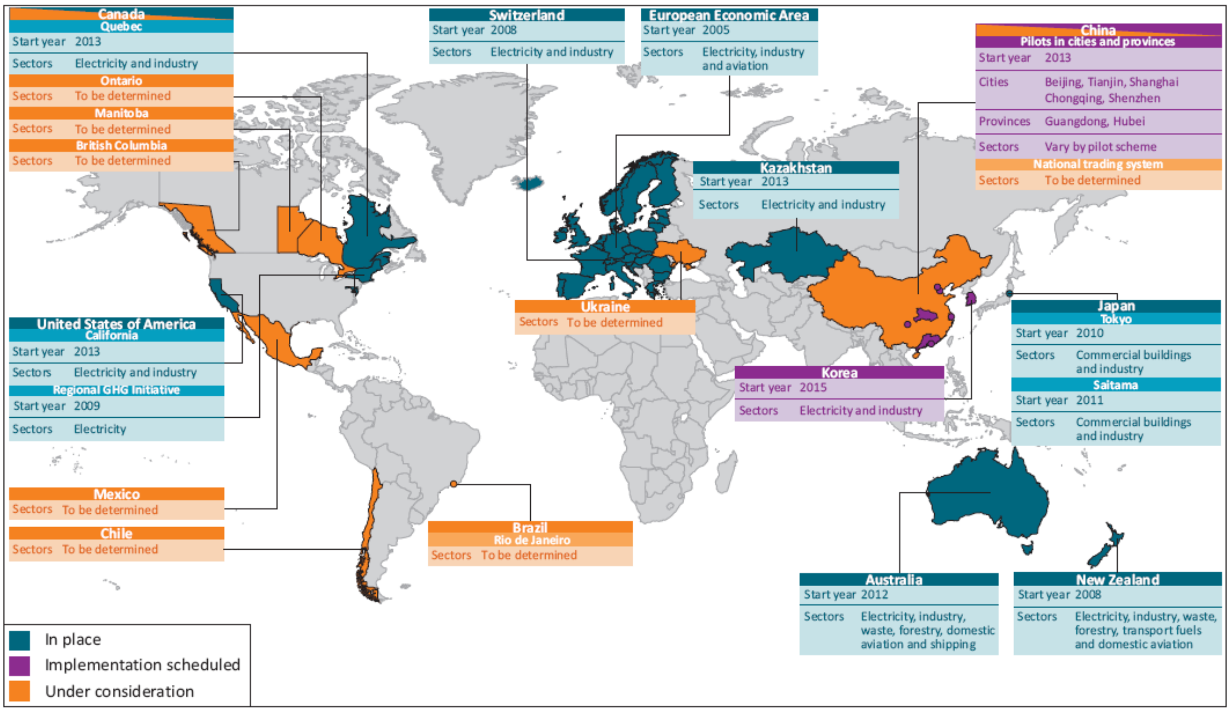

This map is without prejudice to the status of or sovereignty over any territory, to the delimitation of international frontiers and boundaries, and to the name of any territory, city or area.

Figure 1. 5 – Current and proposed emissions trading schemes. [10]

European Union has been very active since the beginning in the promotion of Kyoto Protocol. EU compromised a reduction in its emission for the period 2008-2012 of 8%, with respect to 1990 levels. In the 2003/87/CE Directive, the European Emission Trading Scheme (EU-ETS) was created in order to regulate the GHG emission market, according with the International Emissions Trading of the Kyoto Protocol. The EU-ETS is a cornerstone of the European Union's policy to combat climate change and its key tool for reducing industrial greenhouse gas emissions cost-effectively. The first - and still by far the biggest - international system for trading greenhouse gas emission allowances, the EU-ETS covers more than 11,000 power stations and industrial plants in 28 EU members plus Iceland, Norway, and Liechtenstein, as well as airlines, covering the 45% of the European GHG emission. The EU-ETS was divided in three steps:

1. Phase 1. From 1 January 2005 to 31 December 2007. This phase was considered a learning step. During this period was established the AAUs price and the emissions market, as well as the necessary infrastructure in order to catalog and control all the companies involved in the system.

2. Phase 2. From 1 January 2008 to 31 December 2012. This phase was the development of EU-ETS and it coincides with the first commitment period of the Kyoto Protocol.

3. Phase 3. From 1 January 2013 to 31 December 2013. This phase pursues the EU 20/20/20 target. 20/20/20 target set three key objectives for 2020: a 20% reduction in EU greenhouse gas emissions from 1990 levels; raising the share of EU energy consumption produced from renewable resources to 20%; a 20% improvement in the EU's energy efficiency.

EU is still very active in combating climate change. Additionally to the environmental point of view, the economic effects of climate change have been extensively discussed. In 2006 it was commissioned by UK government the Stern Review about climate change [8]. In this work, the main conclusion is that the benefits of strong, early action on climate change far outweigh the costs of not acting. The measurements need to mitigate climate change suppose nowadays the 1% of GDP, but in the future can achieve the 20%. The Review provides prescriptions including environmental taxes to minimize the economic and social disruptions. Moreover, it is evaluated the potential impacts of climate change on water resources, food production, health, and the environment. This work has been widely discussed with several supporters [11-14] and detractors [15, 16], but it is a very good review of scientific and economic effects of GHG emissions as a global externality of enormous proportions. According with this work, and in order to obtain an alternative to the IET proposed in the Kyoto Protocol, several approaches have been proposed, as carbon tax, etc…[17-19]

Kyoto protocol is centered in reduce the CO_2 emission and to associate a real price to the ton of CO_2 emitted. Thus, in order to reduce the carbon intensity of the energy supply sector, and therefore the economic penalties linked with emissions, a wide range of technologies will be necessary to reduce energy related CO_2 emission substantially. Figure 1. 6 shows how different technologies contribute to meeting the energy sector target of cutting CO_2 emissions by more than half by 2050, in order to maintain increase of temperature in 2ºC.

Energy efficiency in end use can suppose 42% of reductions. Much of this can be realized now, with net benefit. Particularly the most important sectors are buildings and transport, but all sectors are susceptible to increase the energy efficiency. The second technology to reduce GHG emission is the increase of renewable sources in power generation, 21%. Great progress already made in photovoltaic (PV) and wind. Offshore wind and concentrated solar power also have large potential. Nuclear could suppose till 8% of emissions. However, great uncertainties remain in the uses of nuclear. Instead of a majority of countries remain committed to nuclear even after the Great East Japan Earthquake and the accident in Fukushima, in March 2011, long-term nuclear uses is under discussion. End-use fuel switching can made up to the 12%. Some can be done fairly easily, some more difficult, particularly in industry. Hydrogen and biomass are the most promising alternative sources. Power generation efficiency and fuel switching could suppose a 3% of the emissions.

Carbon capture and storage (CCS) can suppose a reduction of atmospheric CO_2 between 14 and 22% [20, 21]. CCS is the only technology available to mitigate GHG emissions from large-scale fossil fuel plants. These technologies consist in obtaining a pure stream of CO_2 from fossil fuels energy processes, the CO_2 obtained is storage in the subsurface, mainly in deep saline aquifers. These technologies are still struggling and several large-scale demonstrations are needed [22]. A novel technique to the capture of CO_2 is the aim of this thesis, and in the next sections a deeper explanation will be provided.

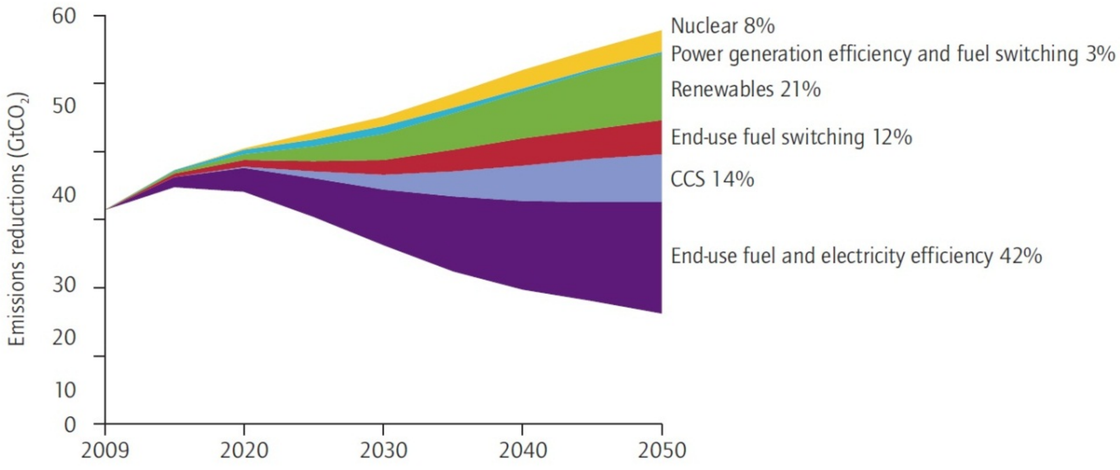

Figure 1. 6 – Emissions reduction potential by technology [20]

1.2 Role of coal in power generation

Approximately 69% of all CO_2 emissions are energy related, and about 60% of all GHG emissions can be attributed to energy supply and energy use [1].The IEA World Energy Outlook 2009 [23] projects that, without changes in current and already planned policies, global energy-related CO_2 emissions will be 57% higher in 2030 than in 2005, with coal demand increasing by 40%. In 2030, fossil fuels would remain the dominant source of energy. The bulk of the additional CO2 emissions and increased demand for energy, 84% of which will come from using fossil fuels, will come from developing countries.

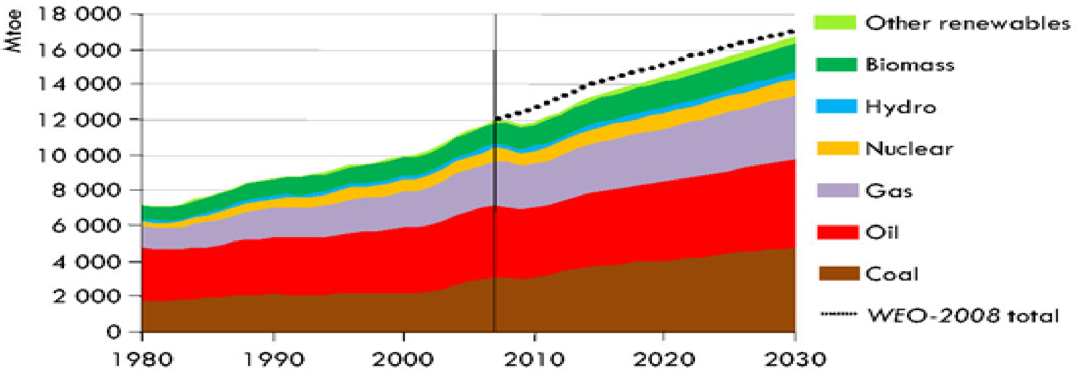

Figure 1. 7 – World primary energy source consumptions [23]

Thus, the coal production and use is far from being in declining. Coal is the second source of primary energy in the world after oil, and the first source of electricity generation. Coal consumptions grew from 4600 million tons (Mt) in 2000 to 7200 (Mt) in 2010 (see Figure 1. 8). Growth in coal demand is strongly dependent of the country. In the OECD countries the consumption is stable; meanwhile the increasing is driven primarily by developing economies, such as China and India.

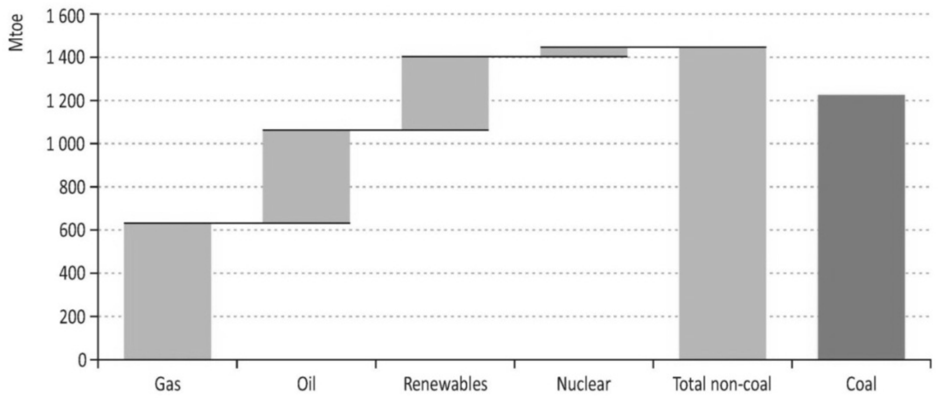

Figure 1. 8 – World distribution of energy sources in electricity generation [24]

90% of coal exports come from only six countries (Indonesia, Australia, Russia, South Africa, Colombia, and the United States). Hence it is logical suppose the need for further diversification in the coal supply and the increase on the autochthonous coal. For these reasons it is estimated that price of coal will increase in the next years (see Figure 1. 9). Instead of the increase on the price of coal, the volatility of the price will be lower than in the cases of oil and gas.

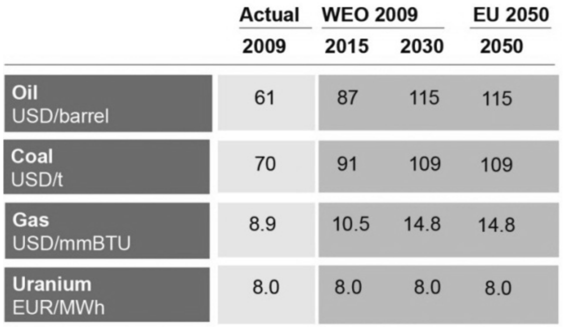

	Actual	WEO 2009		EU 2050
	2009	2015	2030	2050
Oil USD/barrel	61	87	115	115
Coal USD/t	70	91	109	109
Gas USD/mmBTU	8.9	10.5	14.8	14.8
Uranium EUR/MWh	8.0	8.0	8.0	8.0

Figure 1. 9 – Cost estimation of energy sources [25]

It has been estimated that there are over 861 billion tons of proven coal reserves worldwide. This means that there is enough coal to last us around 112 years at current rates of production. In contrast, proven oil and gas reserves are equivalent to around 46 and 54 years at current production levels [26]. Coal reserves are available in almost every country worldwide, with recoverable reserves in around 70 countries, but they are concentrated in a 70% in four countries (U.S., Russia, China, India and Australia) [27]. However there is a controversy about the useful time of the reserves. The most conservative studies estimate that actual reserves are sufficient to cover the current demand for almost 200 years [28, 29]. Other studies, on the contrary, proposed that coal might not be so abundant, widely available and reliable as an energy source in the future [30, 31].

In the case of European Union, the coal reserves are concentrated in Poland and Germany, with a relative high importance of the East countries as well as UK and Spain. The EU reserves are mainly centered in lignite, and a 25% of the global consumption of coal is imported. The consumption of coal in EU is stable in the last years, as well as imports, as shows Figure 1. 10. This consumer policy of is mainly drive by Germany and Poland, which obtain lower costs on the coal extraction than other countries. Usually, the price of autochthonous coal is 2 or 3 times higher than imported one. However, the use of local resources allows a higher independence of the third countries; lower variability on prices; and the maintenance of local structures centered in mining, avoiding the restructuring of coalfields and the socioeconomic cost associated.

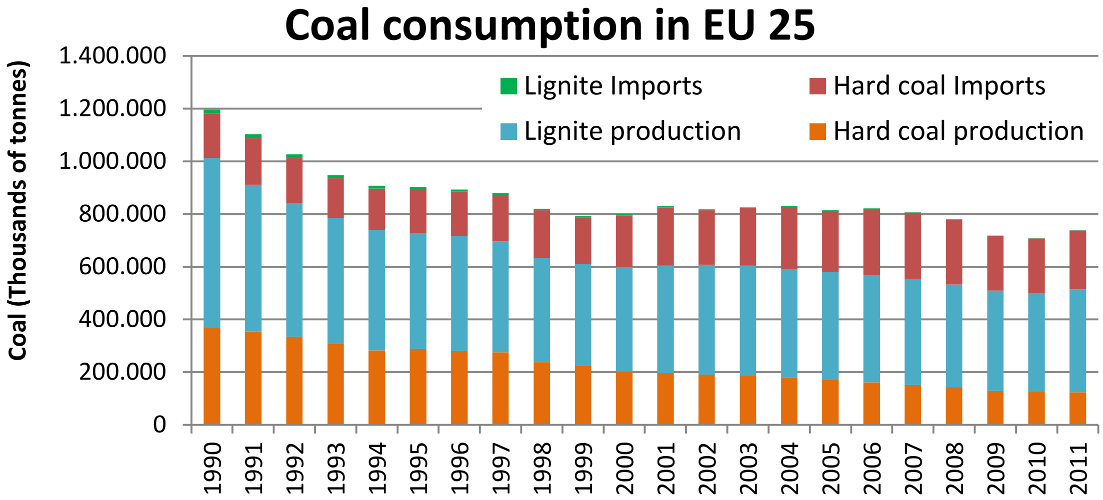

Figure 1. 10 – European coal consumption. This statistics includes all the uses of the coal, (power, industrial, etc…). Eurostat considers Brown Lignite as lignite. Black Lignite is included into hard coal production [32]

1.3 Comparison of Italian and Spanish electrical systems

Italian and Spain generation electrical systems present very different mixes. The Spanish electric system presents a well distributed energy sources, in line with OECD countries. Coal, nuclear and renewable (mainly eolic) suppose approximately the 60% of energy sources, in similar proportion (19.3%, 24.1% and 22.1%). The other energies considered are big hydroelectric (7.7%), co-generation and other special regime no renewable (12.7%) and natural gas combined cycle power plants (14.1%). Moreover, in the Spanish system, the imports/exports of electricity are almost balanced, with a surplus on the exports.

The Italian case is strongly different. Since 1987, as consequence of the nuclear power referendum following the Chernobyl accident, Italian government decides shutdown the four operative nuclear power plants, and it stopped the construction of a fifth plant, under commissioning phase [33]. The power supply was substituted by oil and natural gas power plants. The increase of prices of the oil reduced the use of this fuel in the last decades, but its role was very important during the 1990’s. Nowadays, the natural gas is the most used energy source in the electric system (43.6%). The role of coal and renewables are significantly lower than in Spanish case. Moreover, Italian system presents a lack in electricity and it imports approximately the 13% of electricity.

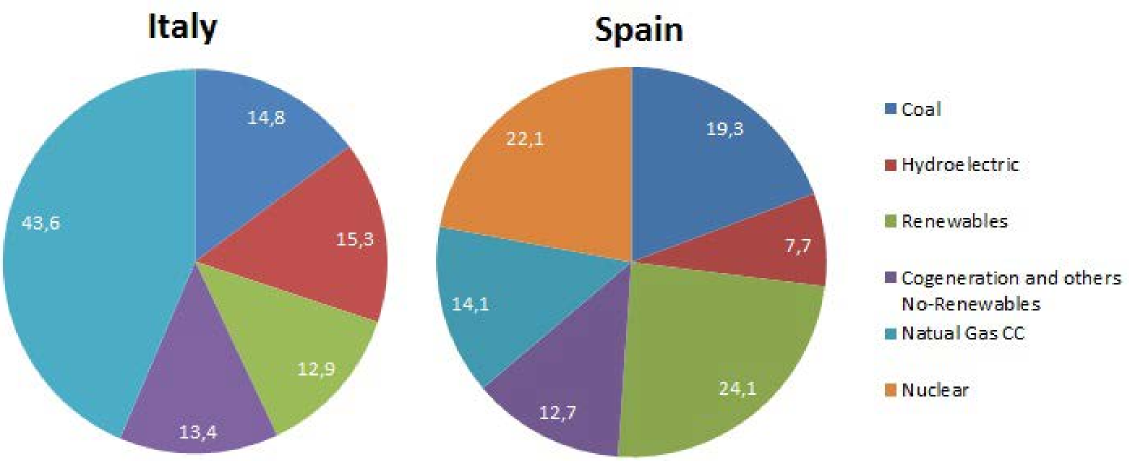

Figure 1. 11 – Italian and Spanish power generation in 2011 by energy source [34-36]

Both countries are strong importers of coal (Figure 1. 12). In 2011, coal consumption in Italy is ~25 Mt/year, of which just ~1 Mt/year are extracted from the unique Italian coalfield located in the Sulcis basin (in Sardinia). Sulcis coal is a sub-bituminous coal with a high content in sulphur and a relative high heating value. 2/3 of the coal extracted is used in power plants and the other 1/3 have an industrial purpose [37]. The proved reserves of Sulcis coal are ~50 Mt [27].

Spanish coal consumption is ~28 Mt/year, of which just ~6 Mt/year are autochthonous. Two types of coal are extracted in Spain. In one hand, Bituminous coal and Anthracite coalfields are located in the provinces of Asturias, Leon, Palencia (~3.5 Mt/year) and Ciudad Real (~0.5 Mt/year). In the other hand, in the province of Teruel ~2 Mt/year of Black Lignite are extracted. The Spanish autochthonous is used almost exclusively as a fuel for steam-electric power generation (90%) and the reserves proved reach ~530 Mt [27, 38]. Spanish coal market have presented a decrease in the consumptions due to legislation issues, and depletion of brown lignite coalfields (as shows Figure 1. 13).

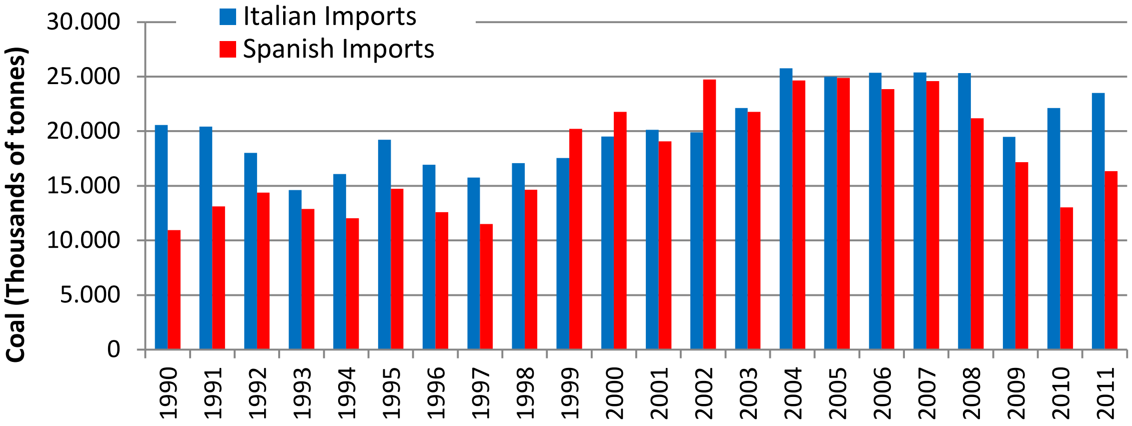

Figure 1. 12 – Italian and Spanish coal imports historical evolution adapted from [32]

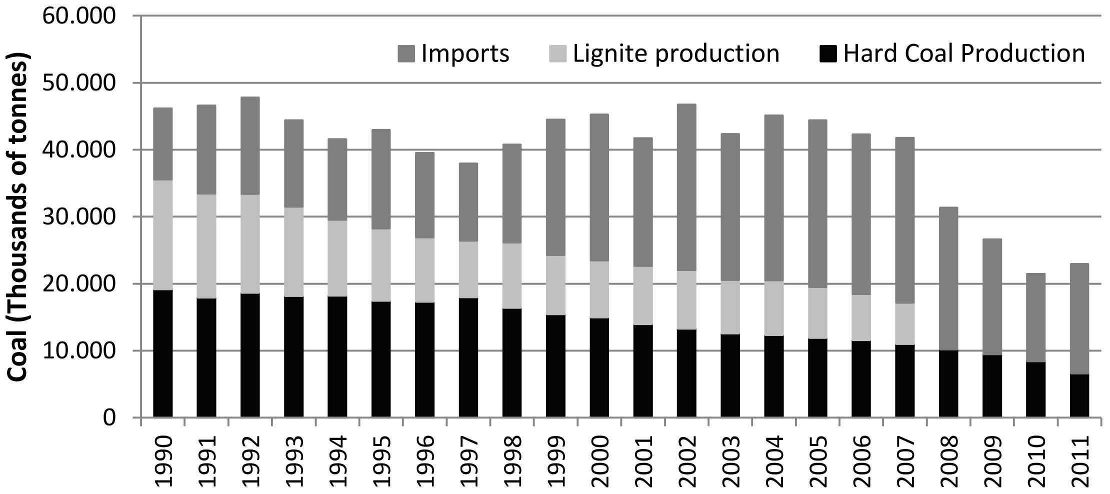

Figure 1. 13 – Historical evolution of Spanish coal production and imports adapted from [32]

Nowadays, 13 coal-fired power plants operate in Italy. Most of the power plants were erected in the 1970's. However, due to the important dependence of the natural gas of the Italian electric sector, during the last decades very important projects were prompted in order to diversify the energy sources. Brindisi Sud and Fiume Santo were commissioned in the first 1990's. On July 2008 the first of three groups of Torrevaldaliga Nord power plant entered into service, and since 2009 the plant operates at full capacity (1980MWe). This power plant was the cornerstone of the clean coal technologies in Italy, because it was the first ultra-supercritical (USC) CCS ready plants commissioned in Italy. The plant not captures CO_2 but presented all the infrastructures necessaries to the implementation at industrial scale.

Two other important projects are under development. In one hand, the plant in Porto Tolle, owned by Enel, projected the conversion of 4 oil groups into 3 high-efficiency (> 45%) coal groups, with a total power of 1,980 MW_e. This plant includes a 250 MW_e large-scale demonstration CCS plant with capture with chemical absorbents, and 120 km pipeline CO_2 transport to offshore saline formation in Adriatic Sea. Due to permitting and legislation issues, the final investment decision has been delayed until 2016. In South Brindisi power plant, the development of a pilot plant of 50 MW_{th} with CO_2 capture and sequestration technology is currently in progress. The pilot plant is part of the first integrated CCS pilot project in Italy combining the Enel's CO_2 post-combustion capture project and the Eni's pilot CO_2 injection project, in the frame of the Enel-Eni collaboration agreement on CCS. The Brindisi pilot facility can treat 10,000Nm3/h of flue gases for the separation of 2.5 t/h of CO_2. By improving the capture process, it allows Enel to increase its know-how in view of the construction of the large-scale demonstration plant at Porto Tolle [39]. In the other hand, the SEI project in Saline Joniche pretended to construct a similar plant to Torrevaldaliga (1680 MW_e USC ready to CCS), in Calabria region. However, recently the project has been stopped due to permitting and legislation issues.

It is worth to note that two IGCC plants operates in Italy since mid-1990's. ISAB (512 MWe located in Sicily) and Sarlux (548 MWe located in Sardinia) plants are attached to refineries. They gasify residual oil from refinery (with high sulphur content) to produce electricity.

Moreover, they produce medium-pressure (MP) steam, low-pressure (LP) steam and hydrogen for the adjacent refineries. These plants are very promising to be adapted to pre-combustion CO_2 capture power plants.

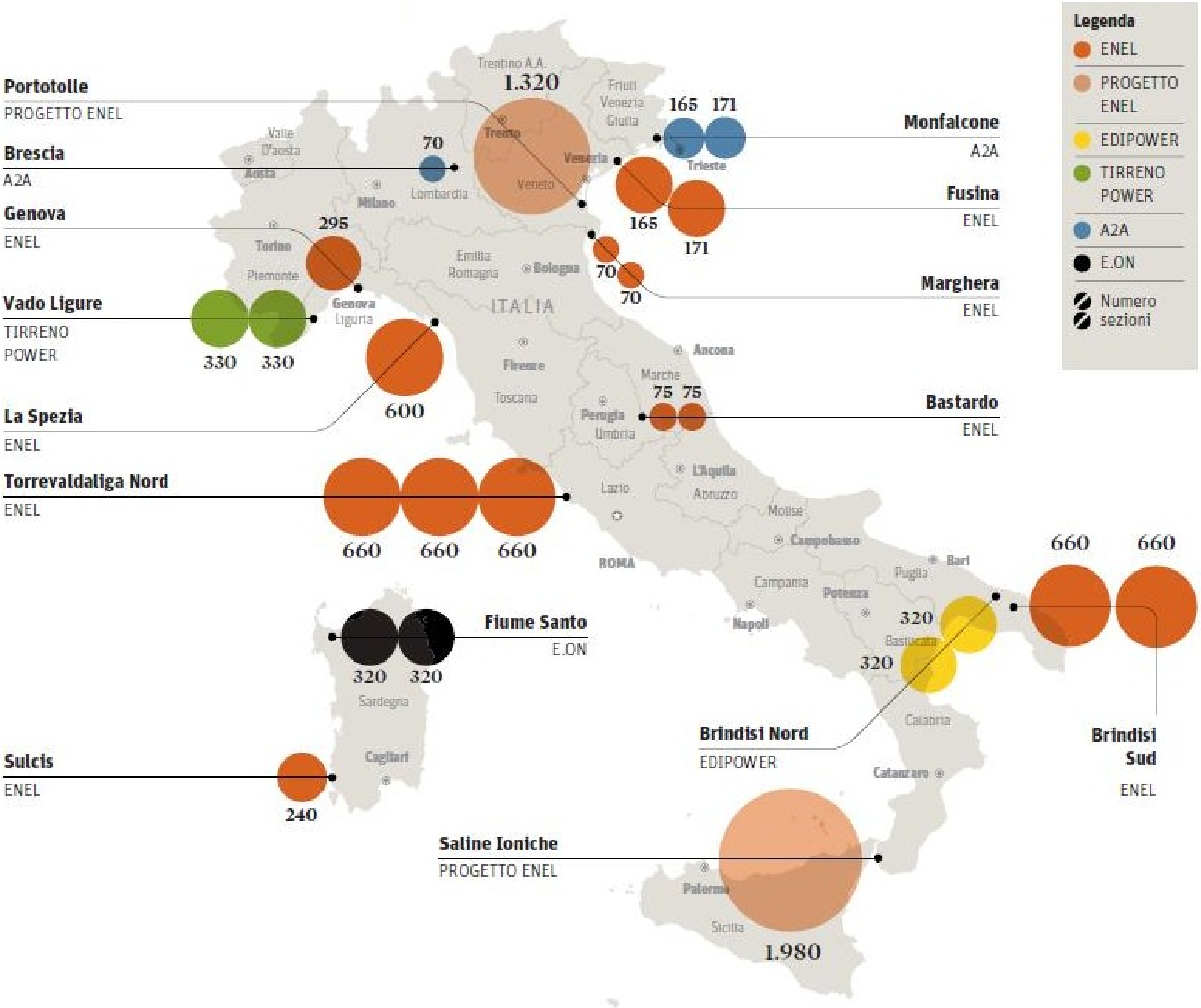

Figure 1. 14 – Coal-fired power plants in Italy [40]

On the contrary to the increase of plants in Italy, in Spain since the liberalization of the electric market (in 1998) no new plants have been erected. Nowadays, 16 coal-fired power plants operate in Spain. Six companies own all the coal plants: Endesa (End. 4), E.On (3), Iberdrola (Iberd. 2), Gas Natural Fenosa (GNF 3), HC Energia (HC.E 2) and Hunosa (Hun. 1) (Anllares Power Plant is investee by GNF and End). The main investments in coal-fired power plants have been centered in the implement of pollutant emission control equipment (i.e. sulfur removal units in Teruel PP), increase of groups in existing PP (e.g. Litoral de Almeria PP), and conversion of groups from autochthonous brown lignite to imported bituminous coal (e.g. Meirama and As Pontes PPs). Three internationally recognized projects in CCS and clean coal technologies have been carried out in Spain in the last years, at pilot, demonstrative and industrial scales.

ELCOGAS Puertollano power plant, is a 335 MW_e integrated gasification combined cycle (IGCC) plant based on the pressurized dry-drag flow gasification process. The plant operates with coal from 1998. The employed fuel is a 50% mixture by weight of coal and petroleum coke. The syngas is produced by reacting the fuel with oxygen and steam at high temperature exceeding 1,500ºC in a reducing environment. After cleaning treatment, syngas is employed as a clean fuel in a high-efficiency combined cycle. The power station design makes use of the maximum integration concept. The ELCOGAS power station presents net efficiency of 42.2%, with very low CO_2, acid gas and particles emissions [41]. Moreover, between 2008 and 2011, a 14 MW_{th} pilot plant was operated with the aim to demonstrate at industrial scale the technical viability of pre-combustion carbon capture technology in a IGCC power plant. The pilot captured 100 tons per day of CO_2 using the pre-combustion technology, being the capture rate higher than 90%. The pilot also produced 2 tons per day of 99.99% purity hydrogen [42].

CaOLing project, funded by EU-FP7, is the largest project in the world to test the concept of post-combustion CO_2 capture by calcium looping. The pilot plant treats 1/150 of the flue gases of the 50 MW_e *La Pereda* CFBC power plant. The post-combustion 1.7MW_{th} carbonation/calcination plant has been operated in steady state for hundreds of hours of accumulated experimental time. The pilot includes two 15 m height interconnected circulating fluidized bed reactors: a CO_2 absorber (or carbonator of CaO) and a continuous $CaCO_3$ calciner operated as an oxy-fuel CFBC [43].

CIUDEN's Capture Technology Developing Plant, fully operative since 2011 (attached to Compostilla Power Plant), is a unique pilot center in CCS technologies, mainly oxy-fuel combustion. The installation includes a 20 MW_{th} PC boiler, a 30 MW_{th} CFB boiler, a fuel preparation unit, a 3 MW_{th} biomass gasifier, a flue gas cleaning train, and a CO_2 processing unit [44-46]. The 30 MW_{th} CFB operation, burning coal using oxygen instead of air, was the initial testing phase of a higher project called Compostilla project (also called OXY-CFB-300). This project includes the construction of a 300 MW_e demo plant at the Compostilla place together with the corresponding CO_2 transport and storage infrastructure, 135 km onshore pipeline for sequestration in saline aquifers. A final investment decision is expected to be made in 2013 for commercial operations to start in 2018.

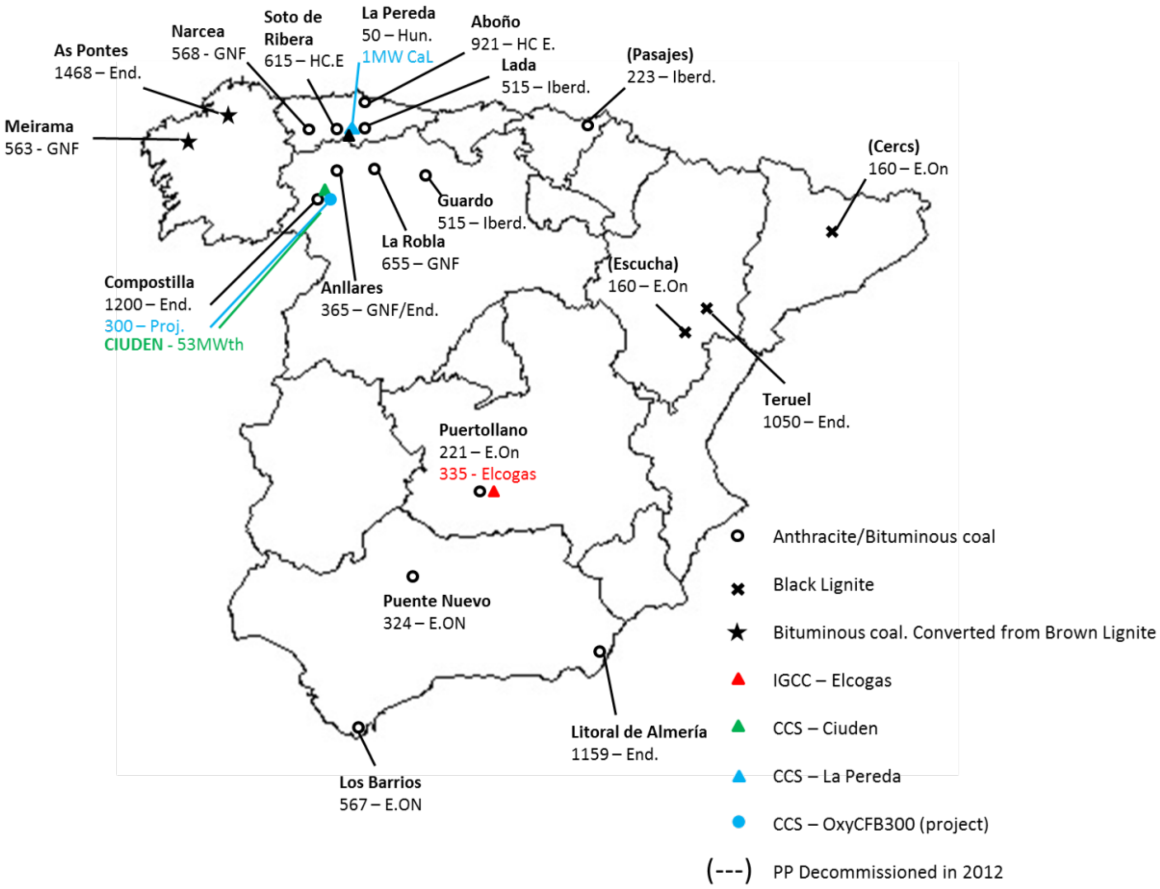

Figure 1. 15 – Coal-fired power plants in Spain and CCS demo projects adapted from [36, 47, 48]

1.4 Carbon capture, transportation and storage

CCS is the only technology available to mitigate GHG emissions from large-scale fossil fuel plants. The purpose of CO_2 capture is to produce a concentrated stream of CO_2 at high pressure that can be transported to a storage site. Although, in principle, the entire gas stream containing low concentrations of CO_2 could be transported and injected underground, energy costs and other associated costs generally make this approach impractical. It is therefore necessary to produce a nearly pure CO_2 stream for transport and storage.

The two main problems associated with CCS are technical penalties of capture and socio-economic issues of the CO_2 capture and storage. Capture process penalizes strongly the performance of the process at which it is applied, and therefore, in the operative costs, as a function of the capture process applied. Thus, in order to reduce the costs a wide variety of solutions has been proposed, and proved at different scales. On the other hand, financial, legal, regulatory and public acceptance issues are crucial to solve, perhaps, the most important challenge: how to pay for CCS.

Since the publication in 2005 of the first IPCC book about CCS [49], international attention have been paid to the CCS technologies, and a wide variety of works review and update the proposals of the IPCC “classical” study [50-52].

1.4.1 CO_2 capture

Industrial applications separating CO_2 in large industrial plants, including natural gas treatment plants and ammonia production facilities, are already in operation today. Currently, CO_2 is typically removed to purify other industrial gas streams, and usually emitted to the atmosphere. Capture processes also have been used to obtain commercially useful amounts of CO_2 from flue gas streams generated by the combustion of coal or natural gas. To date, however, there have been no applications of CO_2 capture at large power plants.

Depending on the process or power plant in question, there are three main approaches to capture the CO_2 generated from a primary fossil fuel, as Figure 1. 16 shows [49]:

- Post-combustion
- Oxy-fuel combustion
- Pre-combustion

Post-combustion systems separate CO_2 from the flue gases produced by the combustion of the primary fuel in air. Oxy-fuel combustion systems use oxygen instead of air for combustion of the primary fuel to produce a flue gas that is mainly water vapor and CO_2. Pre-combustion systems process the primary fuel in order to obtain a stream of pure CO_2 and other of hydrogen-rich syngas, which has several applications as energy carrier.

These main systems can be applied to power plants, and to energy-intensive manufacturing industries such as iron and steel, cement and refining sectors in order to decarbonizing its activities [53].

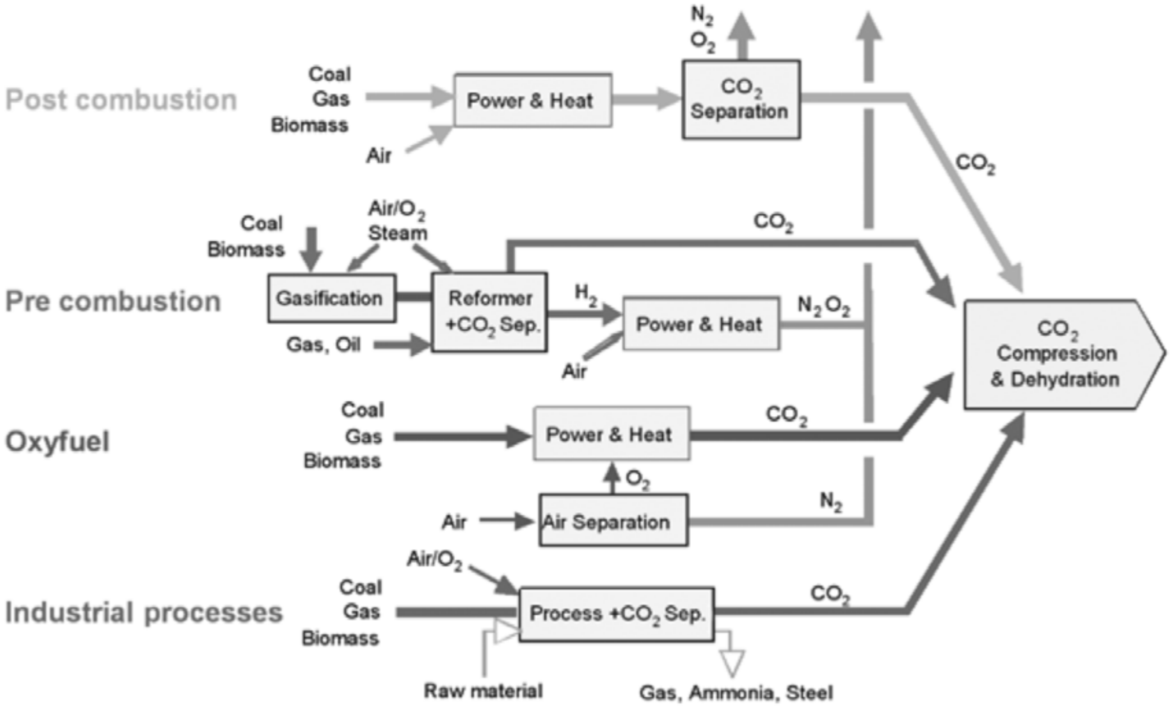

Figure 1. 16 – Overview of CO_2 capture processes and systems [49]

For coal-fired power generation, no single CO_2 capture technology outperforms available alternative capture processes in terms of cost and performance. Average net efficiency penalties for post - and oxy-fuel combustion capture are 10% relative to a pulverized coal plant without capture, and 8% for pre-combustion capture compared to an IGCC. Cost figures vary substantially depending on the type of power plant and fuel used. According with IEA, average costs of CO_2 avoided are 55 USD/ton of CO_2, applying the currently mature capture technologies to a typical sub-critical pulverized coal power plant without CO_2 [54-56].

Table 1. 1 – Estimated energy penalties and costs of mature capture technologies in power plants [56]

Capture route	Post-combustion Amines	Pre-combustion Rectisol	Oxy-fuel combustion	Post-combustion Amines
Reference plant without capture	PC	IGCC	PC	NGCC
Net efficiency with capture (LHV, %)	30.9	33.1	31.9	48.4
Net efficiency penalty (LHV, % points)	10.5	7.5	9.6	8.3
Relative net efficiency penalty	25%	20%	23%	15%
Overnight cost with capture (USD/kW)	3 808	3 714	3 959	1 715
Overnight cost increase (USD/kW)	1 647	1 128	1 696	754
Relative overnight cost increase	75%	44%	74%	82%
LCOE with capture (USD/MWh)	107	104	102	102
LCOE increase (USD/MWh)	41	29	40	25
Relative LCOE increase	63%	39%	64%	33%
Cost of CO_2 avoided (USD/tCO_2)	58	43	52	80

This price is excessive compared with the suggestions of IPCC. Compression, transport and geological storage cost is approximately 10 USD/ ton CO_2. These technologies are mature and the cost is stable. However, the cost of capture is more uncertain. A value higher than ~20 USD/ton CO_2 cannot be competitive with price of emission market or proposed carbon taxes [57] [49]. Obviously, if CCS costs are greater than the price of CO_2 in the emission trading scheme, the companies will prefer to pay by pollute, instead of implement CCS technologies.

With the aim to reduce the cost of capture, several novel technologies have been proposed. Figure 1. 17 shows the grade of maturity and application fields of different technologies. Some novel techniques as chemical looping combustion, calcium looping or hydrogen-IGCC, are very promising from a technical and economic point of view. However, they must be tested at industrial scale in order to validate the real costs. Moreover, it is necessary to create a legal framework for the real implementation of emission markets that would make competitive the investment in CCS.

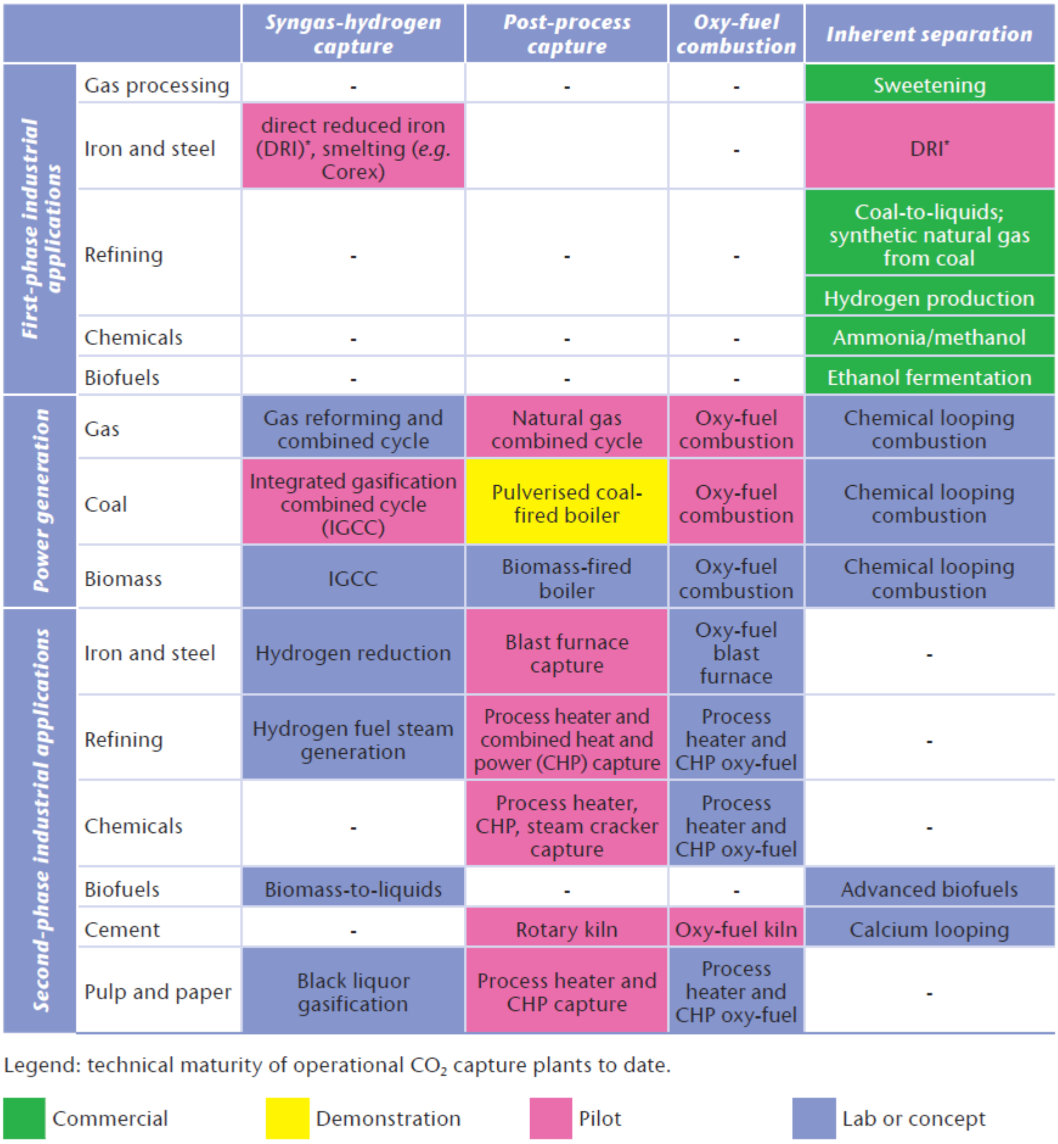

		Syngas-hydrogen capture	*Post-process capture*	*Oxy-fuel combustion*	*Inherent separation*
First-phase industrial applications	Gas processing	-	-	-	Sweetening
	Iron and steel	direct reduced iron (DRI)*, smelting (*e.g.* Corex)		-	DRI*
	Refining	-	-	-	Coal-to-liquids; synthetic natural gas from coal Hydrogen production
	Chemicals	-	-	-	Ammonia/methanol
	Biofuels	-	-	-	Ethanol fermentation
Power generation	Gas	Gas reforming and combined cycle	Natural gas combined cycle	Oxy-fuel combustion	Chemical looping combustion
	Coal	Integrated gasification combined cycle (IGCC)	Pulverised coal-fired boiler	Oxy-fuel combustion	Chemical looping combustion
	Biomass	IGCC	Biomass-fired boiler	Oxy-fuel combustion	Chemical looping combustion
Second-phase industrial applications	Iron and steel	Hydrogen reduction	Blast furnace capture	Oxy-fuel blast furnace	-
	Refining	Hydrogen fuel steam generation	Process heater and combined heat and power (CHP) capture	Process heater and CHP oxy-fuel	-
	Chemicals	-	Process heater, CHP, steam cracker capture	Process heater and CHP oxy-fuel	-
	Biofuels	Biomass-to-liquids	-	-	Advanced biofuels
	Cement	-	Rotary kiln	Oxy-fuel kiln	Calcium looping
	Pulp and paper	Black liquor gasification	Process heater and CHP capture	Process heater and CHP oxy-fuel	-

Legend: technical maturity of operational CO_2 capture plants to date.

🟩 Commercial 🟨 Demonstration 🟪 Pilot 🟦 Lab or concept

Figure 1. 17 – Routes to CO_2 capture in power generation (by fuel) and industrial applications (by sector) [20]

1.4.1.1 Post-combustion

These systems normally use a liquid solvent to capture the small fraction of CO_2 (typically 3–15% by volume) present in a flue gas stream in which the main constituent is nitrogen (from air). For a modern pulverized coal (PC) power plant or a natural gas combined cycle (NGCC) power plant, post-combustion capture systems would typically employ organic physical solvents (such as Rectisol, Selexol), and amine-based chemical solvent (such as monoethanolamine (MEA) or 2n-methyldiethanolamine (MDEA)) [50, 58-61]. These two technologies are mature at industrial scale.

In chemical absorption, strong bonds are created between solvent and CO_2. The rupture of these bonds requires large amounts of energy. In order to reduce the energy penalties due to the regeneration of solvent, new generation solvents (as piperazine (PZ)) has been tested with better reversibility and 20% lower energy consumptions [62].

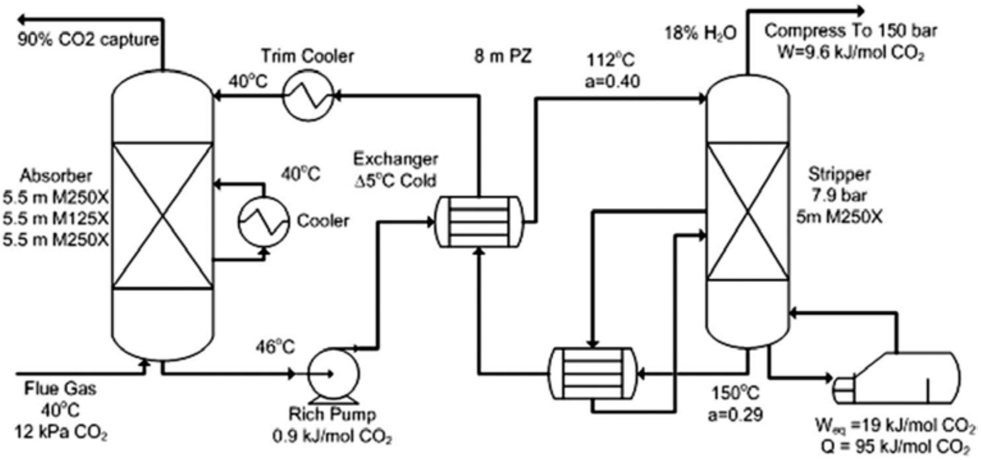

Figure 1. 18 – Scheme of post-combustion system with amines (Intercooled Absorber/Interheated stripper with 8mPZ) [52]

On the other hand, in physical absorption the bonds generated between solvent and CO_2 are weaker than in chemical absorption. Bonding takes place a very high pressures and CO_2 is released when pressure is reduced. Thus, the energy requirements are centered in driving the compressors for gas pressurization. The amount of energy per CO_2 ton captured is inversely proportional to CO_2 concentration. Thus, this systems are economical competitive only for concentrations higher than 15% CO_2 [50].

There exist a large number of other different technologies for CO_2 capture with potentially superior thermodynamic efficiency than amine-based solvents, such as ionic liquids, membranes and carbonate looping.

Recently, it has been suggested the use of ionic liquids (ILs) as alternative solvents. In addition to a potentially lower energy demand in the solvent regeneration step, ILs have higher stability and easier regeneration than conventional amine-based CO_2 extraction [63-65].

Concerning CO_2 capture by membrane separation, both polymeric and inorganic membranes are used in order to produce clean fuel from a mixture gas. Inorganic membranes are very attractive for CO_2 removal in IGCC power plants even though their costs are very high. In contrast, gas separation using polymeric membranes is today commercially available. Nevertheless, CO_2 capture in large-scale power production by means of polymeric membranes still presents inadequate performances due to their lack of high-temperature stability. Research is mainly addressed for improving the performance of the membranes by increasing their selectivity and permeability and also decreasing their cost [66-68].

Calcium looping (CaL) is a CO_2 capture scheme using solid CaO-based sorbents to remove CO_2 from flue gases. This technique is based in the reversible gas–solid reaction between CO_2 and CaO(s) to form $CaCO_3$(s). Calcium looping is under demonstrative stage, but it presents some important advantages compared with amine-based systems. Firstly, for carbonation-calcination it uses circulating fluidized bed reactors, a mature technology at large scale. Secondly, solid adsorbents (usually called sorbents) derive from cheap, abundant and environmentally benign limestone and dolomite precursors. Finally, the efficiency penalty estimated to a power plant is ~7%.Moreover, this technique, as membranes technologies can be applied also to pre-combustion systems. Many excellent reviews have recently been published on the current status of CaL; see for example [69-72].

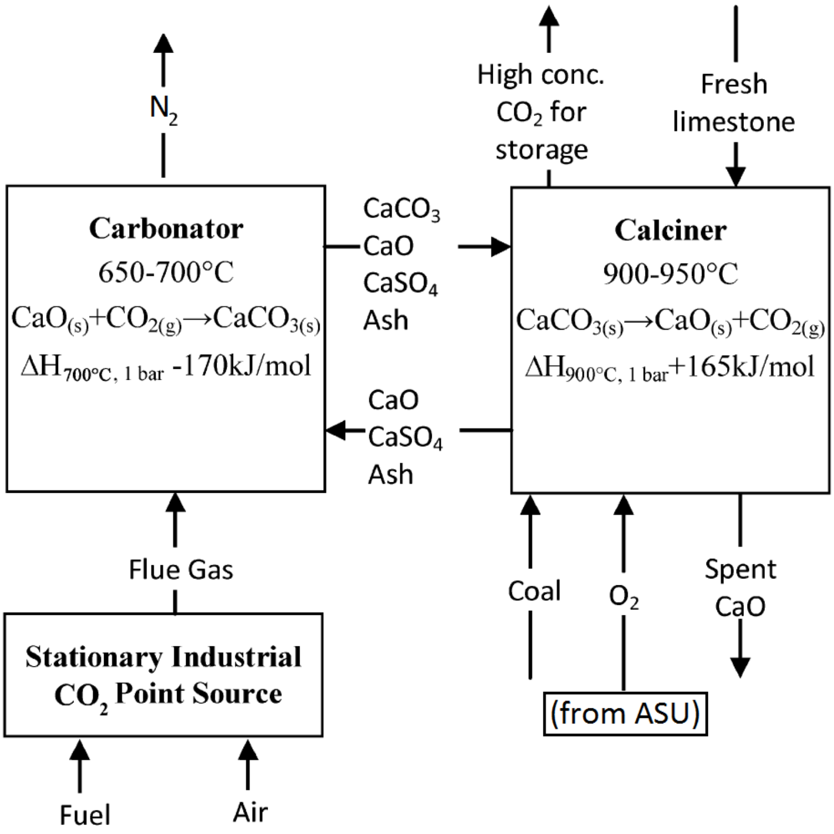

Figure 1. 19 – Scheme of post-combustion system with CaL adapted from [72]

1.4.1.2 Oxy-combustion

Oxy-fuel combustion systems use oxygen instead of air for combustion of the primary fuel to produce a flue gas that is mainly water vapor and CO_2. This results in a flue gas with high CO_2 concentrations (greater than 80% by volume). The water vapor is then removed by cooling and compressing the gas stream. Oxy-fuel combustion requires the upstream separation of oxygen from air, with a purity of 95–99% oxygen by means of an Air Separation Unit (ASU). The oxygen stream is combined with recycled flue gas (RFG) to produce an oxygen enriched gas for the oxidant. The recycle is necessary to moderate the otherwise excessively high flame temperature that would result from burning in pure oxygen. As a method of CO_2 capture in boilers, oxy-fuel combustion systems are in the demonstration phase.

Oxy-fuel combustion can be applied to several fuels, including coal, natural gas or blends of biomass and coal. Most interest has focused on oxy-coal combustion due to the abundance, reliability and high carbon content of the fuel. In comparison to air-fired plants, the implementation of oxy-fuel operation supposes strong plant configuration changes and additional unit operations. The optimum recycle ratio is generally 0.7; this yields oxygen levels in the oxidant environment that typically range from 25 to 30% because at these conditions, the flame and heat transfer characteristics reasonably approximate those of air-fired pulverized fuel (PF) boilers. Oxygen excess is 15–20% for air-firing conditions but for oxy-fuel conditions is limited to 10% in order to minimize ASU operational costs. Flue gas oxygen content is typically 3%. In general terms, oxy-fuel combustion induces reduction of plant efficiency by 8–12%, mainly associate to ASU.

By recycling the CO_2 (and possibly H_2O), several changes in heat transfer can be expected due to the changes in gas properties. These changes are affected by gas radiative properties, and gas thermal capacity. Unlike symmetric diatomic gases such as N_2, triatomic gases such as CO_2 and H_2O are not transparent to radiation. Their partial pressures are significantly higher in oxy-fuel combustion flue gas than those in air-fuel combustion, and therefore, the absorptivity and emissivity of the flue gas substantially increases. Hence, the radiative heat transfer from the flame will change. In addition, carbon dioxide and water vapor have high thermal capacities compared to nitrogen. This increase in thermal capacity increases the heat transfer in the convective section of the boiler. However, the amount of gas passing through the boiler in the oxy-fuel case is lower, and increased heat transfer in the radiative section of the boiler results in lower gas temperatures entering the convective pass. Both of these factors will act to lower the heat transfer in the convective section of the boiler. The heat transfer in the radiative and convective sections of the boiler will need to be optimized to ensure efficient operation.

The flue gas stream should be cooled, scrubbed and dried before being diverted for the primary recycle. Particulates are removed in order to avoid accumulation of solids in the boiler and prevent the flue gas recirculation fan and gas passages from unnecessary wear due to erosion. Moreover, flue gases must be desulphured before recirculation, in order to reduce corrosion problems. Moreover, oxy-fuel combustion provides a way to reduce emissions of NOx. In addition, NOx generation mechanism changes in oxy-fuel flames.

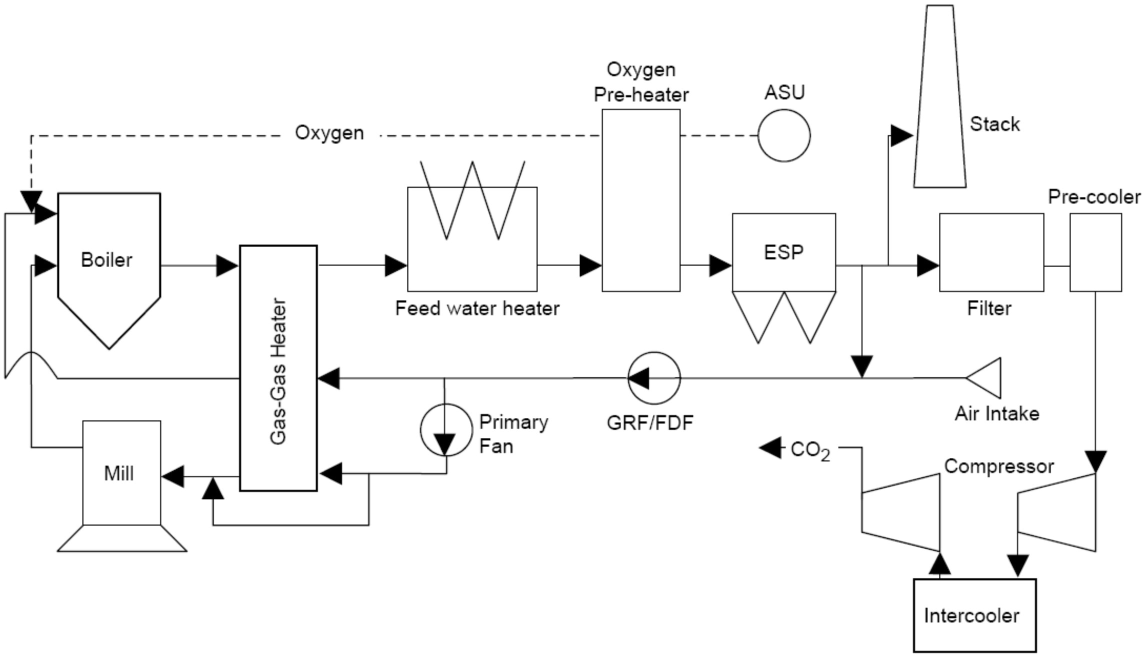

Figure 1. 20 – Scheme of a coal oxy-fuel power plant [73]

Until recently, the obvious route for oxy-fuel combustion was via conventional pulverized coal-fired (PC), and there is already one large European oxy-fuel PC demonstration plant (Vattenfall's Schwartze Pumpe 30 MW_{th} plant in Germany). However, recently oxy-fired fluidized bed combustion (FBC) has also become increasingly important as a potential technology offering both fuel flexibility and the possibility of firing or co-firing biomass with CO_2 capture. For utility applications, circulating fluidized bed combustion (CFBC) is employed, and this technology is available in the supercritical mode at sizes of up to 460 MW_e (erected by Foster-Wheeler in Lagisza, Poland). CFBC is now a widely used technology for the power industry for difficult fuels. The oxy-fuel combustion in CFB has been tested at 30 MW_{th},at CIUDEN. It is worth to remark the FLEXI BURN CFB project (funded by FP7 EU), with participation of CIUDEN and Foster-Wheeler, and other. This project aims to develop and demonstrate a power plant concept based on the Circulating Fluidized Bed (CFB) technology combined with CCS. The plant will be based on the super critical once through (SC-OTU) technology and oxygen-firing with carbon capture, hence, providing high efficiency, operational flexibility and potential for an almost 100% reduction in CO_2. Several groups worldwide are working in oxy-fuel development, and many excellent reviews have recently been published on the current status of coal oxy-fuel combustion (e.g. [73-77]).

One of the main advantages of the oxy-fuel technologies is the viability of retrofitting and repowering options. However, the energy penalties present a relative high value. In order to increase the net efficiency, some high efficient novel processes have been conceptually proposed as Graz Cycle [78], Advanced Zero Emission Power Plant (AZEP), Water Cycle (WC) [79], Solid Fuel Cell Integrated with a Gas Turbine cycle (SOFC+GT) [80] and Chemical-looping combustion.

Chemical-looping combustion can be considered a variant of oxy-fuel combustion. In this technology, metal oxides are used to carry oxygen and heat between successive reaction loops, producing an inherent separation of CO_2. This process is configured with two interconnected fluidized bed reactors: an air reactor and a fuel reactor (Figure 1. 21). The solid oxygen carrier is circulated between the air and fuel reactors. In CLC, the fuel is fed into the fuel reactor where it is oxidized by the lattice oxygen of the metal oxide. Complete combustion in the fuel reactor produces CO_2 and water vapor. Therefore, the CO_2 formed can be readily recovered by condensing water vapor. Once fuel oxidation completed the reduced metal oxide M_yO_{X-1} is transported to the air reactor where it is reoxidized to M_yO_x.

CLC research has mainly focused on gaseous fuels, but in the last years important work has been dedicated to adapting the process to solid fuels. Chemical-looping combustion (CLC) of solid fuels is a technology with the potential of reducing the costs and energy penalty dramatically for CO_2 capture. The potential for low costs is based on the similarity to coal combustion in fluidized beds. The concept is being examined and developed on pilot scale, and shows promise for demonstration by 2020 [81-83].

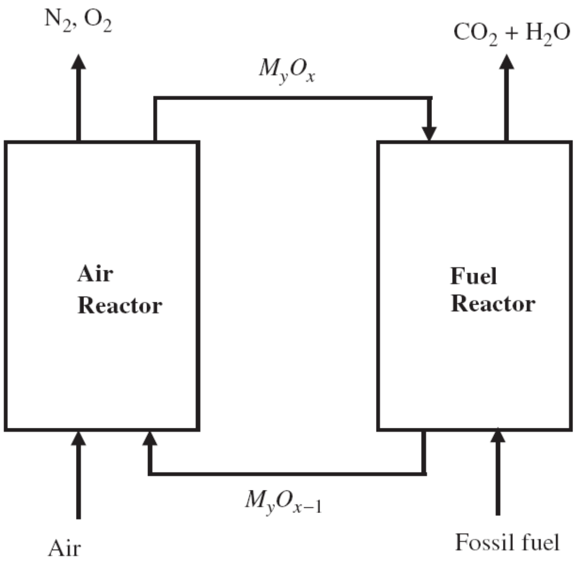

Figure 1. 21 – Scheme of a CLC system

1.4.1.3 Pre-combustion

In the pre-combustion systems the primary fuel is processed in a gasification reactor (for solid fuels) or in a reforming reactor (for natural gas natural gas, naphtha or heavy oils) with steam and oxygen to produce a mixture consisting mainly of carbon monoxide and hydrogen (“synthesis gas”). Additional hydrogen, together with CO_2, is produced by reacting the carbon monoxide with steam in a second reactor (a “shift reactor”). The resulting mixture of hydrogen and CO_2 can then be separated into a CO_2 gas stream (send to storage), and a stream of hydrogen.

Instead of the complexity of gasification and shift reactors, compared with other capture technologies, the high concentrations of CO_2 produced by the shift reactor (typically 15 to 60% by volume on a dry basis) and the high pressures often encountered in these applications are more favorable for CO_2 separation. Pre-combustion would be used at power plants that employ integrated gasification combined cycle (IGCC) technology, with a higher global performance and lower costs than oxy-fuel and post-combustion techniques [49, 54, 55, 79, 84].

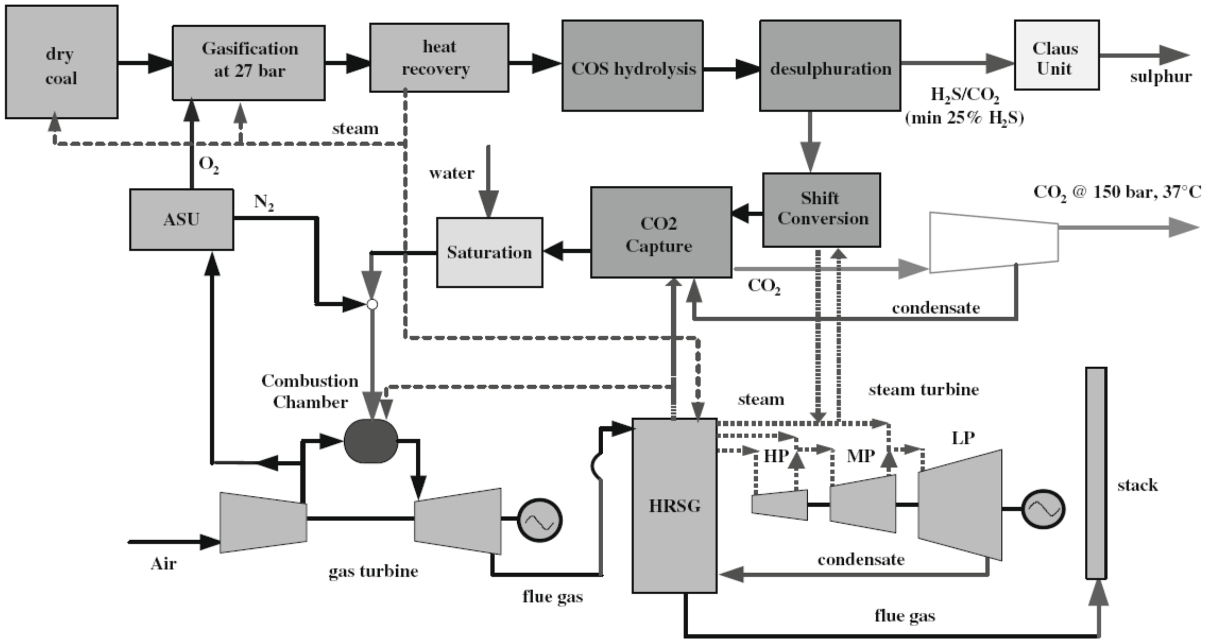

Figure 1. 22 – Scheme of a Quench-IGCC-slurry with capture of CO_2 [85]

Hydrogen is a carbon-free energy carrier. Hydrogen is a vector capable of generating energy without producing CO_2 (in combustion chambers and fuel cells), could be used to produce electricity and heat on a small scale for urban transportation, and can be stored once generated. Instead of the actual system limitations, hydrogen could play a key role in the future of energy [86].

The hydrogen turbine is the unit that is common for all pre-combustion technologies for all fuels. Pure hydrogen presents several complex challenges for flame stability due to its very high flame speed when premixed, and its high temperatures when non-premixed. The high flame temperatures resulting from hydrogen combustion are attenuated by the addition of nitrogen and/or steam. Modifications to the combustors and fuel mixing system are the principal requirements when converting a natural gas turbine to burn hydrogen-rich fuels. Although hydrogen has almost three times more energy by mass than natural gas, by volume the energy density is much lower [87]. Very important advances have been carried out in the hydrogen turbines in the last years. In 2009 the world's first industrial-scale power plant to be fully fed by hydrogen has been built in the Porto Marghera area (Italy). The experimental plant is a combined cycle in which a 12 MW_e hydrogen-fuelled gas turbine is well integrated with the existing coal-fuelled plant.

Furthermore, the removal of hydrogen in dehydrogenation and synthesis gas reactions with membranes has been widely studied. Two different approaches have been investigated: Integration of a membrane into the reformer and integration of a membrane into the high temperature shift reactor. Product removal may occur by H_2 permeation through a Pd-alloy or composite Pd-ceramic membrane or a ceramic porous membrane [66, 67].

Many novel pre-combustion concepts or improvements have been published. Most of the most promising technologies are focused in the auto-thermal reforming (ATR) and the sorption enhanced steam methane reforming process (SE-SMR). SE-SMR combines catalytic shift conversion (of carbon monoxide and steam to hydrogen and carbon dioxide) with a high temperature CO_2 adsorption system using a mixture of solid catalyst and adsorbent. With this technology, the shift reactor is not necessary and simplicity and performance increase. The conversion and CO_2 removal steps are carried out in a multi-bed pressure swing adsorption unit which is regenerated using low pressure steam which is subsequently condensed to leave a relatively pure CO_2 stream [88]. Moreover, this process present the advantage of a high flexibility for production of H_2 and electricity [89], can be combined with membranes SE-SMR has been studied alone or integrate with membranes [90] or fuel cells (ZEG Cycle [91]). Different configurations for the gasification of coal have been proposed in order to improve thermal and CO_2 capture efficiencies, such as the HyPr-RING process [92], the LEGS process [93] or the "Calcium Looping Process" (CLP) [94]. Moreover, a negative emission cycle with biomass gasification in interconnected CFB have been demonstrated at pilot scale (AER cycle [95]).

This SE-SMR method is the base of this thesis and it is explained in deep in subsequent sections.

1.4.2 CO_2 transportation

CO_2 transportation is considered a mature technology. CO_2 is regularly transported safely in pipelines across large parts of the U.S. and Canada. Natural gas contents CO_2 naturally. During the transport of liquefied natural gas CO_2 crystallizes, producing important operative problems. Thus CO_2 is separated from natural gas and re-injected in the gas deposit. CO_2 is re-injected in order to maintain the pressure in the deposit, reducing the extraction costs. Hence, CO_2 is transported from and to refineries and deposits.

The best conditions to transport CO_2 is under supercritical conditions ($P>73.8$ bar and $T<31.4$ ºC). Under these conditions handling and transport are fast and easy. Compression of CO_2 implies a cost, higher in the case of atmospheric capture techniques (e.g. CaL in post-combustion) than at pressurized systems (e.g. IGCC pre-combustion). Moreover, the CO_2 must be dried and purified previously in order to avoid operational problems [51].

Some transport ways have been proposed, by train, by ship and by pipelines. Train and ship transport is proposed in order to reuse the available technologies for liquefied gas transport. However, they are more limited and expensive than pipelines [49]. In any case, the cost of pipelines is strongly dependent on diameter, as well as the length, thus a good planning is required in order to project the pipelines[86].

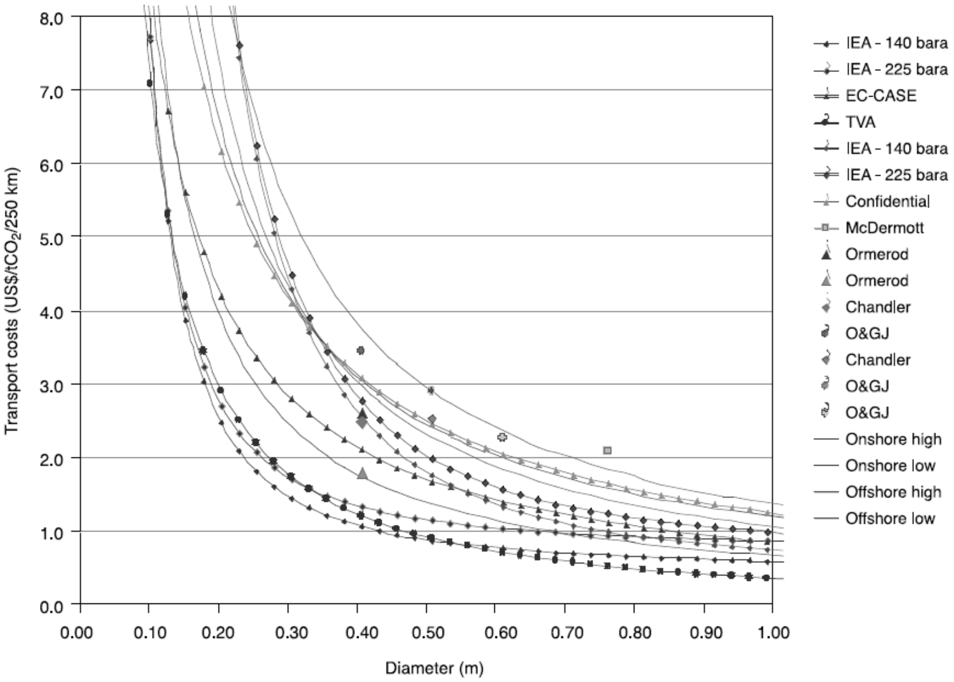

Figure 1. 23 – Cost of CO_2 transportation (each 250km) as function of diameter pipeline and pressure [49].

1.4.3 CO_2 storage

Safe and secure CO_2 storage has been demonstrated, and is still being demonstrated, at a number of sites across the world, with multi-year injections of around 1 Mt per year at a number of sites. Total CO_2 storage capacity is also being proven, but will be sufficient for many years of CO_2 emissions.

Geological storage is cheaper and less uncertain option to CO_2 storage, at medium-term, than other options as ocean storage or mineral carbonation [49]. Figure 1. 24 shows the four ways suggested by IPCC to underground geological storage:

1. Depleted oil and gas reservoirs.
2. Use of CO_2 in enhanced oil and gas recovery.
3. Storage in deep saline formations (offshore or onshore).
4. Use of CO_2 in enhanced coal bed methane recovery.

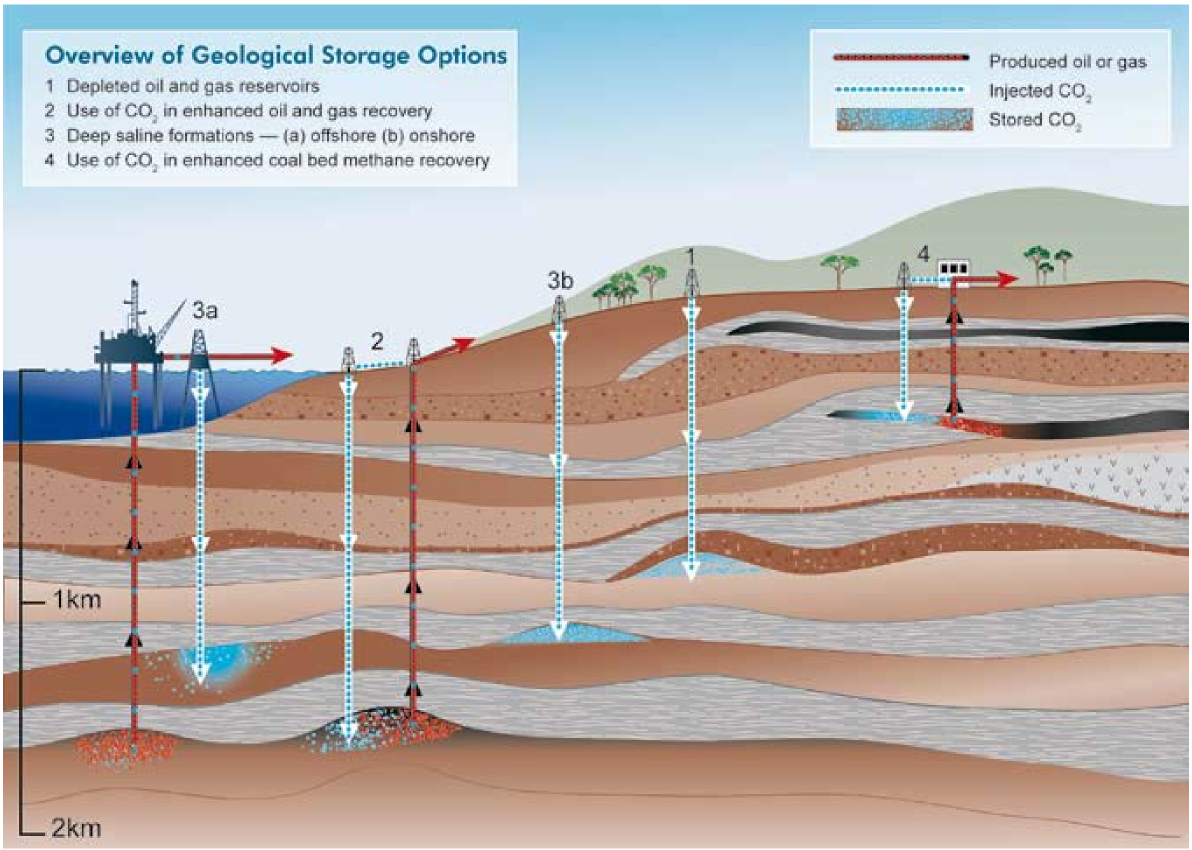

Figure 1. 24 – Methods for storing CO2 in deep underground geological formations [49]

Depleted oil and gas reservoirs are prime candidates for CO_2 storage for several reasons. First, the oil and gas that originally accumulated in traps did not escape demonstrating their integrity and safety. Second, the geological structure and physical properties of most oil and gas fields have been extensively studied and characterized. Third, computer models have been developed in the oil and gas industry to predict the movement, displacement behavior and trapping of hydrocarbons. Finally, some of the infrastructure and wells already in place may be used for handling CO_2 storage operations. Depleted fields will not be adversely affected by CO_2 (having already contained hydrocarbons) and if hydrocarbon fields are still in production, a CO_2 storage scheme can be optimized to enhance oil (or gas) production.

CO_2 has been injected to enhance oil recovery (EOR) in wells for over three decades and has become the second largest EOR technique after steam flooding [96]. The selection of EOR technologies depends on a number of technical and economic variables including oil density and viscosity, the minimum miscibility pressure, microscopic sweep effects, and the formation of vertical and lateral heterogeneities. Thus, CO_2-EOR is limited to oilfields deeper than 600 meters where a minimum of 20% to 30% of the original oil is still in place and where primary production (natural oil flood driven by the reservoir pressure) and secondary production methods (water flooding and pumping) have been applied. Few oil fields have reached this stage [50], but several projects are operating in the world as Figure 1. 25 shows.

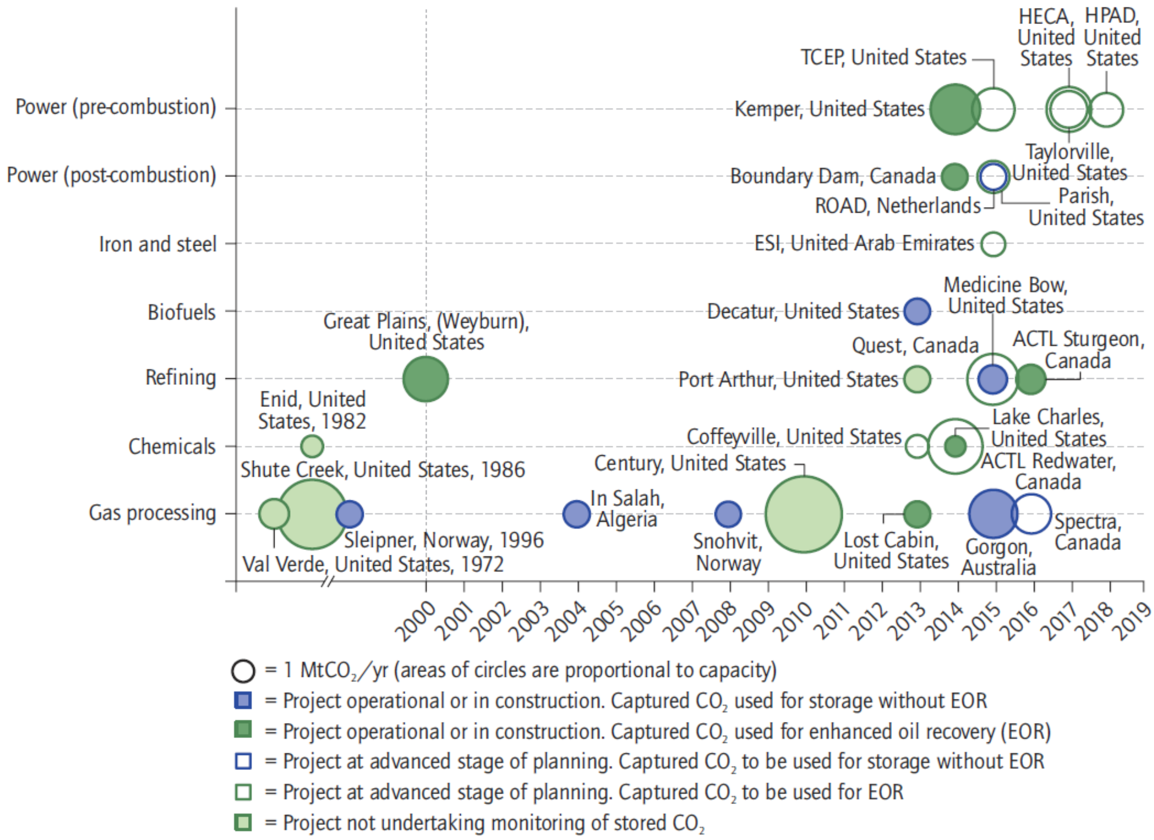

Figure 1. 25 – Large-scale CO_2 capture projects in operation, under construction or at an advanced stage of planning as of end-2012, by sector, storage type, capture potential and actual or estimated start date [20]

Deep saline aquifers represent in the long term the largest potential CO_2 sink. They have generally been much less well-characterized than oil and gas fields due to the absence of commercial drivers. Saline aquifers are layers of sedimentary rocks that are saturated with water. These formations are widespread and contain enormous quantities of water, but are unsuitable for agriculture or human consumption. Many aquifers, particularly those in sandstone and carbonate rocks, are permeable enough for water to be pumped from them or for fluids to be injected. Sedimentary basins can be further subdivided by a number of criteria [97]. Based on this analysis, only some basins are suited for CO_2 storage, and several work has been realized in order to characterize them [98-100], including Italian and Spanish cases [101, 102].

Inaccessible by mining coal seams are those that are either too deep or too thin to warrant commercial exploitation. Most coal contains methane absorbed into its pores. The injection of CO_2 into deep inaccesible coal seams can be used both to enhance the production of coal bed methane and to store CO_2. The first application of enhance coal bed methane (ECBM) has been under consideration, along with nitrogen injection, for more than a decade and it is still under demonstration. To be suitable for ECBM, coal-bed reservoirs need to meet several criteria as coal-bed depth (up to 1 500 metres), pressure and temperature; coal rank, composition and ash content; local hydrology and ability to dewater; sufficient thickness of coal seams and good lateral continuity; and minimum faulting and folding.

1.5 The ZECOMIX project – A novel pre-combustion cycle

Zero Emission Coal MIXed (ZECOMIX) project is a 100kW$_e$ ENEA's pilot plant designed in order to testing experimentally a novel CO_2 pre-combustion method. The aim of the project is to demonstrate at semi-industrial size the production of hydrogen and electricity from coal. The novelty in the proposed process is that, despite the conventional gasification process used in IGCC plants, the coal hydrogasification is an exothermic reaction and no energy input is needed to produce syngas. In addition, efforts have been made to integrate in the proposed plant a SE-SMR system. This technology is based in the ZECA cycle (which integrates coal hydrogasification with fuel cell to produce electricity [103, 104]). The main modification is to operate at high pressure, which allows the integration with a hydrogen turbine. This modification allows to obtain very high efficiency of the cycle (approximately 50%) [105-107]. Figure 1. 26 shows the scheme operation of the cycle.

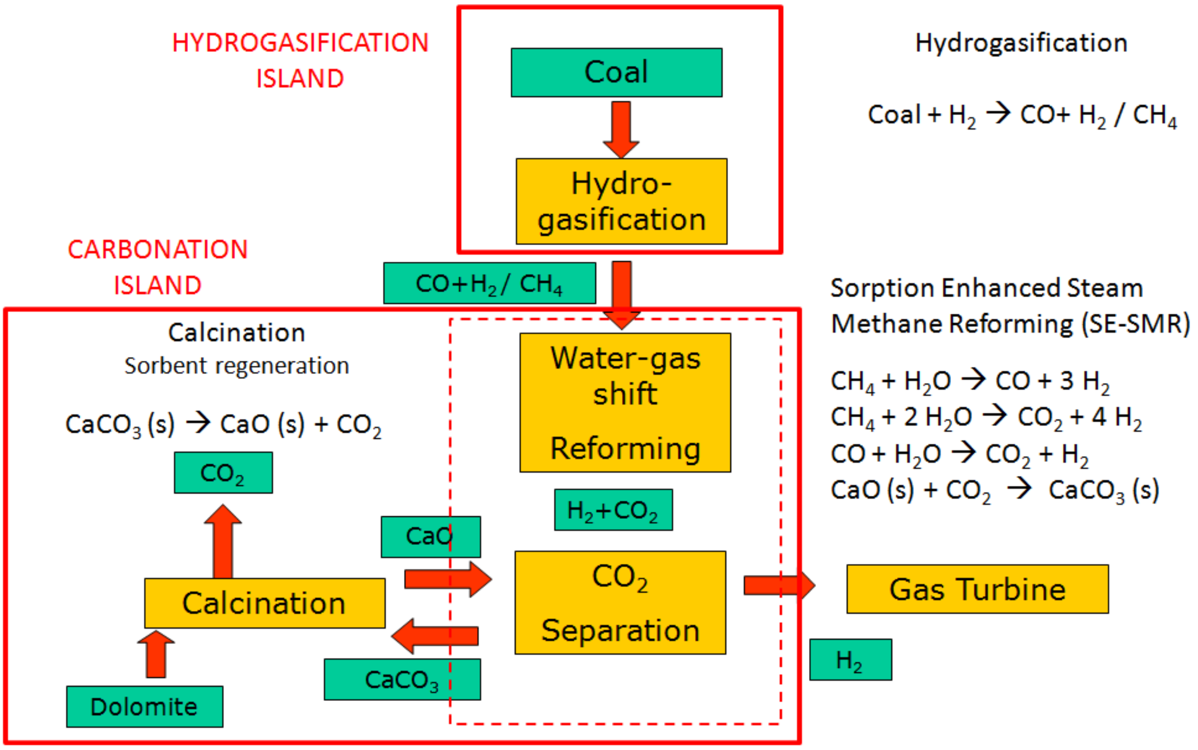

Figure 1. 26 – Scheme of ZECOMIX cycle

The plant is divided in four sections: coal hydrogasification island, steam methane reforming with water gas shift unit, carbon capture unit and a power plant based on an hydrogen-fuelled internal combustion turbine. The most notable aspect of the whole process is the way by which carbon dioxide is separate from the syngas in the aforementioned carbon capture unit, called carbonator, where CO_2 capture and steam methane reforming are produced simultaneously.

Firstly the coal is gasified with hydrogen in a fixed bed. This process is produced at medium-high pressure (7-80 bar) and temperature (800-1200°C). A methane-rich syngas is produced. The syngas is sent to the carbonator reactor, after a sulphur and ash removal process.

In the carbonator the process called SE-SMR takes place in a bubbling fluidized bed. Gas phase is formed by syngas mixed with steam. Solid phase is composed by reforming catalyst and a CO_2 solid sorbent. Catalyst is necessary to the reforming reaction. The addition of a solid sorbent for the selective removal of CO_2 has a double aim. On one hand, the equilibrium of the reforming reaction is shifted beyond their conventional thermodynamic limits, increasing hydrogen production and removing the carbon on the syngas. On the other hand reaction reforming and capture are energy-balanced at lower temperature (from 850ºC to 600ºC), with an important reduction of energy demand. The hydrogen-rich syngas produced is sent to a hydrogen modified micro-turbine with a nominal power of 100 kW_e.

The capture capacity of solid sorbent is naturally limited to the CaO accessible grains presents in the sorbent. When sorbent is saturated it will be driven to a calciner, where a thermal regeneration process of the sorbent takes place. During calcination (at 900-1000ºC) a pure CO_2 stream is produced.

Hydrogasification kinetics is slow at low pressure, thus under the best conditions the reaction takes place at T=600-800ºC and P=30-60 bar. The pressurized operation of hot gases is a very expensive in a pilot plant. Thus, during the project and erection phase of the ZECOMIX plant, an atmospheric configuration has been also considered. A 50 kg/h atmospheric coal steam gasifier has been constructed. This gasifier allows a higher flexibility in the plant, because syngas produced can be tested in the hydrogen turbine. Moreover, if SE-SMR would be tested at atmospheric pressure, syngas can be doped with methane in order to simulate the syngas generated in the hydrogasification step. The layout of ZECOMIX plant is presented in Figure 1. 27.

ZECOMIX pilot plant presents several challenges such as coal hydrogasification optimization, pressurized gas cleaning system, modified hydrogen turbine operation [108], hydrogen equilibrium shift of syngas reforming [85], etc… However, during this thesis we have focused our work in modeling and simulating the SE-SMR process. This technology is still under development and it is one of the most promising routes to energy efficient hydrogen production with CO_2 capture.

SE-SMR process with fluidized beds has been only demonstrated at laboratory scale. Thus it is difficult to predict the behavior of the system at industrial scales. This work is devoted to the modeling, by means of computational fluid dynamics (CFD) tools, of the carbonator reactor of the ZECOMIX plant (approximately 400 kW_{th} power output). In order to develop an accurate model the first aspect to discuss is the selection of an appropriate CO_2 solid sorbent.

Firstly, natural carbonates (as limestones and dolomites) have been proposed. However, this sorbents presents a low useful life, due to a decay in the carrying capacity of CO_2 with regeneration cycling. If useful life is low, solids sorbent must be substituted by fresh sorbent frequently. During the substitution of sorbents, an increase of the cost is generated due to the cost of acquisition and calcination of fresh material, and to losses of catalyst. Thus a method to increase the CO_2 capacity of the sorbents has been studied.

Secondly, a novel manufactured sorbent have been synthesized. Synthetic sorbents present a higher cost than natural ones. However, if they are treated correctly, they can achieve a good activity for hundreds of cycles, becoming economically viable.

The CO_2 capture reaction has been modeled for both sorbents. This model and reforming kinetics have been implemented in a multiphase model in model to simulate the carbonator reactor at laboratory scale. Once the complete model has been tested, it has been used (with some modifications) to scale-up the process to the semi-industrial ZECOMIX size.

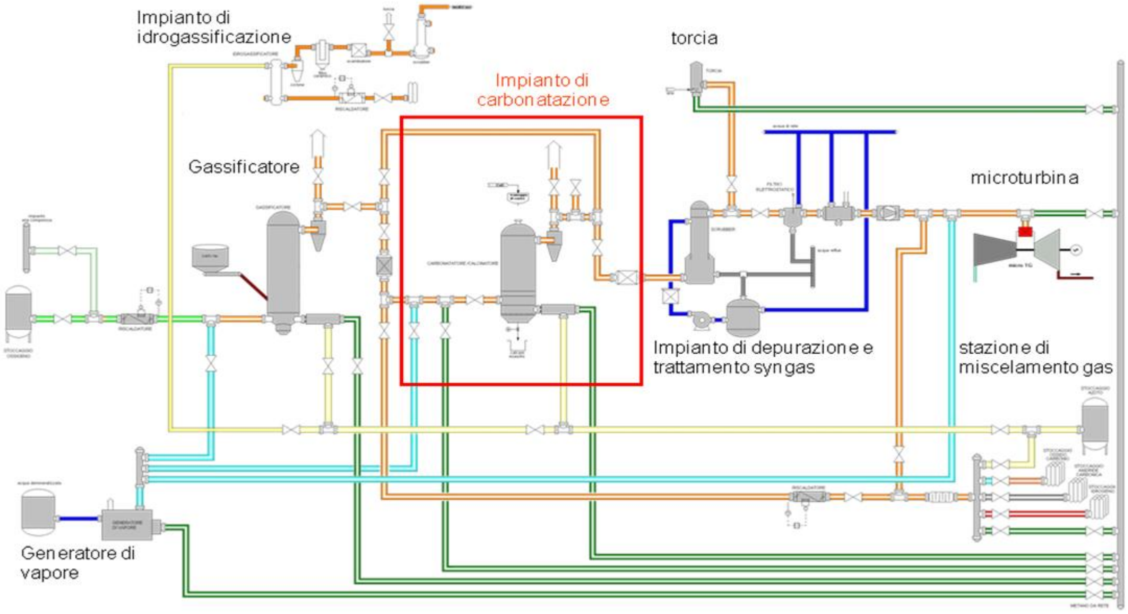

Figure 1. 27 – Layout of ZECOMIX pilot plant. In red is the carbonator reactor.

1.6 Hydrogasification of Sulcis coal

ZECOMIX plant has been designed to operate with Italian autochthonous coal. This work is centered in the carbonator reactor of ZECOMIX. However, some preliminaries works on coal hydrogasification process have been carried out.

Most of the Italian coal reserves are located in the Sulcis basin (South-West zone of Sardinia Island). Sulcis is a sub-bituminous coal and presents high sulphur content (6-7 %wt. as received). In Table 1. 2 the typical composition of Suicls coal is summarized. In spite of the use of this type of low rank fuel represents a decrease on the power plants efficiency, due the small heating value and the need of sulphur removal equipment, Sulcis coal is a very important option to ensure a mid-term energy supply in Italy.

Table 1. 2 – Proximate and ultimate analysis of Sulcis coal

PROXIMATE ANALYSIS	[wt %]
Moisture	5,25
Volatile	40,73
C Fixed	40,23
Ash	13,79
LOW HEATING VALUE [MJ/kg]	21
ULTIMATE ANALYSIS	[wt %] D.A.F.
Carbon C	71,12
Hydrogen H	5,09
Nitrogen N	1,94
Suphur S	7,34

Hydrogasification kinetics is very slow at low pressure, thus a high pressure must be used in order to accelerate the reaction. Typically, the best operating conditions are T=600-800ºC and P=30-60 bar.

$$C\,(s) + 2H_2 \rightarrow CH_4 \;;\; \Delta H^0_{298} = -75\,kJ\,/mol \qquad (1.\,1)$$

Hydrogasification of coal and other chars is a much slower process than steam or carbon dioxide gasification; moreover, the rate of gasification in pure hydrogen decreases sharply with conversion for most carbons [109, 110]. Some treatments as partial oxidation of partially hydrogasified or heat-treated chars, or addition of catalyst (K_2CO_3) enhance the rate of hydrogasification either by removing strongly chemisorbed hydrogen or by generating surface structure active in hydrogasification. [111]

Until 2012, there are very few works about Sulcis coal gasification and combustion [112-115]. However in the last years several studies have been published in order to characterize this coal under hydrogasification [116-118] and pyrolysis [119, 120] , as well to its implementation in CCS technologies [121-124].

In order to obtain the optimal operation point for hydrogasification process an equilibrium model has been applied in a commercial chemical process software (ChemCad 5.2[125]). The best operational conditions have been obtained as 600ºC and 30 bar. No significant changes in composition or conversion have been observed if pressure or temperature are higher, as shown in Figure 1. 28 [126].

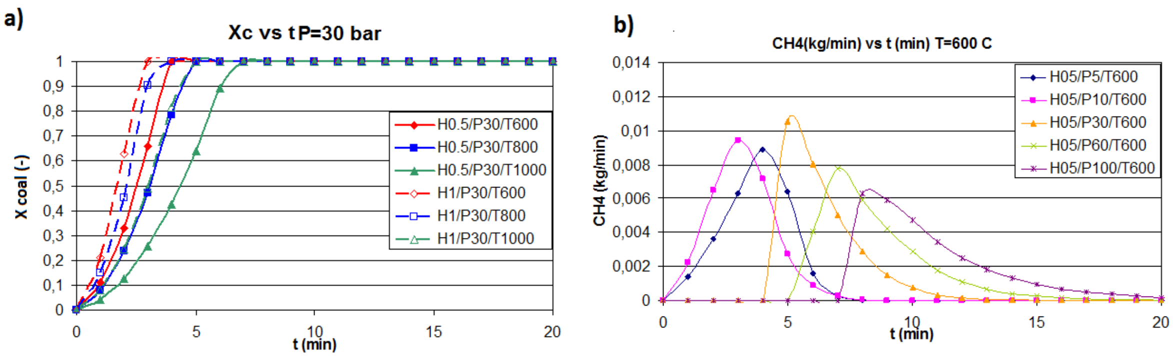

Figure 1. 28 – Coal conversion at P=30bar for different temperatures and hydrogen flow rate (a) and methane evolution at different pressures at T=600ºC (b) during hydrogasification equilibrium simulation

This type of simulations is very useful but presents some limitations. The use of equilibrium model is a strong hypothesis due to the slow rate of hydrogasification reaction and the uncertainties of the process. On the other hand, the species present in the product gas must be fixed a priori. In other words, the gas-solid reaction are supposed in equilibrium and the species generated are fixed by the user, thus kinetics of each reaction are neglected.

Thus, some works have been carried out in order to develop a kinetic model of Sulcis coal hydrogasification. This process can be divided in four steps:

1. Heating and drying, up to 100ºC. During this step the moisture present in the fuel is released. It is a endothermic reaction, thus, if moisture of the fuel is very high a decrease of temperature is produced. If the decay of temperature is excessive the reaction cannot takes place.

2. Devolatilization, between 350 and 900ºC. Once the drying process is concluded, the particle heats up to the temperature necessary for the beginning of the devolatilization process. Devolatilization or pyrolysis is the process where a wide range of gaseous products are released though the thermal decomposition of the fuel, leaving a solid porous residue called char.

3. Volatiles reaction. Once the volatiles are released they reacts with the atmosphere gas. Depending on the atmosphere conditions different products are obtained.

4. Char hydrogasification, up to 900ºC. Char hydrogasification is the last step in the process. It is a slow process compared to devolatilization and gas phase reactions, therefore the efficiency of the reactor depends mostly on this stage. The char consists mainly of fixed carbon, ash, nitrogen and sulphur. Char reactivity depends on its morphology and on the reaction conditions such as temperature, pressure and oxygen partial pressure. In the hydrogasification process the dominant reaction is presented in Eq. 1.1. However other difficult to characterize side reactions take place.

Devolatilization and char hydrogasification are the most important processes to characterize the global process of hydrogasification.

In order to model devolatilization step some global models have been applied to thermogravimetric (TGA) tests in order to characterize kinetics of Sulcis coal devolatilization. The scope is to obtain, under laboratory conditions, kinetic parameters that can be applied to industrial conditions. Some models have been evaluated, and in general presents good results compared with similar coals. However, there is not only a global model capable to reproduce very accurately the complete devolatilization process, due to the important influence of secondary pyrolysis in this coal.

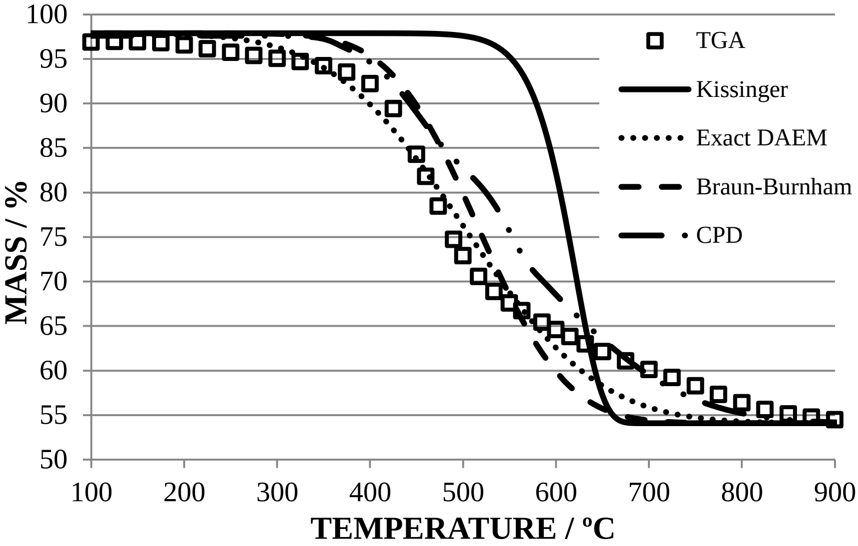

Figure 1. 29 – Experimental values of mass loss during coal devolatilization at 100 K min-1 and the predicted ones assuming different global pyrolysis models.

Thus, a novel 2-Distributed Activation Energy Model (2-DAEM) has been developed in order to model accurately the coal devolatilization. A typical approach divides in primary and secondary pyrolysis the devolatilization step. Between 400-700ºC the primary devolatilization takes place. In this phase, the weakest bridges may break to produce molecular fragments that can recombine producing tars (condensing at room pressure and temperature), or can be released as light volatile compounds (mainly CH_4, C_2H_4, CO_2, and, depending on coal sulphur content, COS and SO_2). For temperatures above 700 °C the condensation of the carbon lattice with evolution of CO and H_2 takes place to produce char during the secondary pyrolysis.

The 2-DAEM distributes the relative weight of primary and secondary pyrolysis in the global devolatilization process, as function of the fuel composition. This method has been demonstrated to be a powerful tool to predict devolatilization kinetics in different rank coals and biomasses.

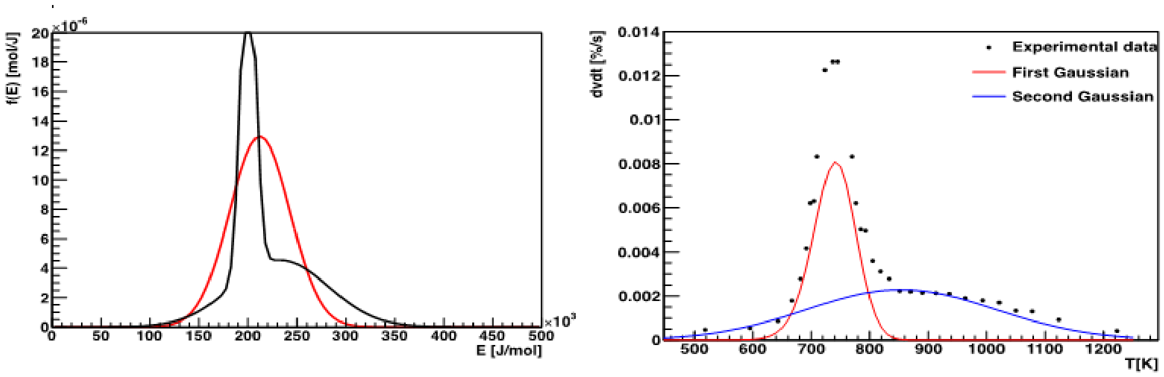

Figure 1. 30 – The distribution activation energy curves as a function of activation energy, in red the curve for 1-DAEM in black for 2-DAEM (left). Comparison between experimental reaction rates and reaction rates obtained with the 2-DAEM kinetic parameters for a heating rate of 100K/min (right)

A more detailed description of models of Sulcis coal devolatilization can be found in Annex A. Devolatilization step is very fast compared with char hydrogasification process. Based in experimental data, intrinsic kinetics of Sulcis char hydrogasification can be obtained [116, 118]. However, instead of the efforts realized in the last years, the global hydrogasification process of Sulcis is not fully characterized, and some studies still must be carried out.

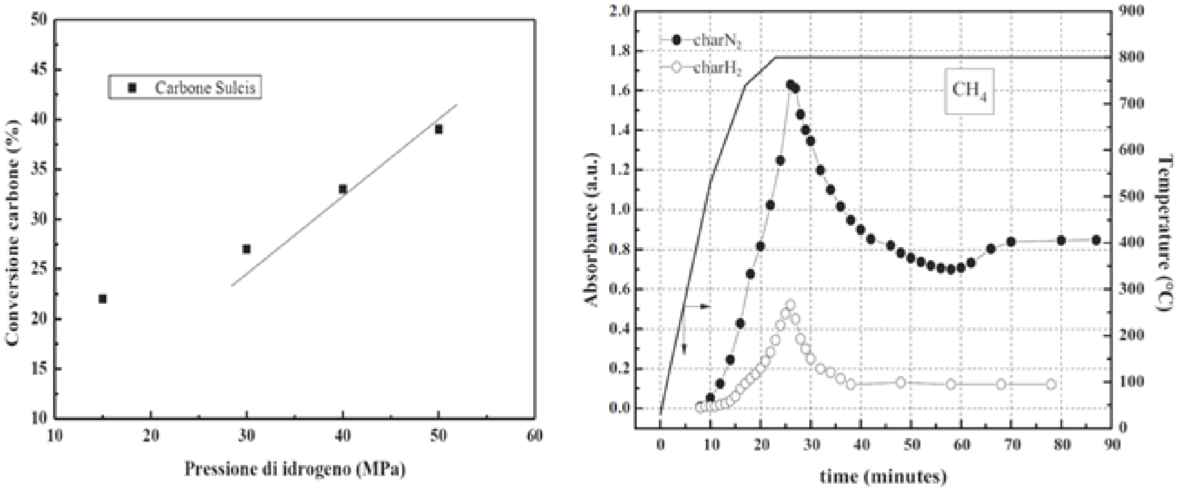

Figure 1. 31 – Experimental coal conversion as function of pressure (left) and methane evolution under N_2 and H_2 atmospheres [116, 118]

2 SOLID SORBENTS FOR HIGH TEMPERATURE CO_2 CAPTURE

The high temperature calcium looping for CO_2 capture is a promising technology to mitigate greenhouse gases emissions in industrial sectors other than power generation. The choice of a high performance sorbent is fundamental to improve the systems based on carbonation/calcination cycles. Calcium-based sorbents have demonstrated a good compromise between cost and performance.

CaO-based chemical looping is being studied as a promising technological option for reducing CO_2 emission into the atmosphere. One of the key advantage of this option which makes it a valuable route in gas decarbonization is the low cost and wide availability of the starting material and its high reactivity when reacts with CO_2. Moreover the CaO based solid sorbent are more environmentally benign compared to other state-of-the-art solutions proposed (e.g. amine-based liquid solvents).

When the CaO is converted to the calcium carbonate, the spent solid sorbent is sent back to the regeneration process where an active sorbent is regenerated for a new carbonate looping. Such a technology could be easily accomplished by means of a fluidized bed where gasification, methane steam reforming or water gas shift reaction occurs improving hydrogen production. As reported in the scientific literature [69, 127-131], when naturally occurring material as calcite or dolomite are used as CO_2 acceptor in a Calcium Loop (CaL), there is a decay of reversibility. The ideal CO_2 sorbent in a CaL must exhibit a number of properties: high and stable CO_2 uptake capacity throughout continuous decarbonizing-regeneration cycling, fast reaction kinetics, uptake capacity and kinetics close to theoretical maximum values, and also mechanical stability and sintering resistance. In an attempt to achieve this goal, researchers have developed novel synthetic sorbents based on e.g. CaO dispersed on calcium aluminate ceramic supports. [132-135].

Considerable importance is being put on naturally occurring carbonates e.g. limestone ($CaCO_3$) and dolomite ($[Ca,Mg]CO_3$) as CO_2 acceptor for decarbonizing reformed/shifted fuel gases or flue gases. When the material is exposed to CO_2, the fresh CaO grains which compose the sorbent are converted into $CaCO_3$. As the sorbent is completely carbonated or the gas-solid reaction shows negligible extent, calcination under atmospheric pressure and temperature greater than 850 °C allows to obtain a regenerated material for further CO_2 uptake cycles. The main drawback of such a process is the marked decrease during the first few cycles with regard to CO_2 uptake when used limestone or dolomite in repeated cycles of carbonation/sorbent regeneration [136, 137]. This loss of reversibility is due to the CaO sintering which happens during the high temperature regeneration step and the pore-mouth blockage [138, 139]: albeit dolomite shows greater resistance to the sintering and pore-plugging when compared to limestone. The higher reversibility is likely due to the presence of MgO which acts as an inert binder during the carbonation of calcined dolomite inhibiting sintering of the active phase grains (CaO) and the pore closure. Due to this ability to retain pore volume through carbonation/calcinations cycles, dolomite derived sorbent is widely studied showing better results among the naturally occurring carbonates. Unfortunately, the negative features of capture decay with cycling shown by naturally occurring sorbents, counteracts the advantage of their low cost and limits their use as CO_2 acceptors under industrially relevant conditions. Thus, there is a need to select sorbent material which shows no decay after repeated cycling. Generally, in order to fulfill high and stable CO_2 uptake capacity two main routes are adopted by the scientific community: the synthesis of new materials [131, 134, 140] and thermal/chemical pre-treating of naturally occurring carbonates for improving their stability during cyclic operation. With regards to the synthetic materials efforts are being made to manufacture materials in an economically viable way with long life times and then slight environmental footprints [141, 142].

Besides the attempts to develop new synthetic sorbents with tailored properties there is also the option to modify naturally occurring carbonates to improve their properties. Thermal pretreating at high temperature (1000 – 1100 °C) of natural dolomite or limestone [143-145] and chemical pretreating as hydration with steam [146-148] or stabilized with metals (e.g Cu, Cr, Co, Mn) [149-151] improves the CO_2 uptake capacity to some extent during cyclic operation at high temperatures. Among the available pretreatments, thermally stabilization is the most promising route as it does not lead to a great raise of carrying capacity in the pretreated when compared to the aforementioned metal-stabilized naturally occurring minerals. Although promising results, most of the thermally stabilized materials have so far exposed at regeneration in a 100% nitrogen atmosphere without taking into account the effects from CO_2 on sintering. In fact, when dolomite and limestone are calcined in a CO_2 containing atmosphere sintering processes can occur [152-154]. In order to enhance the contact between the solid sorbent and the CO_2 and facilitate regeneration step, carbonation/calcinations cycles are accomplished in fluidized bed (FB) reactors. Instead of the FB presents some shortcomings compared to other reactors (e.g., entrained, fixed bed): large volume, thus investment, scalability problems, etc. this mature technology appears as the most suitable to perform carbon dioxide separation. Because it guarantees temperature homogeneity throughout the vessel, good gas-solid mixing, reduced mass and heat transfer resistances due to the possibility to operate with small particles. Hence this chapter is devoted to the study on the, in one hand, the thermal treatment during the first calcination of a natural sorbent (Dolomite – $CaCO_3 \cdot Mg\ CO_3$), and, on the other hand, the study of the behavior of a synthetic sorbent (Mayenite – $CAO/Ca_{12}Al_{14}O_{33}$) under realistic conditions and the effect of thermal treatments in the activation of the sorbent.

2.1 State-of-art of solid sorbents for high temperature CO_2 capture

2.1.1 Natural sorbents

The first proposals for the use of calcium-based sorbents to capture CO_2 from flue gases at high temperature were realized by Silaban and Harrison [146] and Shimizu et al. [155], during the 1990's. However, the basic calcination/carbonation loops for the use of limestone as CO_2 acceptor were studied from the 1950's [156-159], and the first patent concerning to the use of lime as CO_2 separator (in gasification of carbon by steam) goes back to 1867, by DuMotay and Marechal.

The calcination/carbonation reactions are:

$CaCO_3$ (s) → CaO (s) + CO_2 (g) ΔH^0_{298} = + 182.1 kJ/mol Calcination (2.1)

CaO (s) + CO_2 (g) → $CaCO_3$ (s) ΔH^0_{298} = - 182.1 kJ/mol Carbonation (2.2)

Calcination reaction is favored at high temperatures. The cycling of carbonation and calcination are produced by means of thermal swing through the equilibrium of CaO-CO_2 system. In other words, calcination is produced if partial pressure of CO_2 in the gas around the particles is less than equilibrium pressure; therefore the temperature is increased in order to obtain a higher equilibrium pressure and promote the calcination. A typical expression for equilibrium decomposition pressure is [137]:

$$P_{eq} = 4.173 \times 10^7 e^{-20474/T} \ atm \tag{2.3}$$

The equilibrium curve is presented in Figure 2. 1.

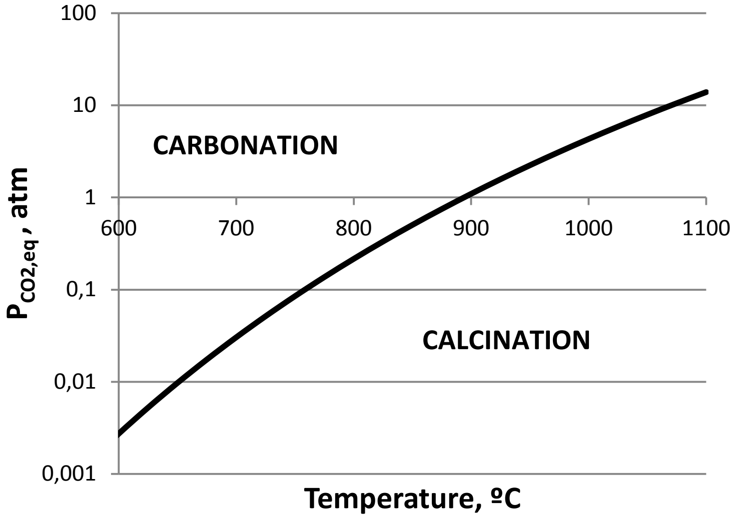

Figure 2. 1 - The equilibrium pressure of CO_2 on CaO.

Instead of the reversibility of carbonation reactions, of CO_2 which are able to retain the particles of CO_2 in the first carbonation cycle is lower than the CO_2 released during the first cycle, and the CO_2 uptake capacity of the sorbents decay with cycling, as shown in Figure 2. 2.

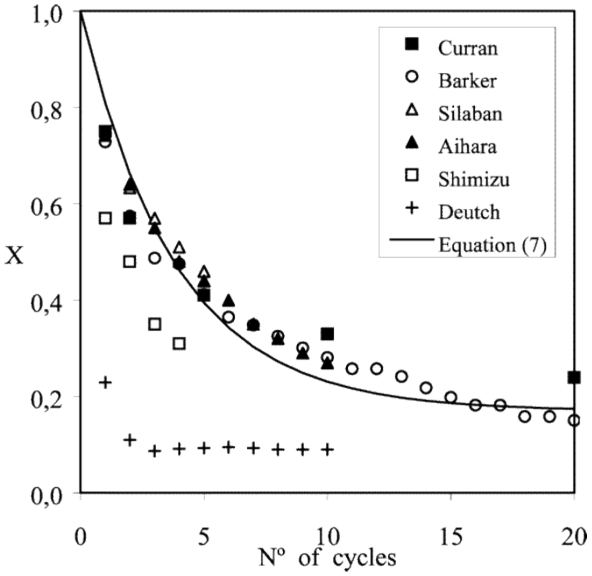

Figure 2. 2 - The decay in maximum carbonation conversion (X) with the number of cycles [160]. Equation (7) corresponds to Equation 2.4 in this work

This decay is due to the evolution of pores in the particles. In the one hand, the large pores increase their diameter with cycling, reducing their activity because the active pores for CO_2 capture are under 220nm [161], and the mesopores formed are less active. On the other hand, due to sintering the occlusion of small pores is produced, losing microporosity. The diameter of active pores is limited by the thickness of product layer that controls the conversion of CaO grains. Abanades and Alvarez [160] developed a very simple and accurate correlation in order to obtain the conversion of particles as function of number of cycles, including the mechanism of evolution of pores for a wide range of conditions:

$$X_N = f_m^N (1 - f_w) + f_w \tag{2.4}$$

Where X_N is the maximum carbonation conversion in the N cycle. f_m is the fractional loss of the conversion due to microporosity losses:

$$X_{N,m} = f_m \cdot X_{N-1,m} = f_m^N \cdot X_{0,m} \tag{2.5}$$

And f_w is the net loss of total porosity in the particle (also called shrinking), and it is proportional to fraction of specific surface associated with the void volumes forming the mesoporosity, and to the thickness of the product layer according

$$X_{N,w} = f_w \cdot (1 - X_{N,m}) \tag{2.6}$$

Both f_w and f_m remain constant with cycling and can be fitted directly from experimental data.

This model has been extensively applied to different sorbents under very different operation ways with very accurate results including very long term cycling [162]. Instead of the attempts to reduce the sintering of the sorbents with cycling, the decay of capture capacity is always observed in the cases of constant short-time carbonation/calcination cycles (less than one hour) [161, 163]. Thus, some cost-effective treatments were developed in order to reduce the limitations of sorbents in, mainly, two different approaches. On the one hand, some thermal treatments of fresh sorbent were proposed with the aim to stabilize the internal structure of solids. On the other hand, regeneration of exhausted sorbents (by means of steam or carbonation) was developed.

2.1.1.1 Thermal treatments of natural solids sorbents

Figure 2. 3 presents the decay behavior of sorbents ($X_{Nage,Nage+1,...}$) and the previous history of solid. The conversion increases by *carbonation*, as far as a maximum limited by the natural *deactivation*. However, if a *pre-calcination* or a *self-reactivation* method is applied to the sorbent, the previous history cannot be estimated and the global performance increases.

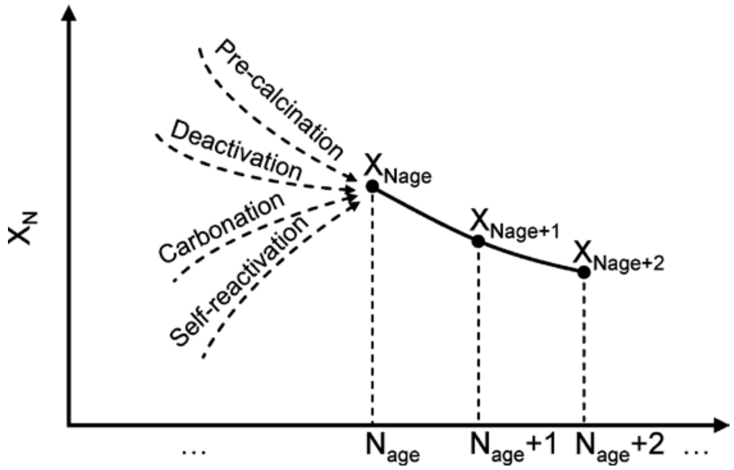

Figure 2. 3 – Schematic representation of thermal treatments previous to the natural decay of solids sorbents with cycling from [164]

Manovic and Anthony [143] observed that, if 500μm calcined limestone is exposed to a nitrogen atmosphere for long time (24h) at different temperatures, the carrying capacity is improved at 900ºC due to internal annealing of the particle, and decay with higher temperatures by sintering. This process is known as *pre-calcination* (Figure 2. 4a). However, when powdering the samples and repeating the experiments an abnormal continuous increase of carrying capacity with cycling (called *self-activation*) is observed (Figure 2. 4b).

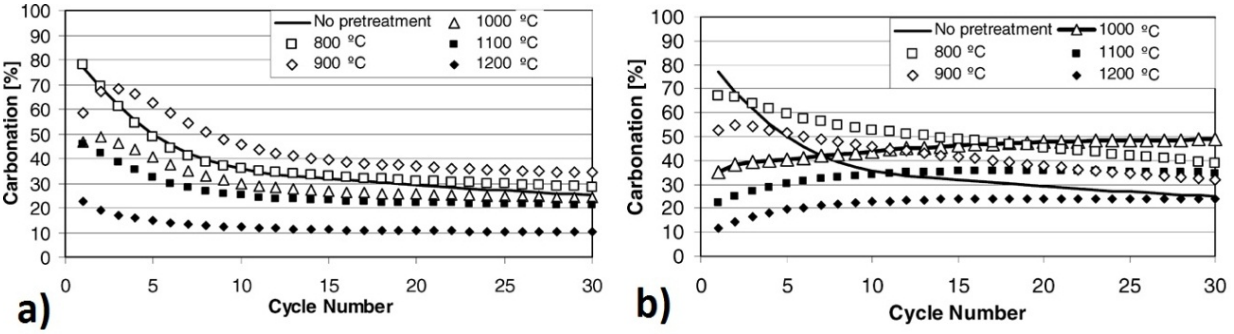

Figure 2. 4 – Limestone behavior by a) Pre-calcination and b) Self-activation methods from [143]

This work is the basis of the development of solid sorbents pellets [165] and the increasing of performance under oxy-fuel calcination conditions [166]. Lysikov et al. [144] proposed a skeleton sintering model that explains the formation of stable structures that prevents the sintering of the particle with cycling. Ozcan et al. observed the same behavior in other sorbents as dolomite or plaster of Paris [167]. In Section 2.2, we proposed a novel pre-calcination method in order improve the carrying capacity of dolomite.

2.1.1.2 Regeneration of spent solids sorbents

Other approach to increase the carrying capacity is based in the regeneration of spent sorbents by means of steam reactivation, or recarbonation. Manovic and Anthony [148] demonstrated that the hydration by steam under pressure is a successful method to reactivate spent sorbent in carbonation/calcination cycling, as well as sulphated particles. During the hydration (from 2 to 24h at 1100ºC) the internal structure of the spent solids changes, due to the formation of $Ca(OH)_2$, with a higher molar volume, increasing noticeably the surface area, reducing the size of sintered grains.

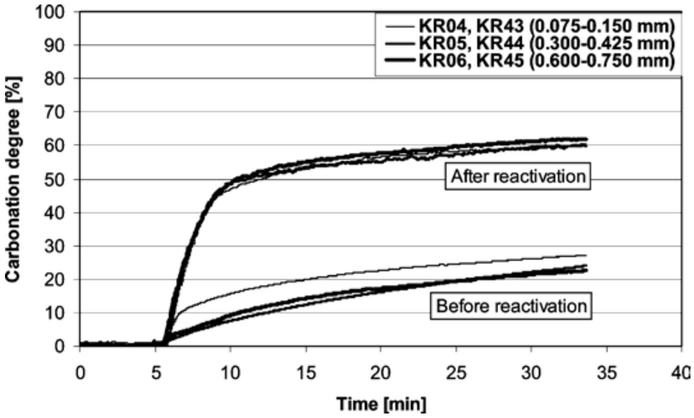

Figure 2. 5 – Steam reactivation effect on sorbent activity during carbonation in the TGA−sorbent calcined/sintered at 1100 °C for 24 h and hydrated by steam from [148]

Lysikov et al. [144], Sun et al.[162], and Chen et al. [139] demonstrated that treated or no pre-treated spent sorbents submitted to an intermediate long carbonation cycle resulted in a substantial recovery in CO2 capture ability. In the subsequent cycles, the calcium utilization efficiency again declined as the cycling continued. Therefore, the increase of surface area due to recarbonation is temporal and decays with cycling.

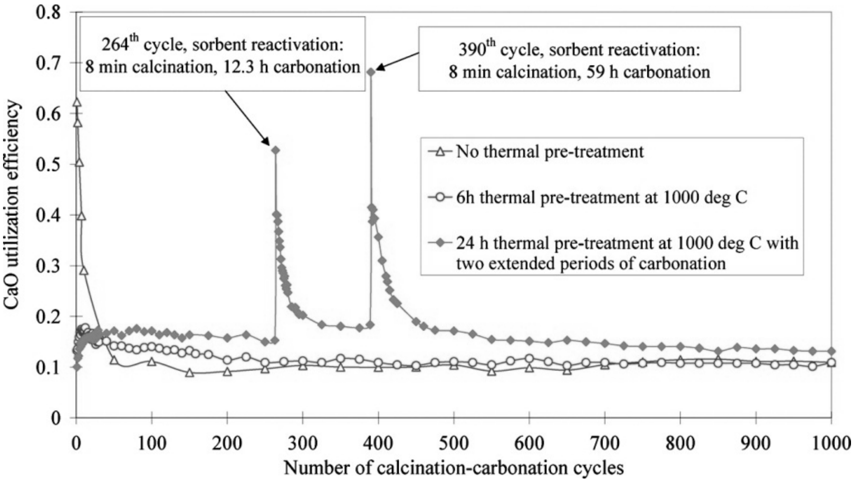

Figure 2. 6 – Results of long-term calcination/carbonation cycling with Strassburg limestone without thermal pretreatment, compared with pretreatment at 1000 °C for 6 h and at 1000 °C for 24 h with two extended periods of carbonation. Calcination/ carbonation cycling was at 850 °C in all cases from [139]

Based in the recarbonation effect observed previously, Arias et al. [168] proposed a modification in the activation of spent solids. It is generally accepted that carbonation reaction presents two different regimes. During the first part kinetics is the limiting step in the reaction and, after some seconds (in Figure 2. 7a 60 sec approx.), diffusional effects dominate the reaction, reducing drastically the rate, until reaching a plateau. In their work they demonstrated that once the plateau is reached, if sorbent is exposed to a higher temperature and CO_2 partial pressure, the carrying capacity and the residual capacity increase noticeably. This *two-step* carbonation presents a behavior different to the direct high concentrated carbonation, in which carrying capacity is lower than in low concentrated atmosphere due to the sintering effect of CO_2.

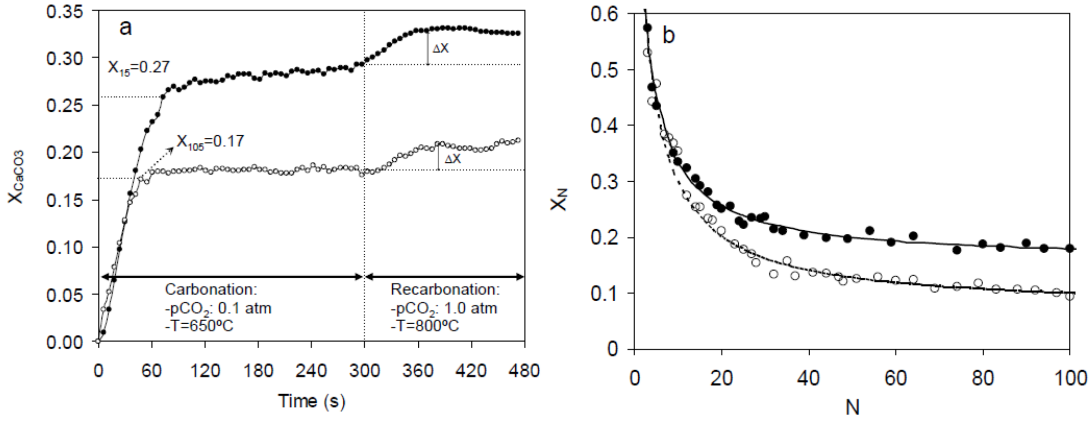

Figure 2. 7 – a) Example of the increase in CO_2 carrying capacity experienced by two particles cycling through the system (black dots, after 15 carbonation calcination cycles and white dots after 100 cycles). b) Evolution of the CO_2 carrying capacity of CaO with the number of cycles (black dots with recarbonation and white dots without recarbonation) from [168].

2.1.2 Synthetic sorbents

Despite of the efforts to improve the carrying capacity of natural lime by increasing the surface area and stabilizing the pore structure, attrition of natural sorbent particles is another main problem in the Ca-looping process. Thus some different types of candidates (i.e. zeolites, activated carbons, calcium oxides, hydrotalcites, organic-inorganic hybrids, metal organics) were proposed in order to improve the CO_2 carrying capacity, adsorption-desorption kinetics, thermal and mechanical stability and regeneratibility [169, 170]. Under the operational conditions for SE-SMR process, the most promising synthetic sorbent are hydrotalcites, lithium-based and calcium-based sorbents (see Figure 2. 8).

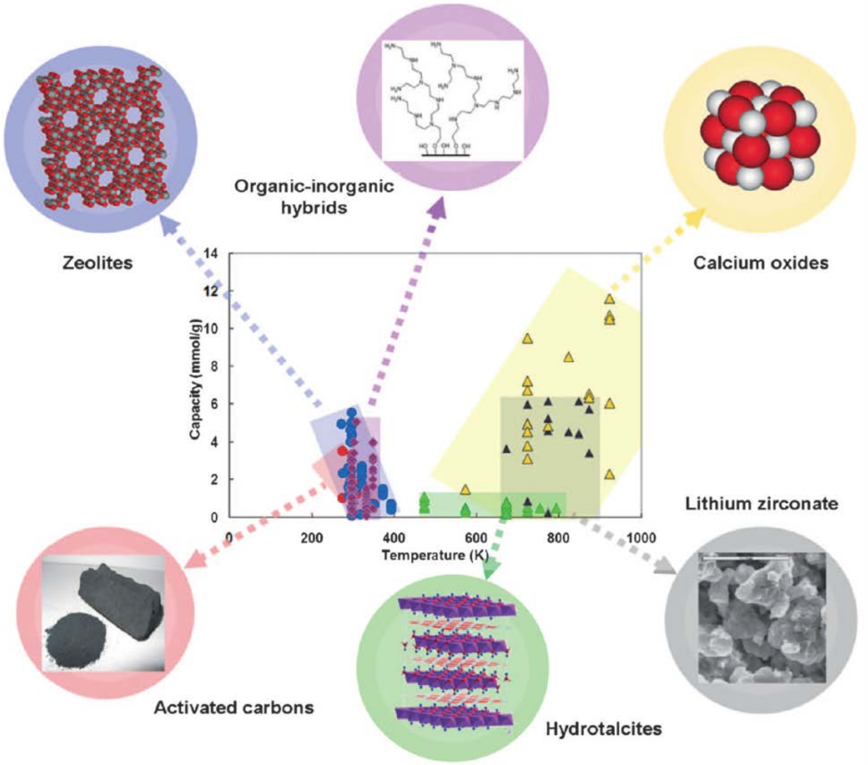

Figure 2. 8 – Schematic representation of the main synthetic sorbents and their carrying capacity and operational temperature window, from [170]

2.1.2.1 Hydrotalcites

Hydrotalcite (HTC) is an anionic clay consisting of positively charged layers of metal oxide with interlayers of anions as carbonates (see Figure 2. 9). This combination implies that the calcined carbonates works as CO_2 acceptor, and the layer of metal oxides can act as catalyst. Due to these properties and to a very good stability, they were proposed for SE-SMR process [171, 172]. However the adsorption capacity and carbonation rate of natural hydrotalcites are sensibly lower than that of lime. Therefore, some processes of doped synthesis were proposed in order to improve the CO_2 capture performance. Reijers et al. [173] proposed the impregnation of HTC with K_2CO_3, meanwhile Meis et al. [174] proposed doping HTC with Mg(Al)O-crystals, increasing in both cases the rate of capture and obtaining a good performance of SE-SMR at relatively low temperatures (250-400 ºC). Other alkali supports (as Cesium, Cs) were evaluated in order to increase the operation temperature to 500ºC [175].

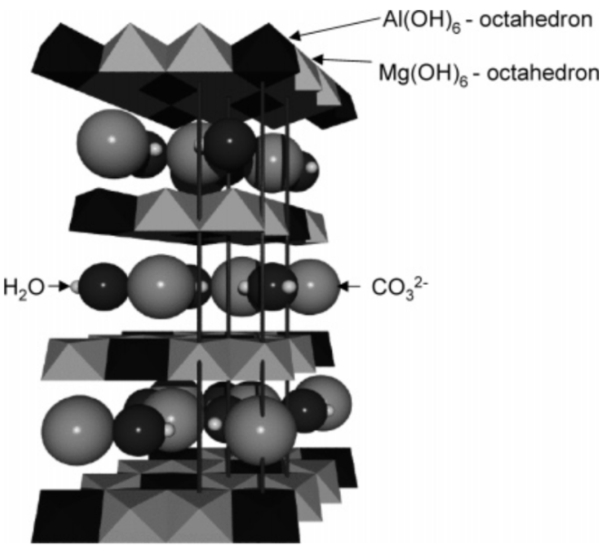

Figure 2. 9 – Structure of natural hydrotalcite, from [173]

2.1.2.2 Lithium-based sorbents

Typically, oxide materials of alkali metals (as Li_2O) has have a lower carrying capacity and a very higher energy requirements during desorption than CaO sorbents, discarding its use as CO_2 acceptor. However, in the late 1990's a newer class of lithium-based oxides (Li_2ZrO_3 and Li_4SiO_4) was proposed for carbon capture. These materials are able to adsorb up to 28 and 36 gCO_2/g sorbent, respectively, according to the following reversible reactions [176, 177]

$$Li_2ZrO_3\,(s) + CO_2(g) \leftrightarrow Li_2CO_3\,(s) + ZrO_2\,(s) \qquad \Delta H = -160\ kJ/mol \qquad (2.7)$$

$$Li_4SiO_4\,(s) + CO_2(g) \leftrightarrow Li_2CO_3\,(s) + Li_2SiO_3\,(s) \qquad \Delta H = -\,142\ kJ/mol \qquad (2.8)$$

The high reversibility, thermal stability up to 600ºC, and carrying capacity of these materials is very interesting, instead of its high price. However, very slow kinetics is the main problem of these sorbents, particularly the zirconate (at 600ºC two days are required to reach equilibrium and adsorption halftime was 12h [178]). Hence, in order to increase the carbonation kinetics, on the one hand, the combination of binary/ternary alkali carbonate eutectic salts to Li_2ZrO_3 was tested. A noticeably improving in the CO_2 uptake rate was obtained particularly with $K_2CO_3/NaF/Na_2CO_3$ eutectic and Li_2ZrO_3 combination at 600°C [179]. On the other hand, the synthesis of sorbent particles from nanocrystalline lithium zirconate were proposed with a considerable improvement of the kinetics [180].

2.1.2.3 Ca-based synthetic sorbents

In comparison with other synthetic sorbents, Ca-based sorbents are the most promising in terms of price competitiveness, carrying capacity and thermal stability. In general, three methods to develop high performance Ca-based sorbents have been developed in order to reduce the sintering of the particles with cycling: a) synthesis of CaO from precursors different to natural limestones, b) addition of dopants, and c) use of rigid and porous supports as CaO carriers [181].

a) Synthesis from different precursors

Precipitated calcium carbonate with a high mesoporous surface area can be synthetized by bubbling CO_2 in a $Ca(OH)_2$ slurry [136]. $CaCO_3$ is obtained by this method and subsequently used in carbonation/calcination cycling, being $Ca(OH)_2$ the precursor. Several other commercial inorganic and organometallic precursors have been studied. These precursors include calcium nitrate tetrahydrate, calcium acetate, calcium propionate, calcium acetylacetonate, calcium oxalate, or, calcium 2-ethylhexanoate, as well as more exotic precursors (e.g. calcium lactacte) [182]. The higher carrying capacity was observed in the cases of calcium acetate and calcium propionate (0.71 and 0.75 gCO_2/g sorbent).

While some studies are centered in obtaining better precursors from chemicals, others are focused in the modification of natural limes by means of chemical treatments. The aim of this works is the synthesis of calcium acetate and calcium hydroxide directly in dissolution of limes in acetic acid and ethanol/water, respectively. By means of these treatments the resistance to sintering and the carrying capacity increases strongly for limestones and dolomites [183, 184].

In any case, these methods suppose two main problems. On the one hand particles obtained are powder, thus the sorbents must be pelletized in order to be used under industrial conditions. On the other hand, these sorbents tested under realistic conditions for long term multicycling present a very similar behavior to natural non-treated sorbents [185].

b) Addition of dopants

The use of sodium salts as dopant of limestones for desulphuration in fluidized bed combustion was studied in the late 1970's with very good results. The presence of salts induces an internal rearrangement, favoring a macroporous-pore distribution in the particles, which optimizes the SO_2 capture [186]. This beneficial effect was also observed for CO_2 capture in TGA experiments. However, during operation in fluidized bed the carrying capacity of doped particles was practically the same as that of non-doped limestones, with a little increase by using NaCl whit respect to Na_2CO_3 [187]. These divergences can be due to the complexity of interpreting data from large-scales systems and to the stability of the porous structure generated in the particles, due to the fact that active pores for CO_2 capture are sensibly smaller than for SO_2 capture. Encouraged by the results of sodium-doped sorbents, researchers studied other alkali-based dopants, obtaining a maximum reactivity for the Cs-doped sorbents. The reactivity of alkali dopants is directly proportional radius of the particles Li < Na < K < Rb < Cs [188].

Recently, Lu et al. developed a new dry dopant method at high temperature, based in refractory dopants (Si, Ti, Cr, Co, Zr, and Ce) with very good promising results [189].

c) Supported CaO sorbents

Another technique useful to enhance the stability of sorbents is reducing the size of the particles to nanometer scale, in this way the diffusion and sintering effects disappear, theoretically, obtaining a conversion over 90% after several cycles [190]. However, once the nanoparticles are compacted in order to form greater particles with industrial interest, the particles present a very pronounced decay in the carrying capacity, almost as natural sorbents [191]. Thus it is necessary a rigid and porous carrier in order to stabilize mechanical and thermally the sorbents.

Some oxides with high melting point has been studied in order to stabilize the CaO: SiO_2 [192], MgO [193], TiO_2 [194], and Al_2O_3. Al-based supports are the most promising carriers in term of stability, price and carrying capacity. Florin et al. [142] obtained a Ca-Al binder from precipitated $CaCO_3$ and $Al(OH)_3$ with a carrying capacity of 0.22 gCO_2/g sorbent over 30 cycles. Pacciani et al. [134] proposed two methods, namely, co-precipitation and hydrolysis of CaO, using mayenite as support. Sorbents obtained by means of co-precipitation present a bad performance, instead the carrying capacity of hydrolysis arrives up to 0.29 gCO_2/g sorbent over 20 cycles.

Li et al. [132] developed a wet synthesis from CaO and $Al(NO_3)_3 \cdot 9H_2O$, where the solid obtained is a mix of CaO and $Ca_{12}Al_{14}O_{33}$ (mayenite) with very good performance (up to 0.45 gCO_2/g sorbent over 15 cycles for 75/25 wt%). Based in this synthesis some modifications were proposed successfully in order to maintain the regeneratibility for cycling as intermediate hydration [141] and the use of calcium precursors (as calcium acetate) [195]. The method proposed by Li et al. is nowadays the most promising synthesis way for the synthetic sorbents and it has been used in the next generation of SE-SMR sorbents which includes in the same particle catalyst and CO_2 acceptor sorbent [196, 197].

In Section 2.3 we explain in detail the method of [132], which has been used for the synthesis of $CaO/Ca_{12}Al_{14}O_{33}$ sorbent. This sorbent has been exposed to severe calcination/carbonation conditions, observing a very good performance due to a very long self-activation period.

2.2 Dolomite stabilized by means of a novel thermal treatment

Dolomite is composed mainly by $CaCO_3$ and $MgCO_3$, which present different decomposition behavior during the decomposition into the respective oxides. Calcination of $MgCO_3$ occurs at lower temperature and much more rapidly than that of $CaCO_3$ [198] according to the irreversible reaction:

$$MgCO_3 \cdot CaCO_3 \rightarrow MgO \cdot CaCO_3 + CO_2 \qquad (2.9)$$

The product of reaction is called half-calcined dolomite. During the half-calcination process, porosity of the dolomite structure highly increases. As the temperature increases, full calcination of the dolomite occurs:

$$MgO \cdot CaCO_3 \rightarrow MgO \cdot CaO + CO_2 \qquad (2.10)$$

and particle achieves its maximum porosity and specific surface area. It is important to note that $CaCO_3$ calcination takes place once $MgCO_3$ is completely calcined. Furthermore, the temperature of calcination of each specie depends of the CO_2 partial pressure [137, 199].

Porosity during high temperature operation is mainly influenced by 1) calcination rate which in turn depends on particle size, temperature, partial pressure of CO_2 and sorbent history and 2) by sintering rate as a function of temperature and gas composition [200]. It is well-known that sintering increases with CO_2 concentration, affecting severely the capture performance of dolomite and limestone [152, 163].

Carbonation reaction has been studied in depth by several authors [138, 146, 201]. However, the calcination process is not even fully understood. The decomposition of calcium carbonate occurs in the boundary between CaO and $CaCO_3$ phases, and depends on sorbent structure [199]. Dolomite is formed by $CaCO_3$ and $MgCO_3$ and the presence of Mg defines its structure and behavior. During calcination $MgCO_3$ decompose quickly and before $CaCO_3$ changing the particle structure. Hence, an accurate control of first calcination conditions could improve the performance of CO_2 uptake.

Thus, a TGA experimental investigation of the effect of different operative parameters on the CO_2 uptake capacity of thermally stabilized dolomite was carried out. In order to emulate dolomite behavior in a fluidized-bed environment, carbonation residence time has been set to 30 min and 2 min to emulate BFB and CFB conditions, respectively. Furthermore, two heating rates steps were set in the experiments 10°C/min and 100°C/min, corresponding to BFB and CFB respectively. As for the thermal pretreatment, the effect of temperature and gas composition on the stability during cyclic operation was studied. Experimental results show a lower effect of CO_2 on sintering of dolomite, compared with classical literature data. Hence, in thermal pretreatment is possible to change the atmosphere of calcinations from an inert atmosphere ($100\%N_2$) to a CO_2 calcination atmosphere (50% CO_2, N_2 balance) improving carrying capacity of sorbent by means of triggered calcination.

2.2.1 Characterization of Dolomite - Experiments in TGA

A Mettler Toledo TG/DSC thermogravimetric analyzer (TGA) was used for cyclic CO_2 capture tests at atmospheric pressure. Bianchi dolomite was selected for this study. This dolomite contains 55.61 % by weight of $CaCO_3$. For all tests the dolomite particle diameter were pre-screened to 400-600 μm. The gas flow was set at 60 ml/min. In order to select the mass sample which offers a negligible resistance through the sample, a number of experiments were done choosing a set of 3, 8 and 16 mg samples. The 3 and 8 mg samples did not present external mass transfer resistance of CO_2 through the height of the sample, contained on the 70 μl alumina crucible. However, in the 16 mg sample tests the external diffusion effect could not be considered negligible. Therefore, the mass sample selected for all experiments was 8 mg, which produces less noisy signal than 3 mg, in a well-dispersed thin-layer sorbent bed. As part of the experimental procedure, blank runs were conducted with an empty crucible to record and subtract the disturbances in the mass change and reaction heat readings when switching the atmosphere between the calcination and carbonation processes.

Thermal stabilization procedure is composed of an initial heat-up period up to 900 °C and an isothermal phase where the sorbent is dwelled for 5 minutes.

Three different thermal pretreatment were carried out from room temperature up to 900 ºC, with a subsequent isothermal 5 min calcination at 900°C where the sample is exposed to 100% N_2 atmosphere (mild pretreatment) or 50% CO_2 (N_2 balance) atmosphere (severe pretreatment). Further samples were pretreated by exposing dolomite to 50% CO_2 (N_2 balance) atmosphere during the heat-up from room temperature to 900 °C with a gas switching to 100% N_2 during 900 °C isothermal calcination, named triggered calcination.

Having completed the thermal stabilization the samples were subjected to thermal swing from 600°C up to 900°C, at different heating rates, without isothermal calcination step, as shown in the temperature history plot reported in Figure 2. 10.

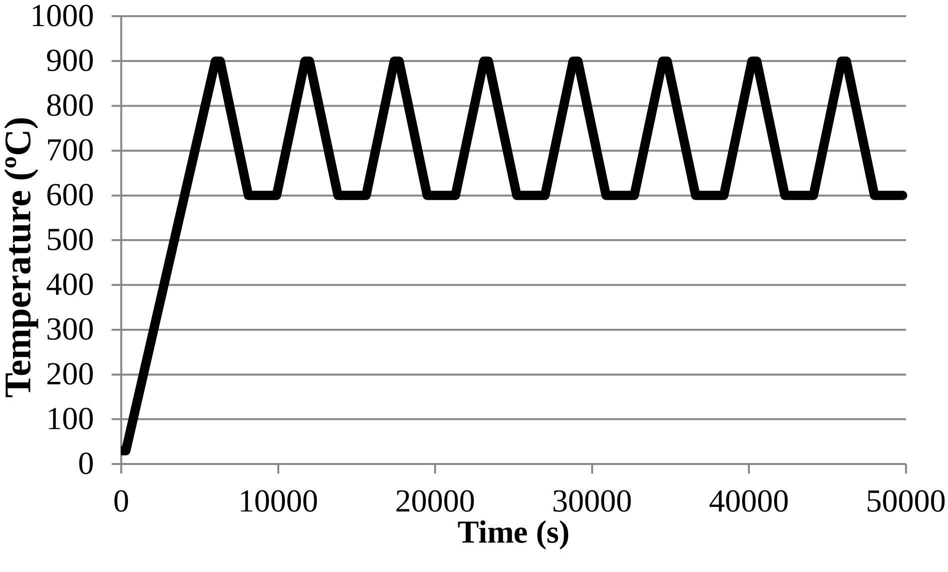

Figure 2. 10 - Thermal experiment programming

An experimental campaign, was carried out in order to evaluate the effect of thermal stabilization in dolomite CO_2 carrying capacity. Table 2. 1 summarizes the 11 experiments corresponding to the study of main influential factors in the calcination phase. The parameters studied were:

- Atmosphere composition during the thermal stabilization: 100% N_2, 50/50% N_2/CO_2 and trigger calcination (composed of 50/50% N_2/CO_2 non-isothermal step followed by 100% N_2 isothermal step at 900ºC). Runs from 1 to 3.
- Heating rate in calcination and carbonation steps: from 10 to 100 ºC/min: Runs from 3 to 6.
- CO_2 concentration: from 50 to 12 % vol: Runs 4 and 6.
- Carbonation time: from 2 to 30 minutes: Runs from 8 to 11.

Table 2. 1 - Summary of run details for pretreatment operation: Mild calcination = 100% N2. Severe calcination = 50/50% CO2-N2. Triggered calcination = 50/50% CO2-N2 + 100% N2

Run	Carbonation		1st Calcination (Isothermal 900ºC for 5 min)		Nth Calcination		N cycles
	CO_2 concentration (%)	Time (min)	Atmosphere composition	Heating Rate (ºC/min)	Atmosphere composition	Heating Rate (ºC/min)	
1	50%	30	Mild	10	Mild	10	15
2	50%	30	Severe	10	Mild	10	15
3	50%	30	Trigger	10	Mild	10	15
4	50%	30	Trigger	100	Mild	100	50
5	50%	30	Trigger	100	Mild	10	15
6	50%	30	Trigger	10	Mild	100	15
7	12%	30	Trigger	100	Mild	100	50
8	50%	2	Mild	100	Mild	100	150
9	50%	2	Severe	100	Severe	100	150
10	50%	2	Trigger	100	Mild	100	150
11	50%	2	Trigger	100	Severe	100	150

Moreover, some pre-treatments usually applied to improve the carrying capacity of limestone and standard-calcined dolomites were studied. A campaign of 15 experiments was carried out in order to study the effect of these pre-treatments in trigger calcined dolomite. The details of operation are summarized in Table 2. 2:

- Long carbonation: from 30 minutes to 72 h: Runs from 12 to 15 [139];
- Long calcination: from 5 to 90 minutes: Runs from 16 to 18 [164];
- Trigger cyclic regeneration, every 5 cycles: Runs 19 and 26, adapted from [202];
- High temperature long calcination: from 900 to 1100 ºC; Runs from 20 to 25 [143].

Table 2. 2 – Summary of run details for pre-treatment effect study

Run	Carbonation	1st Calcination (Heating rate 100ºC/min)		Nth Calcination (Heating rate 100ºC/min)	N cycles
	Carbonation Time 50% CO_2 [min]	Atmosphere composition	Isothermal 900ºC time [min]	Atmosphere composition	
12	1st 2 h- Nth 30 min	Mild	5	Mild	50
13	1st 2 h- Nth 30 min	Trigger	5	Mild	50
14	1st 72 h- Nth 30 min	Mild	5	Mild	50
15	1st 72 h- Nth 30 min	Trigger	5	Mild	50
16	30	Trigger	30	Mild	50
17	30	Trigger	60	Mild	50
18	30	Trigger	90	Mild	50
19	30	Trigger	5	Mild (each 5 cycles trigger)	45
20	30	Mild	360	Mild	30
21	30	Trigger	360	Mild	30
22	30	Mild	360 (1000°C)	Mild	30
23	30	Trigger	360 (1000°C)	Mild	30
24	30	Mild	360 (1100°C)	Mild	30
25	30	Trigger	360 (1100°C)	Mild	30
26	30	Trigger	5	Trigger	30

The number of cycles studied was limited by the useful life of these types of sorbents. Attrition and decay of carrying capacity limit the cycling period of dolomites to a maximum of 30 cycles, being necessary purges in order to maintain the performance of the cycles[203].

2.2.2 Effect of first calcination: Triggered vs. Standard calcination

The first experiments were carried out in order to study the effects of gas composition during the thermal pretreatment on porosity, and, thus, on CO_2 carrying capacity. Two typical calcination atmospheres have been studied: 100% N_2 (Run 1), 50/50% N_2/CO_2 (Run 2) in one-step calcination. Moreover, due to the nature of dolomite which presents two different crystalline phases, triggered calcination is realized in order to control the releasing of CO_2 through the particle during the calcination of the two main carbonates which dolomite is composed of. Having completed the release of moisture from the solid sample, the calcination of the dolomite occurs at temperatures greater than 500 °C. Particularly the sample exposed to CO_2 free atmosphere (100 % N_2) shows a smooth weight loss when the temperature exceeds 650 °C indicating that $MgCO_3$ and then $CaCO_3$ are converted into the respective oxides with a release of CO_2 and calcination is yielded.

When the investigated material is exposed to CO_2 containing atmosphere (50 % CO_2, N_2 balance) the decomposition of the carbonates is inhibited during sample heating. Particularly, the decomposition of MgCO3 happens at temperatures greater than that of CO_2 free calcination and the weight decrease of the sample starts at temperatures higher than 750 °C ,

Upon completed a first weight loss (half-calcination) the presence of CO_2 further inhibits the calcination of the remaining carbonate ($CaCO_3$). As shown in Figure 2. 11, CaCO3 is mostly decomposed into CaO when the flow of CO2 was stopped when the temperature reaches 900 °C and the sample is exposed to pure nitrogen atmosphere (Fig. 2.11: curve 2-step ‘trigger’). The sample experiences a very rapid linear weight loss followed by a sharp transition to a much slower reaction rate where the calcium carbonate is completely converted into oxide.

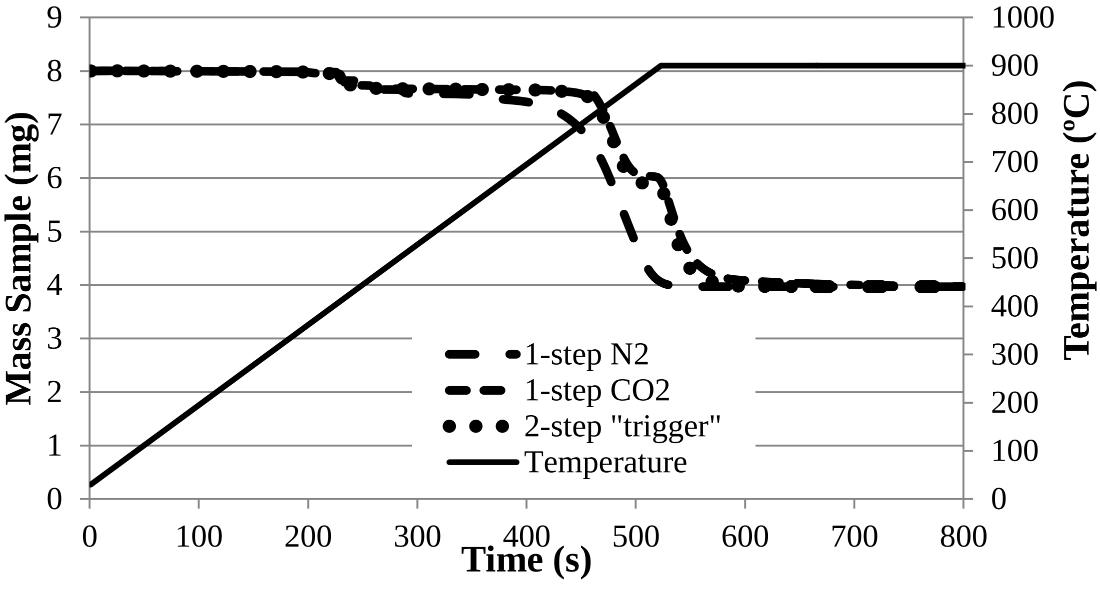

Figure 2. 11 – Comparison between experimental TGA mass loss under standard calcination and trigger calcination. Temperature history is also reported.

Calcined samples produced with the three calcination methods were subjected to multi-cycling CO_2 capture. The three investigated samples showed the same CO_2 uptake capacity for the first carbonation step indicating that the first thermal pretreatment does not influence the reactivity of the three calcined sorbents. However, remarkable differences in CO_2 uptake capacity were observed during the cycling, as shown in Figure 2. 12. Calcined particles produced under N_2/ CO_2 atmosphere (Run 2) show, indeed, a greater capture capacity decay during the first 15 cycles (0.21 to 0.14 gCO_2/g) when compared to the calcined produced under pure nitrogen (Run1). Gas composition strongly affects sintering of CaO grains, having CO_2 more sintering capacity than N_2. Interestingly, sample pre-treated dolomite shows a significant better performance in one step, up to 44% capture capacity, than CO_2-calcined dolomite and 30% N_2 calcined one.

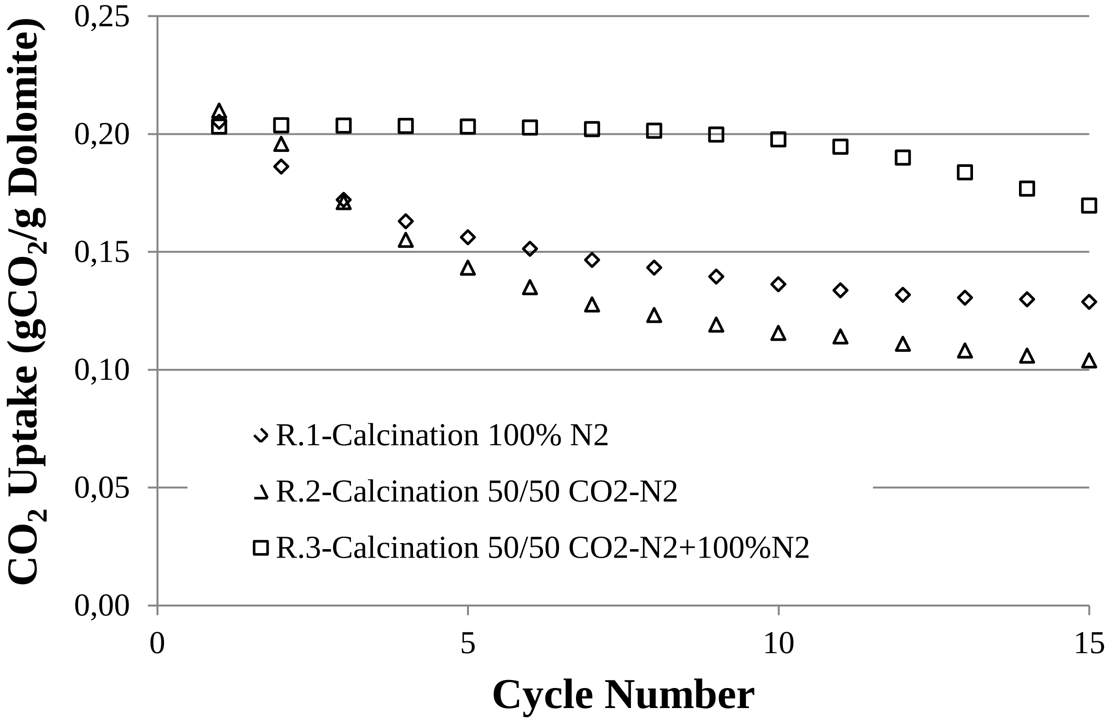

Figure 2. 12 - CO2 uptake at heating rate of 10°C/min for different calcination methods over 15 cycles.

The variation on carrying capacity is defined as:

$$X_{CO2} = \sum \frac{(CO2\ uptake\ run\ (gCO2/g\ dolomite) - \ CO2\ uptake\ ref\ (gCO2/g\ dolomite))}{(\ CO2\ uptake\ ref\ (gCO2/g\ dolomite))} \times 100 \qquad (2.11)$$

Where X_{CO2} is the CO_2 carrying capacity (%), subscript *run* is the run study case and *ref* is the reference case.

In fact, the pre-treated dolomite keeps constant the CO_2 carrying capacity during the first 10 cycles (0.20 gCO_2/g), and decreases slowly with the further cycles. The transition from CO_2/N_2 to pure N_2 during calcination could likely triggered a sintering-resistant structure in the particle, by gas diffusion in the pore. Moreover, the presence of MgO inhibits blockage of the pores during grain growth [138, 161, 204].

2.2.2.1 Effect of heating rate

Experiments showed in Figure 2.12 were carried out at a constant heating rate of 10ºC/min. High heating rates promotes densification, reducing porosity by enhancing sintering of grains, instead of grain growth [205, 206] and, therefore, reducing the CO_2 carrying capacity of sorbents. Hence, in order to know the effect of heating rate on CO_2 uptake, four heating rates were studied: all calcination/carbonation cycles at 10ºC/min; all cycles at 100ºC/min; first calcination at 10ºC/min and successive cycles at 100ºC/min; first calcination at 100ºC/min and subsequent ones at 10ºC. Figure 2. 13 shows the effects of heating rate on CO_2 capture capacity. The highest CO_2 uptake, in the first 15 cycles, corresponds to the case in which all cycles were done at 10ºC/min, and decreases at higher heating rates. In the cases of 100ºC/min the effect of a constant uptake for 6 cycles is observed, with higher carrying capacity than the cases of lower heating rate, and a strong decay in next cycles. This behavior is observed independently if the 100ºC/min calcination is in the first cycle (with subsequent 10ºC/min calcinations), or if the first calcination is at 10ºC/min and subsequent 100ºC/min calcinations. Hence, we can consider that pre-treatment in the first calcination produces this constant CO_2 carrying capacity in the first cycles, and that the pre-treatment depends on of the heating rate, being more stable the structure in the cases of lower heating rate.

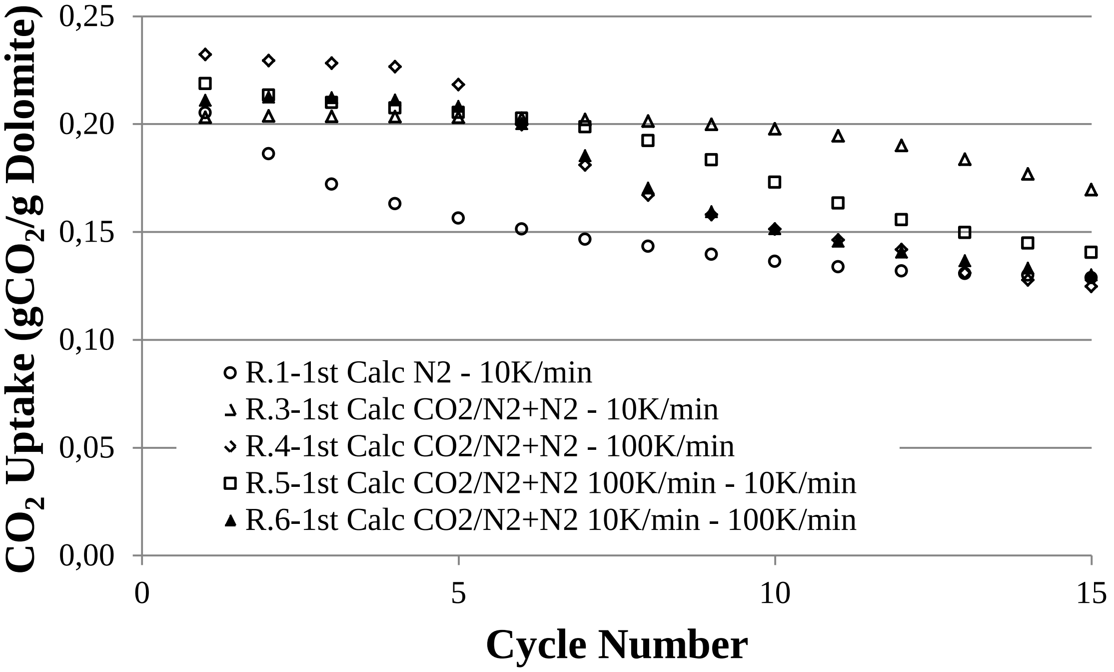

Figure 2. 13 – CO_2 uptake at different heating rates over 15 cycles

2.2.2.2 Effect of CO_2 concentration

In order to widely investigate the effectiveness of the pretreatment presented here, the calcined sample was also subjected to a 2-step calcination and exposed to 12 % CO_2 (N_2 balance) to emulate post-combustion CO_2 capture. The behavior of CO_2 uptake is around a 5% lower in the case at 12% than in that of 50% vol. CO_2, as shown in Figure 2. 14. This decay is congruent with literature data [137].

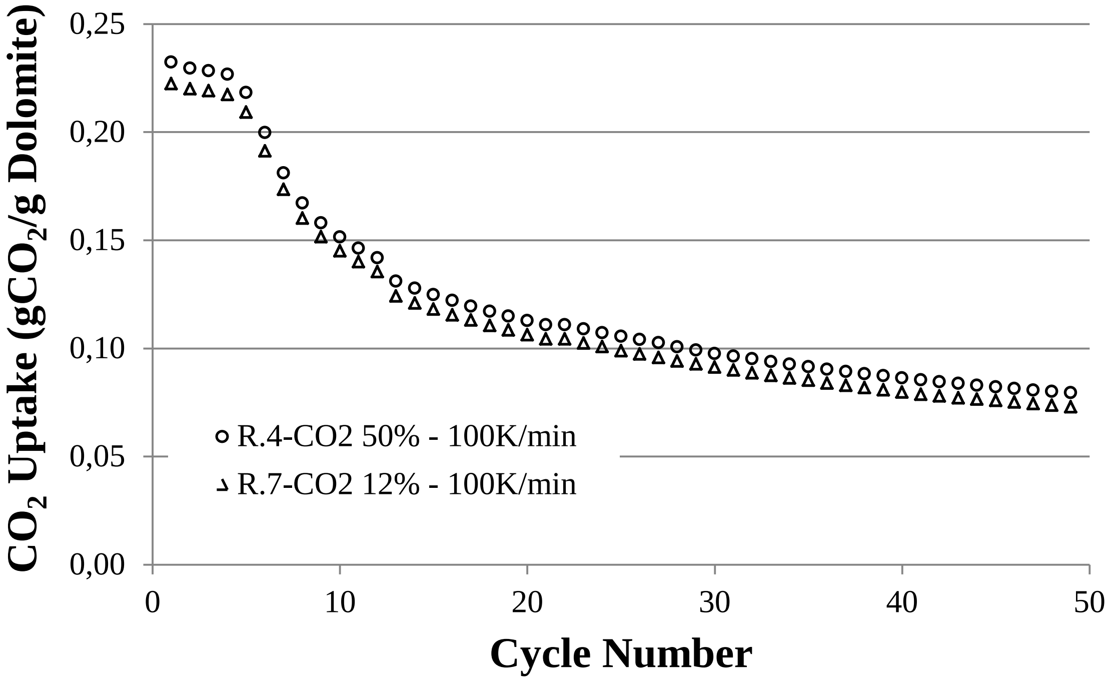

Figure 2. 14 – Uptake of pre-treated dolomite over 50 cycles for different CO_2 concentrations

2.2.2.3 Effect of carbonation time

Sintering is strongly dependent and increases with time [207, 208]. Therefore, a dolomite particle subjected to carbonation or calcination process for long time presents a reduction of the specific surface and reactivity. Figure 2. 15 shows as triggered calcined dolomite presents a high constant CO_2 uptake capacity in the first cycles if carbonation lasts 30 minutes than 2 min. Nevertheless up to 30 cycles the sintering affects in a higher degree the 30 minutes-carbonated dolomite than the 2 minute-ones, equating the carrying capacity. It is important to note this unexpected effect of the novel calcination method respect to results obtained elsewhere [159].

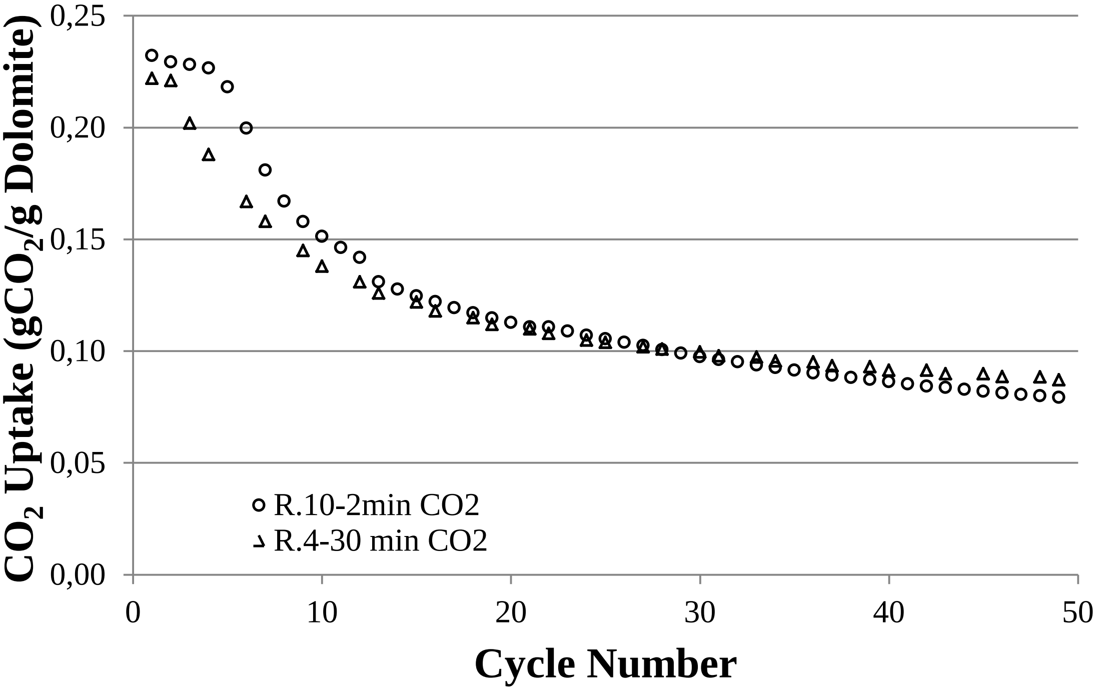

Figure 2. 15 – CO_2 uptake of pre-treated dolomite at 100°C/min heating rate over 50 cycles for different carbonation time

In an attempt to study the effect of regeneration condition on pretreated sorbent, both simple (100% (mild) and 50% (severe) N_2 calcination atmosphere) and 2-step calcined samples were subjected to successive CO2 capture cycling where the regeneration occurs under 100% N_2 (mild regeneration) or 50:50% CO_2/N_2 (severe regeneration) atmosphere for 150 cycles, in order to obtain the values of the minimum residual carrying capacity [162]. Single mild calcined samples were calcined under mild condition for all 150 cycles (Run 8). Analogously, single severe calcination cycles were repeated for all experiments (Run 9). Trigged calcined samples were regenerated under mild (Run 10) and severe conditions (Run 11). Figure 2. 16 shows as triggered pretreated dolomite presents a higher CO_2 capture capacity than one step calcined ones. Under the investigated conditions the improvement of CO_2 uptake is 12.3% in the 100% N_2 calcination and 24.5% in the 50%CO_2 calcination atmosphere, with respect to the one-step calcination, mild and severe respectively. It worth to note that 2-step pretreated sorbent shows a higher CO_2 uptake capacity when regenerated under severe condition. It is also observed a lower CO_2 uptake in the cases of severe first calcination than in mild, according with Figure 2. 3.

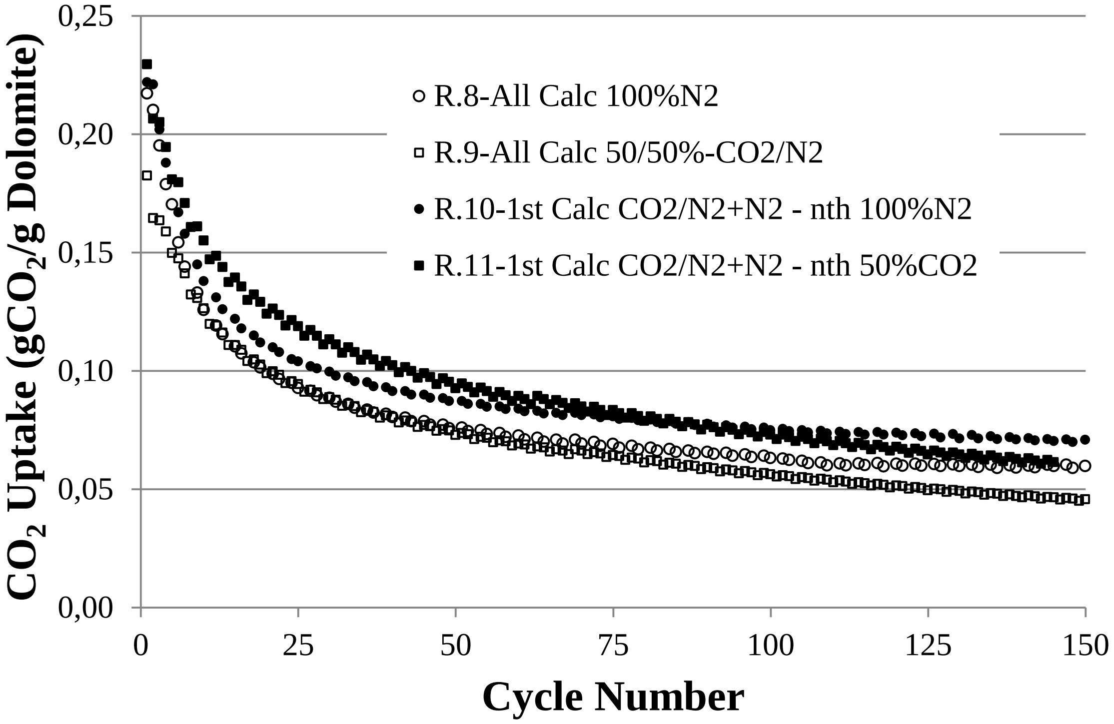

Figure 2. 16 – CO2 uptake of different calcination methods dolomite over 150 cycles for different CO_2 concentration calcination and carbonation

2.2.3 Effect of combined pre-treatments

As reported in Figure 2. 15, an increase in carbonation time reduces CO_2 uptake. However, a long-term carbonation (72h) was demonstrated to be a good method in order to regenerate exhausted dolomite [139]. Here, such a process is investigated as a possible route to pre-treat the sorbent material. Thus, single-mild calcined and triggered-calcined samples were carbonated for long times, from 2, (Run 12 and 13, respectively) to 72 h (Runs 14 and 15), with the aim to evaluate the combined effect of long carbonation during the first calcination.

As shown in Figure 2. 17a the single calcined samples present a slightly increase in the carrying capacity, a result congruent with literature data. However, this effect is not present in the triggered calcined samples. As shown in Figure 2. 17b, there is a decrease in carrying capacity with carbonation time. The CO_2 captured with 2 min carbonation is higher than with 30 min. With 2 and 72 hours carbonation, CO_2 carrying capacity is reduced ~ 17% and 33%, respectively compared to 30 min calcination. However, samples pretreated with triggered calcination show similar behavior regardless of the precarbonation operation. Long pre-carbonated samples (2 and 72h, Runs 13 and 15, Figure 2. 17a) and the samples as presented in Figure 2. 15 (no-precarbonation) experience constant carrying capacity in the first 5 cycles, similar asymptotic decay curves (with convergent residual capacity). Moreover, self-activation effect were observed in the 72h carbonated case [143]. Thus we infer that the structure generated by means of the trigger calcination needs a minimum first carbonation time in order to be stabilized.

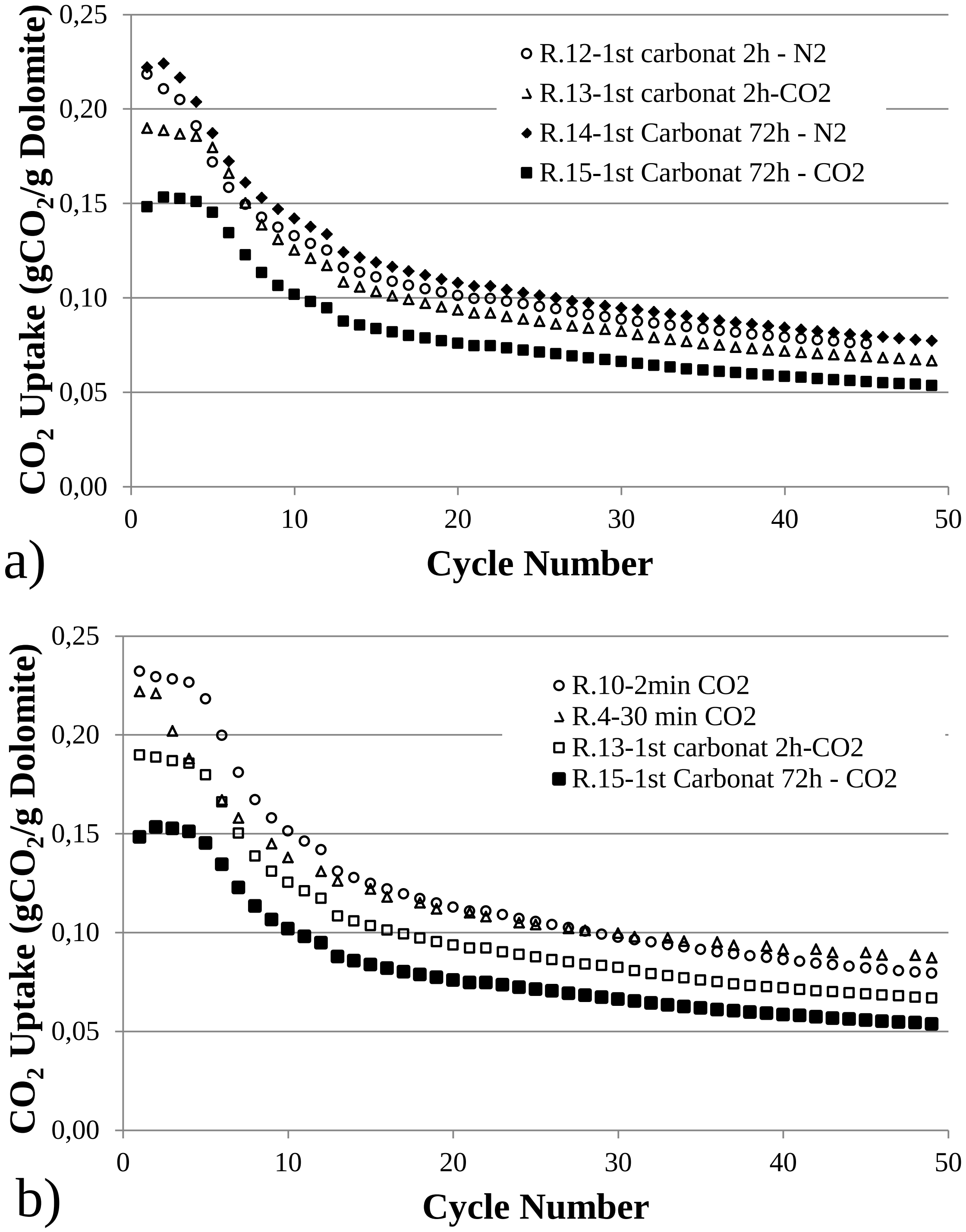

Figure 2. 17 – CO2 uptake under different carbonation times a) Long carbonation times for standard and trigger calcination b) Comparison of effect of carbonation time for trigger calcined samples

As commented previously, sintering increases with time and it stabilizes the pore sized distribution, without producing changes on the particle porosity. Nevertheless, the specific surface area decreases strongly if particles remains during time at high temperature, reaching an asymptotic value before 50% conversion [209].

Different authors report the reduction of CO_2 carrying capacity of limestone with increasing of first calcination time [127, 144, 210]. However, in the experiments carried out in this work, this effect has not been observed in the pure-nitrogen isothermal calcination (increasing calcination time from 5 to 90 min). The behavior of sorbent is independent of calcination time, as shown in Figure 2. 18.

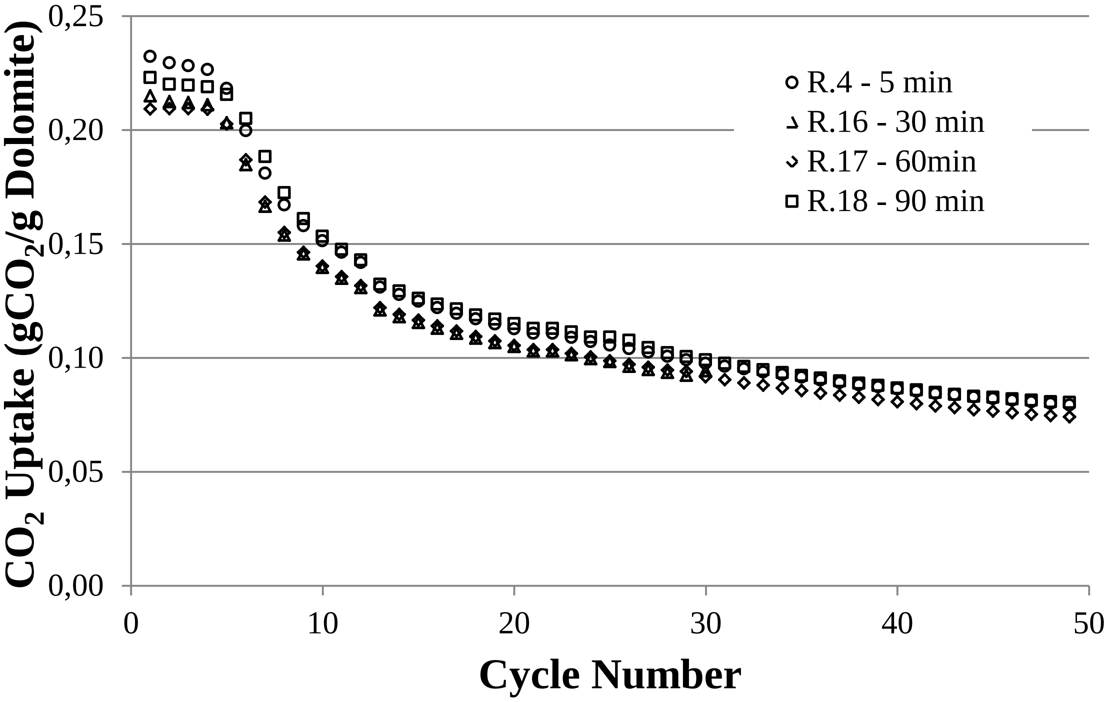

Figure 2. 18 – CO2 uptake under different first calcination times for triggered calcined dolomite

This fact suggests that the structure formed during thermally pretreatment is likely stable and rich in relatively large pores (diameter ≥ 220-350 nm), more resistant to sintering and closure than minor ones. Those pores could reduce their diameter with cycling because of cracks and channel formation throughout the particle increasing the pore volume (≤ 220nm) [39]. Then a competitive phenomenon could likely happen during the first cycles (sintering and crack formation) explaining the constant carrying capacity in the first calcination/carbonation cycles.

Manovic and Anthony [143] studied the effect of thermal treatment on CaO-based sorbents. They observed that calcination under high temperature (1000–1100 ºC) for long time (6-48 h) the sorbent structure changes, produces a stable porous skeleton, which increases sorbent conversion with cycling. However, this effect has been scarcely investigated in naturally occurring dolomites. Thus, six experiments were carried out in order to evaluate the effects of thermal pre-treatment in N_2 atmosphere and trigger calcination, and whether self-activation is presented (Runs 20, 22 and 24 for single mild calcination and Runs 21,23 and 25 for triggered calcined; at 900, 1000 and 1100ºC for 6h).

The experiments of single calcined pre-treatments have not shown an increase of CO_2 uptake with cycling, and a reduction of carrying capacity has been observed (Figure 2. 19). This effect is consistent with the sintering general theory in which the porosity of particles decrease with long-time high-temperature exposure [207]. In the case of trigger calcined dolomite, carrying capacity performance decreases (respect to 900 ºC 5-minutes isothermal pretreated) in 11, 8 and 18% for 6 hours and 900, 1000 and 1100ºC respectively. In the case of 900 and 1000ºC during the first 6 cycles, CO_2 carrying capacity remains constant. However for the 1100 ºC calcination case, the decay of performance starts on the 3rd cycle, due to a strong effect of sintering. Thus, for both cases (simple and trigger calcined dolomites) the thermal pre-treatment is not effective in order to increase the carrying capacity. This behavior can be explained for the presence of MgO, which creates a more porous structure in dolomite than in limestone, at the same time more susceptible to be affected for sintering. Moreover, it is possible to hypothesize that during trigger calcination there is a formation of micropores, which are more affected by sintering and they collapse during long high-temperature calcination, reducing CO2 uptake capacity with respect to the 5-minute pretreated one. A more detailed explanation about the texture changes in the particle is described in the next section.

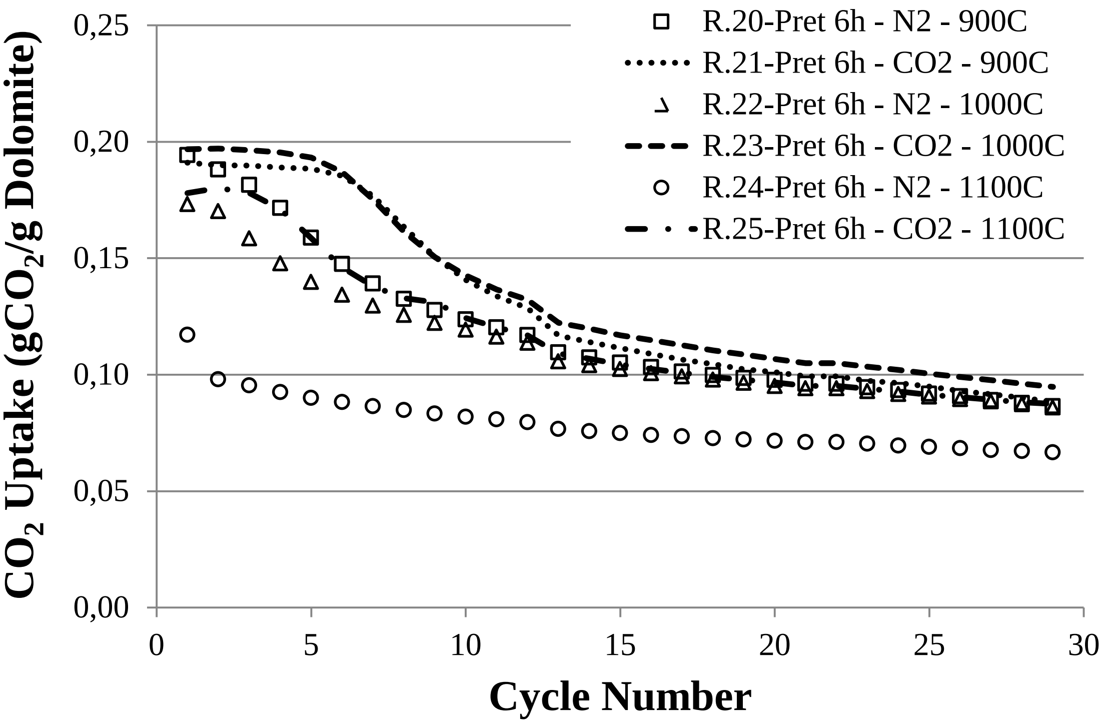

Figure 2. 19 – CO2 uptake under different thermal treatments (long time and high temperature) for trigger calcined dolomite and standard pure nitrogen calcination.

The triggered calcination presented an increase of performance with respect to classical calcination in all cases. However, in order to evaluate the effect of the triggered calcination over the first calcination, two experiments were carried out. In one set of experiments trigger calcination were carried out for all cycles (Run 26). In other experimental run, the trigger calcination has been used as a regeneration process each 5 cycles (4 calcinations in N_2 + 1 trigger calcination, Run.19), as suggested for other regeneration studies [147, 148, 211].

Figure 2. 20 shows the results of these approaches, compared with the reference case. It is observed as, in the 5th cycles, when trigger calcination is used as regeneration, carrying capacity increases for that cycle, but decays strongly in the subsequently ones. However in the

case in which trigger calcination is produced in all cycles a ~ 21% decay in the global performance is observed, with respect to the case in which is applied to the first calcination with subsequently mild calcinations. This is probably due to the rapid calcination in the second stage of triggered calcination method, when composition suddenly changes particle structure is stressed, weakening the stable structure formed in the first calcination. This hypothesis could likely explain the decay after each regeneration cycle (R.19) and the similar trend for the investigated samples after the10th cycle, as reported in Figure 2. 20.

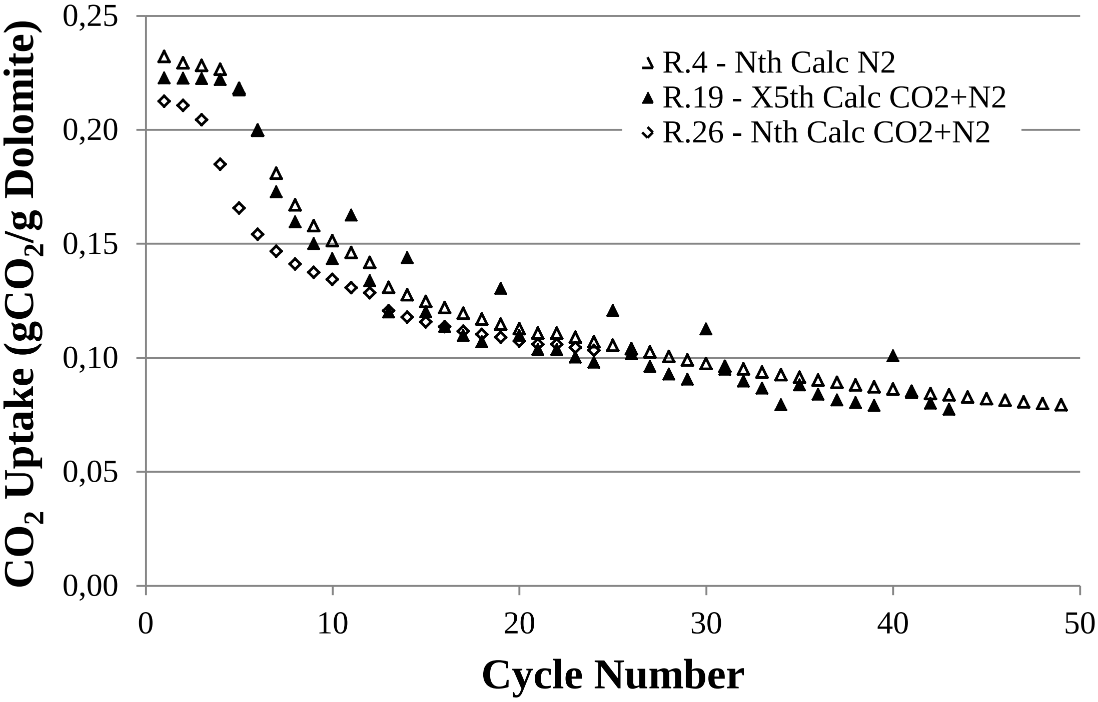

Figure 2. 20 – CO_2 uptake under periodic trigger calcinations

2.2.4 Estimation of kinetic parameters and specific surface area

In order to corroborate the theory of the formation of a stable structure, an indirect method to obtaining the specific surface area has been applied. It worth to note that during the uptake of CO_2 an initial rapid conversion was found followed by a slower second stage. During the first period the reaction is kinetically controlled and all diffusional resistances are practically negligible. In the second stage, instead, the formation of a layer of calcium carbonate in the grains inhibits further contact between the solid reactant and the bulk fluid in the pore, reducing reaction rate until reaching a plateau [201, 212]. This behavior is presented in Figure 2. 21.

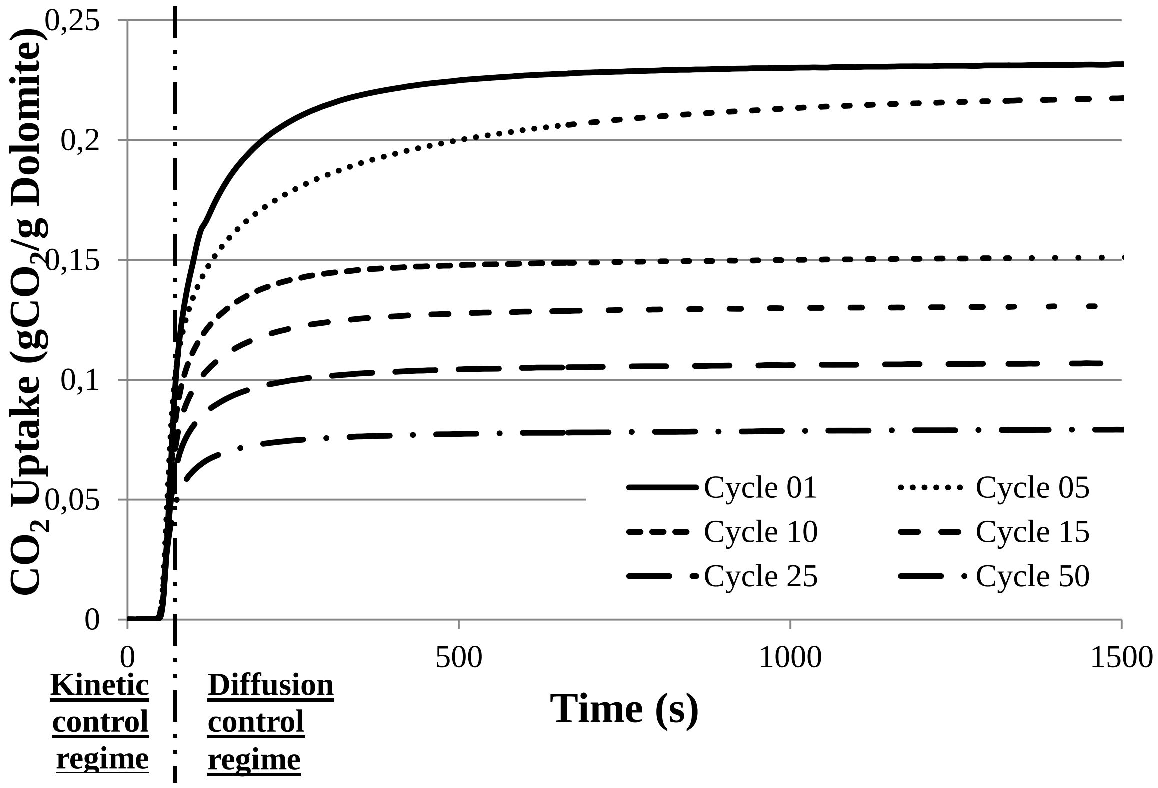

Figure 2. 21 – Representative TGA curves recorded of CO_2 uptake with cycling, showing the difference between kinetically- and diffusion controlled regimes

Some grain models have been developed in order to model the carbonation reaction. After an initial nucleation process, the beginning of carbonation reaction is controlled by kinetics, reaching a maximum rate value in this first period [158]. The maximum slope of the curve defines the reaction rate under kinetic control, according to [213]:

$$\frac{dX}{dt(1-X)^{\frac{2}{3}}} = 3r_0 \qquad (2.12)$$

Where X is the CaO conversion, and r_0 the reaction rate, during the very beginning of the CO_2 capture reaction. In integral form:

$$\left[1-(1-X)^{\frac{1}{3}}\right] = r_0 \times t \qquad (2.13)$$

Eq. 2.13 shows that, when reaction is under kinetic control the plot of $[1-(1-X)^{1/3}]$ vs t should be a straight line of slope r_0 [214], as shown in Figure 2. 22a. This fitting was repeated for the most representative tests, for the cycles 1, 5, 10, 25 and 50 (as shown in Figure 2. 22b).

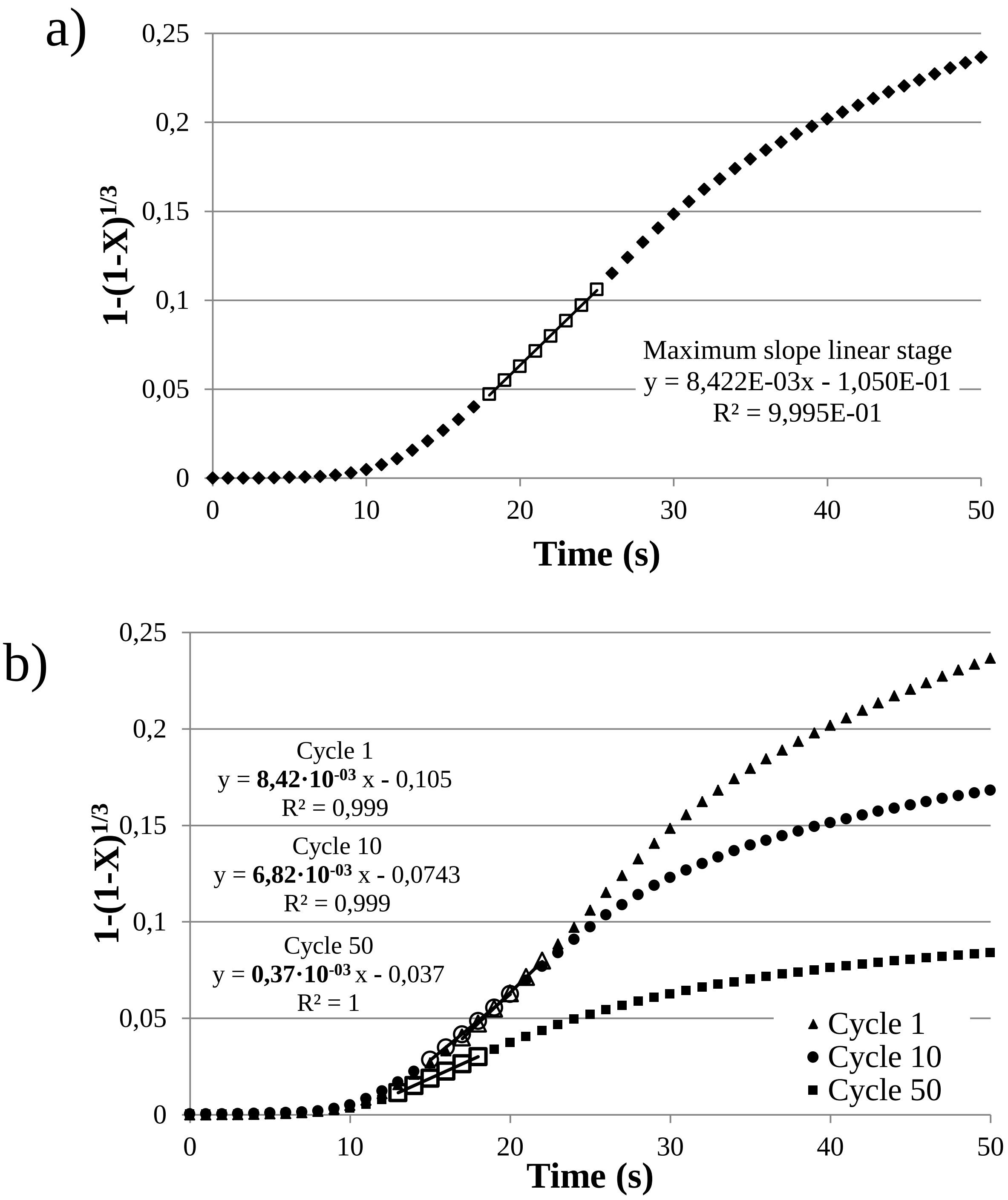

Figure 2. 22 – Extraction of maximum slope from TGA for a) first carbonation cycle and b) 1st, 10th and 50th cycle of Run 4

According to Sun et al. [214], under experimental conditions ($P_{CO2} - P_{CO2,eq} > 8$kPa$\rightarrow$ reaction order = 0) kinetic parameter for dolomite are $k_0 = 1.04 \cdot 10^{-3}$ mol/m^{2}s e E=24± 6 kJ/mol, and:

$$\ln r_0 = \ln(56 k_0 S_0 / 3) - \frac{E}{RT} \qquad (2.14)$$

Thus, as reaction rate and kinetic parameters, combining the values obtained by fitting Eq. 2.13 and Eq. 2.14, the initial value of specific surface S_0 can be obtained at the beginning of each cycle. Therefore, it is possible to obtain the values of superficial surface area indirectly, by means of calculation of reaction rate in the very beginning of the reaction. These values are obviously approximate but could serve to evaluate the important hypothesis of stable structure formation during triggered calcination. It is important to note that CO_2 uptake depends mainly on the internal composition of particle. Surface area and distribution of porosity are the main parameters that play a key role in kinetics and diffusion of CO_2 throughout the solid particle. Thus, it is necessary to know the evolution of all these properties to develop a mechanistic theory of structural changes with cycling.

Different solid particles with the same specific surface area can show very different carrying capacity due to the internal tortuosity [215]. Since the pioneering work of Kozeny [216] numerous works demonstrated the correlation between porosity and tortuosity, and the relationship with specific surface area and other properties as pore size distribution [217-219]. Thus, although the method applied in this work does not provide directly information about porosity, the evolution of pore volume can be estimated by means of carrying capacity and superficial surface area.

Table 2. 3 shows the values of superficial surface for the most representative experiments carried out. The values obtained present good agreement with literature data [214, 220, 221].

Table 2. 3 – Specific surface area of representative runs. S=standard calcination. T = triggered calcination

	Specific Surface , S [m^2/g]														
Cycle	**R.1 S**	**R.3 T**	**R.4 T**	**R.8 S**	**R.10 T**	**R.12 S**	**R.13 T**	**R.14 S**	**R.15 T**	**R.19 T**	**R.20 S**	**R.21 T**	**R.24 S**	**R.25 T**	**R.26 T**
1	19,3	20,2	23,6	26,3	21,3	14,4	15,1	50,1	50,1	13,0	41,8	22,0	28,8	10,1	12,1
5	25,7	29,2	22,6	5,3	15,2	12,0	14,5	11,6	3,7	12,0	16,0	19,2	23,4	8,0	11,6
10	34,2	38,1	18,3	5,0	12,2	8,1	13,9	11,0	0,7	11,9	13,3	18,2	19,7	8,0	10,7
25			12,9	4,4	7,4	7,2	12,9	9,7	0,7	10,1	12,7	12,3	23,5	5,2	8,3
50			9,3	3,9	6,0	5,4	9,2	8,3	0,6	8,0			22,9		
100				3,8	5,4										
150				4,5	4,9										

The reduction of CO_2 capture capacity is linked with the possibility of CO_2 to react with CaO grain presents in the particle. The permeability of the particle depends on specific surface (S) and porosity (P). During the run R.1, the solid sample shows a decay of CO_2 uptake capacity (see Figure 2. 12) whereas the specific surface increases with the cycling. This phenomenon could be likely explained by an increase of the particle tortuosity during the experimental run.

However, in the case 3, with triggered calcination, S shows a very similar behavior to N_2 calcination (run R.1), but CO_2 capture capacity remains constant with the cycling. Thus we infer that the material pretreated by means of triggered calcination could likely experience a lower increase of its tortuosity when compared to the material regenerated under mild condition (R.1). The increase of surface with the cycling disappears when the heating rate is increased from 10 °C/min (runs R.1 and R.3) up to 100 ºC/min. Thus, it is possible suppose that slower heating rates probably increase the internal stability of the particles. Solid sorbents pretreated with triggered calcination, indeed, present a constant CO_2 capture capacity for a number of cycles with respect to the specimen subjected to higher heating rates.

When the runs 1 and 4 were compared the case 1 presented a higher S with cycling than case 4, except in the first cycle. However its CO_2 capture capacity is lower: this observation could corroborate the theory of a stable internal structure in the triggered-calcined particles, with a lower tortuosity and formation of cracks, with a subsequent easy access to the un-reacted CaO grains.

In most of cases, it is observed that, under the same conditions, the decay of S with cycling is steeper in the N2 calcination than in the triggered calcination cases. This fact explains the best performance of triggered-calcined samples, but doesn’t explain the constant CO_2 uptake capacity for first cycles neither the differences of S due to the treatment.

A plausible hypothesis, based in the evolution of the tortuosity is proposed. During the first cycles, the stable structure resists pore blockage due to sintering effects and grain occlusion, mainly due to the formation of preferential routes for the releasing of CO_2 during the fast calcination step, which enhances the CO_2 diffusion through the particle volume increasing the CO_2 uptake capacity, and producing a structure with a distribution of mean pore diameter below 220 nm. Moreover, residual values of S (over 100 cycles) are higher in the cases of triggered calcination than N_2 ones. This effect has been analogously observed in other sorbents [215].

In order to obtain this stable structure a reasonable exposure time to CO_2 in the first cycle is necessary. Comparing different experimental runs: 4, 10, 13 and 15, a decreasing of the specific surface with carbonation time was observed (see Figure 2.22b). However, this trend does not corresponds to the CO_2 uptake capacity. With increases from 2 to 30 min exposure time, CO_2 uptake decreases and S increases. Increasing calcination time specific surface decreases more strongly than CO_2 capture capacity, reaching a plateau in a few cycles in the cases of long calcination time (72h), which do not correspond to a CO_2 performance plateau. This last case, Run 15, present a very stable structure and a lower specific surface (S~3.7 m^2/g in the 5th cycle), which indicates the formation of very reactive pores and a very stable structure. In the cases of N2 calcination (Runs 1, 8,12 and 14) an increase of both CO_2 uptake capacity and the specific surface with carbonation time was observed, as reported in previous works [162].

Long time calcination have been extensively used in literature as thermal treatment in order to increase CO_2 uptake capacity of limestone [70, 139, 143, 145, 222, 223]. However this effect was lower in the cases of dolomite, except for long time calcination (i.e.24h) [139], and as shown in the case R.20 the performance increases with calcination time. However, for 6-hour calcination there is a strongly decrease of performance with temperature (from 900 to 1100 ºC) (run 24), and an increase of specific surface .This fact could be likely explained by the effect of the formation of non-active pore (diameter > 350 nm). In the case of triggered-calcined particles, the reduction of performance is also observed (Runs 21 and 25), however it is associated to a decay of S. This fact corroborates the idea of a stable structure in which CO_2 performance is limited by the initial specific surface, with porosity almost constant due to the triggered calcination in the initial calcination. Thus the evolution of tortuosity affects directly the CO_2 capture and is dominated by the initial surface area. Moreover the sintering effects due to temperature have been observed, according with general theory of sintering, reducing S and CO_2 uptake capacity of sorbent with time.

Decay on material performance has been observed in the cases of periodic trigger calcination along the experimental runs, (Run 26) and each 5 cycles (Run19). Among all the investigated experimental conditions, the initially triggered material has shown the best performance. This fact is due to the fact that decay in the specific surface with cycling is stronger if triggered calcination is applied on calcined dolomite instead of fresh sorbent. If triggered calcination is used sequentially each 5 cycles (as shown in Table 2. 4), an increase in the CO_2 capture performance is observed in the regeneration cycle, however, in the next step the decay of specific surface and performance decreases strongly producing a global decay with cycling, smoother than in the case in which all calcinations are triggered. A plausible explanation the effect of $MgCO_3$ calcination which drives the formation of a stable structure with active pores. The material under subsequent triggered calcinations could experience a destabilization of the structure, probably due to the migration of CaO grains in the interior of particle, as in analogous particles [224].

Table 2. 4 – Specific surface area Run 19. Detailed of S in the regeneration step

R.19 - Cycle	**S (m^2/g)**
1	13,05
5	11,96
10	11,93
25	10,05
26	7,28
27	9,46
29	9,35
30	10,08
50	7,95

2.2.5 Conclusions

It has been observed that first calcination defines the behavior of multi-cycling carbonation performance. Pre-treated dolomite by means half-calcination in CO_2 -containing atmosphere with a subsequent 900 °C isothermal calcination presents better carrying capacity than one-step calcination under N_2 or CO_2 atmosphere, due probably to the structural changes in the lattice of dolomite particle.

Triggered-calcined samples present a stable porosity with cycling. This fact provides better performance than other calcination methods in which porosity decreases with cycling, and, hence, the CO_2 capture capacity also decreases. This theory was validated by means of an indirect method in order to obtain the specific surface area, and relate S with CO_2 capture performance.

The effect of several variables (such as CO_2 concentration, heating rate, calcination and carbonation time) and some pre-treatments has been tested under triggered calcination, producing a reduction of CO_2 uptake, due to the internal structure effects. The best performance sample was the triggered simplest calcination under industrial condition (low calcination and carbonation time, without other thermal treatment). Thus, this simple method can be applied directly in carbon capture cycles, increasing noticeably the performance of dolomite as CO_2 acceptor

2.3 Self-reactivation and regeneration of Mayenite ($CaO \cdot Ca_{12}Al_{14}O_{33}$)

2.3.1 Synthesis of solid sorbent

The synthesis has been performed according to [132] where powdered CaO (about 99.8%, after calcination) and aluminum nitrate $Al(NO_3)_3 \cdot 9H_2O$ (> 98%) have been selected as precursors in the synthesis of the binder phase. A wet method has been used to ensure an intimate mixing of starting materials: Distilled water has been mixed with 2-propanol acting as surfactant. The calcium oxide has been calcined at 900°C for 2 h in the presence of air to remove humidity and decompose any traces of $CaCO_3$ into CaO. The amounts of CaO and aluminum nitrate were chosen such that the mass ratio of the active phase CaO to binder phase was 75:25 and 85:15. The compounds were added to the water and the mixture has been stirred at 75 °C and 700 rpm. After 60 minutes stirring, the solution has been dried at 120 °C for 18 h to obtain a dried cake. In order to form the binder $Ca_{12}Al_{14}O_{33}$ the material has been ground and heated up to 850 °C. Before reaching the temperature for $Ca_{12}Al_{14}O_{33}$ formation the sorbent precursor has been dried at 500 °C for 180 minutes to evaporate nitric oxides and produce Al_2O_3 in a controlled mode. The solid-solid reaction between Al_2O_3 and CaO to form $Ca_{12}Al_{14}O_{33}$ requires several hours, but the reaction rate can be improved by a further grinding of the manufactured material as specific surface area is maintained higher and fresh surface is brought in contact. As a consequence, after cooling to room temperature the material has been ground again in a mortar and heated up to 850 °C for 90 minutes in order to react Al_2O_3 with CaO to form $Ca_{12}Al_{14}O_{33}$. After having completed the final calcination and the subsequent cooling to the room temperature the sorbent material has been ground and sieved. The powder used in this investigation had particle sizes in the range 180 to 500 μm.

2.3.2 Characterization of Mayenite – Experiments in TGA

A number of experimental investigations at a laboratory scale have been performed to characterize a synthetic solid sorbent to accomplish the uptake of CO_2 from a gaseous mixture. The reactivity and CO_2 uptake capacity during cycling of the sorbent were analyzed by using a GC-10 Mettler-Toledo thermo-gravimetric analyzer (TGA). This apparatus can measure minute mass changes of solid samples placed in a furnace with a variable and well-controlled temperature and gas atmosphere. Blank runs were conducted with an empty crucible to record the disturbances in the mass change readings when moving the experiment from calcinations to carbonation process. To avoid the effect of the sample size on carbonation and regeneration processes, such as the external mass transfer resistance of CO_2 through the sample, ~2.90 mg samples were used. The experimental protocol used for performing the solid chemical looping consisted of three steps:

- **Regeneration phase:** This phase is conducted by heating the sample up to a programmed temperature at 100 °C/min rate (maximum heat rate allowed by this apparatus). A mixture of nitrogen and carbon dioxide flows over the sample. During this phase the $CaCO_3$ is decomposed into CaO. The sample is calcined for 15 min at 900 or 1000 °C in order to guarantee the complete calcination of sorbent. Three representative regeneration conditions have been used (N_2 balance gas):

- *Mild condition*: temperature 900 °C, with 14 % CO_2;
- *Moderate condition:* temperature 1000 °C, with14 % CO_2 ;
- *Severe condition:* temperature 1000 °C; with 86 % CO_2.

- **Cooling and carbonation phase:** The temperature is then lowered with the rate of 100 °C/min to reach 600 °C selected for CO_2 sorption. The atmosphere remains 84% nitrogen and 16% carbon dioxide. When the temperature goes below 700-750 °C the CO_2 begins reacting with CaO to form $CaCO_3$.

- **Isotherm carbonation phase:** Having completed the cooling phase, the temperature is maintained constant at 600 °C for 20 minutes. The reacting atmosphere has been programmed to study the effect of CO_2 content in the gas to decarbonise: (N_2 balance gas):
  - *Higher CO_2 content*: atmosphere composed of 25 % CO_2
  - *Lower CO_2 content:* atmosphere composed of 14 % CO_2.

2.3.2.1 Treatment of the sorbent precursor

During the synthesis process water could be added to the powder obtained with the second sorbent precursor grinding. Few water drops have been added to the particle in order to obtain a sort of paste: CaO reacts with H_2O to form $Ca(OH)_2$. Then the hydrated material has been heated up to 850 °C to form the binder phase as reported earlier (Sec 2.1).

2.3.2.2 Treatment of the sorbent material

The synthesized material has been thermally treated to see whether the advantage found for the dolomite and calcite [139, 143] persists on the investigated material. Thus solid specimens have been carbonated at 600 °C for 80 minutes, exposing them to a prolonged carbonation with a controlled atmosphere composed of 14% CO_2 (N_2 balance gas). Long carbonation has been realized with the aim to stabilize the sorbent structure as reported in [162]. After the thermal treatment in TGA has been completed, the solid sorbent has subsequently undergone the multi-cycling regeneration-carbonation process in order to avoid influences on the investigated specimen (e.g reaction between sample and CO_2 in the room atmosphere). Comparison between synthesized sorbent and thermally pretreated sorbent are presented in this work. Particularly the capacity to retain carbon has been investigated by cycling the material up to 150 cycles. In order to study the effect of a cyclic treatment on the material, solid specimens have been exposed to a further prolonged carbonation with a previous calcination step (1000 °C with 14 % CO_2, N_2 balance). When the sorbent is treated in such a manner, the material is named here as double-treated.

2.3.3 Self-reactivation of Mayenite

Figure 2. 24 shows conversion-time curves for different numbers of regeneration-carbonation cycles regenerated in moderate condition. At the beginning of each single cycle, besides a short nucleation period, a linear kinetically-controlled mass growth was found followed by a

transition to a much slower reaction rate. This transition has been found to be smoother when compared with that occurred during the carbonation of naturally occurring sorbent investigated in the dolomite experiments. No plateau is reached during the last slower phase and the surface reaction continues to play a key role in the whole process. Such a smooth transition was found in [143] where experimental test on CO_2 capture for pre-treated limestone were presented. Moreover, Figure 2. 24b shows that with increase in cycle number the initial slope of the conversion-time curves increases from the first to the tenth cycle. The increase of the sample weight with first cycles could likely explained with the phenomenon, named self-reactivation. Analogous effect was observed also in the field of chemical looping combustion where a particular O_2-carrier showed a gain in reactivity during reduction/oxidation cycle performed in a thermo gravimetric analyzer [224] . After the 10th cycle the linear growth shows the same slope up to the 80th cycle carbonation-regeneration loop of the experimental test. Moreover, after that cycle, as reported in Figure 2. 24a, TG curves were found to be similar denoting a good reversibility through the multi–cycling CO_2 capture. In addition, Figure 2. 24b shows that with the increase of cycling up to 10th carbonation–regeneration step the sample mass achieved after each single loop has been increased when compared with the previous loop. In order to compare the self-reactivation of synthetic sorbent to the performance of naturally occurring sorbent, dolomite sample (Bianchi dolomite: 55.6% $CaCO_3$ and 44.2% $MgCO_3$) has been selected and exposed to the same condition reported in Figure 2. 23. The uptake of the two sorbents for each single cycle was evaluated according to the following ratio:

$$CO_2\ uptake = \Delta m_N \big/ m_0 \tag{2.15}$$

where Δm_N represents the mass augment of the solid specimen at each single N-th cycle and m_0 represents the weight of the sample inserted in TGA.

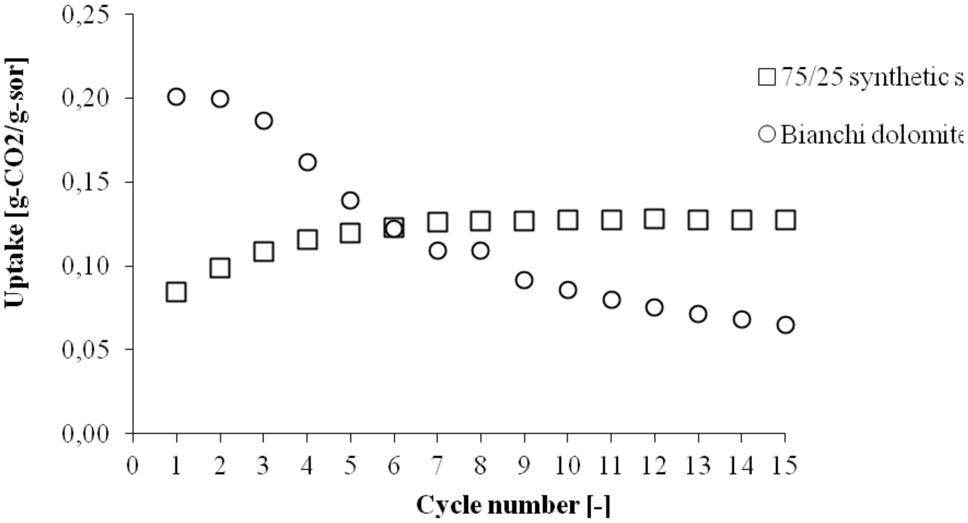

Figure 2. 23 – Comparison between 75 % CaO synthetic sorbent and “Bianchi” dolomite in term of carbon retain capacity.

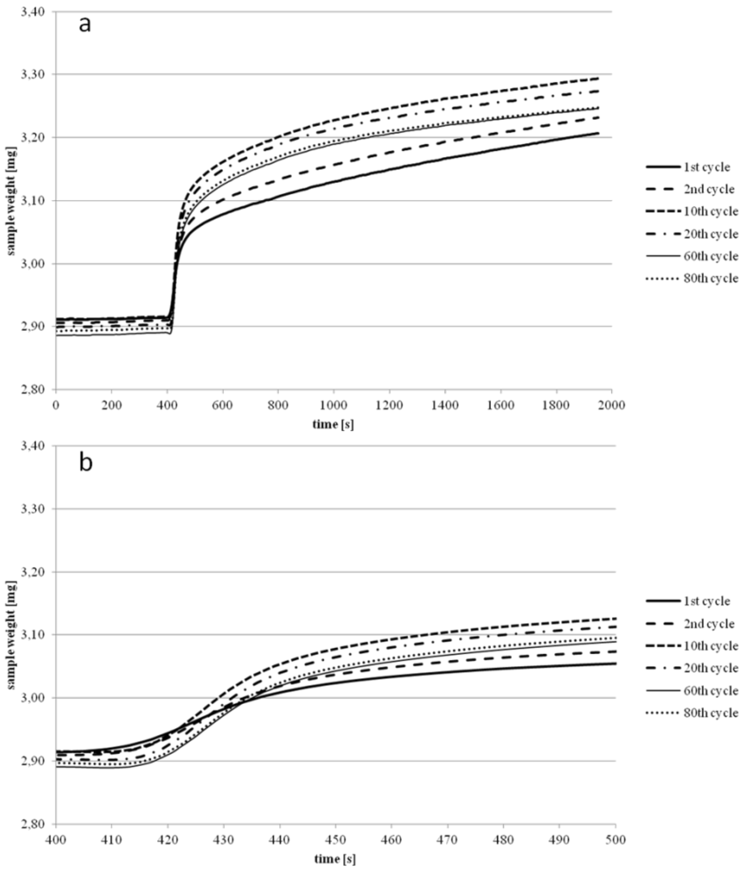

Figure 2. 24 – TG curves collected for specimens subjected to moderate regeneration condition up to 80 cycles: (a) mass growth shows no plateau; (b) self reactivation effect: the slope of initial linear mass growth increases with the number cycle.

Even if the dolomite shows a larger uptake when compared to that of synthetic sorbent, a decay in the capacity to retain carbon during the first few cycles was found for Bianchi dolomite whereas the synthetic sorbent shows higher uptake while the material is cycled during CO_2 capture tests.

2.3.3.1 Effect of sorbent precursor hydration

Improvement of sorbent activity has been also observed for the sorbent obtained by chemical pretreatment of the sorbent precursor. By adding water after the second grinding (see Sec 2.3.2.1) the obtained sorbent shows greater uptake when compared with the sorbent whose precursor was dry (see Figure 2. 25). Carbon dioxide uptake of the former sorbent was ~94% higher when compared to the latter at the second cycle. In subsequent cycles the uptake has been at least ~60% higher than that obtained with dry precursor. Such an improvement could be likely be explained with the formation of calcium hydroxide in the sorbent precursor due to the presence of water and the subsequently calcination (for the binder formation see Sec 2.3.2.2) leaving more pore volume. In fact the molar volume of $Ca(OH)_2$ is greater than that of CaO. Thus when the hydrated precursor would undergo calcination process water vapor would be formed and it would leave the particle producing extra pore volume. Moreover the migration of water vapor towards the outer part could likely create cracks throughout the sorbent particle exposing more specific surface area to the carbon dioxide. Consequently the specific surface area is higher and more CaO surface is brought into contact with the CO_2.

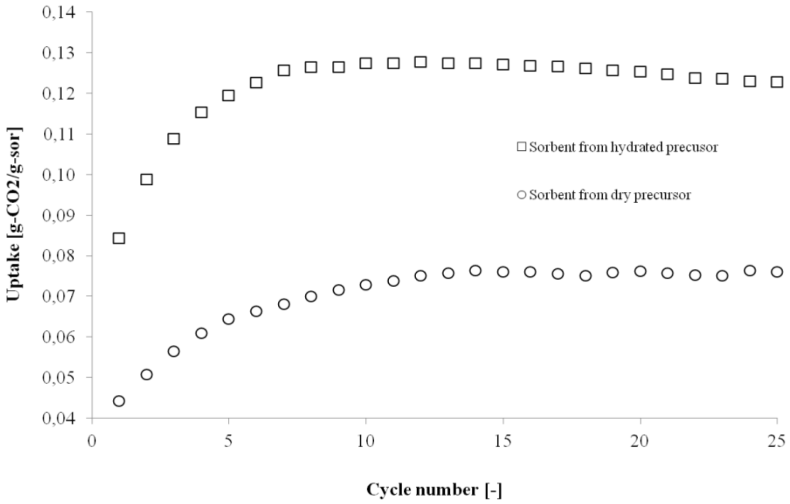

Figure 2. 25 – Comparison between material obtained from hydrated precursor and dry precursor when subjected to moderate regeneration condition for the 75% CaO sorbent.

2.3.3.2 Pore size distribution curves

The specific surface and the pore volume distribution were analyzed in a Micromeritics Tristar II using N_2 physisorption and desorption isotherms at −196 °C (Brunauer–Emmett–Teller BET method [225]). The pore volume distribution was evaluated by using Barrett-Joyner-Halenda (BJH) method [226].

The formation of larger and smaller pores has been indeed found as reported in Figure 2. 26 where the BJH curves for the two kinds of sorbent are presented. As it is possible to see the sorbent synthesized with dry precursor shows a lower single–peaked pore size distribution (average size 30 nm) whereas for the material obtained from hydrated precursor a wider pore size distribution has been observed. Particularly, the formation of higher volume with larger pores (100 nm) have been detected which permits CO_2 to get the inner core of the particle with a major CaO utilization whereas smaller pores play a key role to the rapid carbonation of the sorbent material. The hydrated precursor derived sorbent present a peak on ~100 nm below 220 nm, which were found to be the more active sizes for CO_2 capture [161]. These pores provide almost all the surface area and determinate the apparent carbonation rates. Then the experimental results presented in the remainder of this work are collected from the sorbent obtained from the hydrated precursor.

The pore size distribution (PSD) curves for sorbents after different carbonation time (20 and 80 minutes) in Figure 2. 26 show that if the sorbent is exposed at different carbonation time the internal structure of the material shows an increase in the pore volume particularly in the range of 100–200 nm diameter pores. Having completed the treatment, indeed, material shows an increase in the specific surface area when subjected to a single calcinations step: for an instance the 85% CaO sorbent's surface is increased from 1.5 m^2/g to 2.6 m^2/g. This specific surface increase could likely explained with the larger amount of CaO which reacts with the CO_2 during the pretreatment of the material. In fact, when the solid specimen is exposed for longer time to the pretreatment the CO_2 diffuses through the particle reaching at its inner core and reacting with more CaO grains. As a consequence when the material is subjected to the calcination step, more CO_2 would be drive off the particle with a formation of cracks and channels throughout the particle increasing the pore volume.

It worth to note that the pore volume shows a remarkable increase when the material is cyclically used in a carbonation–regeneration loop (see Figure 2. 26). As a consequence more specific calcium oxide surface would be exposed during the first cycles enhancing the reaction between active phase (CaO) and CO_2. Moreover the pore size shifts from 100 nm to 60 nm permitting a major CaO utilization with an increase in specific up to 4.0 m^2/g for the sorbent 85% CaO sorbent. Such a phenomenon could likely explain the augment of the slope shown by the uptake curves in Figure 2. 24. A similar behavior has been found for the sorbent obtained from dry precursor (Figure 2. 26): with the cycling the average pore size moves from 30 nm to 60 nm. Then it appears that cycling the synthetic sorbent there is an increasing of the pore volume which is favorable to CaO–CO_2 reaction. Such a positive effect of cycling on the growth of pore volume decreases with increased the calcination temperature as described in more details in the following section.

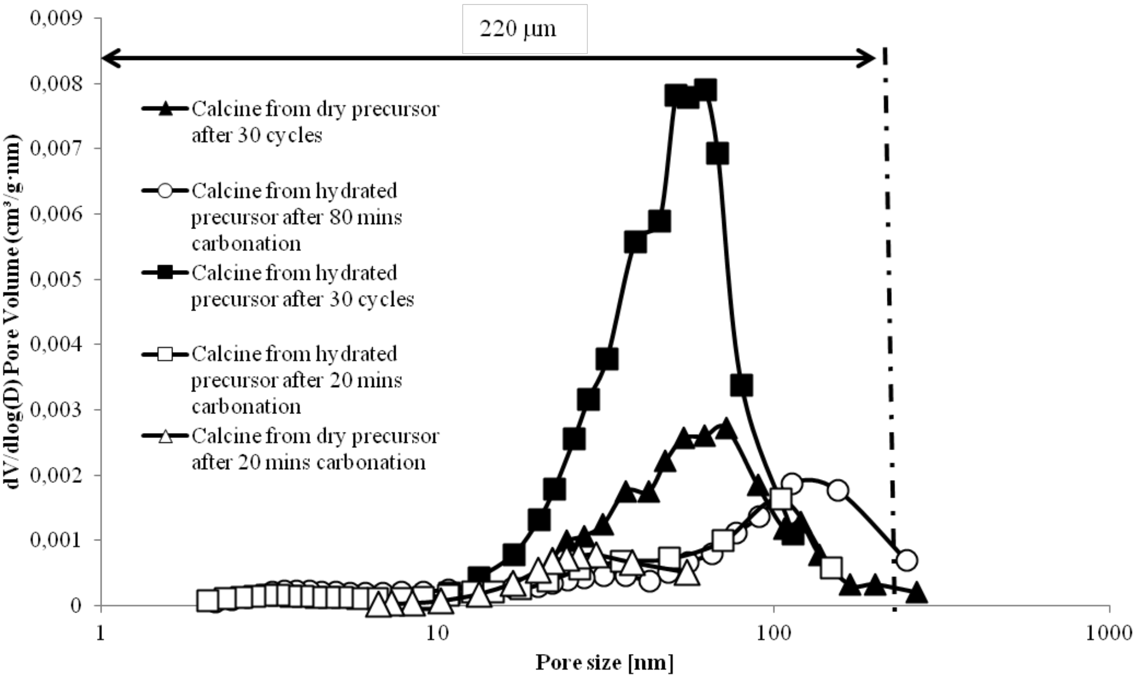

Figure 2. 26 – Pore size distribution of material obtained with hydrated precursor and dry precursor. Pore volume growth after 30 cycles of carbonation–calcination: PSD curves for the cycled 85 % CaO sorbent show an increase in pore volume peaked at 60 nm

2.3.3.3 Influence of the regeneration condition

Figure 2. 27 and Figure 2. 28 show the influence of regeneration condition on synthesized sorbent uptake. In particular, it can be seen that with the increase of both temperature and the CO_2 molar fraction in the atmosphere during the sorbent regeneration the self-reactivation period decreases.

- Mild condition

When the sorbent is regenerated with mild condition, the self-reactivation period is extended up to ~60th cycle for the untreated and single treated 85% CaO sorbent (Figure 2. 27a). When such a material is double-treated and regenerated in mild condition, no significant self-reactivation period has been detected but the material shows a very good stability up to the 150th cycle.

As for the 75% CaO sorbent a self-reactivation period has been found up to the 30th cycle for the 75%CaO sorbent (untreated single- or double treated) (Figure 2. 28a).

- Moderate condition

As reported in Figure 2. 27b – Figure 2. 28b, if the material is regenerated in moderate condition the self-reactivation period is reduced to the first 15 cycles for the untreated sorbent. When the material is single treated self-reactivation is further reduced. However, when the material is double treated, self-activation is not observed. Moreover a lower uptake capacity and loss of stability with cycling have been detected. Particularly, the double treated 85% CaO sorbent shows self-reactivation at later cycles whereas the 75% CaO decreases its performances at each single cycle. Such a result is consistent with [152-154] where the authors have found that the presence of CO_2 in the calcination step favors sintering process.

- Severe condition

The 85% CaO sorbent regenerated in severe condition does not present considerable self-reactivation period (see Figure 2. 27c). Besides an initial short period (10 cycles) where the untreated 85% CaO sorbent shows stability in CO_2 capturing, a slight loss of performances has been found up to the 100th cycle. In addition the ability to retain carbon decreases in later cycles even if the material is single- or double treated.

Perhaps the most remarkable result is reported in Figure 2. 28c where the uptake of the sorbent subjected to severe regeneration condition is shown. In contrast with 85 % CaO sorbent, the untreated 75 % CaO sorbent shows self-reactivation period up to the 60th cycle of the carbonation looping. Besides an initial decrease of the performance, the single pretreated sorbent shows a continuously increment of its CO_2 capture capacity up to 150th cycle. In order to confirm such an unexpected behavior another experimental run has been accomplished confirming the previous observation (see black dots in Figure 2. 28c) with a good reproducibility. Finally for the double treated specimen no self-reactivation period was found at the beginning where a loss of CO_2 uptake has been observed followed by a period of good stability; beyond such a period a self-reactivation was observed reaching a maximum at ~150th cycle.

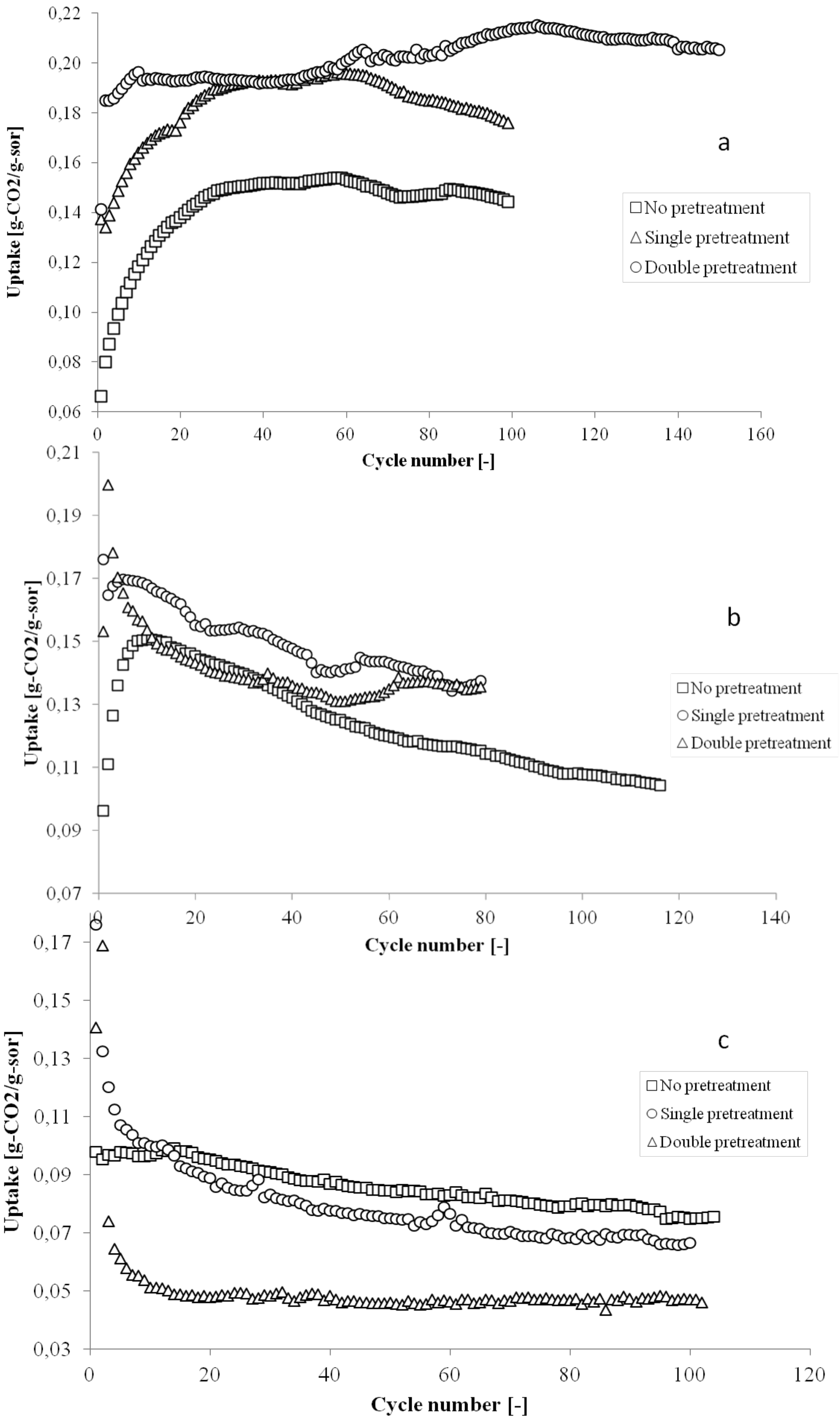

Figure 2. 27 – Carbon capture capacity of 85% CaO sorbent when subjected to different regeneration condition: (a) mild regeneration: 900 °C, 14/86 %v (CO2/ N2); (b) moderately severe regeneration: 1000 °C, 14/86 %v (CO2/ N2); (c) severe regeneration: 1000 °C, 86/14 %v (CO2/ N2).

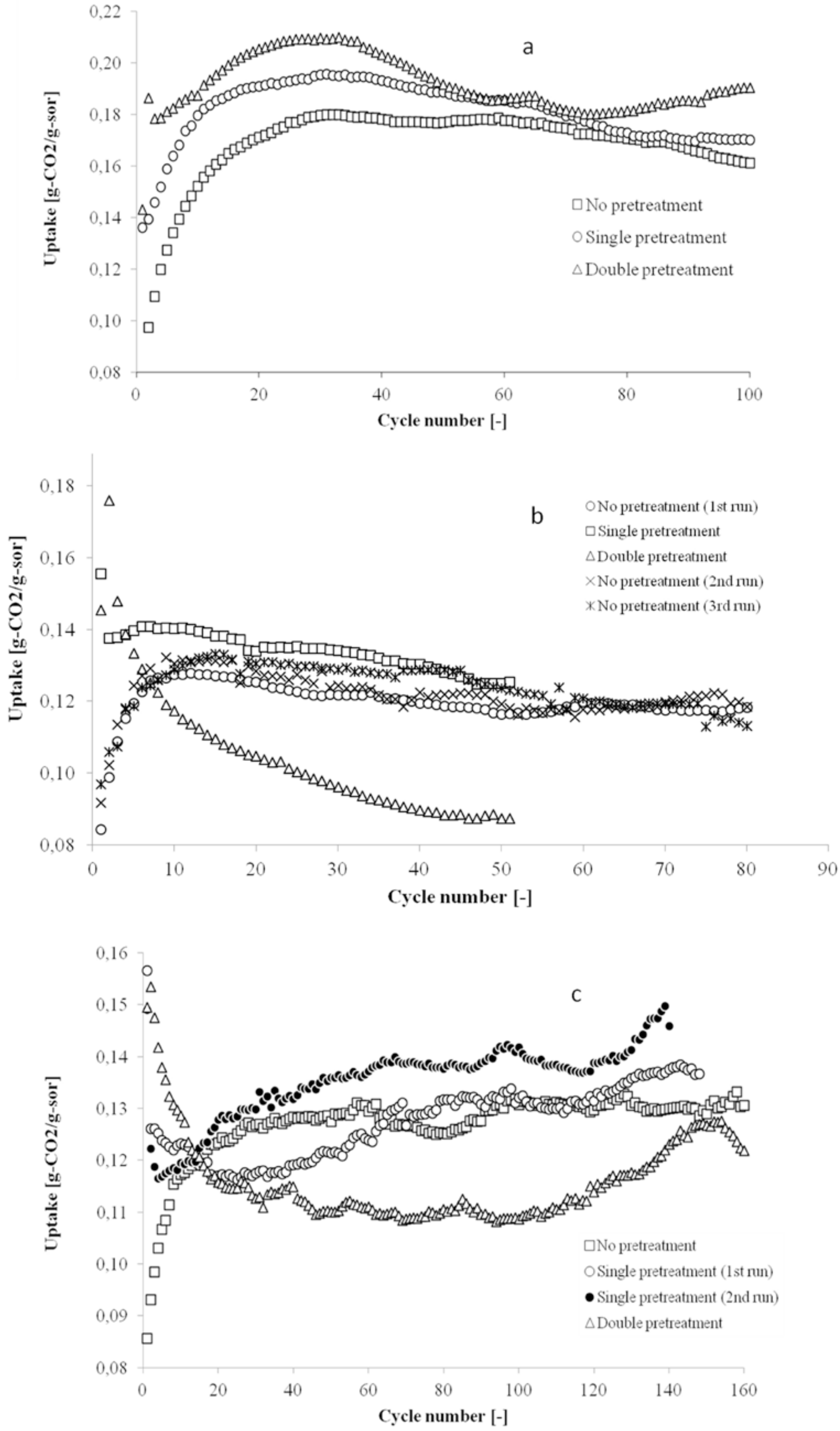

Figure 2. 28 – Carbon capture capacity of 75% CaO sorbent when subjected to different regeneration condition: (a) mild regeneration: 900 °C, 14/86 %v (CO_2/ N_2); (b) moderately severe regeneration: 1000 °C, 14/86 %v (CO_2/ N_2); (c) severe regeneration: 1000 °C, 86/14 %v (CO_2/ N_2). Further runs in (b) e (c) have been presented to show the good reproducibility of the experimental data.

2.3.3.4 Influence of CaO load

As shown in Figure 2. 29, the self-reactivation has been observed also for the 85% CaO sorbent. During the first cycles the uptake of CO_2 for the 85% CaO sorbent is greater to that of 75% CaO sorbent because there is more active phase (CaO). But as the cycling runs the pore plugging occurs likely due to the reduced amount (15%) of binder leading to more CaO being less dispersed and thus more inaccessible to CO_2.

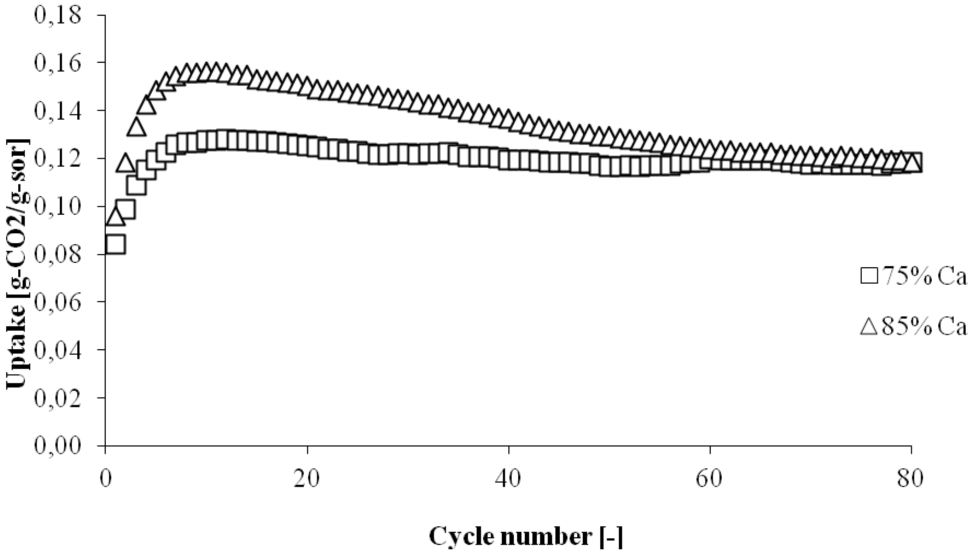

Figure 2. 29 – Effect of CaO load: increasing the load of active phase a decreasing of capacity has been observed.

In fact during repeated cycling the grains grow and sinter together via formed 'necks' as reported in Figure 2. 30. The sorbent morphology before and after the CO_2 capture cycling was observed with a JEOL JSM 5510LV scanning electron microscope (SEM), with 25 kV of accelerating voltage under high vacuum. The images were obtained by secondary electrons. One can see the genesis of a neck structure for a 75% CaO sorbent. The circle (a) focuses the neck between two different bodies, at a later stage the neck increases its cross section (b) and when the neck reaches at its maximum size the two bodies merge together in a single body (c). This structural alteration could lead the blockage of pores and the formation of isolated volumes throughout the particle and it is likely an important factor leading to reduced uptake kinetics and capacity. Another possible explanation could be the greater amount of CO_2 released during the calcination step of 85% CaO sorbent. In fact, as this sorbent has a major Ca utilization, carbon dioxide captured is greater when compared to that reacted with the 75% CaO sorbent (see Figure 2. 29). Then when the former sorbent is cyclically regenerated, it releases a major amount of CO_2 which accelerates the sintering process. It worth to note that the external surface of the recarbonated sorbent showed in Figure 2. 30 does not show mosaic pattern (as found for the naturally occurring sorbent [160-162, 227]) permitting further diffusion of CO_2 through the inner core of the particle. Such microstructure of the particle could also explain the smoother transition to the slower carbonation rate (Figure 2. 24) when compared with steeper one showed by the naturally occurring sorbents [129, 138, 160, 201].

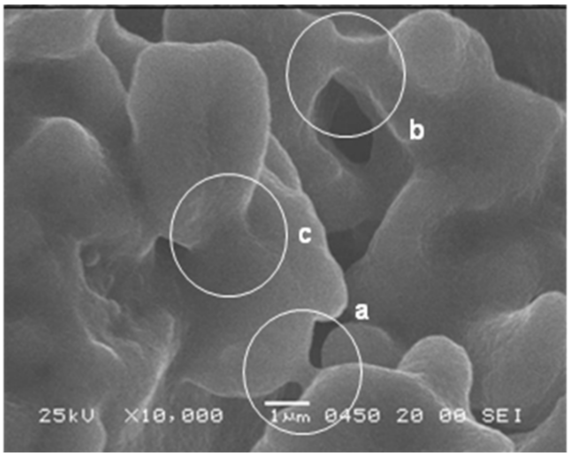

Figure 2. 30 – Micrograph of 75 % CaO sorbent after 60 carbonation/regeneration cycles.

2.3.3.5 Influence of thermal treatment

Thermal treatment influences the uptake of the material and its morphology as well. Table 2. 5 shows the relative change of uptake capacity when the material is thermally treated. For instance, when the 85% CaO sorbent is single treated the increase of CO_2 uptake has been, at least, ~26% higher than the untreated sorbent with a maximum at the third cycle, ~68%. For the double treated sorbent a higher increment of CO_2 uptake has been found showing a better performance than single pretreated sorbent. The positive effect of thermal pretreatment on the uptake kinetics has been also confirmed for the 75 % CaO sorbent. As reported in Table 2. 5 the capability of reacting with CO_2 is greater when the treated sorbent is compared to the untreated one. As one can see, the single pretreated specimen shows a higher uptake when compared to the as synthesized sorbent was observed, with a maximum increase of a ~43 %.

Table 2. 5 - Relative change of the CO_2 uptake for the treated materials with respect to untreated material.

		CaO load [%]			
		75		85	
Regeneration condition	Thermal treatment	Minimum [%]	Maximum [%]	Minimum [%]	Maximum [%]
Mild	Single	1	43	22	68
	Double	4	63	26	112
Moderate	Single	6	39	7	48
	Double	-16	36	-2	41
Severe	Single	1	35	-6	118
	Double	-9	50	-5	-2
	Single	0	31	/	/

2.3.3.6 Influence of CO_2 content during carbonation

The 75 % CaO sorbent has been further investigated by exposing a solid specimen at a 14% CO_2 (N_2 balance) during the isotherm carbonation phase to study the stability of the material at lower CO_2 molar fraction. The measured uptake is reported in Figure 2. 31 where extra experimental runs performed at the same condition are presented. The white and black circles in Figure 2. 31 are the same circles displayed in Figure 2.28 (c). By lowering the molar fraction (from 25 % to 14%) during the CO_2 capturing phase the uptake decreases as you can see in Figure 2. 31. This effect is due likely to the minor effect of the driving force during CO_2 capture. In fact by decreasing the molar fraction in the carbonation phase both reaction rate and diffusion throughout the sorbent is inhibited. Finally self-reactivation effect has been observed at the beginning of the multi-cycling tests for the untreated specimens and at later cycles for the thermally treated material.

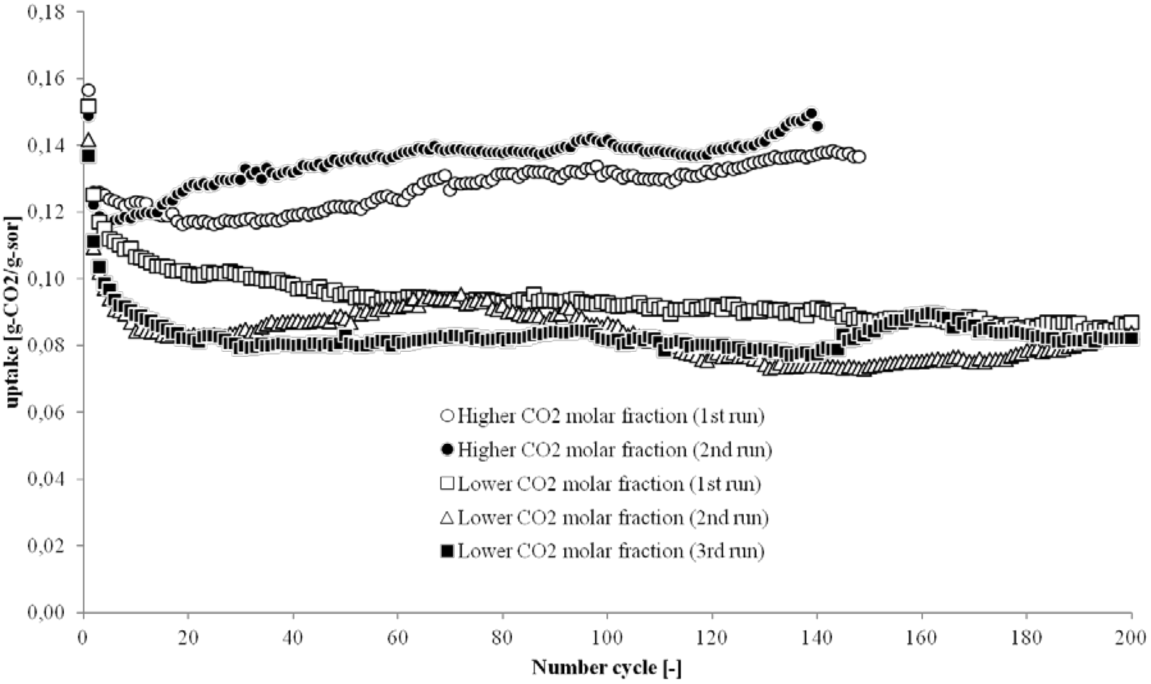

Figure 2. 31 – Comparison between the uptake of the pre-treated 75% CaO sorbent when exposed to severe condition: influence of CO_2 molar fraction during carbonation phase. The CO_2 uptake decreases likely due to the minor driving force for the CO_2-CaO reaction. Higher CO_2 molar fraction: 25%, CO_2, lower CO_2 molar fraction 14% CO_2: N_2 balance. Further runs show good reproducibility of the experimental data.

2.3.4 Conclusions

The multi-cycling CO_2 sorption-desorption tests on synthetic CaO-$Ca_{12}Al_{14}O_{33}$ sorbent show that the reversibility of the CO_2 uptake in repeated cycles is significantly improved compared to that of dolomite. Two types of the sorbent precursor have been selected. The former has been grounded and heated up without adding water whereas some water drops have been added in the latter during the intermediate synthesis phase. Even if sorbents obtained from dry and hydrated precursor have showed pore size below 220 nm, an increase on the CO_2 carrying capacity has been observed in the sorbent obtained from hydrated precursor likely due to the much more volume found below 220 nm during the final calcinations in the synthesis phase. Preliminary experiments aimed at increasing the capacity to retain carbon show an increasing in CO_2 uptake when exposing the material to a carbonation (14% CO_2, N_2 balance) at 600 °C for 80 minutes prior the multi-cycling experiment. Improvement of sorbent uptake due to the thermal treatment confirming results published elsewhere [139, 143] where naturally occurring sorbents (limestone, dolomite) showed better uptake capacity and stability when exposed to thermal pretreatment. Here, thermal pretreatment of the manufactured sorbent leads to some improvement in the CO_2 uptake in subsequent cycles. Even if, the single pretreated 85% CaO sorbent, shows a slightly increase in pore volume, it has shown a self-reactivation period and a superior CO_2 carrying capacity in comparison to the relative untreated sorbent. Particularly when such a sorbent is subjected to cycling an increase in pore volume has been detected. This is probably due to the formation of cracks throughout the microstructure of sorbent particle which increases the available CaO. Once the pore volume has been formed during the first cycles (self-reactivation period is completed) the sorbent exhibits a good capacity to retain this pore volume. Finally, the influence of regeneration condition on the self-reactivation period was studied. Particularly such a period is reduced when increasing both temperature and carbon dioxide during the regeneration step.

Unexpected results have been found for the 75 % CaO sorbent which shows a continuously increase in CO_2 capture up to 150th cycle under severe regeneration condition. The good reversibility showed by this material in severe regeneration condition makes it a good candidate for CO_2 acceptor in a carbonate looping. In fact, in such a technology option a high concentrated CO_2 stream is required for final disposal. Carbon dioxide is collected at the outlet of the calciner where regeneration of the sorbent occurs. As a consequence the ideal CO_2 acceptor should withstand high CO_2 concentration in the calciner to achieve a good regeneration extent to begin properly another carbon capture cycle. Finally as reported in Figure 2. 31 the CaO utilization suffers from the low presence of carbon dioxide. In particular the investigated material shows better performance in higher concentrated CO_2 stream (25% CO_2 at 600 °C) even under severe regeneration condition making it a suitable sorbent for pre-combustion CO_2 capture.

3 CFD MODELING OF A SORPTION ENHANCED - STEAM METHANE REFORMING REACTOR

3.1 A brief introduction to fluidization

Gas-solid fluidized beds are widely applied in many chemical processes involving physical and/or chemical transformations, and for this reason they are the subject of intense research in chemical engineering science. Several excellent textbooks have been published covering a wide number of subjects devoted to fluidization, from basis to very detailed and specific topics (e.g. [228-230]). A brief summary of fluidization follows, for the sake of completeness of the discussion.

The first large scale commercial plant based on fluidized bed technologies was erected in the United States in 1942 during II World War for fluid catalytic cracking (FCC), because of the need to produce enormous quantities of aviation gasoline. After the war, this successfull technology was made public, and since this moment has been used for industrial applications such as Fischer-Tropsch synthesis, phthalic anhydride synthesis, methanol to gasoline and olefin processes, cracking of hydrocarbons, coal combustion, coal gasification, cement clinker production, Titanium dioxide production, calcination of $Al(OH)_3$, granulation drying of yeast, heat exchange or absorption processes.

Fluidization is a process whereby a bed of solid particles is transformed into something closely resembling a liquid.

This description done by Gibilaro [231], aside from its generic character is very accurate. If a fluid passes upward through a bed of solids, at very low velocity, it percolates across the interstitial space between the particles. When gas flow increases, particles start to move in restricted regions and the bed expands until reaching a point in which all the particles are suspended in the gas phase. This point is known as bed at *minimum fluidization*, and the weight of the particles is counterbalanced with upwards draft exerted by the gas. In this point, the pressure drop though any section is equal to the weight of fluid and solids in this section, as in a true liquid medium. This relation was obtained by Ergun in 1952, and it is nowadays widely used [232].

If gas velocity (U_g) increases beyond the *minimum fluidization velocity* (U_{mf}) large instabilities with formation of bubbles and channeling of gas are observed. The bed expansion continues, but pressure drop remains through the bed. This fluidization regime is usually known as aggregative fluidization. It is important to note that depending of the properties of particles the bed can be bubbling or slugging (in the case of fine particles, due to bubble coalescence).

With a subsequent increase of velocity, the velocity of gas can exceed the terminal velocity of the particles (U_t), starting their entrainment. Under these conditions, instead of bubbles, it is possible to observe a turbulent motion of solids clusters and voids with different sizes and velocities. The beds under these conditions are called *turbulent beds*. Increasing gas velocity particles enters in transport regimes, that depending on gas velocity can be fast fluidization (typical of circulating fluidized beds) or pneumatic conveying.

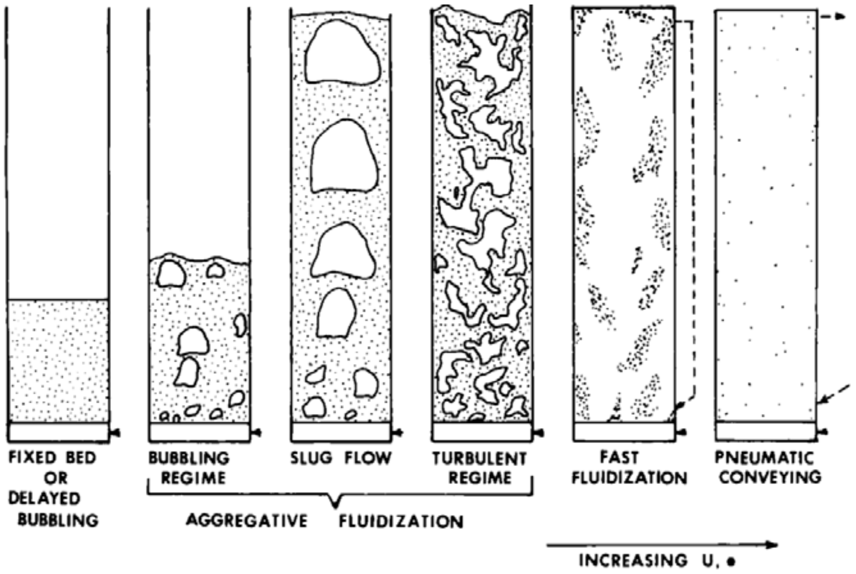

Figure 3. 1 – Principal flow regimes for upward flow of gas trough solid particulate materials, from [233]

As general rule, it is possible to suppose that:

- If $U_g < U_{mf}$ → Fixed bed
- If $U_{mf} < U_g < U_t$ → Dense–phase fluidized bed
- If $U_t < U_g$ → Disperse–phase fluidized bed

However, instead of this global description, very different behaviors of fluidized bed are observed under the same fluidization type (for example it is possible work under bubbling regime with a velocity higher than terminal if particles are fine). Until the work of Geldart [234], numerous attempts failed in the prediction of fluidization regime and the transition from one mode to another. Geldart proposed a very simple, powerful and useful classification of fluidization regimes focused in the properties of the particles. By carefully observing the fluidization of all sorts and sizes particles Geldart proposed four types of particle behavior as function of density and particle diameter (Figure 3. 2).

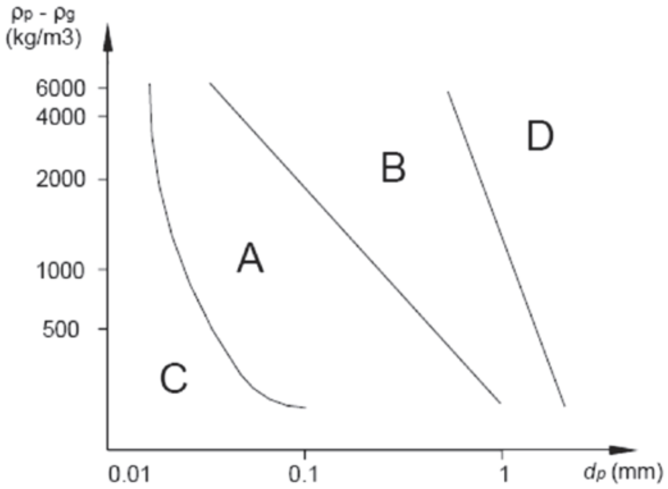

Figure 3. 2 – Geldart classification of particles for air ambient conditions. Adapted from [234]

Geldart particle types are, from smallest to largest particles:

- Group **C**: cohesive, or very fine powders ($d_p < 30$ μm) (e.g. flour or cement). Normal fluidization of this type of particles is very difficult because van der Waals and other cohesive forces are stronger than those due to gas. Channeling occurs instead of fluidization. Mechanical powder compaction, prior to fluidization, greatly affects the fluidization behavior of the powder, even after the bed had been fully fluidized previously. A very good characterization of this type of particles can be found in [235].

- Group **A**: aeratable, or small mean particle size and/or low particle density (<1.4g/cm^3) (major example is the FCC catalyst). Easily fluidized particles with smooth fluidization at low gas velocities; and controlled bubbling with small bubbles at higher gas velocities. Large bed expansion before bubbling starts. When fluidized by air at ambient conditions, result in a region of non-bubbling fluidization beginning at U_{mf} , followed by bubbling fluidization as fluidizing velocity increases. Gas bubbles rise faster than the rest of the gas.

- Group **B**: sand-like, or particle size 40 μm to 500 μm and density 1.4 to 4 g/cm^3. Majority of gas-solid reactions occur in this regime, based on particle size of raw materials. Gas bubbles appear at the minimum fluidization velocity U_{mf}. Small bubbles form at the distributor and grow and coalesce as the rise though the bed. Bubble size increases linearly with distance and it is independent of particle diameter.

- Group **D**: spoutable, or large and/or dense particles. Very erratic behavior giving large exploding bubbles, or severe channeling, or spouting behavior. Bubbles coalesce rapidly and flow to large size. Bubbles rise more slowly than the rest of the gas percolating through the emulsion. Dense phase has a low voidage. These particles are used in drying and roasting process (e.g. coffee beans wheat, lead shot).

Geldart classification is very useful to predict the behavior of solids under fluidization conditions. However is not sufficient to predict the regime in which the bed will be. For engineering applications it is necessary know the type of particle and also the fluidization regime to design the reactors and predict the gas-solid contacting mode. That is, the Geldart B particles present a behavior different to Geldart A ones, but, moreover it is necessary know if the particle will be under bubbling or circulating regime (or another regime). Figure 3. 3 is an excellent summary of the possible paths through particulate regimes as the velocity of the fluidizing gas is increased within the bed.

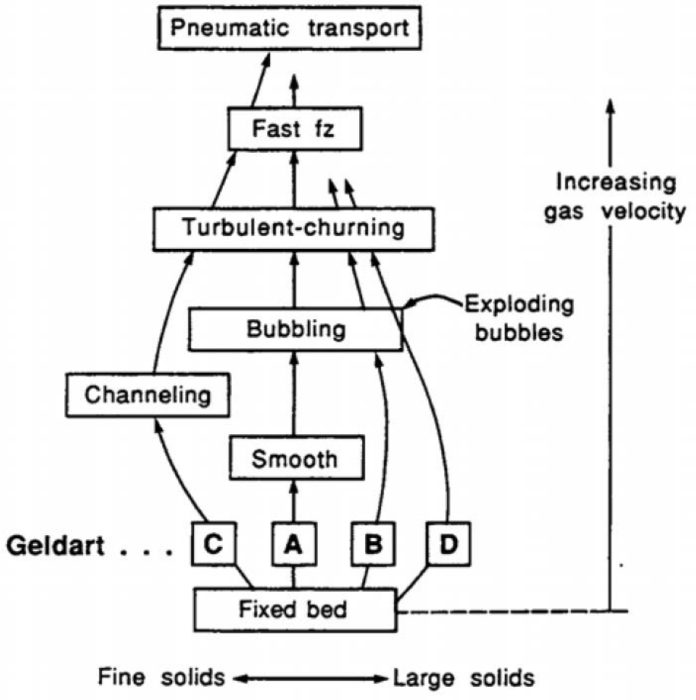

Figure 3. 3 – Possible paths of fluidization, from [228]

Some investigators have mapped these regimes, but the most widely used is the Grace's diagram [233, 236]. With a methodology similar to the Geldart work, Grace stabilished the relation between fluidization regime and Geldart particle groups. Moreover, he compared the different theories to calculate minimum fluidization velocity and the boundaries between particle types. Thus, as shown in Figure 3. 4, it is possible predict the fluidization regime and particle type by means of dimensionless superficial gas velocity (U^*) and dimensionless particle diameter (d_p^*) $(U^*$and d_p^* are derived from dimensionless particle Reynolds Re_p and Archimedes Arnumbers).

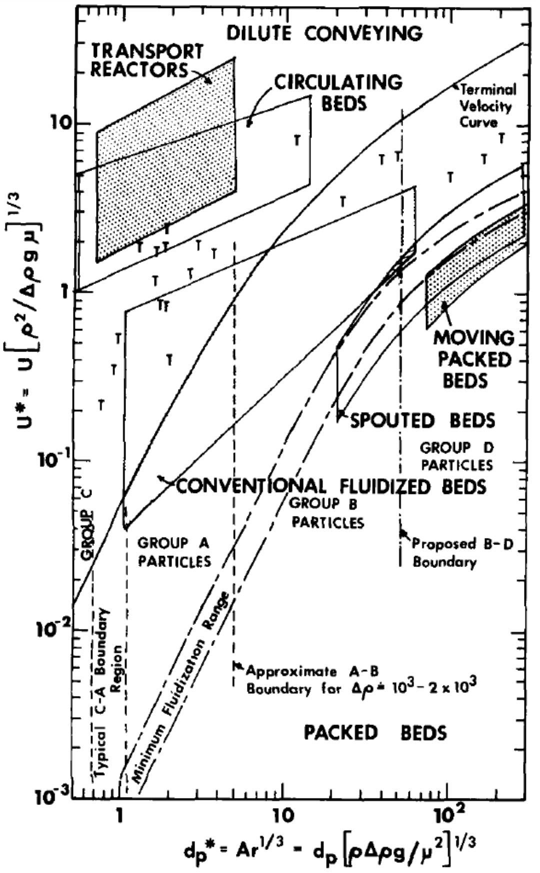

Figure 3. 4 – Grace diagram of fluidization regimes, from [233]

As explained previously, this work is centered in the study of SE-SMR reaction. Due to the particularities of this process, BFB is most convenient reactor. In order to improve gas-solid mixing and to operate in the most stable regime the particles are ground to meet Geldart B-group. Thus, further explanation about hydrodynamics will be centered in these systems.

Bubbling fluidized reactors are commonly divided in three parts:

- Distributor which serves to homogenize the injection of fluidizing gas and to stop solids from flowing back during normal operation and shut down support the bed. This part ha as a considerable effect on proper operation of the fluidized bed.
- Bubbling bed. The bed height depends on gas contact time, length to diameter (L/D) ratio needed to provide staging, space needed for internal heat exchangers and solids retention time.
- Freeboard. The freeboard or disengaging height is the distance between the top of the fluid bed and the gas-exit nozzle. At least two actions can take place in the freeboard: classification of solids and reaction of solids and gases.

When gas velocity is equal to minimum velocity, bubbles are generated at the exit of the distributor. The rising bubbles move gas and particles upward as well as a corresponding flow of particles downward. As a bubble reaches the upper surface of a fluidized bed, the gas breaks through the bubble geysering upward the solids. The downward pull of gravity and the upward pull of the drag force of the upward-flowing gas act on the particles. The larger and denser particles return to the top of the bed, and the finer and lighter particles are carried upward. The distance above the bed at which the entrainment becomes constant is the transport disengaging height (TDH).

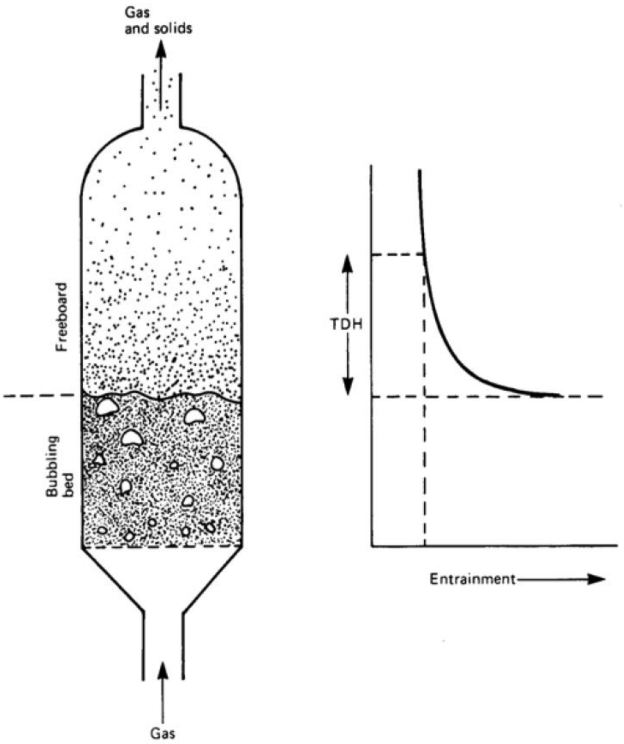

Figure 3. 5 – Bubbling Fluidized Bed with entrained particles in the freeboard region above the dense bubbling bed, from [237]

In order to model fluidized bed mechanics is crucial to describe accurately the behavior of bubbles to predict the gas-solid contact. Bubbles form at the distributor exit ports where fluidizing gas enters the bed. Bubbles are generated because the velocity at the interface of the bed just above the distributor holes represents a gas input rate in excess of what can pass through the interstices with a frictional resistance less than the bed weight and hence the layers of solids above the holes are pushed aside until they represent a void through whose porous surface the gas can enter at the incipient fluidization velocity. If the void attempts to grow larger the interface velocity becomes insufficient to hold back the walls of the void and hence they cave in from the sides cutting off the void and presenting a new interface to the incoming gas. This mechanism is illustrated in Figure 3. 6.

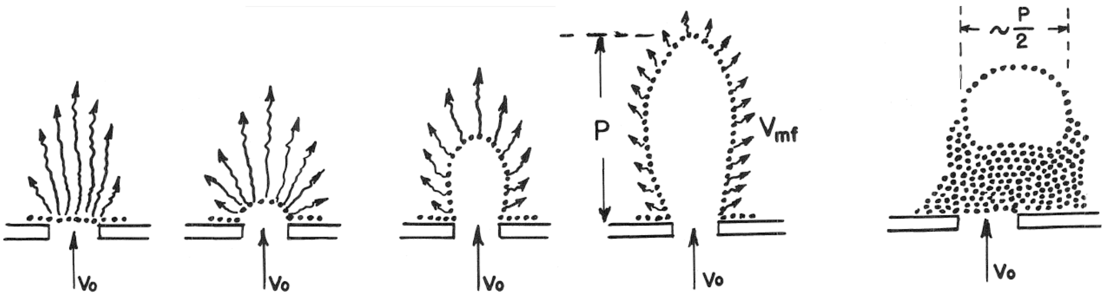

Figure 3. 6 – Bubble formation mechanism, from [238]

The number, velocity and size of bubbles affect strongly the movement in the bed. A common approach to understand and attempt to model the behavior of the bed is to suppose that the aggregative fluidization consist in two phases: the bubble phase and the emulsion (o particulate phase). The flow rate through the emulsion phase is equal to the flow rate for minimum fluidization, and the voidage is essentially constant at ε_{mf}. Any flow in excess of that required for minimum fluidization appears as bubbles in the separate bubble phase.

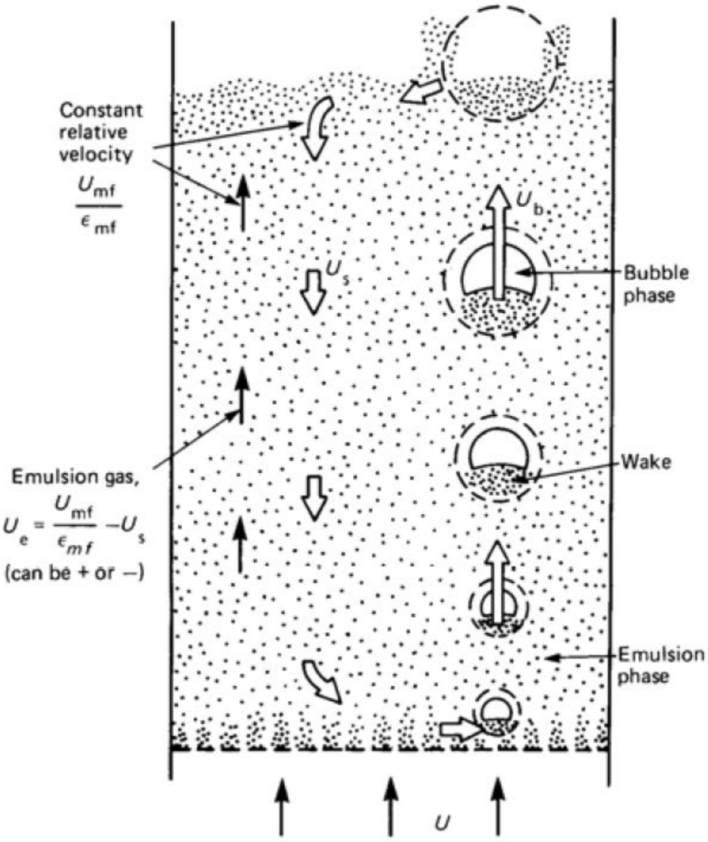

Figure 3. 7 – Bubbling fluidized bed hydrodynamics, , from [237]

However bubble phase is more complex to hypothesize. The first complete model for bubble phase was developed in 1961 by Davidson [239]. This theory was capable of explaining many phenomena relating to bubbles in fluidized beds observed experimentally. This model supposes that the bubble is spherical and it is surrounded by a “cloud” of particles which serves simultaneously to change the motion of the bubble and to exchange properties with emulsion phase. Davidson solved these equations in terms of particle motion, the pressure distribution within the fluidizing fluid, the absolute velocities of the fluidizing fluid, and the exchange between the bubble and the particulate phase. He found that the geometry of the stream function is crucially affected depending whether the bubble velocity is larger or smaller than interstitial minimum fluidization velocity. The fluidizing fluid in this case moves downward relative to the bubble motion. The fluid flows past the fictitious cloud sphere. Inside the cloud, the fluid leaves the roof of the bubble and recirculates back to the base of the bubble as shown in Figure 3. 8. Obviously this model was very simplified and it has been modified and improved, for example to approximate better the form of particles and include the effect of bubble wakes (Figure 3. 8).

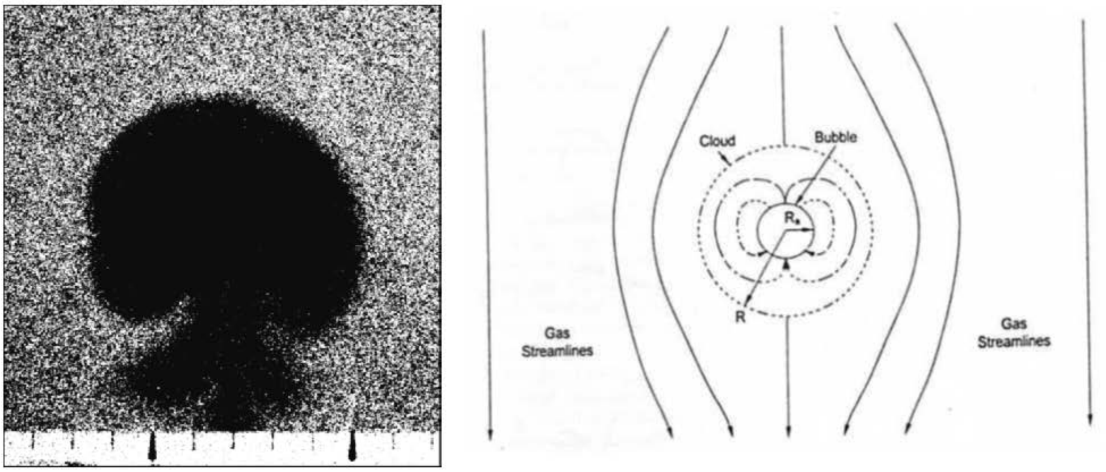

Figure 3. 8 – Bubble formation in a 2D BFB (left) [240]. Davidson fast bubble model scheme (right)[230].

Several of the approximations done by Davidson are still very useful to model the bubbling beds in micro and macro-scales. On the one hand, the velocity of bubble affects strongly the behavior of the bed (in terms of bed expansion and voidage). The rising velocity can be calculated directly from the bubble diameter and it is independent of the type of bed materials [241, 242]. On the other hand an empirical rule for estimate bubble grow was proposed to link bubble velocity and diameter. The bubbles in fluidized beds grow in size due primarily to four factors: the hydrostatic pressure on the bubbles decreases as they rise up the bed; the bubbles may coalesce by one bubble catching up with another; the bubbles which are side by side may coalesce; and, the bubbles may grow by depleting the continuous phase locally. Several models have been developed to predict the growth of bubbles as shown in Figure 3. 9 [238, 243, 244].

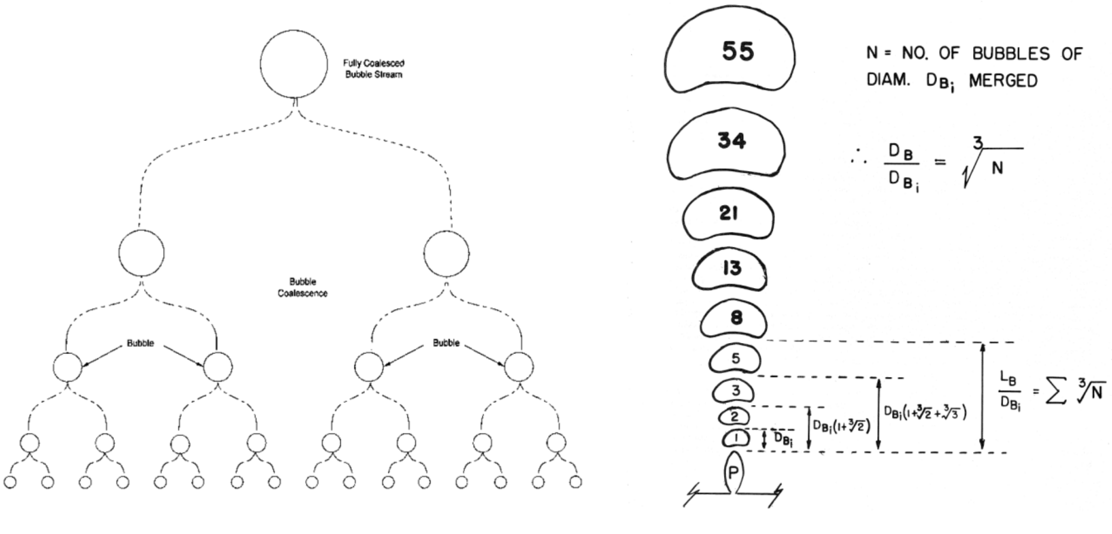

Figure 3. 9 – Bubble grow mechanism according with Darton et al. (left) and Zenz (right) models [229].

The first complete general two-phase model was proposed by Kunii and Levensipel [228], and it includes the effect of cloud and wake of the bubbles, more detailed analysis of conditions of emulsion and bubble phase, and freeboard effects. The K-L model has been implemented in engineering applications successfully, and, with some modifications, it is widely used nowadays (e.g. [245] or [246]).

3.2 CFD modeling of bubbling fluidized beds

In the last decade, a paradigm shift has occurred in the study of fluidization from two-phase flow theory to computational fluid dynamics (CFD). An example of the acceptation of CFD in the fluidization community is the plenary lecture by Prof. J.A.M. Kuipers at FLUIDIZATION IX in 1998 [247]. CFD is a very powerful tool to simulate fluidized beds but present some disadvantages compared with global system models, as shown in Table 3. 1 [248]

Table 3. 1 – Classification of the various models used for simulating dense gas-solid flow

	CFD Models	Global System Models
Advantage	More exact solution available Phenomena follow from calculation a priori	Simple models and simple solutions facilitate understanding After adjustment of parameters accurate macroscale prediction
Disadvantage	Detailed knowledge required about the elementary processes Macroscopic behavior not always accurately predicted	Experimental validation and adjustment of parameters necessary Meaning of parameters sometimes unclear due to lumping

Over the years, several research groups have developed a large number of numerical models in order to predict the behavior of gas-solid systems. From a generalist point of view there are two different approaches to model both phases: Eulerian and Lagrangian. The Eulerian approach adopt a continuum description of the phase, which is then governed by a Navier-Stokes-type equation. The Lagrangian approach considers the phase as a collection of a discrete number of particles that obey Newton's law. According with these two options for each phase, the fluidized bed CFD models can be classified as shown in Table 3. 2 and Figure 3. 10 [249].

Table 3. 2 – Classification of the various models used for simulating dense gas-solid flow

	Name	**Gas phase**	**Solid phase**	**Gas-solid coupling**	**Scale**
1	Discrete bubble model	Lagrangian	Eulerian	Drag closures for bubbles	Industrial (10 m)
2	Two-fluid model	Eulerian	Eulerian	Gas-solid drag closures	Engineering (1 m)
3	Unresolved discrete particle model	Eulerian (unresolved)	Lagrangian	Gas-particle drag closures	Laboratory (0.1 m)
4	Resolved discrete particle model	Eulerian (resolved)	Lagrangian	Boundary condition at particle surface	Laboratory (0.01m)
5	Molecular dynamics	Lagrangian	Lagrangian	Elastic collisions at particle surface	Mesoscopic (<0.001 m)

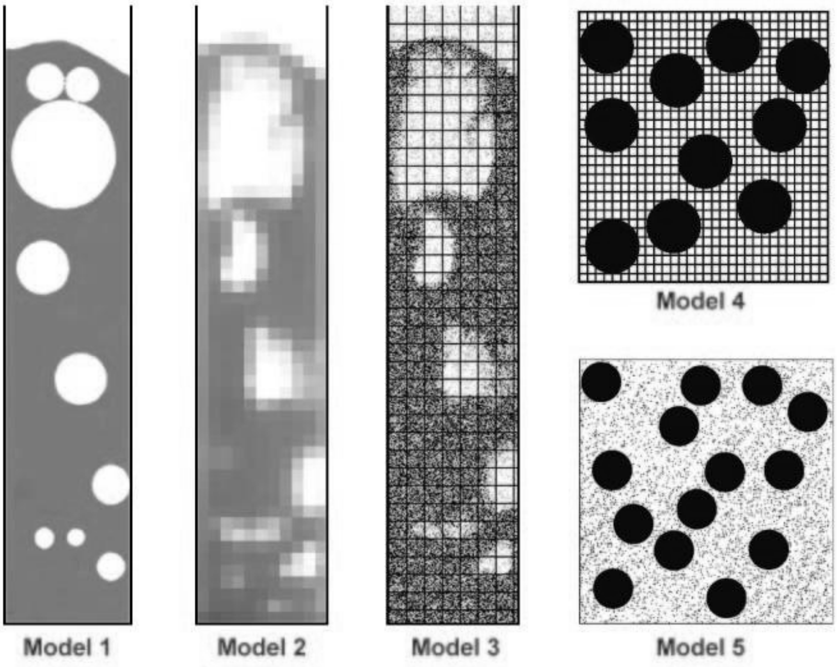

Figure 3. 10- Graphical representation of the models summarized in Table 3. 2. The grid indicates the scale on which the continuum phase is solved.

The Discrete Bubble Model (model 1) is a very promising technique for very large reactors, but it is still under development, particularly for the problems to refined the rules of coalescence and break-up of the bubbles [250, 251]. In the Resolved Discrete Particle Model (model 4), particles motion is solved by means of a Lagrangian method, and gas phase is fully resolved, by means of Direct Numerical Simulations (DNS) at Kolmogorov scales, or by means of Lattice Boltzmann methods. This method is very expensive in terms of computational resources, and it is not fully developed due to the problems of implementing the stick boundary condition, in which the fluid velocity vanishes at the surface of the solid spheres [252]. In the Molecular Dynamics Model (model 5) both gas phase and solid phase are represented by particles. Thus gas-solid interactions are represented as collisions between gas particles with solid particles. This model can be implemented by Lattice Gas Cellular Automata’s, but it is useful only at very small scales, far from fluidized bed interest [253].

Therefore, the most useful methods, from an engineer point of view are the Unresolved Discrete Particle Model (also termed as Discrete Element Model, DEM, model 3) and the Two-Fluid Model (TFM, also known as E-E model, model 2). DEM solves the solid flow by means of a Lagrangian approach, whilst the gas flow is solved by means of the classical Eulerian CFD approach (finite-difference/finite-element techniques). DE models are devoted to investigate particle-particle, particle-gas and particle-wall interactions, and their effects in mixing and formation of heterogeneous flow structures. Very interesting reviews of these methods can be found in [254] and [255]. Meanwhile TFMs abandons the concept of solid phase formed by a discrete number of particles, and it considers that both gas phase and solid are described as fully interpenetrating continua, using a set of generalized Navier-Stokes equations. TFM include indirectly the effects of particle-particle interactions by means of appropriate closure equations.

These two methods (TFM and DEM) have been extensively compared (e.g. [256-260]) with very good results compared with experiments, and comparable computational costs and accuracy at laboratory scale simulations. However, when the size of system increases to semi-industrial or industrial size the TFM model presents a notable computer saving with respect to DEM, that surpass the efforts to develop most efficient numerical methods for solving the Lagrangian phase [261].

Therefore, we used in this work the two-fluid model, embedding the kinetic theory of granular flow for particulate phase stress, for the numerical simulation of gas fluidization.

3.2.1 Kinetic Theory of granular flows

TFM model solves governing equations of continuity and momentum equations for each phase. Thus, proper modeling is necessary to obtain accurate and better results. The coupling between the phases depends on the type of mixture being involved in the system. A common approach to close conservation equations is using kinetic theory in case of granular flows (KTGF).

KTGF assumes that particle heat and mass transfer characteristics are due to nearly elastic random oscillations of particles suspended in fluids. Thus, solid phase presents a behavior similar to gases, and kinetic theory can be assumed with some modifications. A Maxwellian velocity distribution can be assumed for the particles. And the KTGF can be used for closure of the solid stress terms, with a drag function which serves to calculate the momentum exchange coefficients. Other constitutive equations are needed to close the granular-phase momentum equation. The energy dissipation due to the collision of inelastic particles is calculated with a particle temperature model.

In KTGF the basic concept is the granular temperature, which is like thermal temperature in kinetic theory of gases. It measures the random oscillations of particles. The thermal temperature has a conversion factor from energy to degrees, the Boltzmann constant. For granular temperature, this constant is one. In granular flow particles dissipate energy due to inelastic collisions. Hence, equipartition of energy does not hold. Therefore, one usually defines the granular temperature as random kinetic energy per unit mass, which is just the average of the three squares of the velocity components in the three directions. Thus the granular temperature is the average of the three variances of the velocities of the particles. With an accurate modeling of the granular temperature equation, it is possible to model the random oscillations of motion and energy including turbulence, without the necessity of use a devoted closure equation for turbulence (as, for example, k- ε models). Thus KTGF model computes the viscosity from the granular temperature, with the principal input of effective restitution coefficient. Moreover, the solution of solid shear stress model includes the collisional, the kinetic and the frictional effects.

The Kinetic Theory of Granular Flows was mainly developed during the 1980’s and early 1990’s by Dimitri Gidaspow at Illinois Institute of Technology, and a very complete description can be found in his book [262]. Based in this theory, Syamlal, Rogers and O’Brien, from U.S. Department of Energy, developed and reformulated some parts of Gidaspow's theory in an open-source code called MFIX [263, 264], which has been subsequently refined and implemented in CFD commercial codes such as FLUENT, being extensively used with very good results [265].

For a better understanding we summarized the governing and constitute equations of the KTGF. For simplicity, an isothermal non-reactive flow is supposed, thus the explanation is centered in the motion equations of the model. Considering *s* as solid phase (for simplicity we consider just one solid phase) and *g* as gas phase, and α_s and α_g are the volume fraction of each phase, the continuity and momentum equations are:

Continuity equation for gas phase:

$$\frac{\partial}{\partial t}\left(\alpha_g \rho_g\right) + \nabla \cdot \left(\alpha_g \rho_g \vec{v}_g\right) = 0 \tag{3. 1}$$

Continuity equation for solid phase:

$$\frac{\partial}{\partial t}\left(\alpha_s \rho_s\right) + \nabla \cdot \left(\alpha_s \rho_s \vec{v}_s\right) = 0 \tag{3. 2}$$

Momentum equation for gas phase:

$$\frac{\partial}{\partial t}\left(\alpha_g \rho_g \vec{v}_g\right) + \nabla \cdot \left(\alpha_g \rho_g \vec{v}_g \vec{v}_g\right) = -\alpha_g \nabla p + \nabla \cdot \bar{\bar{\tau}}_g + \alpha_g \rho_g \vec{g} + K_{gs}\left(\vec{v}_s - \vec{v}_g\right) + F \tag{3. 3}$$

Momentum equation for solid phase:

$$\frac{\partial}{\partial t}\left(\alpha_s \rho_s \vec{v}_s\right) + \nabla \cdot \left(\alpha_s \rho_s \vec{v}_s \vec{v}_s\right) = -\alpha_s \nabla p - \nabla p_s + \nabla \cdot \bar{\bar{\tau}}_s + \alpha_s \rho_s \vec{g} + K_{gs}\left(\vec{v}_g - \vec{v}_s\right) + F \tag{3. 4}$$

As explained before, the kinetic energy associated with the particle velocity fluctuations is represented by the **granular temperature** (Θ_s) which is proportional to the mean square of the random motion of particles:

$$\frac{3}{2}\left[\frac{\partial}{\partial t}\left(\rho_s \alpha_s \Theta_s\right) + \nabla \cdot \left(\rho_s \alpha_s \vec{v}_s \Theta_s\right)\right] = \left(-p_s \bar{\bar{I}} + \bar{\bar{\tau}}_s\right) : \nabla \vec{v}_s + \nabla \cdot \left(k_{\Theta_s} \nabla \Theta_s\right) - \gamma_{\Theta_s} \tag{3. 5}$$

The constitutive equations of KTGF are used for determinate the stresses ($\bar{\bar{\tau}}_s$), viscosity (μ_s), and pressure (p_s) of the solid phase, that are dependent of the granular temperature. Several closure models have been developed for different groups and implemented in commercial codes [266]. However the most used are those by MFIX group [263]. If any model is from different author reference is specified.

Solids stress-strain tensor can be defined as:

$$\bar{\bar{\tau}}_s = \alpha_s \mu_s \left(\nabla \vec{v}_s + \nabla \vec{v}_s^{\,T}\right) + \alpha_s \left(\lambda_s - \frac{2}{3}\mu_s\right) \nabla \cdot \vec{v}_s \bar{\bar{I}} \qquad (3.\ 6)$$

where λ_s is the bulk viscosity and μ_s is the solid shear viscosity that takes into account the frictional, collisional and kinetic effects of the granular flow, as shown in

Figure 3. 11.

Granular bulk viscosity [267]:

$$\lambda_s = \frac{4}{3}\alpha_s \rho_s d_s g_0 \left(1 + e_{ss}\right)\left(\frac{\Theta_s}{\pi}\right)^{1/2} \qquad (3.\ 7)$$

Solid shear viscosity:

$$\mu_s = \mu_{col} + \mu_{kin} + \mu_{fr} \qquad (3.\ 8)$$

where:

Kinetic part of the shear viscosity:

$$\mu_{kin} = \frac{\alpha_s d_s \rho_s \sqrt{\Theta_s \pi}}{6\left(3 - e_{ss}\right)}\left[1 + \frac{2}{5}\left(1 + e_{ss}\right)\left(3e_{ss} - 1\right)\alpha_s g_0\right] \qquad (3.\ 9)$$

Collisional part of the shear viscosity:

$$\mu_{col} = \frac{4}{5}\alpha_s \rho_s d_s g_0 \left(1 + e_{ss}\right)\left(\frac{\Theta_s}{\pi}\right)^{1/2} \qquad (3.\ 10)$$

Frictional part of the shear viscosity [268]:

$$\mu_{fr} = \frac{p_s \sin\phi}{2\sqrt{I_{2D}}} \qquad (3.\ 11)$$

where ϕ is the angle of internal friction, I_{2D} is the second invariant of the deviatoric stress tensor, and e_{ss} is the restitution coefficient. KTGF is extremely sensitive to restitution coefficient of the particles, thus this parameter must be selected accurately.

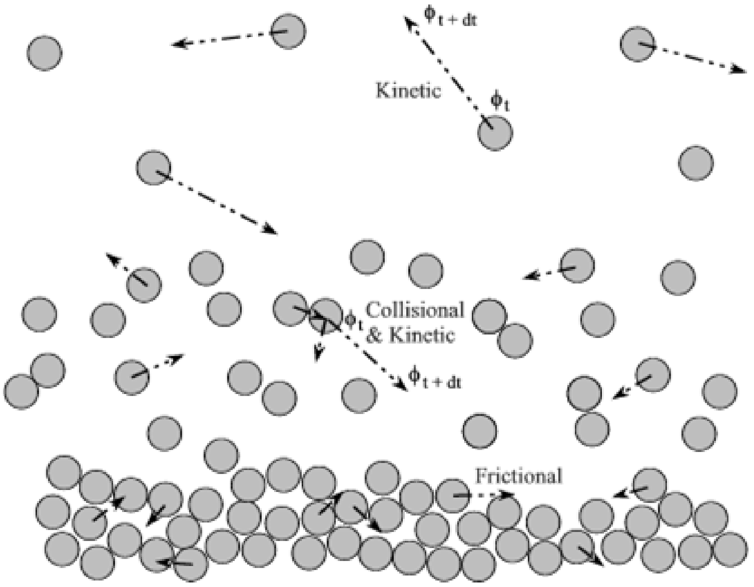

Figure 3. 11- Schematic representation of frictional, collisional and kinetic effects in granular flows, from [269]

The **solids pressure** p_s is defined as [267]:

$$p_s = \alpha_s \rho_s \Theta_s + 2\rho_s (1 + e_{ss}) \alpha_s{}^2 g_0 \Theta_s \tag{3. 12}$$

where g_0 is the radial distribution, a correction factor that modifies the probability of collisions between grains when the solid granular phase becomes dense, and presents the form of [270]:

$$g_0 = \left[1 - \left(\frac{\alpha_s}{\alpha_{s,\max}} \right)^{\frac{1}{3}} \right]^{-1} \tag{3. 13}$$

In order to close the momentum equations is necessary to define the forces balance (*F*) and the interphase momentum exchange coefficient (*β*).

In multiphase flows global force balance is very intricate since a number of mechanisms act simultaneously and interact with each other. Therefore, only very simplified analyses are possible. According with [262] the **forces** balance mainly depends on the sum of external body force (drag and gravity forces), lift force, and virtual mass force:

$$F = \vec{F}_{ext} + \vec{F}_{lift} + \vec{F}_{vm} \tag{3. 14}$$

Lift forces act on a particle mainly due to velocity gradients in the gas flow field. Virtual mass effect occurs when the solid phase accelerates relative to the gas phase. The inertia of the gas-phase mass encountered by the accelerating particles (or droplets or bubbles) exerts a "virtual mass force" on the particles. In most cases, the lift and vitual mass forces are insignificant compared to the drag force. A detailed description of drag, lift and virtual mass forces can be found in [271, 272]. Other forces as buoyancy, centrifugal forces, conventional Basset, Magnus and Saffman forces, form and friction forces, as well as turbulent migration and other instability mechanisms, can be also considered negligible in our case [273]. Thus, they have not be considered in this formulation.

The **interphase momentum exchange coefficient** K_{gs} (or β) can be written in the following general form:

$$K_{gs} = K_{sg} = \beta = \frac{\alpha_s \rho_s f}{\tau_s} \tag{3. 15}$$

Where τ_s is the particulate relaxation time, defined as:

$$\tau_s = \frac{\rho_s d_s{}^2}{18\mu_g} \tag{3. 16}$$

And f is defined differently for the different exchange-coefficient models. All definitions of f include a drag function (C_D) that is based on the particle Reynolds number (Re_p). It is this drag function that differs among the exchange-coefficient models, and the application of a different drag model, significantly impacts the flow of the solids phase [274]. The most used K_{gs} are:

- **Syamlal-O'Brien model** [275]

$$\beta = \frac{3\alpha_s\alpha_g\rho_g}{4v_{r,s}^2 d_s} C_D\left(\frac{Re_p}{v_{r,s}}\right)\left|\vec{v_s} - \vec{v_g}\right| \tag{3. 17}$$

$$C_D = \left(0.63 + \frac{4.8}{\sqrt{Re_p/v_{r,s}}}\right)^2 \tag{3. 18}$$

where $v_{r,s}$ is terminal velocity of solid phase

- **Wen-Yu model** [276]

$$\beta = \frac{3\alpha_s\alpha_g\rho_g\left|\vec{v_s} - \vec{v_g}\right|}{4d_s} C_D \alpha_g^{-2.65} \tag{3. 19}$$

$$C_D = \frac{24}{\alpha_g Re_p}\left[1 + 0.15\left(\alpha_g Re_p\right)^{0.687}\right] \quad if\ Re_p < 10^3 \tag{3. 20}$$

$$C_D = 0.44 \quad if\ Re_p \geq 10^3 \tag{3. 21}$$

- **Gidaspow model** [262]

When $\varepsilon_g > 0.8$

$$\beta = \frac{3\alpha_s\alpha_g\rho_g\left|\vec{v_s} - \vec{v_g}\right|}{4d_s} C_D \alpha_g^{-2.65} \tag{3. 22}$$

$$C_D = \frac{24}{\alpha_g Re_p}\left[1 + 0.15\left(\alpha_g Re_p\right)^{0.687}\right] \tag{3. 23}$$

When $\varepsilon_g \leq 0.8$

$$\beta = 150\frac{\alpha_s(1-\alpha_g)\mu_g}{\alpha_g d_s^2} + 1.75\frac{\alpha_s \rho_g \left|\overrightarrow{v_s} - \overrightarrow{v_g}\right|}{d_s} \tag{3. 24}$$

3.2.2 Modified drag model for coarse grid simulation

In the numerical simulation of dense gas–solid flows in BFBs, it is generally accepted that the effect of particulate phase stresses is of secondary importance compared to the effect of inter-phase drag force. Therefore, the key issue is to establish a correct sub-grid scale (SGS) models for drag force capable to account for the effect of unresolved scales on the resolved mesoscales in coarse-grid simulations [274, 277, 278].

Wang et al. [279], proposed a SGS model for drag force in BFB of Geldart B particles. This model were derived on the basis of detailed and extensive lattice Boltzmann simulations [280].

This model assumed that the drag coefficient for a homogeneous system, with solid volume fraction ε_s, can be represented by:

$$\begin{aligned}\beta_{hom}\left(\varepsilon_g, \varepsilon_s, Re_s\right) &= 180\,\frac{\mu_g \varepsilon_s^2}{d_p^2 \varepsilon_g} + 18\frac{\mu_g \varepsilon_g^3 \varepsilon_s\left(1 + 1.5\sqrt{\varepsilon_s}\right)}{d_p^2} \\ &+ 0.31\,\frac{\mu_g \varepsilon_s Re_s}{d_p^2 \varepsilon_g}\frac{\left[\varepsilon_g^{-1} + 3\varepsilon_g \varepsilon_s + 8.4\,Re_s^{-0.343}\right]}{\left[1 + 10^{3\varepsilon_s}\,Re_s^{-0.5-2\varepsilon_s}\right]}\end{aligned} \tag{3. 25}$$

Therefore, based on the above-mentioned assumption, the drag coefficient that results from the gas-particle interaction within the dense phase (or emulsion phase) is equal to:

$$\beta_d = \beta_{hom}\left(\varepsilon_{g,d}, \varepsilon_{s,d}, Re_d\right) \tag{3. 26}$$

where

$$\varepsilon_{g,d} = 1 - \varepsilon_{s,d} \qquad , \qquad Re_d = \frac{\rho_g d_p \left|\vec{U}_d\right|}{\mu_g} \tag{3. 27}$$

Where $\varepsilon_{g,d}, \varepsilon_{s,d}$ and $\vec{U}_d$ represent the voidage, solid volume fraction and superficial gas velocity of the dense phase, respectively. Hence, the corresponding drag force is

$$\vec{F}_d = \beta_d \frac{\vec{U}_d}{\varepsilon_{g,d}} \tag{3. 28}$$

For any computational cell with mean voidage, ε_g, only part of the computational cell is occupied by the emulsion phase. Assuming the volumetric fraction of bubble phase in a computational cell as δ_b, then the volumetric fraction of the emulsion phase is $1-\delta_b$. Therefore, $\varepsilon_g=\delta_b+(1-\delta_b)\varepsilon_{g,d}$. Hence, the true drag force of each computational cell is given by:

$$\vec{F}_{cell} = \beta_d \frac{\vec{U}_d}{\varepsilon_{g,d}} \frac{\varepsilon_s}{\varepsilon_{s,d}} \tag{3. 29}$$

where $\varepsilon_s/\varepsilon_{s,d}$ is the fraction of the cell that is occupied by the emulsion phase. Following the two-fluid model, the drag force of each computational cell ($\vec{F}_{cell}$) is related to the inter-phase drag coefficient (β_{cell}) through

$$\vec{F}_{cell} = \beta_{cell} \left(\vec{u}_g - \vec{u}_s\right) \tag{3. 30}$$

The problem that now arises is that neither $\varepsilon_{s,d}$ nor $\vec{U}_d$ is *a priori* known. Therefore, for any computational cell with gas velocity ($\vec{u}_g$), particle velocity ($\vec{u}_s$) and voidage (ε_g) with known gas and solid properties, the correlation of Adanez et al. [281] is used to calculate $\varepsilon_{s,d}$, instead of the proposed originally by Werther and Wein [282]:

$$\frac{\varepsilon_{s,d}}{1-\varepsilon_{mf}} = 0.19 Re_p^{0.77} Ar^{-0.31} \tag{3. 31}$$

where

$$Re_p = \frac{\rho_s d_p (\vec{u}_g - \vec{u}_s)}{\mu_g} \quad , \quad Ar = \frac{\rho_g d_p^3 (\rho_s - \rho_g) g}{\mu_g^2} \tag{3. 32}$$

This modification was selected because the Werther and Wein correlation was developed for turbulent beds and it does not fit very well the bubbling regime. It is important to note that Adanez et al. proposed this correlation for the dense region of circulating beds. However, it is generally accepted that the behavior of this zone is very close to a bubbling fluidized bed [283], thus we applied it for our BFB simulations.

With $\varepsilon_{s,d}$ known, the velocity $\vec{U}_d$ can be calculated using the Richardson and Zaki relationship [284]:

$$\frac{|\vec{U}_d|}{U_t} = \varepsilon_{g,d}^{n} \tag{3. 33}$$

Where

$$n = \frac{\ln(U_{mf}/U_t)}{\ln(\varepsilon_{mf})} \tag{3. 34}$$

Finally, the true drag force $(\vec{F}_{cell})$ is evaluated, from which the effective drag coefficient is calculated as

$$\beta_{cell} = \frac{|\vec{F}_{cell}|}{|\vec{u}_g - \vec{u}_s|} \tag{3. 35}$$

which is fed back into the CFD calculation.

3.3 Gas-solid reaction modeling

The performance of a reactor depends on the input, the kinetics, and the flow and contacting pattern of gas with solid. The kinetics can usually be evaluated in an experimental unit or can be gotten from literature. However, the flow and contacting has to be evaluated in the piece of equipment to be used.

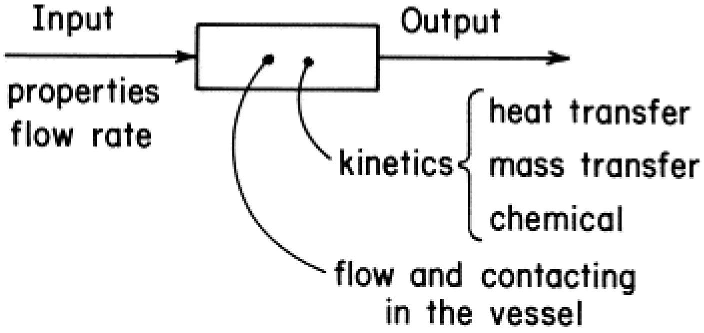

Figure 3. 12 –Information needed to relate output to input of a process reactor, from [285]

As commented in previous section the flow and contacting pattern have been modeled by means of CFD two-fluid model with KTGF. This section is devoted to the implementation of kinetics of steam methane reforming and CO_2 capture. Two kinetic schemes from literature have been adopted [138, 286], with the necessaries modifications for this work.

3.3.1 Steam Methane Reforming model

Steam methane reforming reaction has been extensively studied due to the industrial interest of the process [287, 288]. Nowadays, practically the 95% of hydrogen is produced by means of methane steam reforming. Hydrogen is predominantly used for petroleum refining and the production of industrial commodities as ammonia, and it is proposed as an energy vector alternative to the fossil fuel based. Moreover, SMR is a very mature technology which presents the most competitive costs respect among all hydrogen production pathways [289].

Steam methane reforming is a heterogeneous catalyst reaction. Thus, reactions involved in the kinetic scheme of SMR are surface reactions. There are a widely variety of catalyst, however, the most extended commercially is the Ni-O, supported in alumina. Several heterogeneous kinetic schemes has been proposed [290-294], however, the most extensively used model was proposed in 1989 by Xu and Froment [286, 295]. This model supposes that there are three dominant reactions:

$$CH_4 + H_2O \leftrightarrow CO + 3\,H_2 \quad , \ \Delta H^0_{298} = 206.2 \frac{kJ}{mol} - \mathrm{R.1} \qquad (3.\,36)$$

$$CH_4 + 2H_2O \leftrightarrow CO_2 + 4\,H_2 \quad , \ \Delta H^0_{298} = 165.0 \frac{kJ}{mol} - \mathrm{R.2} \qquad (3.\,37)$$

$$CO + H_2O \leftrightarrow CO_2 + H_2 \quad , \ \Delta H^0_{298} = -41.2 \frac{kJ}{mol} - \mathrm{R.3} \qquad (3.\,38)$$

Two first reactions correspond to SMR to carbon monoxide and dioxide. Reaction 3 occurs contemporary to the other ones, and it corresponds to water-gas shift (WGS) reaction. The thermal global balance of the reactions is endothermic and, usually, a part of natural gas is burned to ensure the necessary heat for the reaction. In this work we proposed that this heat is provided by carbonation. The capture reaction provides the heat necessary and it enhances the equilibrium of reactions to the right, improving the SMR global performance.

The kinetic scheme proposed by Xu and Froment includes the catalytic reactions (1-3) as:

$$r_1 = \frac{k_1}{P_{H_2}^{2.5}(DEN)^2} \cdot \left(P_{CH_4}P_{H_2O} - \frac{P_{H_2}^3 P_{CO}}{K_I}\right) \tag{3. 39}$$

$$r_2 = \frac{k_2}{P_{H_2}^{3.5}(DEN)^2} \cdot \left(P_{CH_4}P_{H_2O}^2 - \frac{P_{H_2}^4 P_{CO_2}}{K_{II}}\right) \tag{3. 40}$$

$$r_3 = \frac{k_3}{P_{H_2}(DEN)^2} \cdot \left(P_{CO}P_{H_2O} - \frac{P_{H_2} P_{CO}}{K_{III}}\right) \tag{3. 41}$$

$$DEN = 1 + K_{CO}P_{CO} + K_{H_2}P_{H_2} + \ K_{CH_4}P_{CH_4} + \frac{K_{H_2O}P_{H_2O}}{P_{H_2}} \tag{3. 42}$$

where the kinetic constants, k_j for j=1,2,3, the equilibrium constants (K_I, K_{II}, K_{III}) and the adsorption constants, K_i for i= CH_4, CO, H_2O, H_2 were evaluated experimentally as a function of temperature according with Arrhenius law. The reaction rate, equilibrium and the adsorption constants are, respectively:

$$k_1 = 1.842 \times 10^{-4} \exp\left[\frac{-240100}{R}\left(\frac{1}{T} - \frac{1}{648}\right)\right] kmol\ bar^{0.5}/kg_{cat}\ h \tag{3. 43}$$

$$k_2 = 2.193 \times 10^{-5} \exp\left[\frac{-243900}{R}\left(\frac{1}{T} - \frac{1}{648}\right)\right] kmol\ bar^{0.5}/kg_{cat}\ h \tag{3. 44}$$

$$k_3 = 7.558\ \exp\left[\frac{-67130}{R}\left(\frac{1}{T} - \frac{1}{648}\right)\right]\ kmol\ /kg_{cat}\ h\ \ bar \tag{3. 45}$$

$$K_I = 4.707 \times 10^{12} \exp\left(\frac{-224000}{RT}\right) bar^2 \tag{3. 46}$$

$$K_{II} = K_I \cdot K_{III}\, bar^2 \tag{3. 47}$$

$$K_{III} = 1.142 \times 10^{-2} \exp\left(\frac{37300}{RT}\right) \tag{3. 48}$$

$$K_{CH_4} = 0.179 \exp\left[\frac{38280}{R}\left(\frac{1}{T} - \frac{1}{823}\right)\right] bar^{-1} \tag{3. 49}$$

$$K_{H_2O} = 0.4152 \exp\left[\frac{-88680}{R}\left(\frac{1}{T} - \frac{1}{823}\right)\right] \tag{3. 50}$$

$$K_{CO} = 40.91 \exp\left[\frac{70650}{R}\left(\frac{1}{T} - \frac{1}{648}\right)\right] bar^{-1} \tag{3. 51}$$

$$K_{H_2} = 0.00296 \exp\left[\frac{82900}{R}\left(\frac{1}{T} - \frac{1}{648}\right)\right] bar^{-1} \tag{3. 52}$$

The reaction rate of the species in the solid phase also depends of the pore diffusion resistance and surface phenomena. Di Carlo et al. [296] estimated effectiveness factors (η_j) in order to model in a simple way these effects, being for the reactions $\eta_1 = 0.7$, $\eta_2 = 0.4$ and $\eta_3 = 0.8$.

Therefore, in order to include the intrapore-diffusion and the dispersion of the catalyst in the bed, the effective kinetics of the reactions r_j^* (for j=1,2,3) are:

$$r_j^* = \eta_j \rho_c \varepsilon_c r \tag{3. 53}$$

Where $\rho_c$is the density of catalyst and ε_c is the volume fraction of catalyst.

This heterogeneous catalytic kinetic scheme has been implemented in a commercial CFD code (Fluent 6.3), by means of a C programmed User Defined Function (UDF[1]).

3.3.2 Carbon dioxide capture model

The reaction of CaO carbonation takes place simultaneously to SMR. This heterogeneous reaction also implies the change of phase of CO_2 during the reaction. The mass transfer phenomena affect the bed fluid dynamics due to density changes in gas and solid phase.

Several kinetic models have been proposed in the technical literature in order to describe the gas-solid reaction, such as the well-known uniform and un-reacted shrinking core models. However, Stendardo and Foscolo [138] noted that these models do not predict accurately the conversion process of calcium oxide, and proposed a novel grain model. In such a model the molar rate of CaO conversion per unit volume of particle can be represented as a function of the local conversion, *X*, of calcium oxide and the average radius of calcium oxide grain δ_{CaO}:

$$CaO + CO_2 \leftrightarrow CaCO_3 \quad , \quad \Delta H^0_{298} = -178\, kJ/mol \tag{3. 54}$$

$$\frac{dX}{dt} = \frac{\sigma_{0,CaO}\, k_s\, (1-X)^{2/3}\left(C_{CO2} - C_{CO2,eq}\right)}{1 + \frac{k_s\, N_{Ca}}{2D_{PL}}\delta_{CaO}\sqrt[3]{1-X}\left(1 - \sqrt[3]{\frac{1-X}{1-X+XZ}}\right)} \tag{3. 55}$$

We observed that, equation 3.55 depends on several parameters. N_{Ca} is the number of moles of calcium carbonate per unit of volume of sorbent particle (in kmol/m^3). δ_{CaO} is the average diameter of CaO grains in the sorbent (in m). Z is dimensionless molar volume ratio of calcium carbonate to calcium oxide V_{CaCO3}/V_{CaO}. C_{CO2} is the molar concentration of CO_2 (in kmol/m^3) and $C_{CO2,eq}$ is the equilibrium concentration of carbon dioxide as a function of temperature according with [137]:

---

[1] A UDF, is a function that you program that can be dynamically loaded with the FLUENT solver to enhance the standard features of the code.

$$P_{CO_2,eq} = 4.137 \times 10^7 \exp\left(\frac{-20474}{T}\right) atm \ ; \ \ C_{CO_2,eq} = \frac{P_{CO_2,eq}}{RT} \tag{3. 56}$$

The initial specific active surface, $\sigma_{0,CaO}$, is proportional to the number of calcium containing grains per unit particle volume, and to the "active" surface of each spherical grain, which corresponds to the volume occupied by un-reacted calcium oxide. This relation establishes the dependency of the specific active surface on the physical and chemical properties of the sorbent, the particle grain size, and the calcium oxide conversion:

$$\sigma_{CaO} = \ \sigma_{0,CaO} \ (1-X)^{2/3} = \frac{N_{Ca}\, V_{CaO}}{\frac{\pi}{6}\delta_{CaO}^3} \times \pi\delta_{CaO}^2 \ (1-X)^{2/3} \tag{3. 57}$$

The intrinsic rate constant of CaO-CO$_2$ reaction, k_s, can be determined experimentally supposing reaction order n=0 with two complementary derivations from grain model under kinetic control proposed by Szeleky et al. [213]. In one hand, Bhatia and Permutter [201] supposed zero activation energy in the temperature range (823-998 K) and obtained a constant value of $k = 5.97 \cdot 10^{-7}$ m^4/kmol s.

$$k_s = k\ /N_{Ca} \tag{3. 58}$$

On the other hand Sun et al.[214] proposed an Arrhenius law for k_s for dolomites :

$$k_s = A_0 \exp\left(\frac{-E}{RT}\right); A_0 = 1.04 \ \times 10^{-3} \ \frac{mol}{m^2 s}; \ E = 24 \pm 6 \ kJ/mol \tag{3. 59}$$

As explained in section 2.2.4, k_s and S_0 are correlated by means of reaction rate according with:

$$\ln r_o = \ln(56\ k_0 S_0/3) - \frac{E}{RT} \tag{3. 60}$$

Thus, it is possible suppose that, for a sorbent in which molar ratio of CaO, k_0 and E are constant, reaction rate is directly proportional to surface area, under kinetic control regime:

$$r_0 \ \propto \ S_0 \tag{3. 61}$$

Therefore, it seems reasonable introduce an effectiveness correction factor in the kinetically-controlled reaction which allows to introduce the effect of variation of surface area in the reaction rate. Supposing as reference case the conditions of first calcination and carbonation used by Bhatia and Permutter and considering that k_s is constant; and applying the model of Sun et al. it is possible to obtain $S_{0,ref}$ (for dolomite in this study corresponds to R.1 in table 2.3, $S_{0,ref} = 19.3\, m^2/g$). For different cases, as cycled and/or pre-treated sorbents, the effective intrinsic rate constant k'_s is defined as:

$$k'_s = k_s \frac{S'_0}{S_{0,ref}} \tag{3. 62}$$

where S'_0 is the surface area of sorbent, obtained from TGA data applying the Sun et al. method.

Finally, in order to define completely the Stendardo and Foscolo carbonation reaction kinetics (Eq. 3.55) it is necessary consider the diffusion of carbon dioxide though the product layer of calcium carbonate that, at more advanced stages of the process, comes to occupy the whole external region of the grains, thereby preventing direct contact between carbon dioxide in the pore space and the active, unconverted calcium oxide surface. The coefficient of diffusion thorough the product layer defined (D_{PL}) as:

$$D_{PL}(X) = D_{PL,0}\exp(-a \cdot X^b) \tag{3. 63}$$

where $D_{PL,0}$ is the initial value of carbon dioxide solid diffusion coefficient (we have assumed a reasonable initial solid diffusivity of $D_{PL,0}$=2×10^{-5} m^2/s) and a and b are fitting parameters (a is a decay parameter). By fitting the grain model to the experimental data, we can obtain, for the final stage of the particle carbonation process, the best estimation for the solid state diffusion coefficient of carbon dioxide through the product layer [297] (Table 3. 3).

Table 3. 3 D_{PL} at 2500 s (temperature 700 °C).

	X_N [-]	D_{PL} [m^2/s]
1st	0.868	1.82×10^{-17}
2nd	0.810	1.77×10^{-17}
3rd	0.739	1.79×10^{-17}
4th	0.675	1.78×10^{-17}

In Table 3. 4, these estimatations are summarized for the first cycle of the multi-cycling carbonation at different temperatures. These values represent the diffusivity through the product layer which is located at the outer surface of the particle where the resistances due to the diffusion are greater compared with the inner part of the particle. Thus, for values of D_{PL} lower than shown in this table is possible to suppose that reaction is under kinetic regime.

Table 3. 4 Model result for dolomite carbonation at different temperatures

	Temperature *[°C]*	D_{PL} *[m^2/s]*
First cycle	500	1.01×10^{-16}
	600	1.99×10^{-15}
	700	3.45×10^{-14}

Arrhenius type dependence was envisaged for the product layer diffusion coefficient. Figure 3. 13 displays the Arrhenius plot for the values reported in Table 3. 4 to obtain, by a least square method, the pre-exponential factor and the activation energy. The values are reported in Eq. (1).

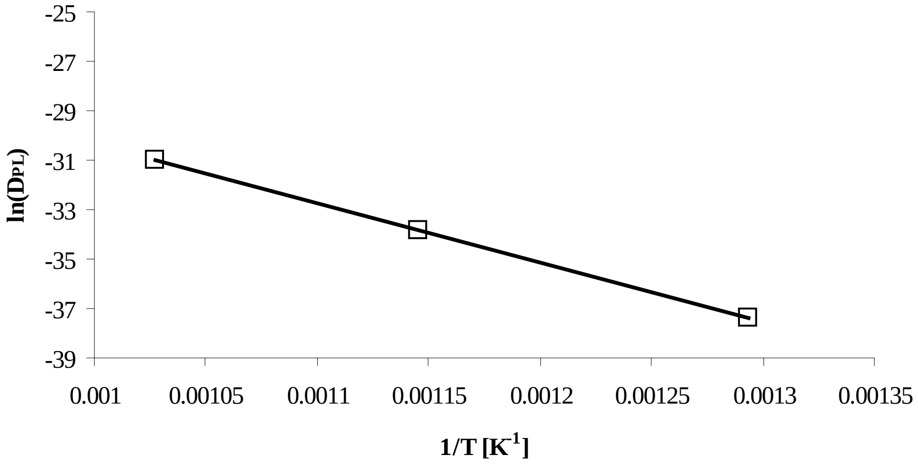

Figure 3. 13 – D_{PL} exponential decay behavior as function of temperature Arrhenius plot for the diffusion through the product layer

The activation energy found in this work (181.62 KJ/mol) is consistent with that calculated, by Bhatia and Perlmutter [201] (179.20 KJ/mol). Thus the diffusion coefficient through the product layer can be written as a function of the temperature in the following manner:

$$D_{PL}(T) = 1.01 \cdot 10^{-16} \exp\left[\frac{181620}{R}\left(\frac{1}{773} - \frac{1}{T}\right)\right] \qquad (3.\ 64)$$

This higher activation energy is likely due to solid state lattice diffusion process. It is worth noticing that, as reported in Mess et al. [212], the diffusion coefficient through a single crystal of CaCO3 assumes a high value: 352 kJ/mol. As a consequence, the presence of impurities and defects in the calcite lattice could be envisaged.

3.3.2.1 Implementation of CO_2 capture model

In an operating plant, it is likely that most interest would be on the kinetically controlled regime, during which most of the achievable uptake of CO_2 occurs. This regime is dominant at the beginning of the CO_2 capture, typically for 1-2 min for a single particle. However, in a BFB, this time spreads over minutes (or hours) as function of the amount of solids, because all particles are not exposed to CO_2. During this phase, the coefficient of diffusion thorough the product layer defined (D_{PL}) is very large.

Under these conditions, diffusional effects can be neglected. Thus, in the general equation of capture reaction rate (Eq. 3.55), denominator becomes 1. And, under kinetically controlled regime Eq. 3.55 becomes:

$$\frac{dX}{dt} = \sigma_{0,CaO}\, k'_s\, (1 - X)^{2/3}\left(C_{CO2} - C_{CO2,eq}\right) \tag{3. 65}$$

Therefore, this equation was implemented in FLUENT, by means of a UDF. This assumption can be considered valid for two reasons. On one hand, this simplified reaction rate improves the convergence of numerical simulations. In the other hand, CFD simulations are strongly time intensives. The simulation of several minutes of BFB operation needs months of wall-clock time. Thus, CFD fluidized bed simulations are limited at few minutes, in which diffusional effects are negligible and kinetically controlled regime dominates the reaction.

In this work two different sorbents were studied, dolomite and CaO-mayenite. Moreover it is interesting to study the effect of treatments in the kinetic-controlled phase (see Chapter 2). Thus the effective kinetic constant rate has been included. Table 3. 5 summarize the values of parameters needed for the modeling of carbonation reaction.

Table 3. 5 Values of parameters used in simulation for dolomite and mayenite sorbents

Parameter	Units	Dolomite CaO.MgO (1:1)	Mayenite $CaO\cdot Ca_{12}Al_{14}O_{33}$ (85:15%)
Moles of Ca per unit volume of sorbent particle	N_{Ca} (kmol/m^3)	16.21 [a]	5.86 [c]
CaO molar volume	V_{CaO} (m^3/ kmol)	$1.69\cdot10^{-2}$ [a]	$2\cdot10^{-2}$ [c]
Intrinsic rate constant	k_s (m^4/ kmol s)	$5.97\cdot10^{-7}$ [a]	$5.97\cdot10^{-7}$ [c]
Reaction constant	k (m/s)	$9.68\cdot10^{-6}$ [a]	$3.5\cdot10^{-6}$ [c]
Grain diameter	δ_{CaO} (m)	$1\cdot10^{-6}$ [b]	$0.7\cdot10^{-6}$ [c]
Surface area, Reference	$S_{0,ref}$ (m^2/g)	19.3	2.6 [d]
Surface area, Non-treated sorbent	S'_0 (m^2/g)	19.3	2.6 [d]
Surface area, Treated sorbent	S'_0 (m^2/g)	23.6	4.0 [d]

[a] from [138] [b] from [129] [c] from [141] [d] from [215]

Under these conditions the carbonation has been compared with TGA data with good agreement as shown in Figure 3. 14. This approach can be considered correct for the first seconds of carbonation reaction, when diffusional effects are negligible, and kinetics dominates the reaction rate.

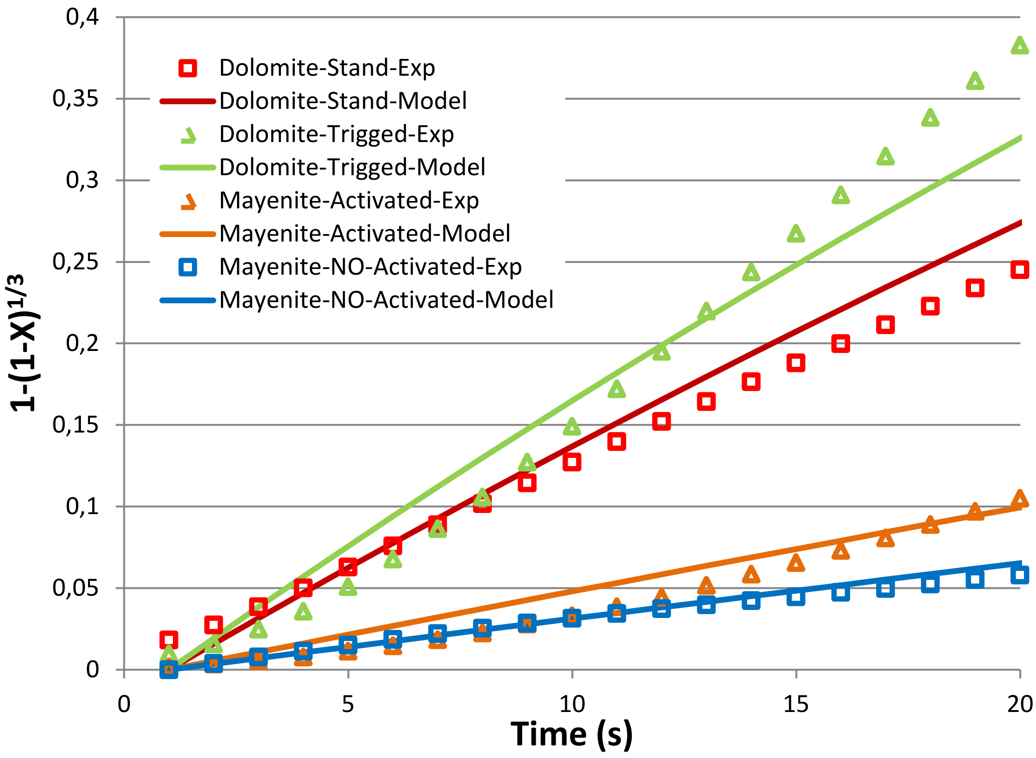

Figure 3. 14 – Comparison of experimental and simulated conversion of sorbents

3.4 Preliminary hydrodynamic simulations

Previously to the simulation of the complete SE-SMR system, two numerical simulation campaigns were carried out in order to establish the best framework to simulate accurately the hydrodynamic behavior of the fluidized beds. On one hand, a 90kW$_{th}$ oxy-fuel test rig (the CIRCE combustor) was simulated, under no reactive conditions, and results compared with experimental data and empirical models [298, 299]. On the other hand, the ZECOMIX reactor was simulated under CO_2 capture regime, without including steam methane reforming reactions.

The aim of this section is to present the highlights of the CFD simulations, as a practical guide to simulate accurately a BFB, using the commercial CFD code FLUENT 6.3. More than 100 simulations were carried out. Thus, we will show the most useful results. For more detailed information we refer to references [300-304].

3.4.1 Numerical method and boundary conditions

Non-axisymmetric or axisymmetric two dimensional domains were assumed in the simulation for simplicity. Initially, in the case of CIRCE combustor simulations a non-axisymmetric domain was studied. In the ZECOMIX reactor, due to present a reactor diameter five times higher than CIRCE one, an axisymmetric approach has been adopted.

The same numerical methods was applied to the simulation of CIRCE and ZECOMIX reactors. An Eulerian-Eulerian description was adopted to resolve the coupling of gas and particulate phase, and it was modeled by solving the Unsteady-state Reynolds Averaged Navier-Stokes equations (URANS) along the computational domain. Non-slip conditions were selected for gas phase and free-slip for solid phase, at the walls. Isothermal simulations were carried out. In this case, isothermal term refers to the fact that energy conservation equation is not considered during the calculation. Isothermal conditions are exact for non-reacting bed. Moreover, in the cases of reacting beds is quite approximate due to a high mixing rate, and because in the case of SE-SMR, the energy of reactions are balanced.

The second order QUICK scheme was used to evaluate the convective terms because it presents less numerical diffusion than first order schemes, improving the bubbles resolution [305]. The pressure-velocity coupling is resolved by means of the phase-coupled SIMPLE (PC-SIMPLE) algorithm[306]. The residual tolerances were set of 10^{-3} for each scaled residual.

The bed was assumed to be at minimum fluidization condition at the beginning of the simulation. The initial solid volume fraction (ε_s) was 0.55 and the maximum value was set at 0.63. The value of restitution coefficient between particles was 0.9 [307], which represent a realistic behavior of Geldart B particles. Table 3. 6 lists the main conditions used in the both simulation campaigns (CIRCE and ZECOMIX).

Moreover, CFD simulations of BFB are very sensitive to closure models. Table 3. 7 shows the closure models of KTGF evaluated. All these models are available by default in FLUENT.

Table 3. 6 Simulation parameter constants

Flow field	Unsteady RANS
Energy Equation	Isothermal
Multiphase model	E-E KTGF Closure
Pressure-velocity coupling	PC-Simple
Discretization	2nd order QUICK
BC Constants	
Initial solids packing	0.55
Maximum solids packing	0.63
Restitution coefficient (e_{ss})	0.9
Inlet boundary conditions	Velocity
Outlet boundary conditions	Pressure
Time steps (s)	0.001 - 0.0001
Convergence criteria	10^{-3}

Table 3. 7 Closure model of KTGF evaluated

Models evaluated	
Turbulence	Laminar / k-ε standard
Drag model	Gidaspow/ Syamlal-O’Brien/Wen-Yu
Solid pressure	Lun/ Syamlal-O’Brien
Radial distribution	Lun/ Syamlal-O’Brien
Granular kinetic viscosity	Gidaspow/ Syamlal-O’Brien
Frictional Viscosity	None /Schaeffer
Frictional Pressure	Johnson/KTGF/ Syamlal-O’Brien

Boundary conditions are strongly different for the CIRCE oxy-fuel reactor (OF) and ZECOMIX reactor (ZC). On one hand, both are cylindrical, but diameter and height are different, as well as particle diameter. Thus, both are Geldart B BFB, but scales are different. On the other hand, there are experimental data of OF operation; meanwhile there are not data of ZC reactor, so the results obtained in OF can be compared quantitatively and ZC just qualitatively. Table 3. 8 and summarizes the boundary conditions used in the simulations.

Table 3. 8 Boundary conditions used in the simulations

	CIRCE Oxy-fuel	**ZECOMIX**
Reactor height	2.5 m	4 m
Reactor diameter	0.2 m	1 m
Static bed height	0.28 - 0.4 m	0.5 m
Solid material	Sand	Dolomite calcined/ no calcined
Particle density	2400 kg/m^3	1550-2200 kg/m^3
Particle diameter , d_p	0.5 mm	0.2 mm
Superficial gas velocity	$1 – 5 \cdot U_{mf}$	$10 – 25 \cdot U_{mf}$
Temperature	Cold tests: 7.5 – 20 ºC	600ºC
	Hot tests: 805 – 870 ºC	
Gas Composition	5/95,19/81,30/70,35/65,40/60 O_2/CO_2	56.6 %H_2, 20.5 %CO_2, 22.9%H_2O
	Air	Air
Cell size	$5 – 10 \cdot d_p$	Variable
Grid number cells	20,000 – 80,000	3,000-1,000,000
Distributor details	Uniform – Perforated plate	Uniform – Perforated plate

3.4.2 Cold flow simulations of an oxy-fuel reactor

These simulations were centered in the study of cold flow hydrodynamics. Some experiments were carried out at low temperature in order to have a higher control of the fluidization conditions than under oxy-combustion conditions. Under these conditions a study of the closure equations of KTGF was undertaken, at different temperatures, initial bed height and fluidization gas composition.

In terms of macroscopic flow behavior, the simulations are not very sensitive to the use of different closure models. Figure 3. 15A presents the time-averaged pressure drop for the diverse drag models, and in the Figure 3. 15B transient pressure drop as a function of time for different fluidization velocities. The results are very similar for all drag models, and the same trends are presented. For example the pressure peak presented due to instabilities generated for the instantaneous change of gas velocity, or the increase of fluctuations, amplitude with gas velocity are practically independent of the choice of drag closure model.

However, on a local scale, drag models significantly affect flow patterns. For example, Figure 3. 16 shows a representative instantaneous snapshot of solid volume fraction. At low superficial gas velocity, the Wen-Yu drag model produces an excessive densification in some zones. When gas velocity increases, the differences between these three drag models are less evident. However, the drag model of Gidaspow presents in its definition a discontinuity in the solid volume fraction of 0.2 (see Eq. 3.22-24). This fact can possibly lead to difficulties in numerical convergence and in the definition of the bubbles. Moreover, the magnitude of this discontinuity in β increases with increasing particle Reynolds number. Thus Syamlal-O’Brien drag model appears to be the most accurate drag model.

Flow predictions are not sensitive to the use of different solid stress models or radial distribution functions, as different approaches are very similar in dense flow regimes (except drag model). This result is congruent with literature [274, 277]. For a major description of the submodels we refers to [262, 266, 274].

Thus, before a comparison of several simulations, the selected models for the case study were Syamlal-O’Brien model for Drag, Solid Pressure, Granular Kinetic Viscosity and Frictional Pressure; Lun model for Radial Distribution; and Schaeffer model for Frictional Viscosity.

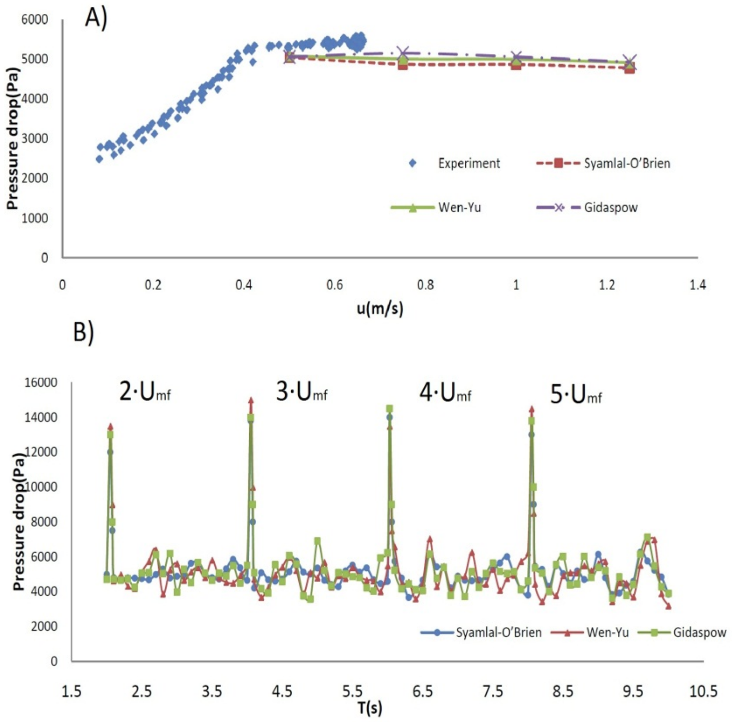

Figure 3. 15 – Comparison of drag models effect, at different velocities, on A) Time averaged global pressure drop (Pa) B) Local unsteady pressure drop fluctuations (Pa). Gas composition Air at 7.5 ºC, 0.4m initial bed high.

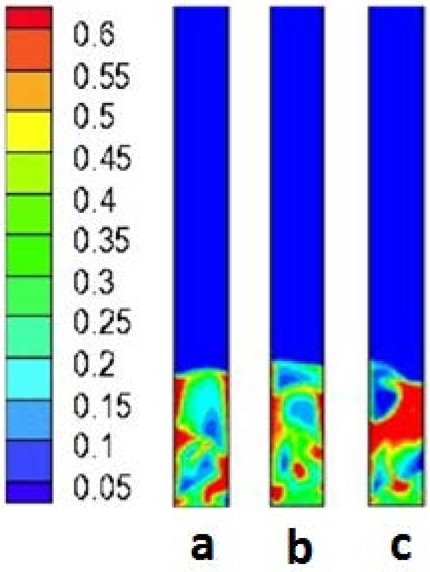

Figure 3. 16 – Solid phase fraction [-] for Syamlal – O'Brien (a) , Gidaspow (b) and Wen-Yu (c) drag models. Initial bed height 0.4m, U = 1m/s, Gas composition 40/60% (O_2/CO_2).

Figure 3. 17 presents the global pressure drop in the bed under air fluidization and 40/60% O_2/CO_2, for 0.28 and 0.4 bed height. Numerical simulations present an over-prediction of pressure drop for the case of 0.28 m bed height and an under-prediction for the case of 0.4m, independently of the gas composition. In any case the error is minor than ±10%, for all numerical experiments. It is important to note that in the simulations the pressure drop remains constant for bubbling regime (under entrainment velocity), according with classical theory. One of the limitations of the model is that pressure drop cannot be calculated for velocities lower than U_{mf}.

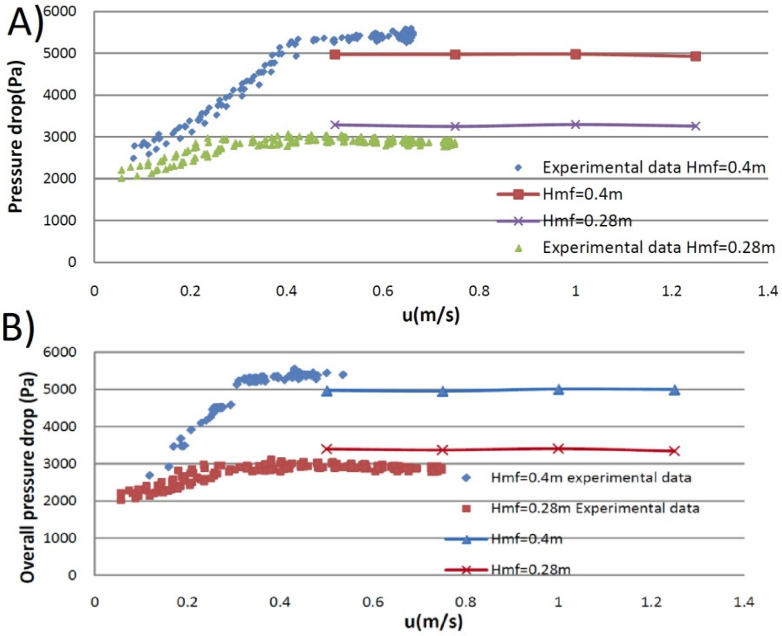

Figure 3. 17 – Comparison between experiments and simulation pressure drop evolution (Pa) with gas velocity (m/s). Gas composition A) Air B) 40/60% (O_2/CO_2) at 7.5 ºC, for 0.28m and 0.4m bed height

Moreover, two different grid types were studied in order to evaluate the effect of distributor in the simulations. Figure 3. 18 presents the behavior of the bed with the increasing of fluidization velocity, for a uniform distributor case. It is observed as the bed expansion increases with velocity, with a good agreement with theoretical values, moreover, the size of bubbles increases with velocity according with the classical theory. This effect is also observed in Figure 3. 15B, due to the fact that the increase of amplitude of pressure fluctuations is related to bubble size. In addition, in the case of U=1.25 m/s a core-annulus structure is suggested, as correspond to a high velocity fluidized beds.

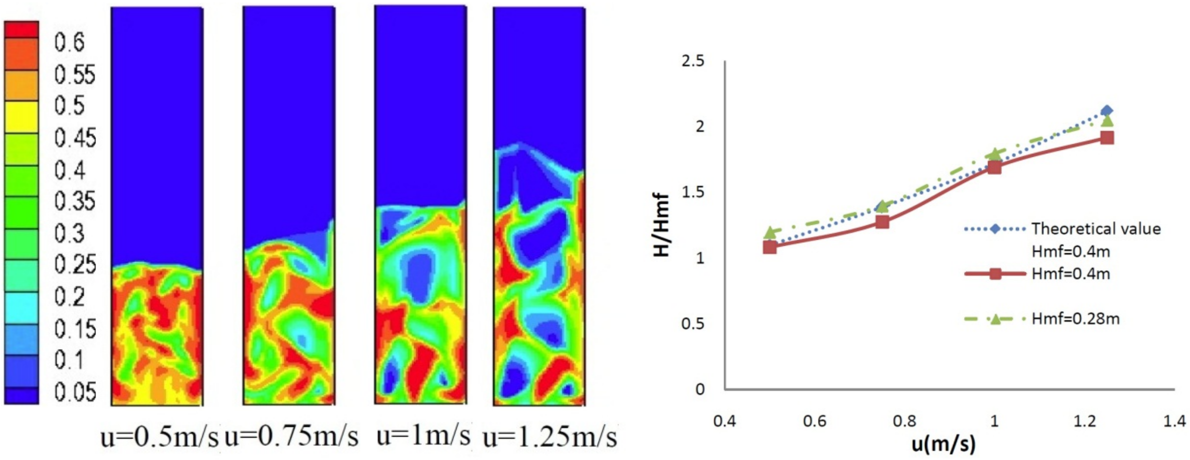

Figure 3. 18 – Solid phase fraction evolution at different gas velocities. Initial bed height 0.4m, Gas composition 40/60% (O_2/CO_2) T=7.5ºC. Uniform distributor. Bed expansion (H/H_{mf}) evolution with gas velocity at different initial bed height, compared with theory[308].

One of the most interesting results obtained in [298] is the effect of distributor pressure drop in the bubble size. In lab-scale units, the pressure drop in the distributor is significantly higher than in industrial reactors. This increase in pressure drop reduces main bubble diameter. This effect can be captured with the inclusion of jets in the grid. In Figure 3. 19 it is possible to observe the growth of the bubbles in the bed, and the coalescence effect in the bubbles is predicted. In addition, the bubbles present different velocities. According with classical theories, due to the "gulf stream" effect, gas rises to the central axis of the reactor, transporting solids from the center of the bed to the walls.

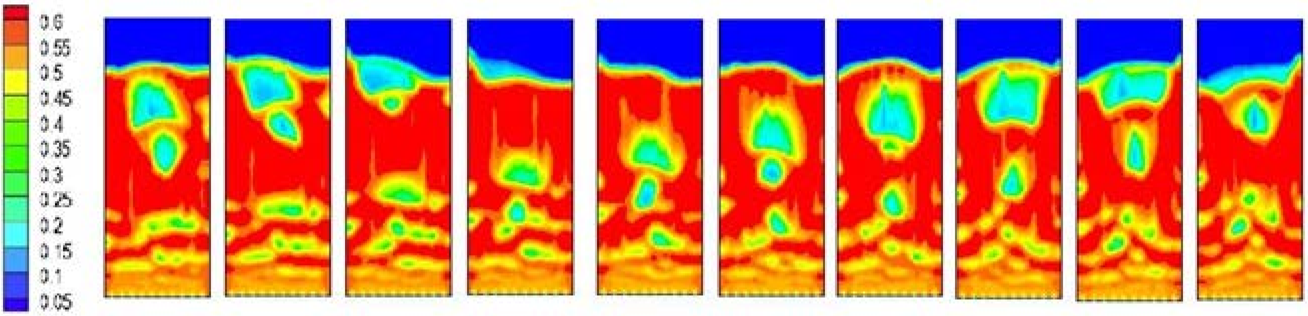

Figure 3. 19 – Solid phase fraction with time. Snapshot taken each 0.05s. perforated plate distributor. Initial bed height 0.4m, Gas composition 40/60% (O_2/CO_2) T=7.5ºC, Gas velocity 0.5m/s.

The fallen particles and the free-slip wall effect reduce the upward velocity of the bubbles close to the walls, as shown in Figure 3. 20.

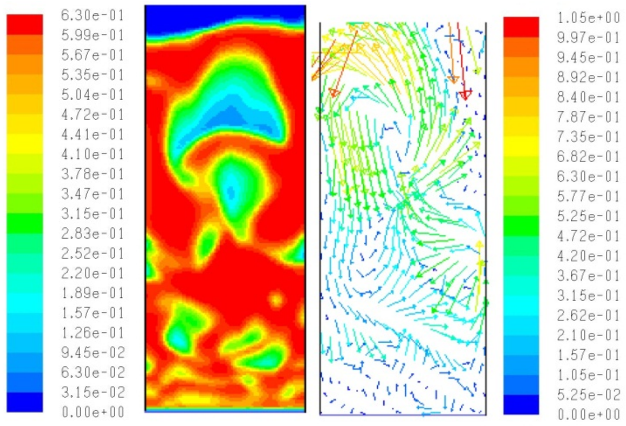

Figure 3. 20 – Solid phase fraction (left) and solid velocity (m/s) (right), with detailed perforated plate. Initial bed height 0.4m, Gas composition 40/60% (O_2/CO_2) T=7.5ºC, Gas velocity 0.5m/s.

Bubble size and velocity are compared with empirical models presenting good agreement. Some representative bubbles have been tracked during the rising across the bed. Due to the buoyancy effects, there are different bubble diameters and their growth is not constant. In Figure 3. 21 it is possible to note the variation of bubble diameter, with different growth between the higher bubbles, which rise in the center of the bed and the smaller ones, located near the walls. Bubble size has been compared with Darton et al. model, with a better prediction of the largest bubbles. In any case, the model predicts very well the growth.

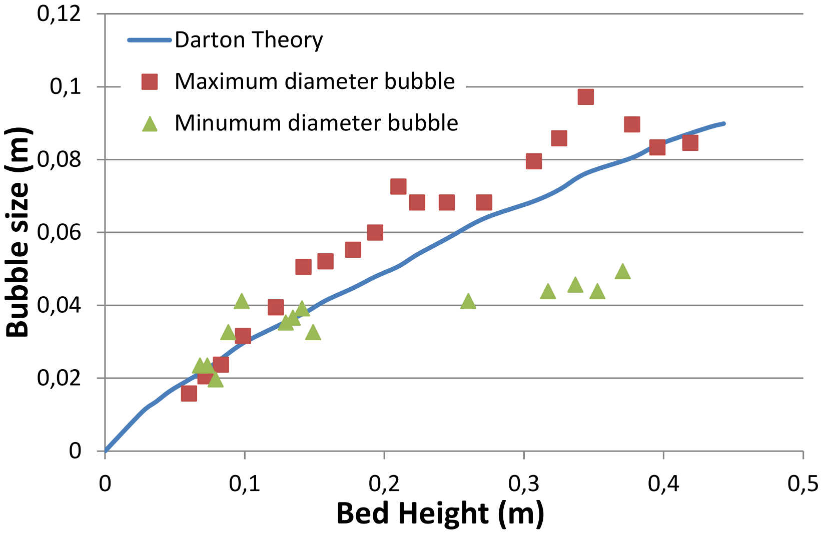

Figure 3. 21 – Bubble size with bed height for cold air simulations at U=0.5m/s

The bubble velocities are compared with Davies and Taylor model, with a very good agreement as shown in Figure 3. 22. Medium values are similar to the theory. However, dispersion of the velocity bubbles is large within the bed, mainly due to the wall effects, breaking up of the bubbles at the end of the bed, and throughflow across the bubbles.

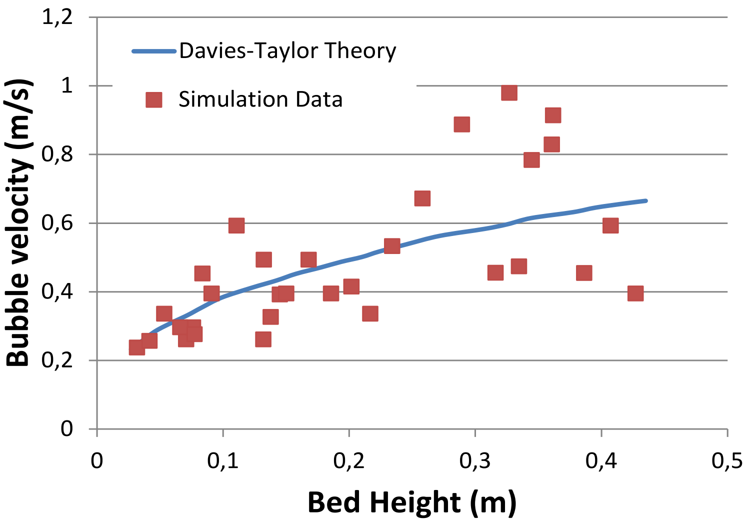

Figure 3. 22 –Bubble velocity evolution (right) with bed height for U=0.5m/s

In the higher part of the bed it is possible to observe slower bubbles due to the downstream movement of the particles and wall effect. Faster bubbles are generated by the eruption of the bubbles during in the rupture at the surface of the bed. Throughflow effect occurs when a significant fraction of the gas flow passes the dense be through the bubble paths. This gas flow increases the velocity of the bubble and its effect is more pronounced for big bubbles than for smaller ones [309].

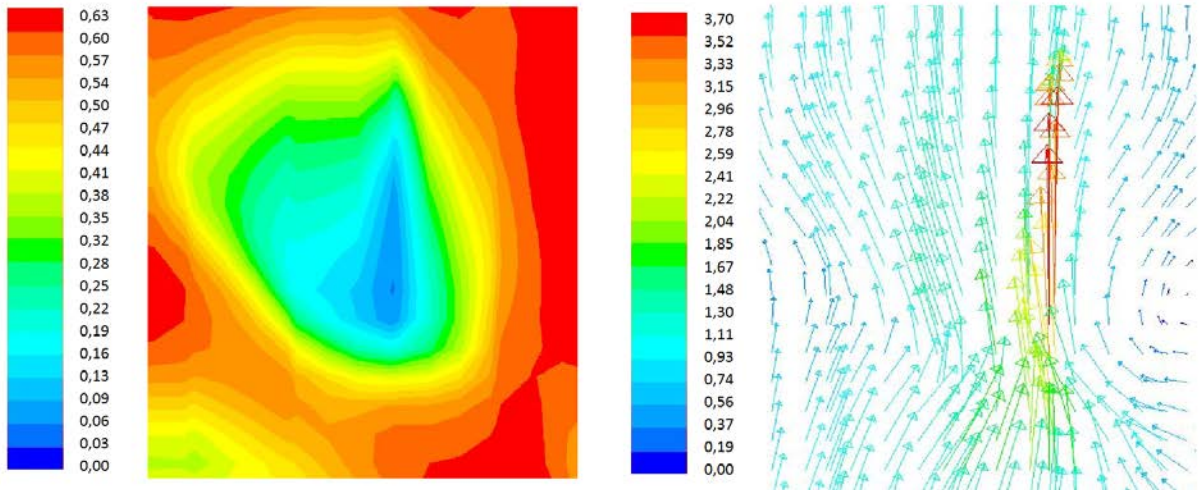

Figure 3. 23 – Throughflow in a bubble. Solid fraction (left) and gas velocity (right) for air fluidization at U=0.5m/s

By means of this CFD simulations campaign has been possible to corroborate that numerical simulations of BFB are very sensitive to drag model, and practically independent of the other closure equations of KTGF. Moreover, results are also very sensitive to the distributor design. In the simulations with a perforated plate distributor (where the grid is more refined) the accuracy of the results increase compared with uniform distributor. Finally, the simulations present a good agreement with theoretical models and experimental data under cold flow conditions.

3.4.3 Preliminary simulations of ZECOMIX reactor

The first approach to simulate the carbonator reactor of ZECOMIX plant was based in the specifications provided by [310]. As a first approach, a two dimensional rectangular and axysymmetrical section formed by 3000 cells was studied [311]. This simplification supposes a reduction of computational cost to evaluate the effect of closure equations and the implementation of CO_2 capture gas-solid reaction.

Firstly the Gidaspow (G) and Siamlal-O’Brien (S-O) drag closures were compared. For the first seconds there are not observed differences in the models. However, before the stabilization of the bed (usually after 5 sec [256]) the resolution of formation of bubbles in the case of G model is lower than in S-O model. Moreover in the case of G model there is observed a strong densification in the central zone.

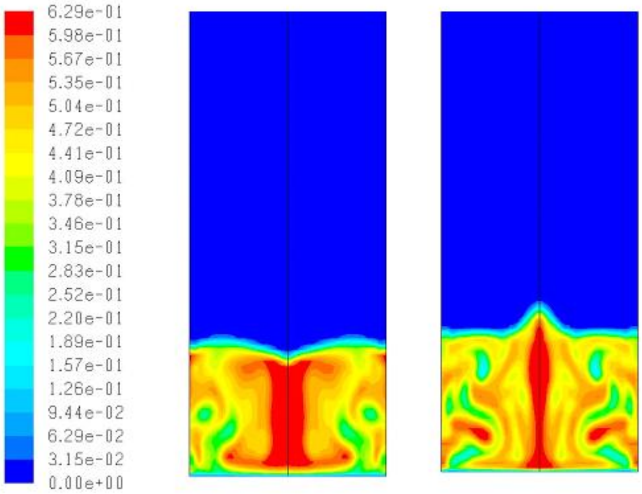

Figure 3. 24 – Solid phase fraction at t =10s with Gidaspow (left) and Syamlal-O’Brien (right) drag functions

Initially, turbulence-free flow was assumed throughout the bed, ignoring the possibility of local regions of turbulence. In general, accounting for time-averaged turbulent behavior and turbulent interactions between phases can make simulation predictions more realistic for beds operating at high Reynolds number. However, unless an appropriate turbulence model with the correct empirical constants and closures is chosen, the model predictions may be less consistent with experimental data than the turbulence-free model [312]. Ding and Gidaspow included the turbulence effects in the definition of Granular Temperature (Eq. 3.5) with good results, demonstrating that it is not necessary include a turbulence model to obtain accurate predictions in dense beds [313]. This approximation has been extensively used (e.g. [307, 314-317]) and it has been applied in this work. We compare in Figure 3. 25 the effect of turbulence, obtaining no significant global differences. By using k-ε turbulence model has been observed a lower bubble definition and an increase in computational costs. Thus, we assume that turbulence can be neglected and the turbulence models available in FLUENT are not used.

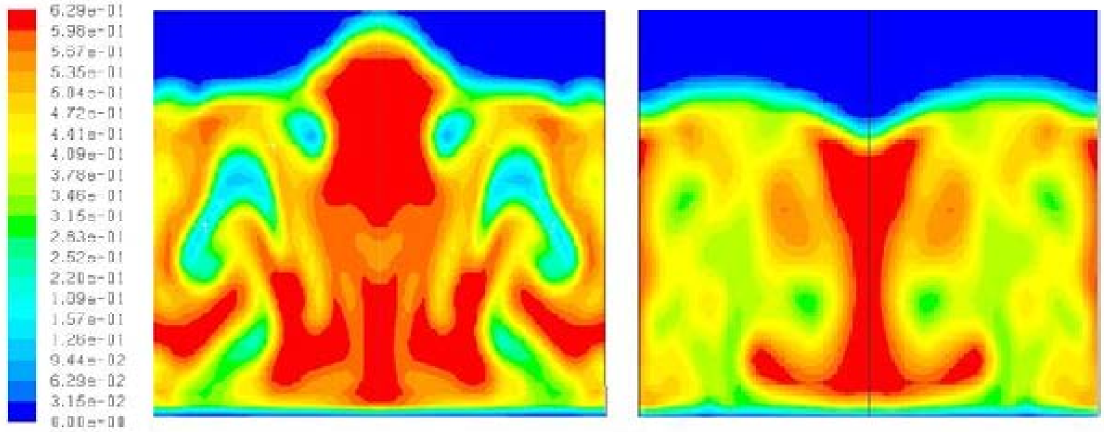

Figure 3. 25 – Volume of fraction of solids at t =20s with Syamlal-O'Brien drag functions without turbulence model (left) and with k-ε model (right)

This 2D axisymmetric grid of 3000 cells do not presents serious problems with the convergence. However the hydrodynamics of the systems is unrealistic. On the one hand the formation of bubbles is not well predicted when simulation time increases. On the other hand, the circulation pattern observed is like that presented in Figure 3. 27a. However for U>10 U_{mf} it can be expected the "gulf stream" effect, like that presented in Figure 3. 27b.

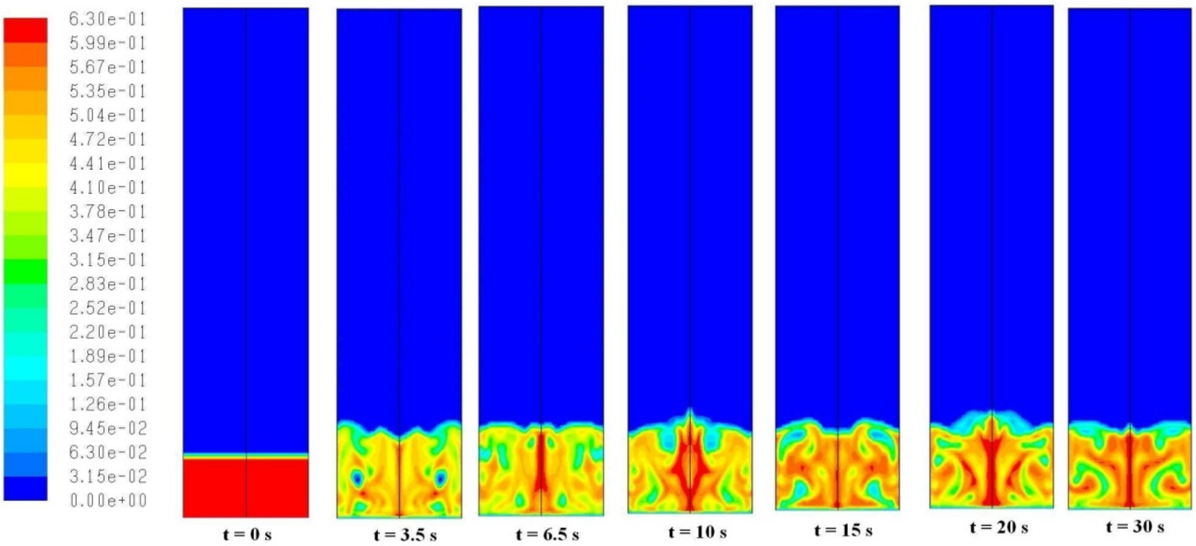

Figure 3. 26 – Solid phase fraction with time in preliminary 2D axysymmetric simulation ZECOMIX reactor

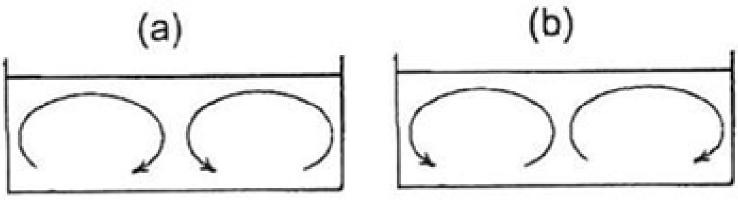

Figure 3. 27 – Movement of solids in BFB. a)Aspect ratio(h/d) <1, U low b)Aspect ratio <1,U high, from [228]

Applying the same grid size that the 2D axisymmetric but not imposing symmetric conditions (increasing grid size from 3000 to 6000 cells), the simulations were repeated. More realism in the bubble formation and in the solids circulation (with "gulf stream" behavior) is observed (see Figure 3. 28). Pressure drop is independent of the mesh type. Thus, 2D-axysymmteric grids are not recommendable BFB (but it can be a good approach to spouted beds [311, 318, 319]).

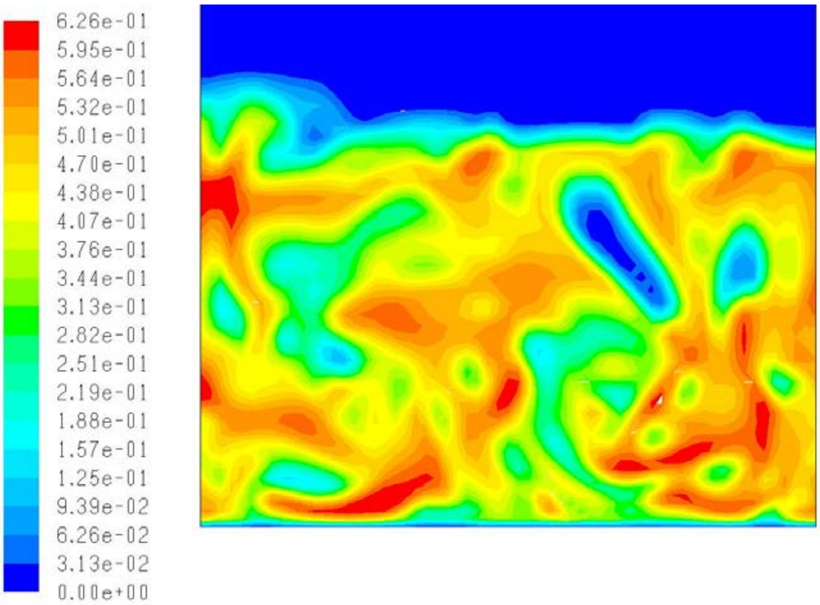

Figure 3. 28 – Solid phase fraction at t =10s with a 6000 cells non-axisymmetric mesh

Wang et al. [279] proposed an optimal cell size for BFB of 2-4 particle diameter. With this cell size, mesh size increase enormously (until 1 million cells). Pressure drop is independent of the grid size but the resolution of bubbles disappears.

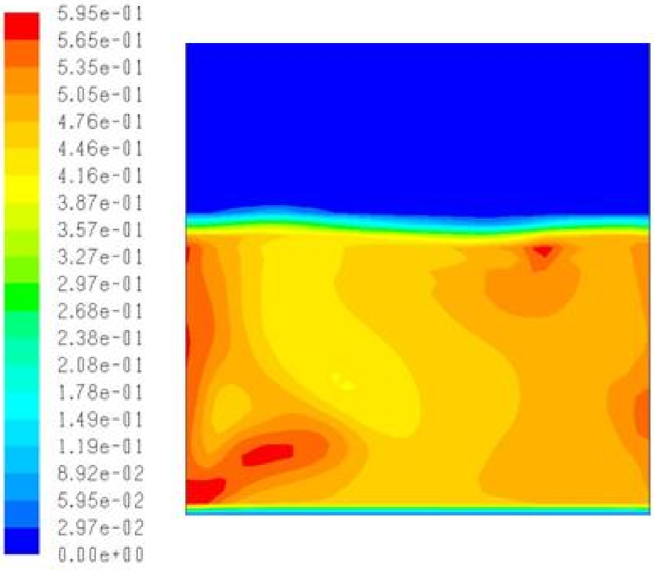

Figure 3. 29 – Solid phase fraction at t =10s with a 1,000,000 cells non-axisymmetric mesh

Finally, based in the CIRCE combustor case, a simulation including a perforated plate as gas distributor has been carried out. A slightly better bubble formation has been obtained in the opr of the bed, respect to the 6000 cells case, and a sensible improvement respect to the 1 million cells case. The number of the cells in the mesh must increase to include jet effect in the holes of the perforated plate (30.000 cells, x5 with respect to uniform inlet). However, calculation time is reasonable and global pressure drop is not altered.

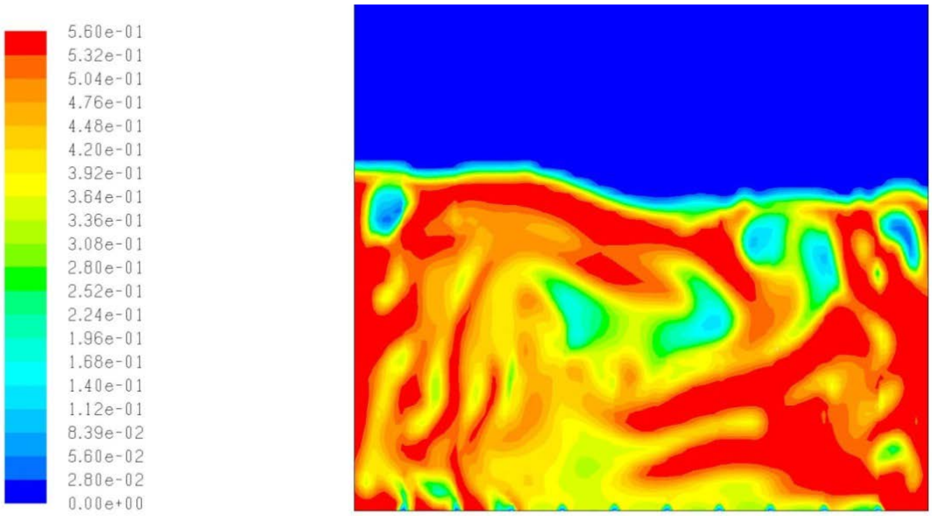

Figure 3. 30 – Solid phase fraction at t =10s with a 30,000 cells non-axisymmetric-detailed-distributor mesh.

In conclusion, according to these findings we will assume a 2D non-axisymmetric coarse grid, with no turbulence model and the Syamlal-O’Brien model for drag in the complete SE-SMR simulations.

3.5 Laboratory Scale SE-SMR simulations

3.5.1 State-of-the-art of SE-SMR process

Nowadays, Sorption-Enhanced Steam Methane Reforming (SE-SMR) process is still under development. Currently, there is any industrial plant which produces hydrogen with this technology. Thus, all literature about SE-SMR refers to laboratory scale experiments or models.

Instead of the first attempts proposed by Brun-Tsekhovoi et al. [320],the group of D.P. Harrison, from Louisiana State University, was the first to propose the SE-SMR process as an alternative to classical SMR process [88]. They demonstrated experimentally the process at medium pressure (15 atm), 500-600ºC, and with a typical steam-carbon ratio (S/C) of 4, in fixed bed using Ni-based catalyst and sorbents as dolomite [321], CaO from $Ca(OH)_2$ precursor [322], and under multicyling operation [323].

Other groups have continued working in SE-SMR at atmospheric pressure, demonstrating the continuous operation [324]; proposing other sorbents as hydrotalcites [325] or CaO pellets[326]; developing hybrid particles or pellets which contains Ni-based catalyst and CO acceptor simultaneously as $CaO\text{-}Ca_{12}Al_{14}O_{33}$ [196], hydrotalcite and CaO-MgO-based sorbents [327].

Johnsen et al. [328] were the first to demonstrate the SE-SMR process in BFB, using separately particles of Ni catalyst and dolomite, at atmospheric pressure and 600ºC. These experiments were reproduced by Di Carlo et al. [296] with slight differences. Moreover, Di Carlo et al. simulated by means of a commercial CFD code their experiments with good agreement. Recently Chen et al. extended this model to hydrotalcites [329].

Modeling of SE-SMR reactors have been also studied at industrial scale with fixed beds [330, 331], with bubbling beds [332-334]. In the modeling works on SE-SMR it is remarkable the work of the group of H.A. Jakobsen, from Norwegian University of Science and Technology (NTNU), which has developed K-L and in-house CFD two-fluid models for SE-SMR process in bubbling and circulating fluidized beds, and hybrid pellets intraparticle diffusion models (e.g. [197, 245, 335-338]). However, these models have not been validated experimentally at full scale.

3.5.2 Numerical simulations of a laboratory scale SE-SMR reactor

Previously to the full-scale simulation of SE-SMR ZECOMIX reactor, the model proposed in previous sections has been validated with literature data. In order to validate the model, the most relevant operational conditions of ZECOMIX reactor [310] have been compared with experimental data reported by Johnsen et al.[328] and Di Carlo et al. [296] (as shown).

Table 3. 9 Operational conditions of lab scale case studies

	JOHNSEN	DI CARLO	CFD
Reactor diameter (m)	0.1	0.08	0.1
Reactor height (m)	1	0.6	1
Dolomite particle diameter (μm)	125-300	180-425	225
Ni-Catalyst particle diameter (μm)	150-250	180-425	225
Dolomite particle density (kg/m^3) Calcined / No calcined	N.R.	1580 / 2300	1550 / 2200
Ni-Catalyst particle density (kg/m^3)	N.R.	2100	2100
Bulk density of the mixture (kg/m^3)	1300	1000-1260	1040
Static bed height (m)	0.3	0.2	0.3
Reforming temperature (ºC)	600	600-700	600
Superficial gas velocity (m/s)	0.032 - 0.096	0.15 - 0.3	0.1-0.2
Dolomite-to-catalyst mass ratio (dimensionless)Dol/Cat	0.4	4-5	2
Steam-to-carbon molar feed ratio (dimensionless) S/C	3	4	4

In order to validate the model, three simulations were carried out. 1 minute of operation time has been simulated in a single 2.2 GHz CPU, using FLUENT 6.3. A 4000 uniform-square-cell mesh (5x5mm) has been used for the simulations (Figure 3. 31). Gas composition was fixed to a S/C=4 (20 %CH_4, 80%H_2O). Calcined dolomite is selected as CO_2 acceptor. A first standard calcination is supposed (kinetic parameters are listed in Table 3. 5). Two different velocities (0.1 and 0.2 m/s) and two different drag models (Syamlal-O'Brien and Modified-Wang) were studied. Simulated time was one minute, at least. The other simulation parameters are listed in Table 3. 10.

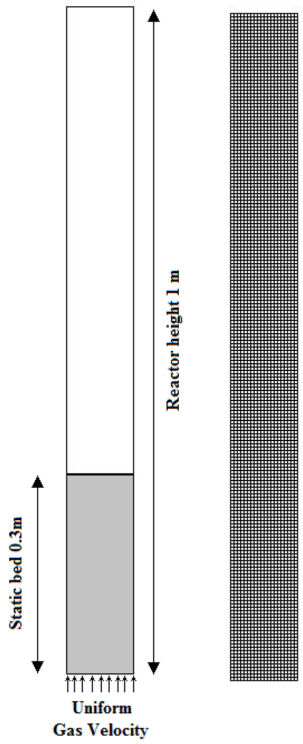

Figure 3. 31 – Schematic view of the 2D-BFB studied and mesh used

Table 3. 10 Numerical parameters of CFD simulations

Flow field	Unsteady RANS
Energy Equation	Isothermal
Multiphase model	E-E KTGF Closure
Pressure-velocity coupling	PC-Simple
Discretization	2nd order QUICK
BC Constants	
Superficial gas velocity	0.1 - 0.2 m/s
Gas Composition	20 %CH_4, 80%H_2O
Grid number cells	4000 - Uniform 5x5mm
Distributor details	Uniform
Initial solids packing	0,6
Maximum solids packing	0.63
Restitution coefficient (e_{ss})	0.9
Inlet boundary conditions	Velocity
Outlet boundary conditions	Pressure
Time steps (s)	0.001
Convergence criteria	10^{-3}
Closure models	
Turbulence	Laminar
Drag model	Syamlal-O’Brien / Modified Wang
Solid pressure	Syamlal-O’Brien
Radial distribution	Lun et al.
Granular kinetic viscosity	Syamlal-O’Brien
Frictional Viscosity	Schaeffer
Frictional Pressure	Syamlal-O’Brien

A hybrid particle approach has been used in the simulations. Dol/Cat ratio was fixed in 2, thus the particles are formed by 1/3 of catalyst, and 2/3 of dolomite. As dolomite presents a CaO/MgO ratio of 1:1, the composition of particle is 1/3 catalyst, 1/3 CaO and 1/3 MgO (inert). Moreover, as demonstrated by Di Carlo, there is not observed segregation of the phases using different particle phase for catalyst and sorbent (if velocity is at least 5 times U_{mf}). Hence, only one Eulerian solid phase can be assumed. Furthermore if Dol/Cat ratio is up to 2, the carbonation reaction provides the heat necessary for steam methane reforming, obtaining an autothermal process. This fact validates the isothermal simulation hypothesis.

The simulations present good agreement with values reported by Di Carlo (Figure 3. 32). The hydrogen mole fraction obtained under the different experiments is ~ 0.92, thus chemical equilibrium is not achieved as in Johnsen experiments (~0.98). The lack of equilibrium is supported by the incomplete conversion of methane (~0.98) and incomplete CO_2 capture (CO_2 outlet mole fraction ~ 0.02). The species distribution across the bed is shown in Figure 3. 33.

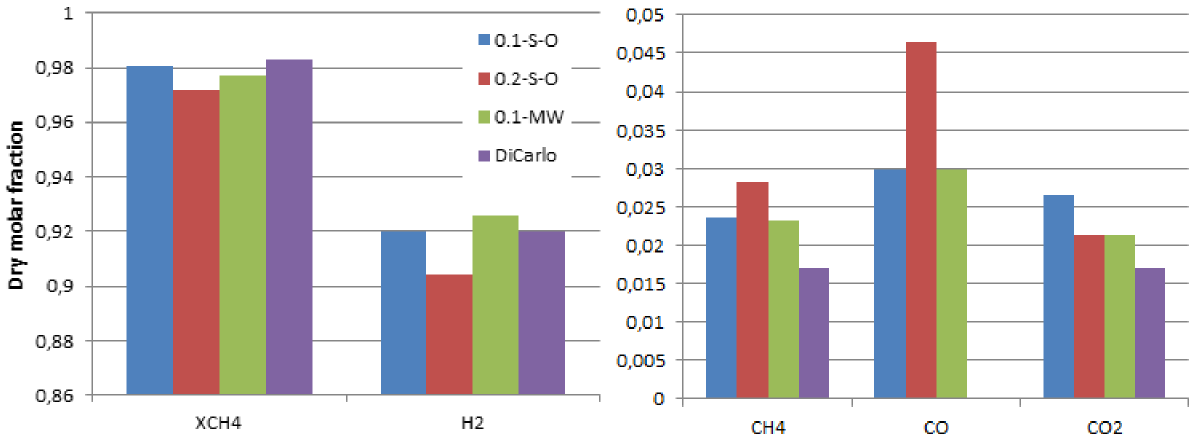

Figure 3. 32 – Methane conversion and H_2, CH_4, CO and CO_2 mole fraction in dry basis

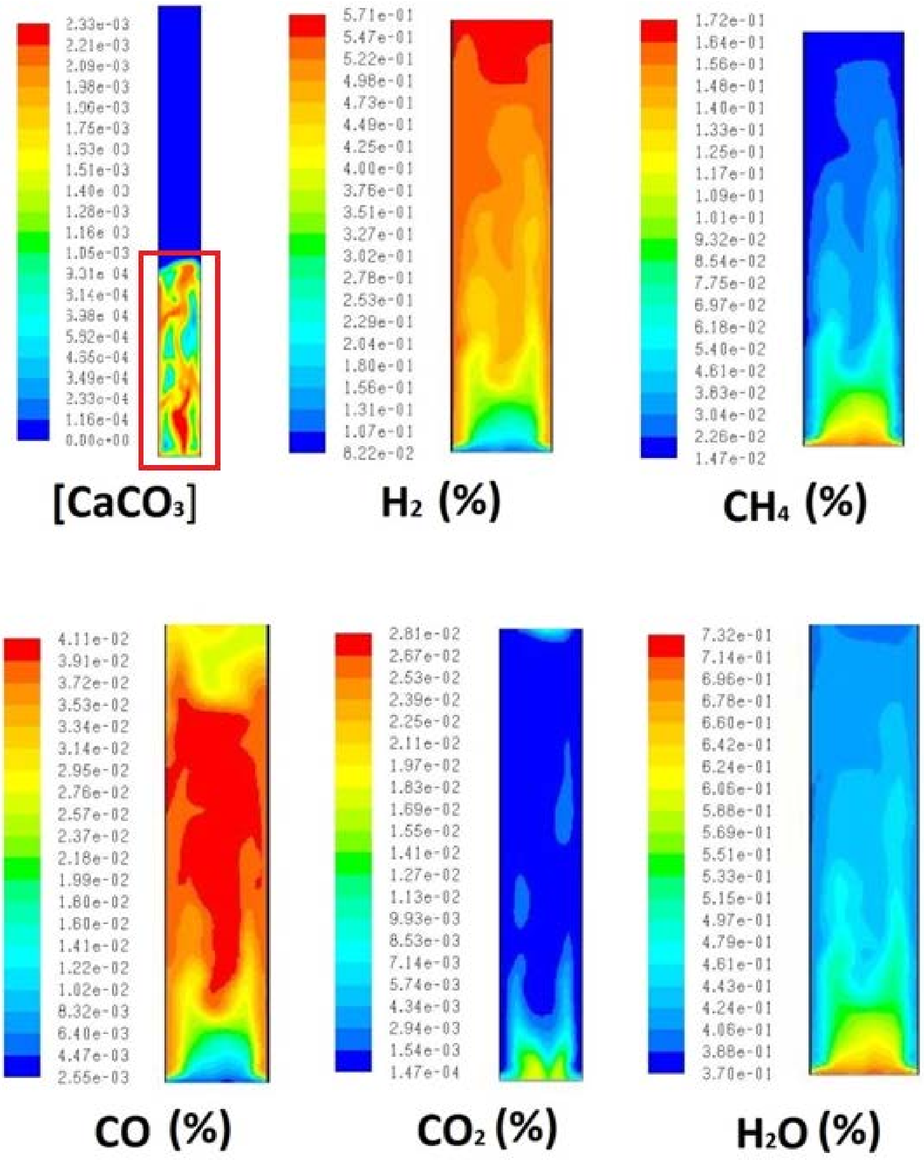

Figure 3. 33 – CaO conversion (in terms of $CaCO_3$ conversion) and H_2, CH_4, CO, CO_2 and H_2O distribution species in gas phase for t=30s U=0.2m/s

Equilibrium is not achieved mainly due to the relatively high gas velocity, which reduces residence time of the gas in the fluidized bed. If residence time is not enough, CO_2 capture is not complete. As shown in Figure 3. 34, on the one hand, the velocities of reforming reactions (R.1-R_CO Eq. 3.36; R.2-R_CO2 Eq. 3.37) are very high and they occur in the bottom of the FB (under 0.1 m); and the water-gas shift reactions (R.3-R_WGS Eq. 3.39) is practically in equilibrium. On the other hand, the CO_2 capture reaction rate is higher in the lower bottom of the reactor, but it spreads over the entire reactor, with fluctuations due to the bubbles. The CO_2 capture reaction affects majorly to reforming conversion to CO_2 (R_CO2) and, in a lower degree to reforming to CO (R_CO). For example the fluctuations in which capture increases, R_CO2 also increases (marked near 0.2m height in Figure 3. 34). Thus CO_2 capture is the limiting step of the SE-SMR reaction.

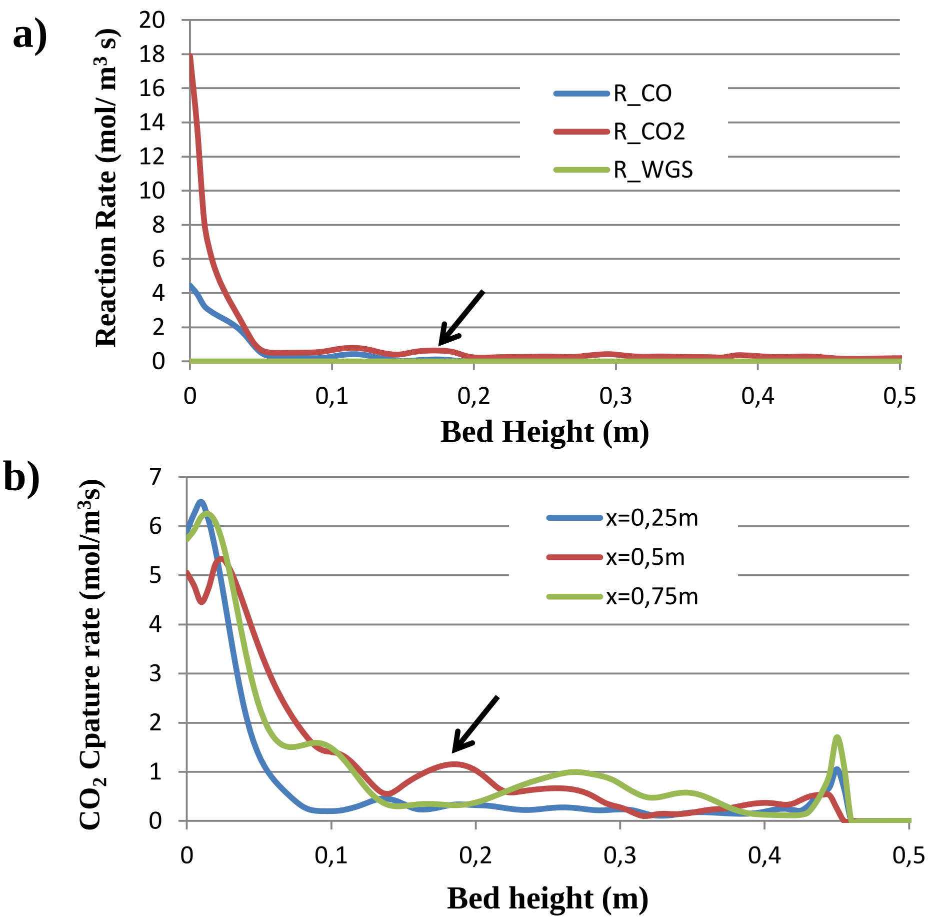

Figure 3. 34 – Reaction rate of SMR (a) and CO_2 capture (b) bed height. U=0.1 m/s

There are slight differences in the species prediction between the cases in which Symalal-O'Brien (S-O) and the Modified-Wang (M-W) drag models have been used. As shown in Figure 3. 35 bed behavior at U=0.1 is very similar using S-O and M-W models. Comparable bed expansion and volume fractions have been obtained, with a difference in the resolution of some bubbles. Moreover, applying a Fast Fourier Transform (FFT) to the transient pressure drop signal the spectra are very similar, with a slight increase in the magnitude. Thus in terms of macroscale and microscale bed behavior there are not strong differences, and, therefore there are not differences in the species distribution. However, there are bigger differences in the response of the system under U=0.2 m/s.

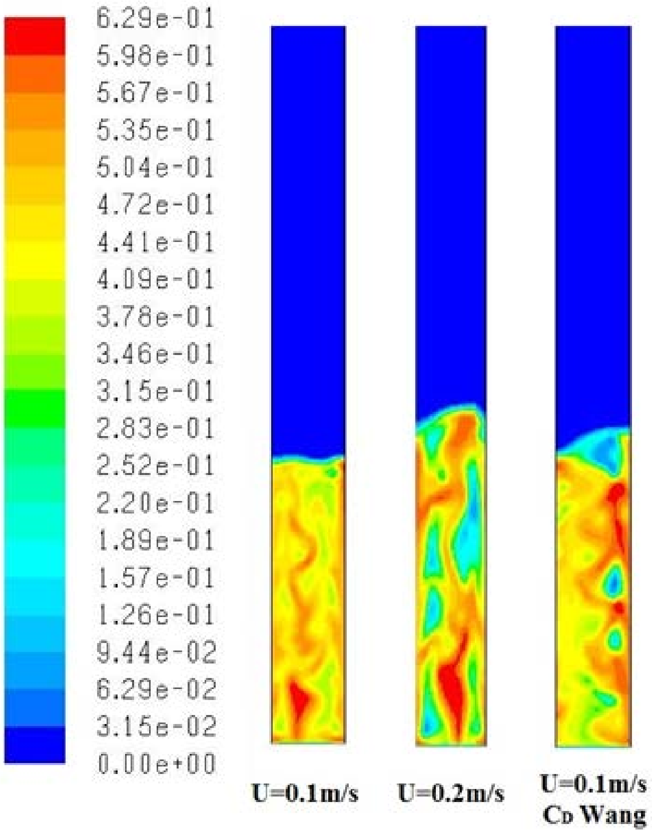

Figure 3. 35 – Volume fraction of solids at t=30 s

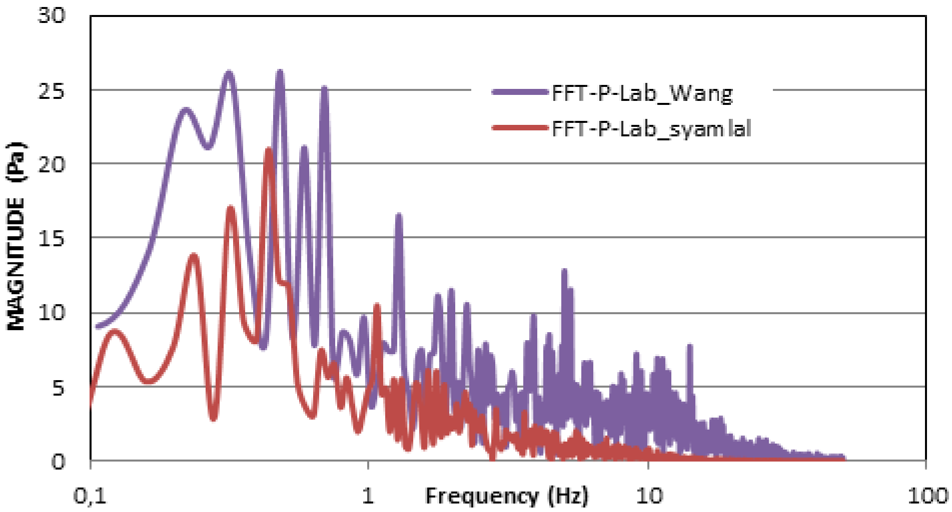

Figure 3. 36 – Power spectra of simulated U=0.1 m/s with S-O and M-W drag models

The increas of velocity affects strongly the behavior of the SE-SMR reactor. On the one hand, methane conversion and hydrogen volume fraction present a relative reduction of ~ 2%, CO volume fraction increases ~ 35% and CO_2 concentration decreases ~ 25%. These variations are due to the lower residence time of methane in the bed, and, to the formation of larger bubbles, which reduce the gas-solid contact. The lower value of CO2 concentration is associated to a lower conversion of methane, and not, to the capture reaction that remains constant. As shown in Figure 3. 37, the global behavior of the bed is dominated by the gas velocity. An increase in the velocity supposes a higher expansion of the bed and a lower local solid fraction, which produces of larger bubbles which can be captured under this mesh resolution.

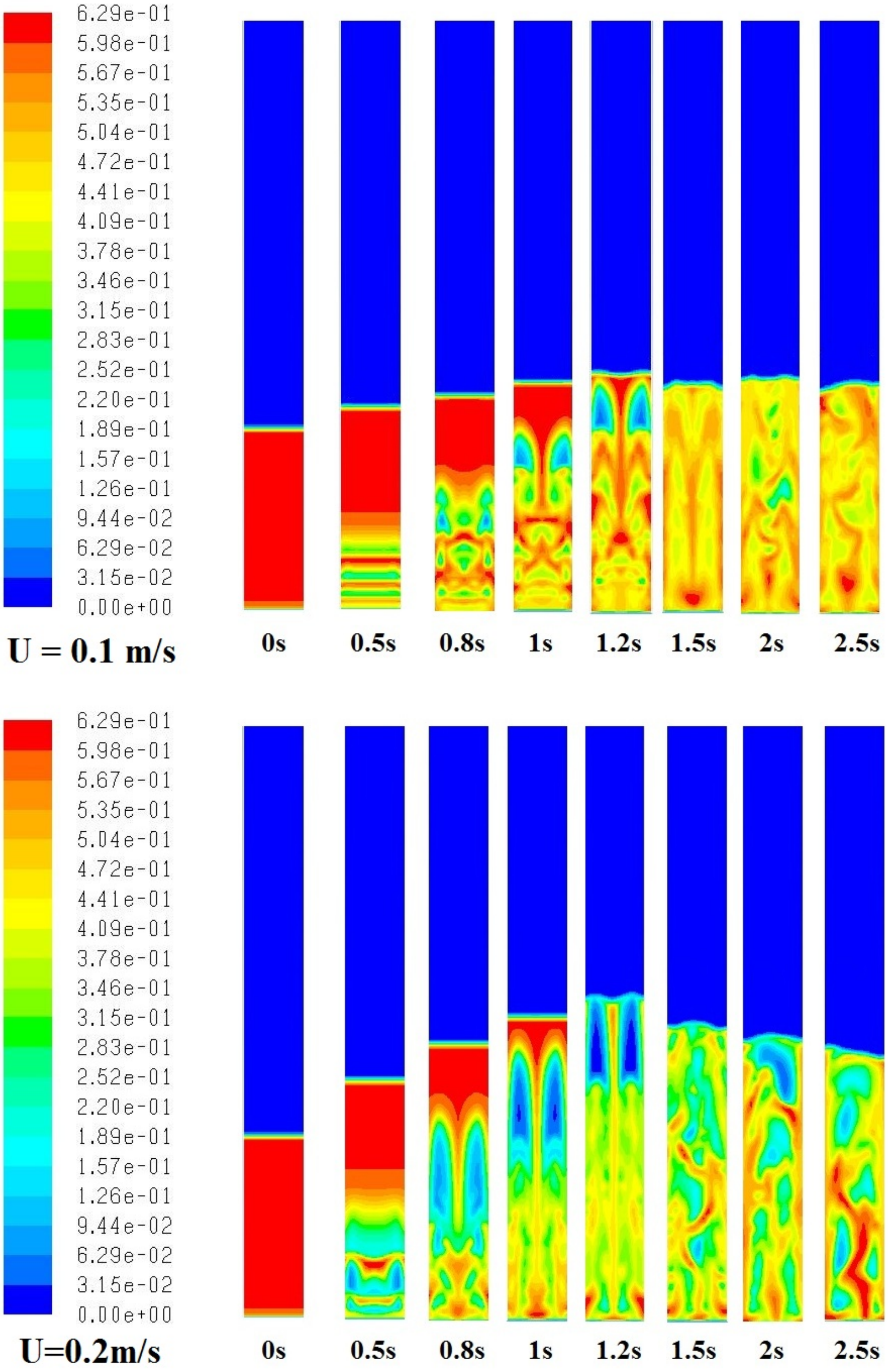

Figure 3. 37 – Bed expansion of simulated bed as function of volume fraction of solids for U=0.1 – 0.2 m/s

In Figure 3. 38 have been are plotted the gas and solid velocities along the bed. Evaluating gas velocity plot is possible to observe two parallel bubbles through the bottom of the bed. At H=0.3m the flow is not symmetric and the coalescence generates an axisymmetric bubble in the right side of the bed with a high velocity. The pressure fluctuation generated by this bubble is balanced with a lower velocity bubble in the left side. Up of the bed (H=0.7m) a typical parabolic free flow is obtained, with a mean value of 0.2 m/s, as defined in the uniform velocity inlet. Gas velocity is higher than solid velocity. However, it is worth to note that solid velocities peaks correspond to gas peaks (related to the bubbles). Thus, the gas in the bubbles moves the solids in the same trend, but in a different magnitude. Moreover is very interesting to note the downdraft movement of the solids near to the walls.

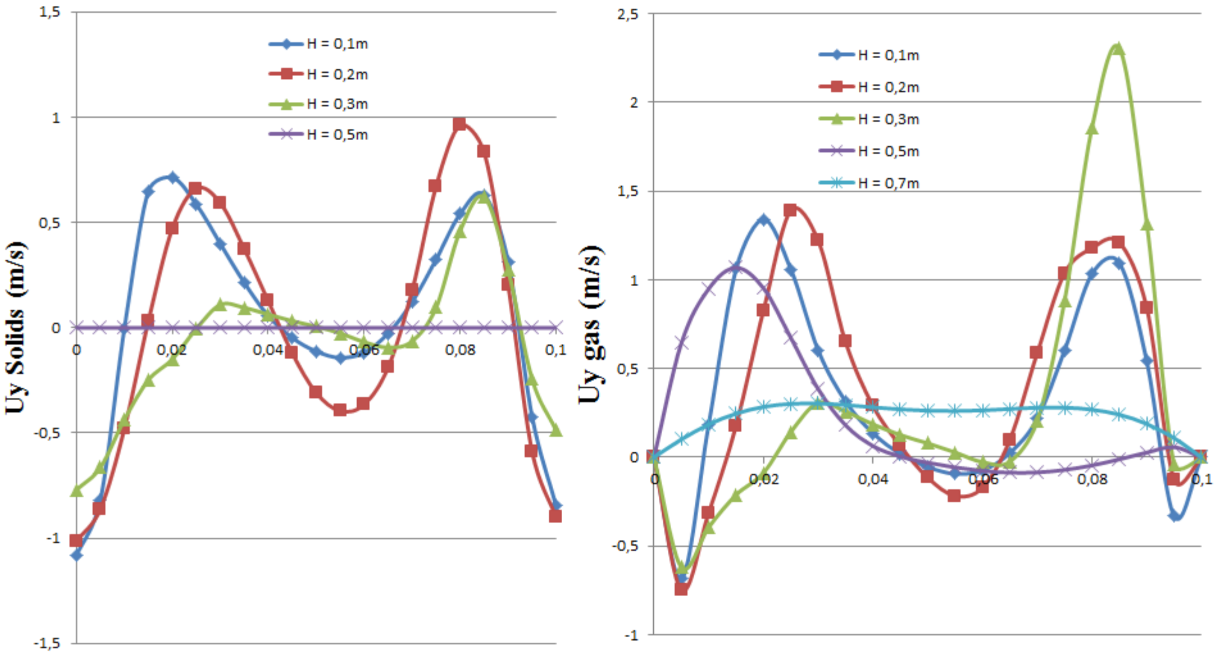

Figure 3. 38 – Solids (left) and gas (right) velocity plots at t=30 s for U=0.2m/s case.

3.6 Summary and Conclusions

In this chapter an introduction to fluidization and numerical methods to simulate bubbling fluidized beds has been presented. A comprehensive CFD model has been developed in order to simulate the behavior of a Sorption-Enhanced Steam Methane Reforming bubbling fluidized bed reactor.

Hydrodynamics of the system have been simulated by means of an Eulerian-Eulerian approach, assuming the Kinetic Theory of Granular Flows for closure of the governing equations. Under this approach a commercial code has been selected for the simulations (FLUENT 6.3) and some sub-models have been developed and implemented in this code by means of UDFs.

Firstly, because the aim of this thesis is to obtain an economic-computational model of an industrial BFB, a drag model from literature (proposed by Wang et al.) has been modified for this case study. The simulation with the implemented drag model not presents strong differences with the Syamlal-O'Brien model (included by default in FLUENT). However it is possible to suppose that at higher scale, with coarser grids, the differences will be sensible.

Secondly, heterogeneous gas-solid reaction models have been implemented. On the one hand, the Xu and Froment model has been selected from literature for SMR. On the other hand, the Stendardo and Foscolo particle model for CO_2 capture with solids sorbents at high temperature has been modified to enlarge its application to different natural and synthetic sorbents, taking into account the thermal history of them. The proposed modified model has been based in TGA experiments. A good agreement has been observed between model and experimental data, for dolomite and mayenite under different activation treatments.

Previously to the simulation of SE-SMR reactor, a hydrodynamic study has been carried out at different scales, in order to establish the best conditions for the simulations. Cold flow simulations of an oxy-fuel reactor (owns by CIRCE) as well as ZECOMIX reactor have been carried out. Some important accomplishments were achieved. Firstly, 2D non-axisymmetric simulations present a more realistic hydrodynamic behavior than 2D axisymmetric cases. Secondly, the most influential submodel in KTGF simulations is the drag model, the effect of the other submodels (solid pressure, radial distribution, granular kinetic viscosity, etc.) is practically negligible. Thirdly, the detailed simulation of perforated plate distributor increase the accuracy of simulations, but it leads an increase of mesh resolution, computation time and convergence instabilities.

Finally, SE-SMR simulations, including all sub-models, were carried out in a laboratory scale reactor. The simulations present a good agreement compared with literature data. Chemical and hydrodynamic results are sensitive to operative variations, and they are congruent with theoretical and experimental predictions.

Thus, this model can be considered correct and validated at laboratory scale. In the next section, the implementation of this model at semi-industrial scale is discussed.

4 NUMERICAL SIMULATION OF THE SE-SMR REACTOR IN ZECOMIX PLANT

4.1 Scale-up of fluidized beds

The purpose of running experiments at laboratory scale is to obtain information to help the engineer to develop large-scale units. Typically the complete design process of a new commercial fluidized bed reactor involves a laboratory scale unit, a larger pilot plant, and a still larger demonstrator unit. The scale-up of bubbling fluidized bed is known to be more difficult than other types of reactors. The history of fluidization contains several examples were the scale-up was extremely successful [228], but great failures have also been reported [339].

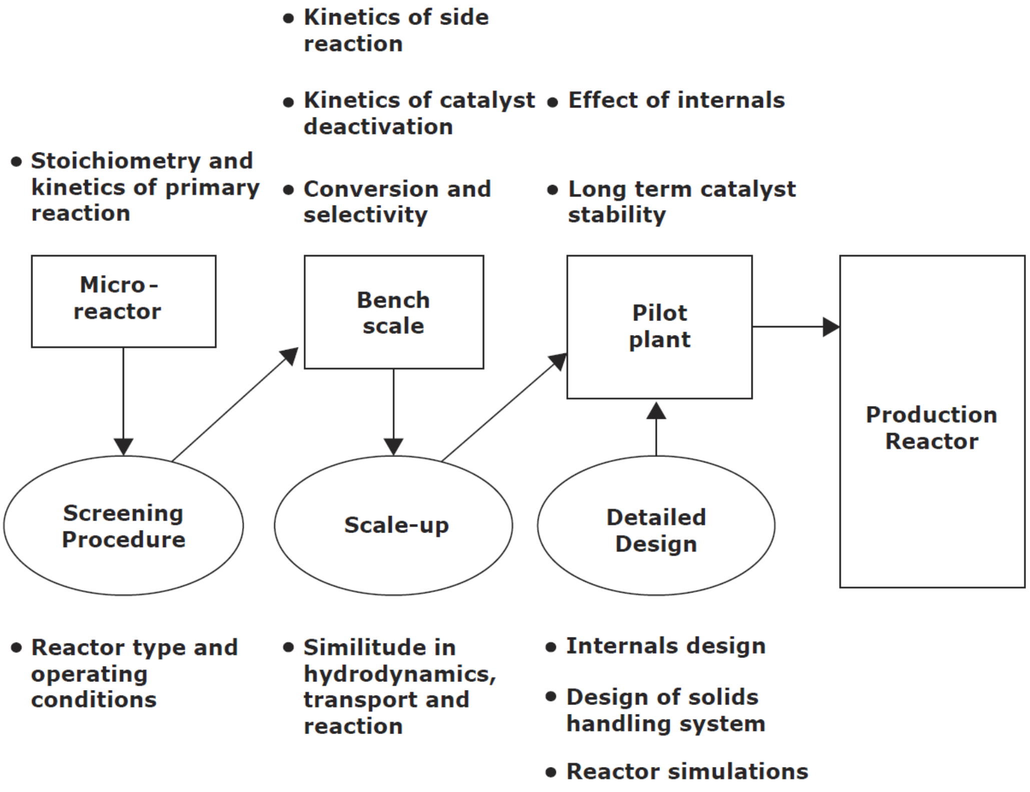

Figure 4. 1 – Scale-up procedure to establish an industrial full-scale catalytic fluidized bed reactor. From [340]

Numerous authors have demonstrated that model simulations can serve as tool in hydrodynamic scaling-up. Traditionally, scaling of hydrodynamic systems is done with the aid of dimensionless parameters which must be kept equal at all scales in order to be hydrodynamically similar. In order to find the relevant dimensionless parameters, dimensional analysis is applied. The principles of dimensional analysis are explained in [341]. There are two approaches which, if done properly, will both lead to the same result [342]:

Buckingham Pi-Theorem [343] is applied if the differential equations governing the behavior of the system are unknown. In brief, the Buckingham Pi-Theorem tries to express the dependence of one parameter (e.g. U_{mf}) as a function of relevant independent parameters (e.g. bulk density, gas viscosity, bed voidage, particle sphericity, particle size, etc.) to its simplest (dimensionless) form. The problem of this approach is that all relevant parameters need to be known, although the Buckingham Pi-Theorem does not explicitly provide information whether the list of dimensionless numbers is complete [344].

Inspectional analysis is used if the governing differential equations and boundary conditions are known and they can be non-dimensionalized to yield a set of dimensionless numbers which completely describe the system [342].

In the beginning of the fluidization studies, the most extended technique to develop the scaling rules has been the application of the Buckingham Pi-Theorem to fluidization model [231, 345, 346].

The Buckingham Pi-Theorem produces, quickly and easily, a set of dimensionless parameters but it no provides a way of determining if the list of independent parameters is complete. The method of non-dimensionalization of the governing equations and boundary conditions does not suffer from this limitation, but the governing equations and boundary conditions must be able to be completely specified, and they must contain all the pertinent independent parameters. The governing equations can also provide guidance as to when certain parameters dominate others (e.g such as when inertial effects dominate viscous effects or vice versa).

The aim of non-dimensionalizing the governing equations is to normalize the equations in order that each term is of order unity or less. This makes it possible to look at the order of magnitude of each term for a particular situation to determine when certain terms are negligible relative to others (referred to as order of magnitude or scale analysis). Order of magnitude analysis can also provide information regarding the functional form of the solution to the equation. Order of magnitude arguments are used, for example, to simplify the Navier-Stokes equations in the development of the boundary layer equations. A very good review about inspectional analysis can be found in [342].

The most extended scaling relationship for fluidized beds were developed by L.R. Glicksman, and co-workers, during the 1980’s. Glicksman approached the problem from a more fundamental viewpoint; scale-up criteria were developed to maintain hydrodynamic similarity in bubbling beds (without consider the presence of kinetic or mass-transfer effects). Thus, he based his work in the proposed idea by Fitzgerald and Crane [347] who claimed that “in principle the motion of a system of particles suspended in a fluid is completely determined by the Navier–Stokes equations with the corresponding continuity equation and the Newtonian equation of motion of each particle to be satisfied at each point of the fluid”.

Based in this principle, Glicksman derived the “full set” [348] of relevant dimensionless scaling laws by non-dimensionalizing the governing equations of motion and conservation of mass of the gas and particle phase by Anderson and Jackson [349] with their boundary conditions (including an Ergun-like equation [232] to non-dimensionalize the drag coefficient). The full set of scaling relations can be written as:

$$\left[\frac{u_0^2}{gL},\frac{\rho_s}{\rho_g},\frac{\rho_s u d_p}{\mu_g},\frac{\rho_g u L}{\mu_g},\frac{G_s}{\rho_s u_0},\frac{L}{D},Bed\ Geometry,\phi,PSD\right] \tag{4. 1}$$

where G_s is the average solids feed rate per unit area from outside the bed through the bottom. This set includes the Reynolds number of particle and gas, the Froude number (u_0^2/gL), the ratio between gas and particle density, the particle size distribution (PSD), the ratio between particle and reactor diameter, particle sphericity ϕ, as well as geometric similarity conditions.

Several assumptions and simplifications were taken in order to obtain this full set of scaling laws: The fluid is regarded incompressible, interparticle forces other than mechanical forces due to collisions are omitted, and the coefficient of restitution and the coefficient of friction linked to interparticle collision are not included. Also, surface forces on particles due to static charge, reactions and heat transfer effects are ignored. A final assumptions made by Glicksman concerns low gas velocities relative to the speed of sound, where the pressure group equation (4.2)

$$\frac{P_0}{\rho_s u_0^2} \tag{4. 2}$$

can be neglected. The deliberate omission of the pressure group provides one degree of freedom, since otherwise this group would fix the particle density ρ_s in the scaling process. By neglecting the pressure group, the particle and gas density as well as the gas viscosity can simultaneously be altered without changing the Reynolds number. This simplification is the only difference with the results of obtained by Broadhurst and Becker by means the application of Buckingham Pi-Theorem [346]. Another simplification by Glicksman was to neglect the particle and gas stress tensors and the pressure gradient term.

In subsequent works, Glicksman et al. [350] modified the full set of scaling laws to reduce the number of assumptions and fixed parameters. The “simplified set of scaling laws”is valid for situations where the fluid-particle drag is either dominated by viscous forces (viscous limits $Re_p < 4$) or dominated by inertial forces (inertial limits $Re_p > 1000$). Glicksman et al. concluded that if the modified scaling laws hold for both low and high Reynolds numbers, they will also be approximately valid throughout the range of particle Reynolds numbers, but with an error in the dimensionless drag parameter in the mid-range of Re_p [344].

Other authors have developed similar scaling relationship by non-dimensionalizing the governing equations of their own models [351]. For example Foscolo et al. [352] obtain a compatible result to Glicksman, but they demonstrated that particle and gas stress tensors and the pressure gradient term (neglected in assumptions of the Glicksman “full set”) are included in the Froude number, which is already part of the full set.

Besides the scaling laws proposed by Glicksman, other authors also developed their own scaling laws. Horio et al. [353]derived phenomenological models of the bubbling bed based on potential theory including the work on pairwise bubble coalescence. Van den Bleek and Schouten [354] introduced chaos analysis into the field of scaling and suggested that if two beds are properly scaled, the rate of information change in both systems will be the same. Therefore, the Kolmogorov entropy K must be kept constant. Moreover, they demonstrated that the dimensionless entropy group is proportional to the Froude number and the bed aspect ratio H/D of the Glicksman scaling law.

It is important to remark that all these relationships are for hydrodynamic scale-up. Only very few works (as Kelkar and Ng work [340]) have been scale-up successfully reactive fluidized bed under very restrictive conditions.

Over the past decades, the approach of scaling with dimensionless numbers has been applied successfully to several fluidized beds in industry and research. However, in recent studies this traditional scaling approach has repeatedly been questioned. Reasons for the emerging criticism are multiple (e.g. the lacking degrees of freedom in the reactor design and the incompleteness of the scaling sets with respect to essential phenomena such as wall effects and particle–particle interactions) [344, 355].

CFD simulations are able to solve the governing equations at all scales, using the correct methods and grid size. However, as discussed previously, the computational cost can be excessive to simulate all the scales. Thus and industrial or semi-industrial cases need of some sub-grid assumptions (such as KTGF) to be solved. The first validation of the Eulerian-Eulerian simulation as a tool for scaling-up of fluidized beds were demonstrated by van Wachem et al. for Geldart B particles [356] and by Krishna and van Baten for Geldart A particles [357]. In the last decade it has been demonstrated that TFM can successfully predict the hydrodynamics of Geldart B particles at industrial scales [358], using fine grid simulations with Gidaspow [359-361], Wen-Yu [278] or Syamlal-O'Brien [362] drag models or by applying different sub-grid drag modifications, as proposed by Li and Kwauk and co-workers with the Energy Minimization Multi-Scale (EMMS) model [363-366]; Sundaresan and co-workers [265, 367, 368]; and Simonin and co-workers [369-371].

Moreover, some researchers have discussed the applicability of Glicksman scaling relationship by means of extensive simulation campaigns and different analysis techniques, such as Kolmogorov-Smirnov test, or S-statistic test for attractor comparison method applied to time pressure signals [344, 372, 373]. These studies obtained good agreement between DEM simulations scale-up and Glicksman rules, but notable differences using TFM simulations. TFM simulations need to define each particle diameter as one phase. Thus, the limitations on the number of Eulerian phases simulated can explain partially the differences between these two validations of scaling rules.

In any case, the validity of CFD as tool for scaling-up fluidized bed reactors has been demonstrated. However, several assumptions must be taken with caution to obtain correct predictions.

4.2 Semi-Industrial SE-SMR simulations

Previously to the simulation of ZECOMIX reactor under real operation conditions, the model presented in chapter 3 has been implemented in a semi-industrial reactor. Several simulations under the same conditions as those of laboratory scales were carried out, but at a semi-industrial scale in order to validate the model. In the ZECOMIX cycle, the syngas feed to the reactor is a mix of different species (CH_4, CO, CO_2, H_2 and H_2O). To validate the model at this scale we estimate a mix of steam and methane in a proportion of Steam/Carbon ratio of 4, and the simulation results were compared with literature data.

4.2.1 Grid and time step independence studies

The numerical method is the same presented in the previous section. 2D non-axisymmetric URANS simulations applying an Eulerian-Eulerian approach with the KTGF for closure and the Syamlal-O'Brien drag model have been undertaken. General conditions of the model and simulation are summarized in Table 4. 1. These conditions have been selected according to technical specifications of the plant [310, 374, 375] and to the experience acquired in previous chapters. Instead of a reactor height of 4m, the freeboard has been prolonged to 10m in order to achieve a plug flow and prevent any backflow occurring at the outlet.

Table 4. 1 - General operational parameters used in the simulations

Reactor diameter (m)	1
Reactor height (m)	4
Dolomite/Catal particle diameter (μm)	500
Dol/Cat particle density (kg/m^3) Calcined / No calcined	1550 / 2200
Bulk density of the mixture (kg/m^3)	1040
Static bed height (m)	0,5
Reforming temperature	623ºC -900K
Superficial gas velocity (m/s)	0.2
Dolomite-to-catalyst mass ratio (dimensionless) Dol/Cat	2
Steam-to-carbon molar feed ratio (dimensionless) S/C	4
Gas Composition	20 %CH_4, 80%H_2O
Grid number cells	1000 - 4000 - 16000
Distributor details	Uniform
Time steps (s)	0.01-0.005

In section 3.4.2 the importance of the distributor in the simulations has been discussed. Since the aim of this work is to obtain a model which allows to obtain accurate simulation with a reduced computational effort, the choice of a detailed distributor supposes a strong increase in the number of cells. Thus, in order to corroborate the hypothesis of a uniform distributor, a 3D detailed simulation of the gas velocity in the ZECOMIX distributor was realized. The distributor is formed by a perforated plate with tubes above the holes, in order to break up the jets, uniformizing the flow field. The results shown in Figure 4. 3 corroborate the uniformity of the flux, very few centimeters above the tubes, with a slight increase in the center zone. The maximum velocity in the center zone is 0.32 m/s, approximately ~12% higher than medium values (0.28 ± 0.04m/s). Hence, the approximation of uniform gas distribution can be considered acceptable.

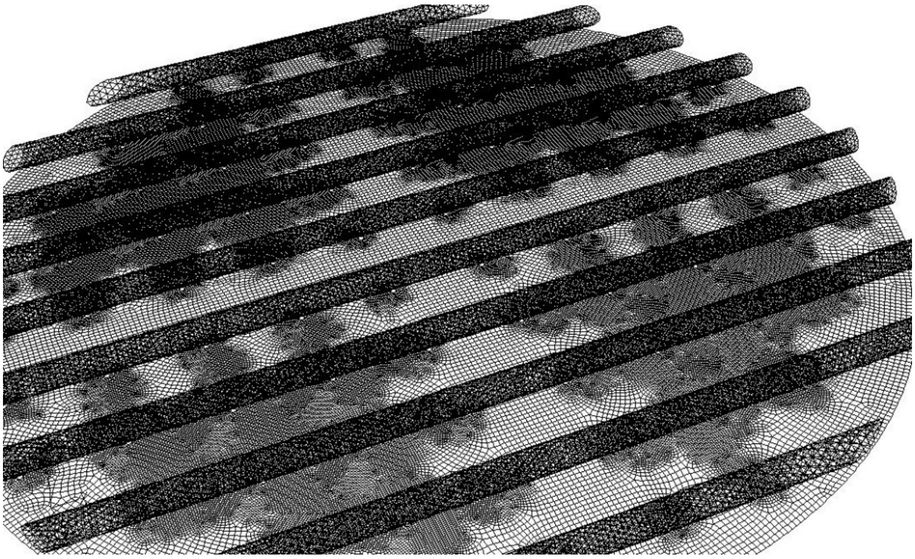

Figure 4. 2 – Detailed grid of ZECOMIX distributor

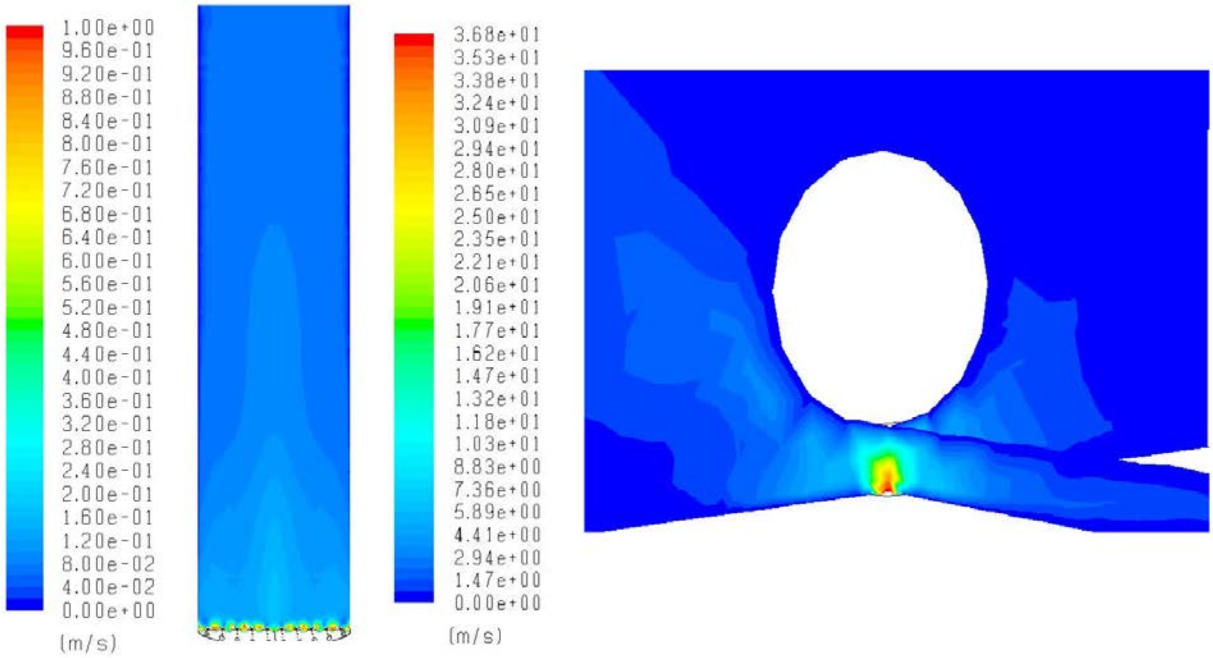

Figure 4. 3 – Velocity field in the ZECOMIX distributor. General view (left) and detailed of jet breakup (right)

In order to evaluate the mesh-independence of the multiphase 2D results, three different grids have been evaluated. The Richardson extrapolation (RE)[376, 377] method has been extensively used for the discretization error estimation [378, 379]. In order to obtain a grid independent solution, it is necessary solve three progressively finer meshes. A grid refinement factor (*r*) greater than 1.3 must be chosen to minimize truncation errors (in this work we selected, $r = 2$). Thus, the medium and fine grids have respectively 4 and 16 times as many points as the coarse grid.

The coarse grid (1000 cells) corresponds to the cell size reported by Wang et al. in the development of the sub-grid drag model [279] explained in the section 3.2.2. Coarse, medium (4000 cells) and fine (16000 cells) meshes are showed in the Figure 4. 4.

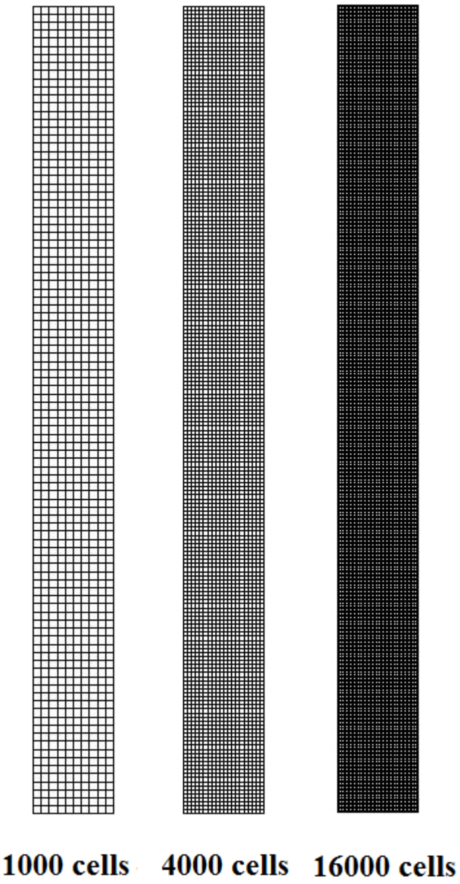

Figure 4. 4 – Mesh complete (left) and detailed for reactor interest zone (right) of fine, medium and fine grids.

Validation of the simulations have been accomplished according with the guidelines suggested by Grace and Taghipour [380], including all the possible literature data similar to the simulations, studying grid independence in the chemical and hydrodynamics patterns, and paying attention to the choice of a correct drag model. Figure 4. 5 summarizes the volume fraction of chemical species (-) and methane conversion (-), CO_2 capture reaction rate (kmol/m^{3}s), solids fraction (-), bed expansion (-) and pressure drop (Pa) for coarse, medium and fine grids, averaged for 30s of simulation.

Slight differences are observed between medium and fine grid, compared with the coarse grid. Relative differences between medium and fine mesh results vary between 0% and 30% (with a medium difference lower than 10%). Thus, the predicted values of independence appear to be satisfactory considering the complexity of the simulation.

Bed expansion, solids fraction and pressure drop present a correct trend in the cases of fine and medium grid (if solid fraction increases, bed expansion decreases, and corresponds to pressure drop). However in the case of coarse mesh an abnormal low pressure drop is observed, due to the bad resolution in the bottom of the bed.

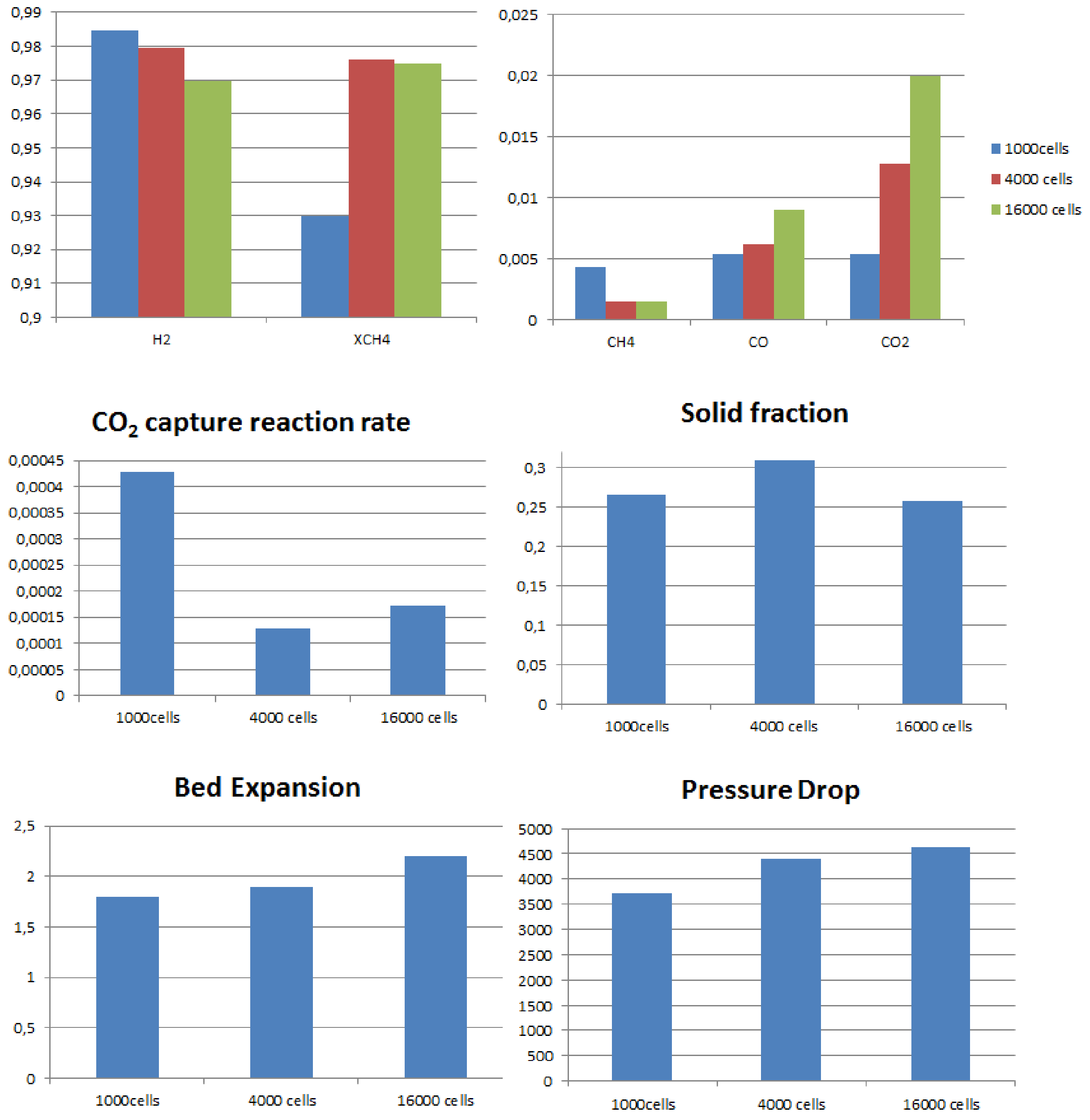

Figure 4. 5 – Volume fraction of chemical species (-) and methane conversion (-), CO_2 capture reaction rate (kmol/m^{3}s), solids fraction (-), bed expansion (-) and pressure drop (Pa) for coarse (1000), medium (4000) and fine grids (16000).

Comparing the results of chemical species at lab scale and semi-industrial scales, it is worth to note as methane conversion and hydrogen production are higher than in the case of lab-scale simulations (0.97 against 0.92). This is due to the equilibrium is achieved. The increase in the performance can be linked with the typical loss in the resolution of the bubbles associated to the use of high size cells, as shown in Figure 4. 6. The results are comparable with literature data for equilibrium experiments as well as numerical simulations [296, 322, 328, 334, 337, 381].

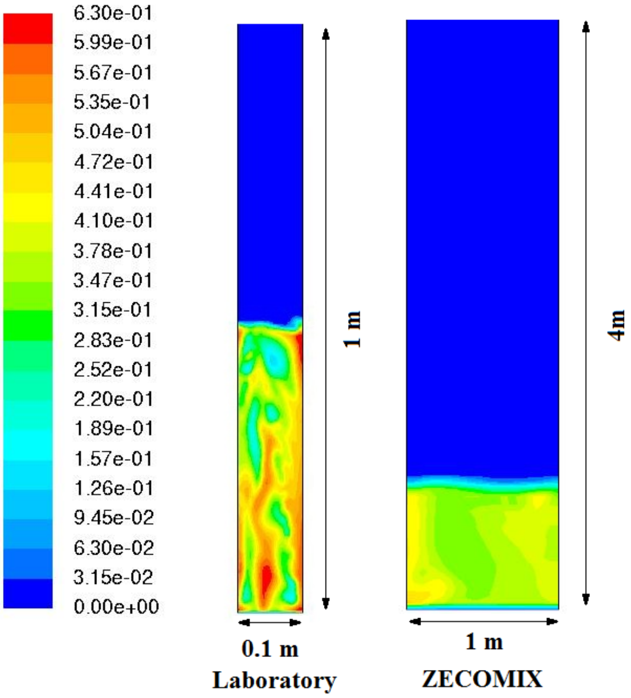

Figure 4. 6 – Solid fraction in the lab-scale (left) and semi-industrial (right) reactors. U=0.2m/s, d_p=0.5mm, 4000 cells-grid.

Obviously, an increase in the number of the cells in the grid supposes an increase in the computational time. Wall clock time of fine mesh case is ~2.5 times that of medium mesh case. For example, for a 1 minute simulated, 60 hours are needed for the medium mesh and 150 hours for the fine grid. Thus, a medium mesh size structure proves to be adequate considering the complexity of the problem, and consequently, this was used in the next simulations.

It is important to note that this grid independence study has been carried out according a methodology for stationary simulations. Rigorous criteria for unsteady pseudo-periodic simulations have not been developed, or at least, not standardized. Hence, this grid independence study is limited can be considered correct considering the limitations of these type of studies.

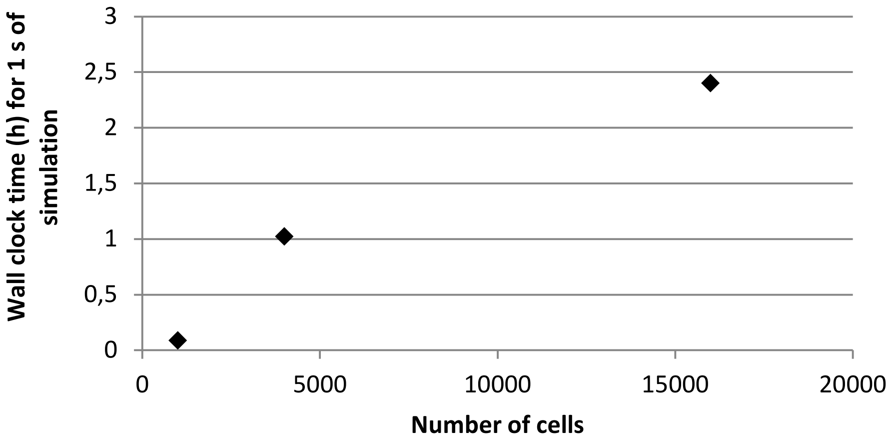

Figure 4. 7 – Wall clock time (h) for each second of simulation as function of the number of cells.

The unsteady simulations discussed in this section have been carried out fixing the time step in 0.01 s. However, as well as the results must be grid-independent, must be also time-step independent, to ensure the convergence of the solution (besides of the convergence of residuals in each time step).On the one hand, if the time step becomes smaller, then the predicted change of a cell property between time t and time $t+\Delta t$ (where Δt is the time step) may become smaller than a fixed convergence criterion, resulting in a larger overall error. On the other hand, if the time step is too large, then a "jump" of a cell property between t and $t+\Delta t$ can be expected to lead to less accurate results. The prediction of properties, as explained before, also depends on the cell size. The dimensionless Courant number (N_C) links time step, cell size and velocity [382]:

$$N_C = \frac{U_{gas}\,\Delta t}{\Delta x} \tag{4. 3}$$

where Δx is the cell size parallel to the advection flow term. In this study Δx corresponds to the cell side size, 5 cm. Keeping N_C low the oscillations in the response decrease, accuracy is improved, and numerical dispersion decreases. Gobin et al. [369] proposed a maximum value for $N_C = 0.3$ for fluidized beds, and Cornelissen et al.[312] confirmed a minimum value for $N_C = 0.03$. According with values and assuming velocities from 0.2 to 0.5 m/s, in this work a time-step independence study has been carried out for Δt=0.01, 0.0075 and 0.005 s. The averaged values obtained are very similar, but only the power spectra of pressure fluctuations are similar to the Δt=0.01s and 0.0075s. Moreover, the Δt= 0.0075s no reproduce accurately the magnitude values of the peaks in the spectrum. To reduce the computational cost and to obtain a more accurate solution, the next simulations were carried out with Δt=0.01s.

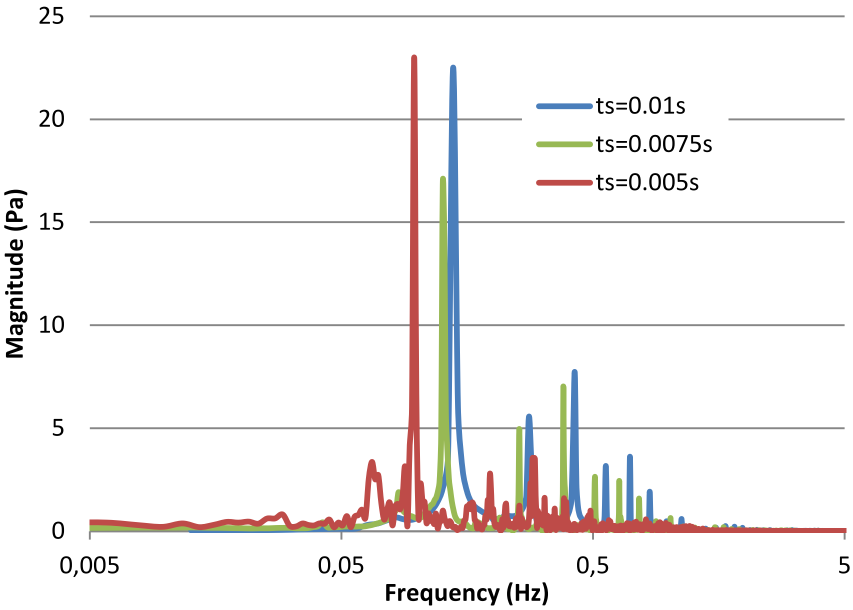

Figure 4. 8 – Power spectra of SE-SMR cases at different time steps. U=0.2m/s, d_p=0.5mm, 4000 cells-grid.

4.2.2 Model sensitivity study

Temperature is the key parameter in the SE-SMR chemical process at large scale [328]. Other parameters affect strongly the performance of the reaction. However, the sensitivity of the model to temperature is a very good indicator of its validity [245]. A study of the effect of the temperature in the reactor has been carried out, with and without including sorbent in the bed. Hence, the effect of the temperature in the SMR and SE-SMR process has been evaluated, as shown in Figure 4. 9.

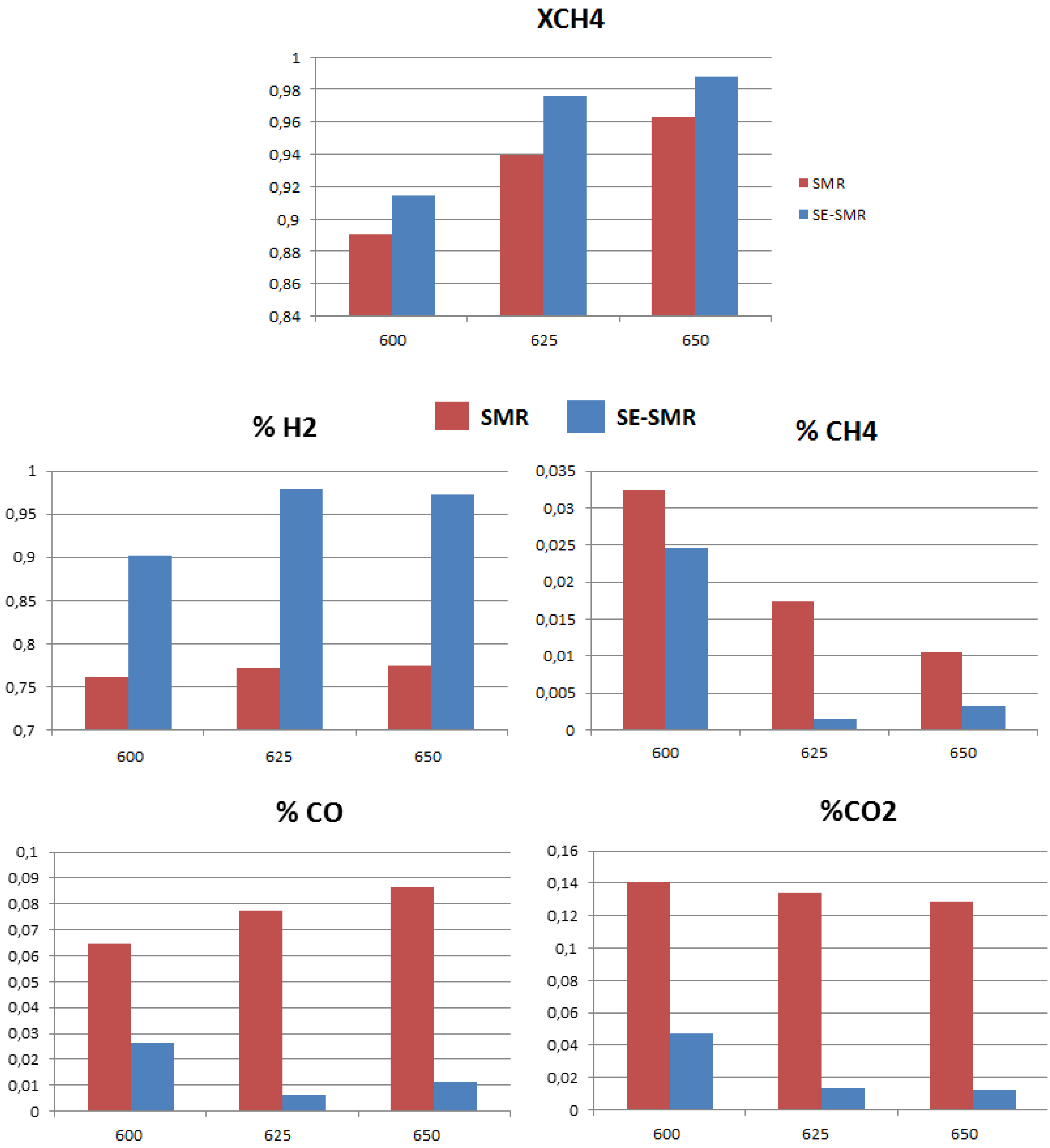

Figure 4. 9 – CH_4 conversion and H_2, CH_4, CO, CO_2 dry mole fraction for SMR and SE-SMR process at T=600,625 and 650 ºC (873 – 900 – 923 K)

Conversion of methane (in SMR and SE-SMR cases) increases with temperature. Reforming reactions are endothermic. Hence, an increase of temperature improves the conversion of methane. The presence of CO_2 sorbent shifts the equilibrium of the 4 reactions to the right. Thus the conversion of SE-SMR reaction is higher than SMR. This increase of methane conversion produces the increases of hydrogen production. In SMR and SE-SMR cases the equilibrium is achieved in all cases (except in SE-SMR at 600ºC which presents a lower H_2 concentration). Hydrogen concentration increases from 0.76 to 0.77 from 600ºC to 625ºC, and it remains constant for higher temperatures, in SMR cases. In the cases of SE-SMR, for temperatures up to 625ºC the H_2 equilibrium concentration decreases, thus hydrogen concentration is lower at 650ºC than at 625ºC (0.98 vs. 0.97) in accordance with theory.

The decay of hydrogen concentration up to 625ºC is due to the reduction of carbon capture efficiency (R.4) [332]. The reduction of CO_2 capture performance is due to increasing temperature, the carbonation reaction is closer to equilibrium and reaction rate decreases. This effect impacts in the CO, CO_2 and CH_4 concentration with increases with temperature.

In the cases of SMR simulations (without CO_2 capture reaction) CO concentration increases with temperature and the CO_2 concentration decreases. This can be explained because of reforming reactions (R.1 and R.2) are competitive, and, R.1, which produces CO, is more dependent on temperature than R.2, as shown in Figure 4. 10. R.1 presents a reaction rate in all the bed r_1=20 mol/s. Instead, r_2 increases from 11 to 14 mol/s, in the range of temperatures studied.

$$CH_4 + H_2O \leftrightarrow CO + 3\,H_2 \qquad --- \qquad \mathrm{R.1} \qquad (4.\,4)$$

$$CH_4 + 2H_2O \leftrightarrow CO_2 + 4\,H_2 \qquad --- \qquad \mathrm{R.2} \qquad (4.\,5)$$

$$CO + H_2O \leftrightarrow CO_2 + H_2 \qquad --- \qquad \mathrm{R.3} \qquad (4.\,6)$$

$$CaO + CO_2 \leftrightarrow CaCO_3 \qquad --- \qquad \mathrm{R.4} \qquad (4.\,7)$$

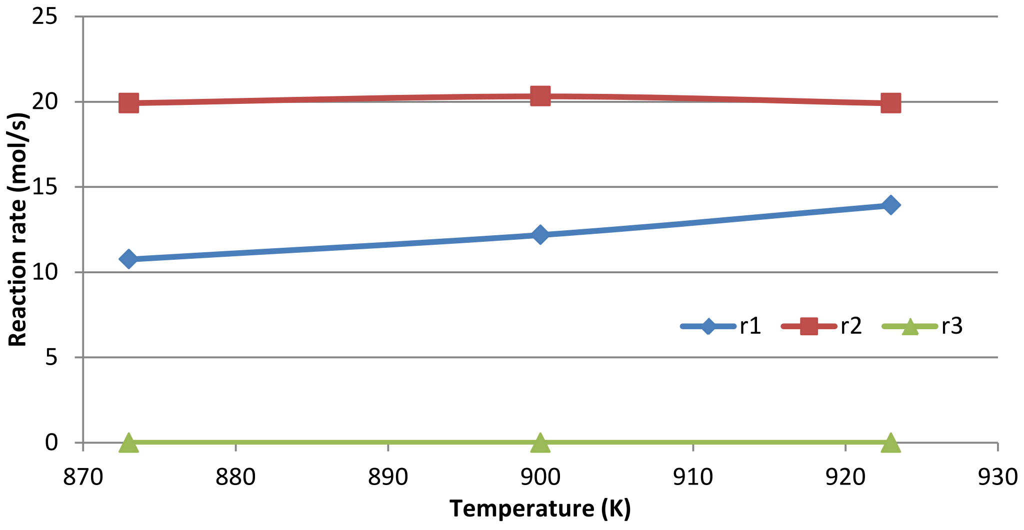

Figure 4. 10 – Reaction rate of reactions R.1, R.2 and R.3 for SMR and SE-SMR at t=60 s as function of temperature

The competence between R.1 and R.2 is strongly affected by the presence of CO_2 capture reaction (R.4). Figure 4. 11 presents the reaction rates across the bed for the cases of SMR and SE-SMR. It is possible to note, as in the case of SE-SMR (in which R.4 is included), that the removal of CO_2 shifts R.2, increasing strongly the reaction rate (r_2). Due to the competence between reactions, the increase of the reaction rate of R.2, reduce the reaction rate of R.1 (r_1). In the first 10 cm of the bed, there are not observed differences in the reaction rate between SMR and SE-SMR process, due to the excess of CH_4 (see Figure 4. 12). When methane conversion achieves equilibrium, CO_2 capture becomes the limiting reaction, thus affecting r_1 and r_2. It is worth to note that at very low CO_2 concentrations (see Figure 4. 12), $r_1$becomes negative, promoting the advance of the R.2. This effect of competence between the reactions was also noted by Xu and Froment, that reported negative reaction rates for the SMR process [295].

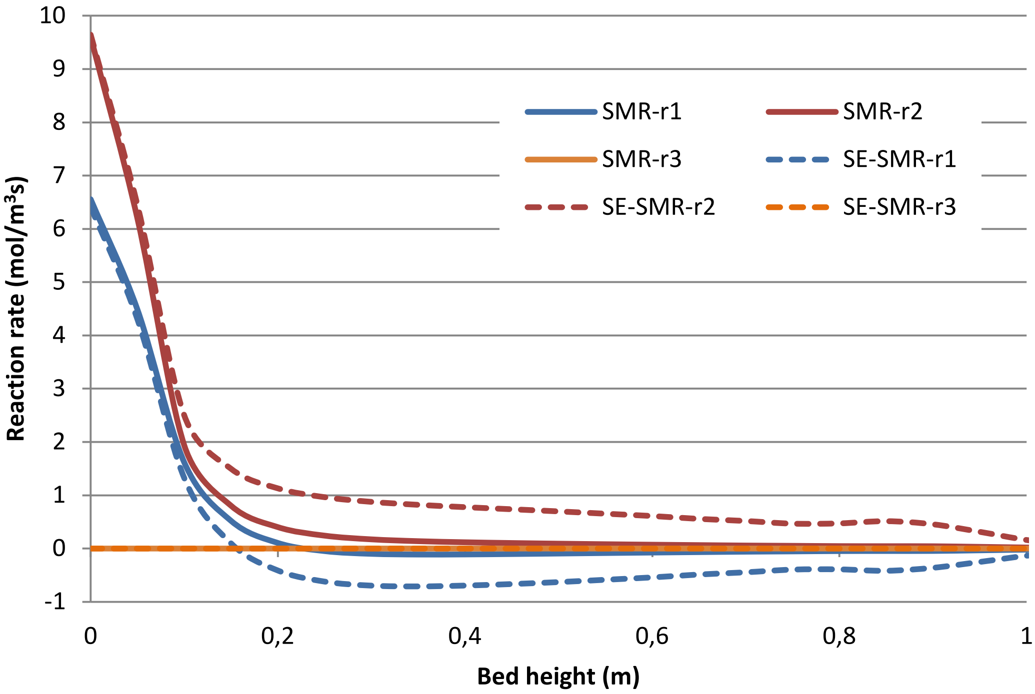

Figure 4. 11 – Axial reaction rate of reactions R.1, R.2 and R.3 for SMR and SE-SMR at t=60 s and 900K

The effect of competence between reactions is also observed in the profile of chemical species presented in Figure 4. 12. In the case of SMR reactions, the reactions advance quickly, until they reach equilibrium. Some small variations in CO and CO_2 can be observed due to fluctuations in the measurement point plotted in the simulations. However, in the SE-SMR case the conversion of species presents two different slopes. The first corresponds to the reaction dominated by reforming reactions (R.1 and R.2), in which the excess of CH_4 shifts the reaction. The second one is dominated by the CO_2 capture reaction (R.4), in which, as explained previously, the carbonation reaction displaces the reforming reaction (to CO_2), increasing the concentration of hydrogen, until reaching equilibrium. R.4 is slower than R.1 an R.2, thus the slope of the second reaction is less steep than in the first stage.

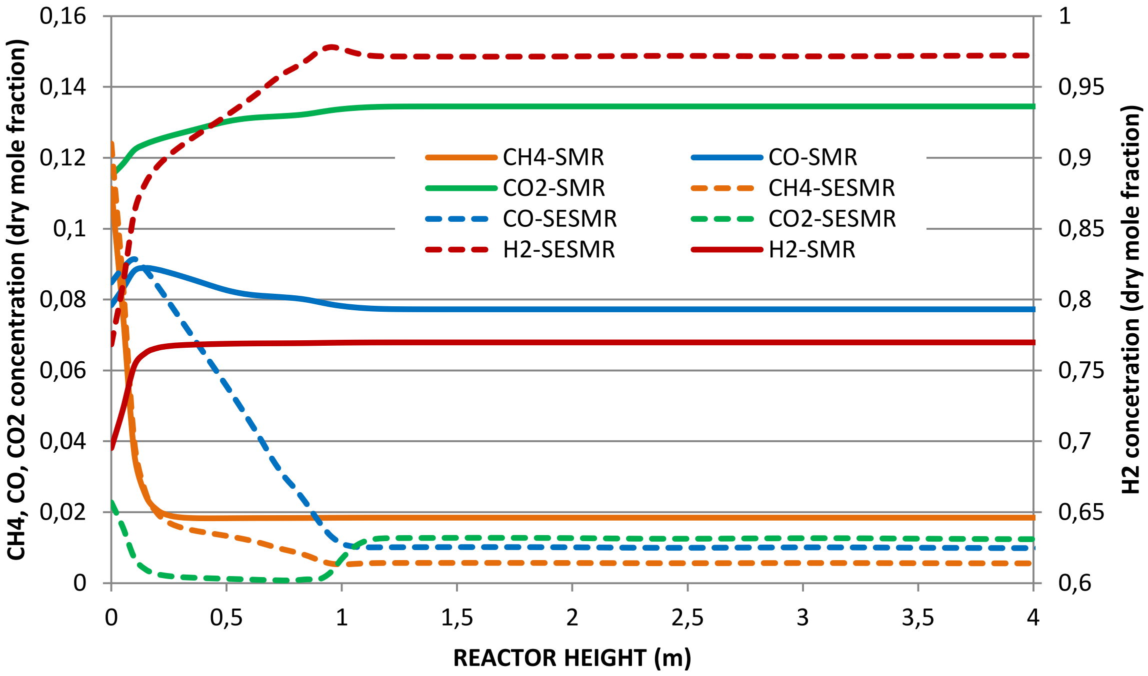

Figure 4. 12 – Axial dry mole fractions of H_2, CH_4, CO and CO_2 for SMR and SE-SMR at t=60 s and 900K

Figure 4. 13 summarizes the cases studied and compared with literature data [245, 296, 328, 337]. Results present a good agreement with literature data. It is worth to note that simulations were carried out in slightly different operational conditions than the equilibrium curves shown in the figure. And it has been checked that hydrogen concentration is not higher than equilibrium values [296].

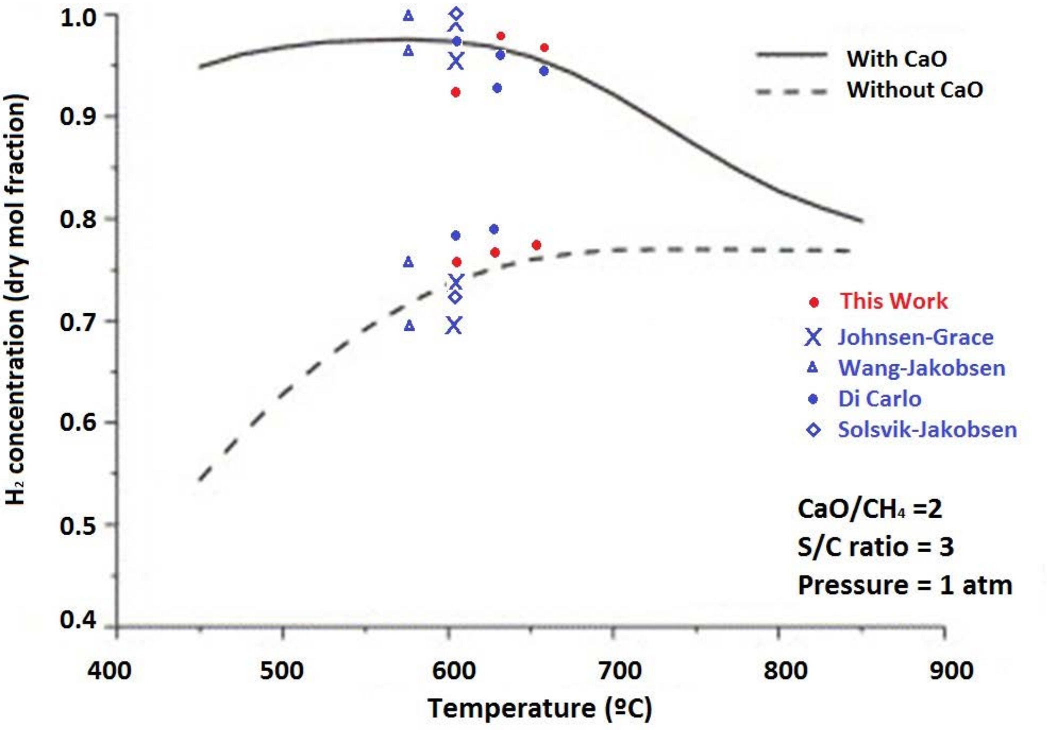

Figure 4. 13 – Hydrogen content at equilibrium as a function of temperature, adapted from [328]

In order analyze the carbonation reaction in the semi-industrial reactor, a simulation of the bed in a typical pore-combustion CO_2 stream (25% CO_2), without catalyst has been carried out. Figure 4. 14 shows the evolution of the conversion of CaO presented in the solid sorbent. The evolution with time presents good agreement with literature values [375]. It is worth to note that as the CaO conversion is not constant all over the bed, there is a higher reaction rate at the bottom, which is made uniform at larger heights due to the mixing.

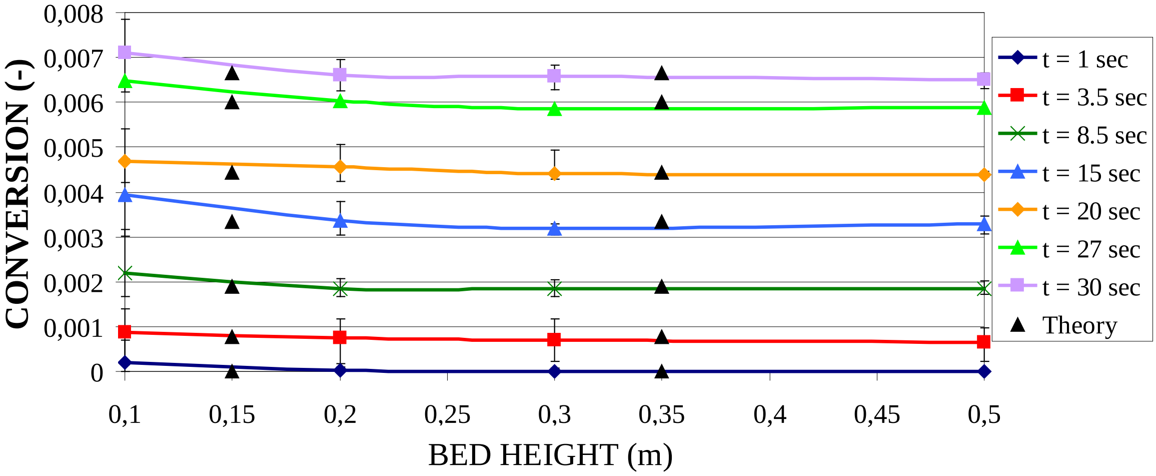

Figure 4. 14 – Axial conversion of CaO, with time at 900K and pure CO_2 concentration

The drag model must be evaluated in order to complete the analysis of the sub-models implemented in the global CFD model [380, 383]. As explained in previous chapter, besides of the Syamlal-O’Brien model, included in Fluent, a sub-grid drag model proposed by Wang et al. [279] has been modified and implemented in the CFD code. At lab scale, not different patterns were observed in the time-averaged and dynamic responses. At semi-industrial scale, the same chemical equilibrium response was obtained, and analogous hydrodynamic patterns. For example, Figure 4. 15, the solid fraction and bed expansion are very similar for both drag models.

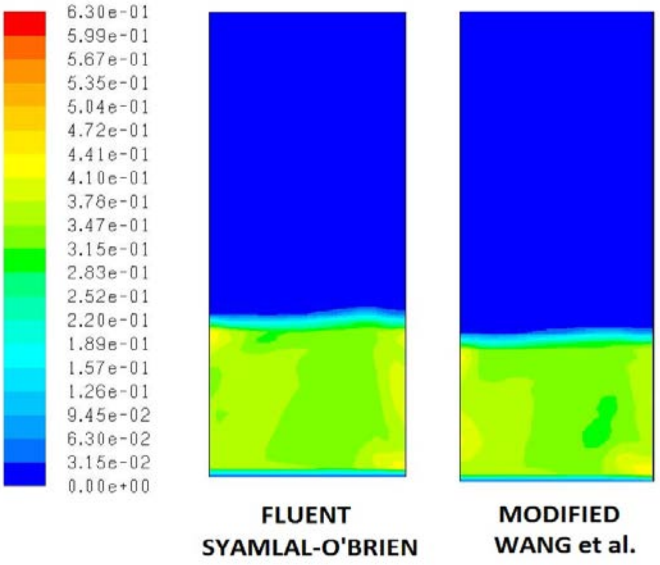

Figure 4. 15 – Solid fraction for SE-SMR at 900K, t=60s

However, evaluating the dynamic response of the pressure drop in some random points, it has been observed that the patterns are strongly different depending on the drag model. Using the Syamlal-O’Brien model, an unrealistic periodic behavior is obtained. However, with the new drag model proposed a realistic pseudo-periodic pattern is obtained, as shown in Figure 4. 16.

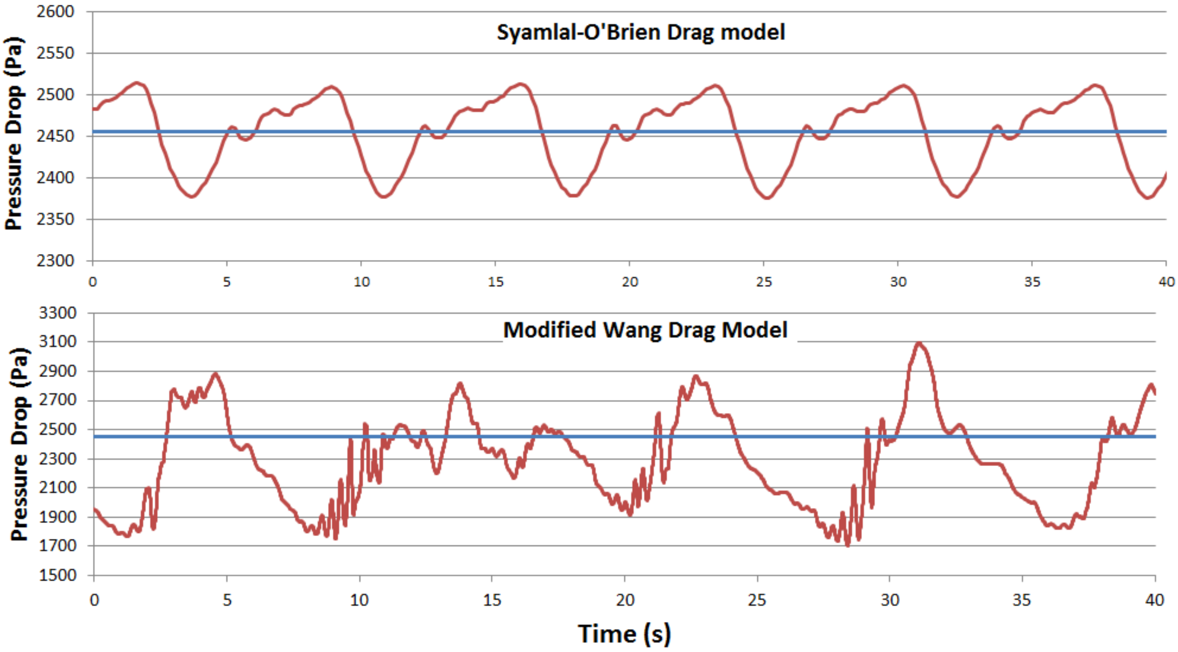

Figure 4. 16 – Time sequence of the pressure fluctuations using S-O and M-W drag models.

The modified drag model presents, besides of a more realistic waveform, an amplitude on the pressure drop (~ 1400 Pa max) more realistic than the Fluent drag model (~ 150 Pa max). Moreover, applying a Fast Fourier Transform (FFT) the power spectra obtained are strongly different, as shown in Figure 4. 17. The spectrum corresponding to the modified model presents a broad band of frequencies between 0 and 10 Hz, as noted in literature [384].

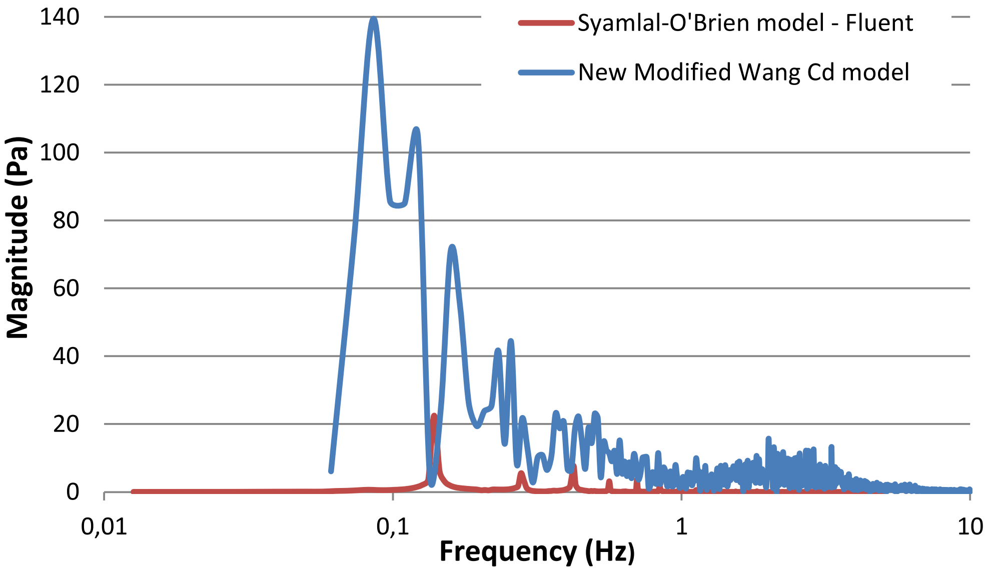

Figure 4. 17 – Power spectra of the pressure fluctuations using S-O and M-W drag models.

The power spectra present two different patterns, which correspond to two characteristics fluidization regimes [385] (see Figure 4. 18). The Modified Wang drag model presents a power spectrum which corresponds to a typical multiple bubble regime (as expected in a high scale bubbling fluidized bed). However, Syamlal-O'Brien model power spectrum presents a behavior similar to single bubble regime, unrealistic for this fluidized bed scale. Thus, the proposed Modified Wang model, presents a behavior more realistic than Syamlal-O'Brien, for the selected cell size.

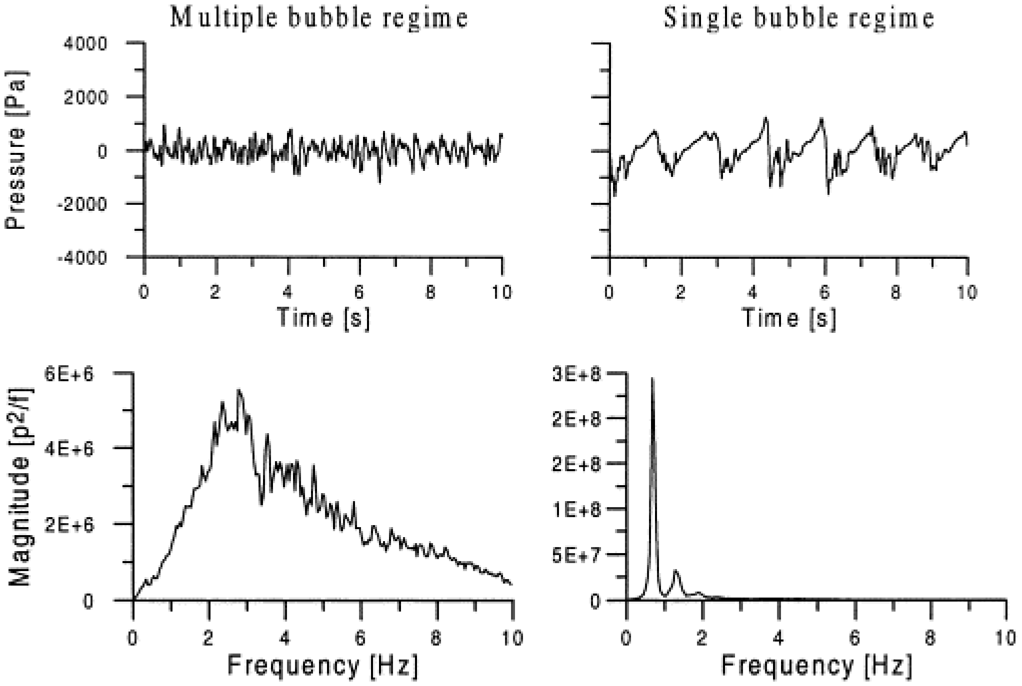

Figure 4. 18 – Time sequence and power spectra of the pressure fluctuations for multiple and single bubble regime, from [385].

4.3 ZECOMIX configurations – Case studies

The ZECOMIX cycle was designed for operation at high pressure (25-30 bar) [105, 107]. The cycle analysis studies were carried out at this pressure, obtaining a net cycle efficiency close to 50%. However, the pilot plant pressure is limited to a lower value. On the one hand, the hydrogen-modified gas turbine operates at 7 bar, thus the maximum cycle pressure must be fixed at this value. On the other hand, due to security requirements and very high cost associated to the operation with pressurized hot gases, gasification and carbonator reactor must operate at atmospheric pressure, and a compression unit was included to operate the turbine.

These changes impact negatively to the cycle efficiency, but they do not change the demonstration aim of the plant. The change in pressure does not allow to include a hydrogasification reactor, due to kinetic limitations, thus a steam gasification reactor was erected. The syngas obtained is mixed with methane in order to simulate the composition that would be obtained in the hydrogasification reactor. These changes are schematically shown in Figure 4. 19.

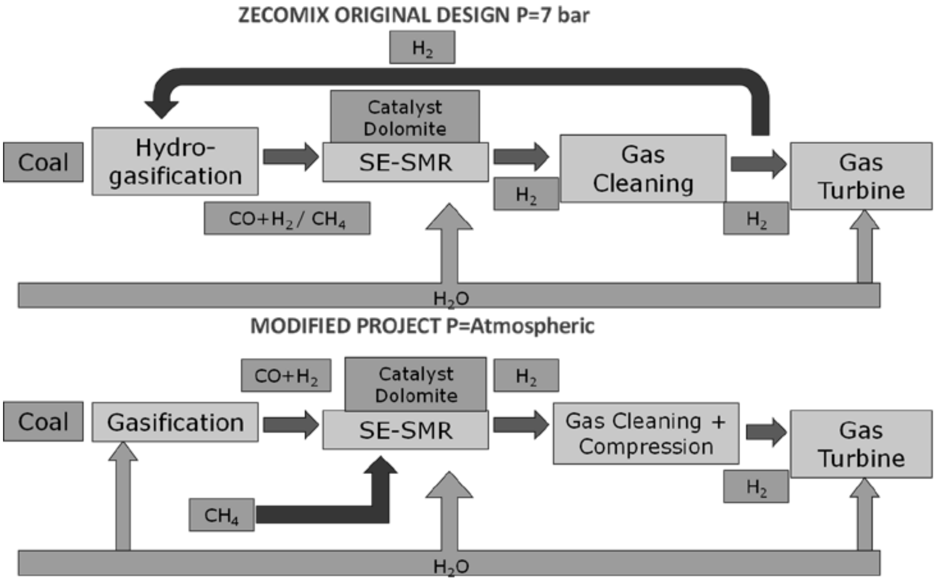

Figure 4. 19 – Schematic configuration of original and modified ZECOMIX pilot plant.

The two different gas compositions are summarized in Table 4. 2. The syngas from hydrogasification composition includes the methane added and, also, the steam necessary to ensure the SMR reaction.

Table 4. 2 – Gas composition under gasification [374] and hydrogasification [310] process.

Syngas composition(%vol.)	Gasification	Hydrogasification
CH_4	2	12,4
H_2	36	12,8
CO	30	8,5
CO_2	12	4,7
H_2O	20	61,6

Thus, pressure and gas composition must be included in the study, in order to predict the behavior of the ZECOMIX reactor. Kinetics is strongly dependent on temperature. Most of the previous studies suggest than optimal temperature is close to 900K [296, 320, 328], in order to be close to equilibrium and reduce the sorbent regeneration heat requirements. However, some researchers estimated a better performance at lower temperatures (~800K) and higher pressures [88, 322, 337]. Hence, the temperature range selected in this study spreads between 800 and 900K.

As explained in the preceding sections, the presence of catalyst and sorbent plays a crucial role in the SE-SMR reaction. On the one hand, without catalyst, the SMR reaction is too slow to be of industrial interest. On the other hand, SMR reaction can be enhanced by the presence of a CO_2 sorbent. Thus, the inclusion or not of solid sorbent and catalyst has been studied in the present work. The presence of catalyst is denoted as SMR-ON and the presence of sorbent Capture-ON, in the description of case study presented in Table 4. 3.

Moreover, two different sorbents, one natural (Dolomite) and one synthetic (Mayenite), were studied under standard calcination conditions, and under pretreatment to improve their carrying capacity and durability. The simulations were carried out for the first carbonation cycle, for simplicity. However, the effect of multicycling in kinetic effects can be easily implemented according with the methodology explained in the previous sections 2.2.4 and 3.3.2

Hydrodynamics of the systems strongly depends on the particle diameter, gas velocity and bed height. Therefore, these three parameters have been included in the study. The range of application of each parameter is limited by the fluidization regime. Thus the maximum and minimum values were defined according to Grace Diagram (Figure 3.4), in order to be always in a bubbling Geldart B regime. Moreover, two different drag models have been studied: Symlal-O’Brien and Modified Wang drag models. Under these hypotheses, the parameter conditions are summarized in Table 4. 3.

Table 4. 3 – Case study parameter levels

	Parameters	Level 1	Level 2
1	Temperature (K)	900	800
2	Pressure (bar)	1	7
3	Particle diameter (mm)	0,25	0,5
4	Gas velocity (m/s)	0,2	0,5
5	Bed Height (m)	0,5	0,25
6	SMR	SMR-ON	SMR-OFF
7	CO2 Capture	Capture-ON	Capture-OFF
8	Sorbent	Dolomite	Mayenite
9	Pretreatment	No pretreated	Pretreated
10	Syngas Composition	Hydrogasification	Gasification
11	Drag Model	Syamlal-O’Brien	Modified Wang

4.4 Taguchi Method for Design of Experiments

According with classical factorial statistics, to evaluate the effect on the response of the ZECOMIX reactor of the 11 parameters summarized in Table 4. 3, it would be necessary to carry out 2^{11} = 2048 experiments. Since each simulation takes, approximately 60 hours, a prohibitive wall clock time of 122,880 hours (~14 years) will be necessary. This problem is inherent to engineering practices: experiments (albeit numerical in this case) cost time and money.

Fortunately, since the pioneering work of Fisher [386], there are a number of statistical techniques available for engineering and scientific studies in order to obtain the maximum information of the processes with the minimum number of tests. Design of Experiment (DOE) is a powerful statistical technique for improving product and process designs and solving production problems. Several structured, reliable and efficient DOE methodologies exists, such as Factorial Design, Fitting Regression Models, Response Surface Methods, etc… [387, 388].

From an engineering point of view Taguchi Methods for Robust Parameter Design have been extensively used in industry. This method were developed by G. Taguchi in Japan during 1950’s and introduced in western industries in the 1980’s [389]. The overall objective of the method is to produce high quality product at low cost to the manufacturer. With this aim, Taguchi’s perspective focus the attention in the variation of the response of the system under different experimental conditions, instead of be centered in the average results as traditional DOE [390].

Taguchi method proposed test pairs of combinations instead of all possible combinations as in factorial design. The bases for Taguchi’s method are the orthogonal arrays, which show what factor levels must be selected each time to do the fewest possible runs. The main idea is to concentrate only on those few runs that are vital for the analysis. An orthogonal array is a fractional factorial experimental matrix that is orthogonal and balanced. Here, the balance property has two meanings. First it means that every column is balanced, that is, each level of the factor appears the same number of times. For example, in the simplest case, to evaluate the effect of 3 different factors in two levels for each factor, L_4 (2^3) array is used. In the L_4 array any column will have 2 “1” levels and 2 “2” levels (see Table 4. 4). The second meaning is that any two columns in the array are also balanced, having the same number of combinations of levels. Other important property of orthogonal arrays is that any two columns of an orthogonal array form a two-factor complete factorial design.

Table 4. 4 – L_4 (2^3) orthogonal array

Experiment	Factors			
	A	B	C	Response
1	1	1	1	R_1
2	1	2	2	R_2
3	2	1	2	R_3
4	2	2	1	R_4

Using Taguchi method, 4 experiments are necessary to evaluate the effect of 3 factors at 2 levels, instead of the $2^3 = 8$ necessary with the full fractional design. As experiments become more large and complex, the use of orthogonal arrays becomes more convenient. For the case study of this work, in which it is necessary to evaluate 11 factors at 2 levels, instead of the 2048 experiments from factorial design, Taguchi proposes a L_{12} (2^{11}) orthogonal array (as shown in Table 4. 5).

Table 4. 5 – L_{12} (2^{11}) orthogonal array

Experiments	FACTORS										
	A	B	C	D	E	F	G	H	I	J	K
1	1	1	1	1	1	1	1	1	1	1	1
2	1	1	1	1	1	2	2	2	2	2	2
3	1	1	2	2	2	1	1	1	2	2	2
4	1	2	1	2	2	1	2	2	1	1	2
5	1	2	2	1	2	2	1	2	1	2	1
6	1	2	2	2	1	2	2	1	2	1	1
7	2	1	2	2	1	1	2	2	1	2	1
8	2	1	2	1	2	2	2	1	1	1	2
9	2	1	1	2	2	2	1	2	2	1	1
10	2	2	2	1	1	1	1	2	2	1	2
11	2	2	1	2	1	2	1	1	1	2	2
12	2	2	1	1	2	1	2	1	2	2	1

It has been said that the strategy behind design of experiments is to gather the most valuable data with the least amount of experimental runs. The analysis of information obtained from the experiments can be processed in four steps:

a) Estimation of the effect that factors have in the average system response.
b) Evaluation of influence of each factor on the system response.
c) Analysis of interactions between factors.
d) Development of a predictive model.

Taguchi method is very powerful, but presents some limitations. Firstly, if several responses would be studied simultaneously, the estimation of effects and the factor influence can be obtained simultaneously, but it is not possible to establish a unique correlation between percent influence and average response of the system. Secondly, the evaluation of interactions requires at least three levels for each factor. Thirdly, to develop a predictive model based in linear regression (as suggested Taguchi), it is necessary that all the interactions between factors are negligible. These second hypothesis is very restrictive for our work, due to the important interactions between gas-solid reactions and hydrodynamics. Thus, we have centered this work in the estimation of effects and the evaluation of factor influence in the response of the ZECOMIX reactor.

The procedure to obtain the estimation of effects and factor influence is resumed in five steps [391]. According to the example shown in Table 4. 4:

1. Calculate the total effect of factors. The total effect of a factor is obtaining by adding the results of experiments (N=1,2,3,4) containing the effects of the factor (F=A,B,C) at each level (L=1,2):

$$\begin{aligned} A_1 &= R_1 + R_2 \ ; A_2 = R_3 + R_4 \\ B_1 &= R_1 + R_3 \ ; B_2 = R_2 + R_4 \\ C_1 &= R_1 + R_4 \ ; C_2 = R_2 + R_3 \end{aligned} \tag{4. 8}$$

2. Compute the correction factor (CF) used for calculation of all sums of squares:

$$CF = \frac{T^2}{N} = \frac{(\sum_{i=1}^{N} R_i)^2}{N} = \frac{(R_1 + R_2 + R_3 + R_4)^2}{number\ of\ experiments = 4} \tag{4. 9}$$

3. Compute the total sum of squares (S_T):

$$S_T = \sum_{i=1}^{N} R_i^2 - CF = R_1^2 + R_2^2 + R_3^2 + R_4^2 - CF \tag{4. 10}$$

4. Obtain the factor sums of squares for each one of the factors (S_F):

$$S_F = \sum_{i=1}^{NL} \frac{F_l^2}{N_{F_L}} - CF \ \ ; e.g.\ S_A = \frac{A_1^2}{N_{A_1}} + \frac{A_2^2}{N_{A_2}} - CF \tag{4. 11}$$

5. Calculate the percent influence of the factor (P_F) as the ratio between the factor sums of squares and the total sum of squares:

$$P_F = \frac{S_F}{S_T} \times 100 \tag{4. 12}$$

Applying this procedure it is possible to obtain the percent influence of the factors in the system response. In this work the factors are 11 (shown in Table 4. 3), and the response of interest are 8: 5 related with chemical behavior (CH_4 conversion, H_2 concentration, CO concentration, CO_2 concentration, CO_2 capture reaction rate), and 3 with hydrodynamics of the bed (solid fraction, bed expansion and pressure drop).

4.5 Results of combined CFD-Taguchi method

The Taguchi method have been extensively applied to industrial cases and, in the last years, it also has been combined with CFD simulations, in the phases of design and optimization of industrial processes and equipment (e.g. [392-394]). In this work, due to the uncertainties of the global system (i.e. price of CO_2, use of hydrogen, operational cost, etc…), the Taguchi method was used to understand the effect of factors in the response of the system, and not to optimize a response (i.e. hydrogen concentration). The case study plan (Table 4. 6) has been obtained combining the most important operational parameters of the ZECOMIX plant (Table 4. 3) and the L_{12} orthogonal array (Table 4. 5).

Table 4. 6 – Summary of simulation details in the L_{12} orthogonal array

Exp.	T (K)	P (at)	Diam Part (mm)	Gas velocity (m/s)	Bed Height (m)	SMR	CO2 Captu	Sorbent	Pretreat	Syngas	Drag Model
1	900	1	0,25	0,2	0,5	SMR-ON	Capt-ON	Dolomite	No	H2-Gas	Syamlal
2	900	1	0,25	0,2	0,5	SMR-OFF	Capt-OFF	Mayenite	Yes	Steam-Gas	Wang
3	900	1	0,5	0,5	0,25	SMR-ON	Capt-ON	Dolomite	Yes	Steam-Gas	Wang
4	900	7	0,25	0,5	0,25	SMR-ON	Capt-OFF	Mayenite	No	H2-Gas	Wang
5	900	7	0,5	0,2	0,25	SMR-OFF	Capt-ON	Mayenite	No	Steam-Gas	Syamlal
6	900	7	0,5	0,5	0,5	SMR-OFF	Capt-OFF	Dolomite	Yes	H2-Gas	Syamlal
7	800	1	0,5	0,5	0,5	SMR-ON	Capt-OFF	Mayenite	No	Steam-Gas	Syamlal
8	800	1	0,5	0,2	0,25	SMR-OFF	Capt-OFF	Dolomite	No	H2-Gas	Wang
9	800	1	0,25	0,5	0,25	SMR-OFF	Capt-ON	Mayenite	Yes	H2-Gas	Syamlal
10	800	7	0,5	0,2	0,5	SMR-ON	Capt-ON	Mayenite	Yes	H2-Gas	Wang
11	800	7	0,25	0,5	0,5	SMR-OFF	Capt-ON	Dolomite	No	Steam-Gas	Wang
12	800	7	0,25	0,2	0,25	SMR-ON	Capt-OFF	Dolomite	Yes	Steam-Gas	Syamlal

A 4000 cell 2D grid has been used. 12 simulations have been carried out adopting an Eulerian-Eulerian approach, with the KTGF for closure terms. Time step of URANS simulations has been fixed at 0.01s. More details about the simulation method and sub-models applied can be found in Section 4.2. The results of the numerical campaign are shown in

Table 4. 7. All values the response vector of have been averaged for 1 minute of simulation time: CH_4 conversion, H_2 concentration, CO concentration, CO_2 concentration, CO_2 capture reaction rate, solid fraction, bed expansion and pressure drop. First cycle has been simulated, so multicycling effect has not been studied. However, it can be included by the method explained in Chapter 3.

Table 4. 7 – Summary of simulation results

Experiment	CH_4 Conversion (-)	H_2 (dry molar fraction)	CO (dry molar fraction)	CO_2 (dry molar fraction)	CaO reaction rate (kmol/s)	Solids fraction (-)	Pressure Drop (Pa)	Bed Expansion (-)
1	0,975	0,979	0,006	0,013	1,28E-04	0,309	4398	1,9
2	0	0,450	0,375	0,150	0	0,324	4409	1,85
3	0,241	0,801	0,071	0,090	5,70E-04	0,29	2195	1,6
4	0,549	0,563	0,065	0,227	0	0,208	2177	2,8
5	0	0,500	0,423	0,049	1,13E-04	0,508	2488	1,2
6	0	0,333	0,221	0,122	0	0,3636	4398	1,6
7	0*	0,443	0,248	0,249	0	0,443	4406	1,3
8	0	0,333	0,221	0,122	0	0,427	2168	1,3
9	0	0,389	0,251	0	2,27E-05	0,212	2279	2,8
10	0,994	0,854	0,078	0,067	6,33E-04	0,447	4448	1,3
11	0	0,525	0,445	0	3,76E-04	0,214	5372	2,7
12	0*	0,444	0,247	0,250	0	0,312	2297	2

*Normalized conversion

4.5.1 Hydrogen concentration

The concentration of hydrogen strongly depends on the presence of catalyst and sorbent (see Figure 4. 20). This result corroborates the sensitivity study done in section 4.2.2. Without catalyst, SMR reaction cannot take place and equilibrium concentration of hydrogen is enhanced by the presence of sorbent. Thus it is reasonable that the two main factors that affect in higher degree hydrogen concentration are SMR-ON and Capture-ON, increasing the concentration when catalyst and sorbent work simultaneously.

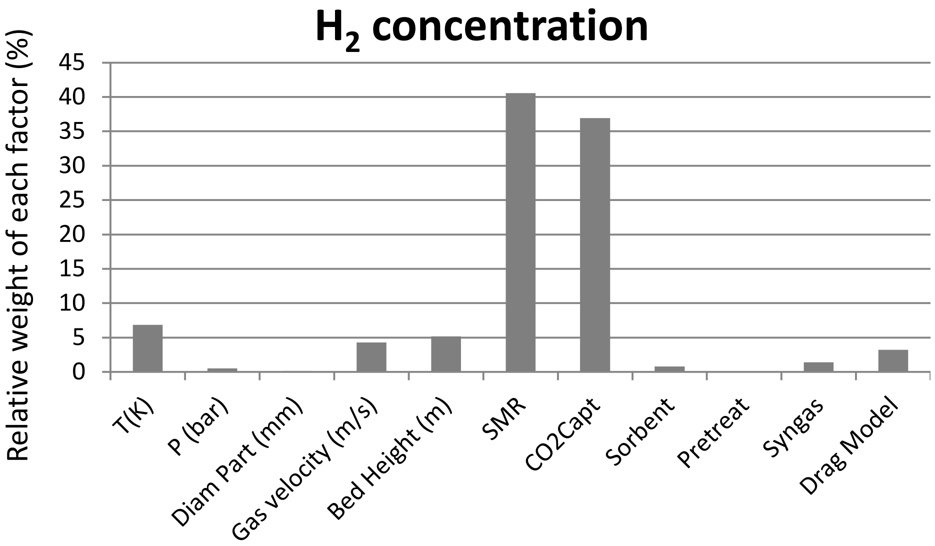

Figure 4. 20 – Influence of operational parameters in hydrogen concentration

In Figure 4. 21 is presented the detail of the lower influent parameters in the hydrogen concentration. As the sensitive analysis demonstrated, the model is very sensitive to the temperature, and H_2 concentration increases with temperature. On the other hand, hydrodynamics of the system also affects the reaction rate. Hydrogen increases with residence time. When the time of contact between gas and solids increases, conversion to H_2 also increases. Thus, gas velocity and bed height are relevant parameters. When bed height increases and gas velocity decreases, hydrogen formation performance is improved. It is also important to note the effect of drag model. Since Modified Wang model improves the mixing of solids, this effect produces an increase in the concentration of hydrogen.

CO_2 capture reaction depends on the sorbent selected and its activation treatment. However, the influence of these factors in hydrogen concentration is practically negligible. This result is very important because if hydrogen concentration is independent of sorbent kinetics, other parameter as regenerability or mechanical resistance drive the choice of the most suitable sorbent for SE-SMR process. The effect of pressure is small in SMR and CO_2 capture reaction kinetics, thus the effect in hydrogen concentrations is also small. The other factors studied are almost negligible in the hydrogen concentration response.

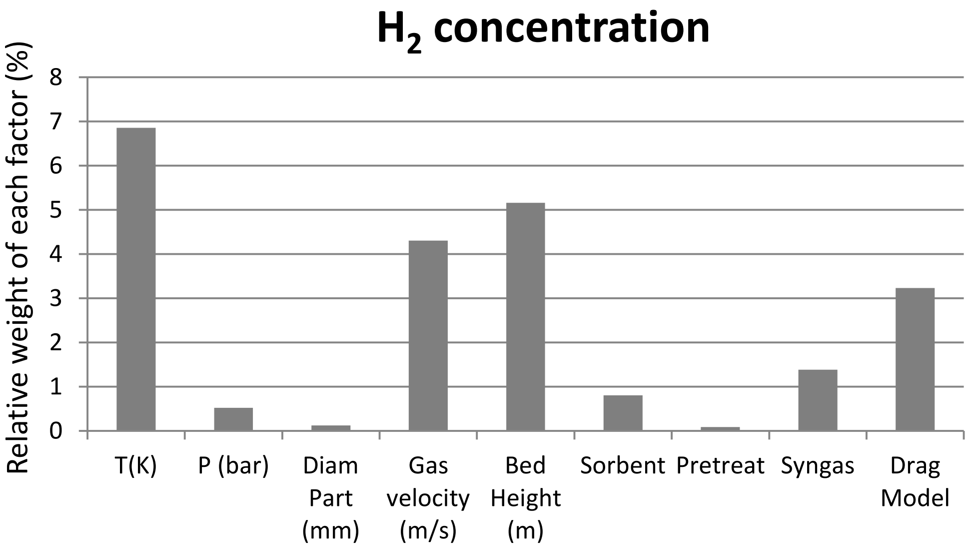

Figure 4. 21 – Influence of less influential operational parameters in hydrogen concentration

4.5.2 Methane conversion

Figure 4. 22 summarizes the relative weight of each variable in methane conversion response. It is possible to note that the main parameters affecting the CH_4 conversion are the syngas composition, the presence of sorbent, temperature and drag model. The syngas from hydrogasification increases strongly the methane conversions, due to the fact that the kinetics is strongly dependent on the CH_4 concentration. In cases 7 and 12, where SMR are considered but sorbent is not present, at 800K, due to the presence of a very low concentration of methane, a low negative values of conversion were obtained. This “negative conversion” is due to the combined low temperature and close-to-equilibrium methane concentration which promotes the effect of reverse reactions. This negative effect is also observed in the case 3, where low

concentration (but higher temperature) produces a very low concentration. These two experiments were discarded from the analysis. The direct effect of reducing the experiments in the analysis of methane conversion is that response is not sensitive to the presence of catalyst, which is not correct.

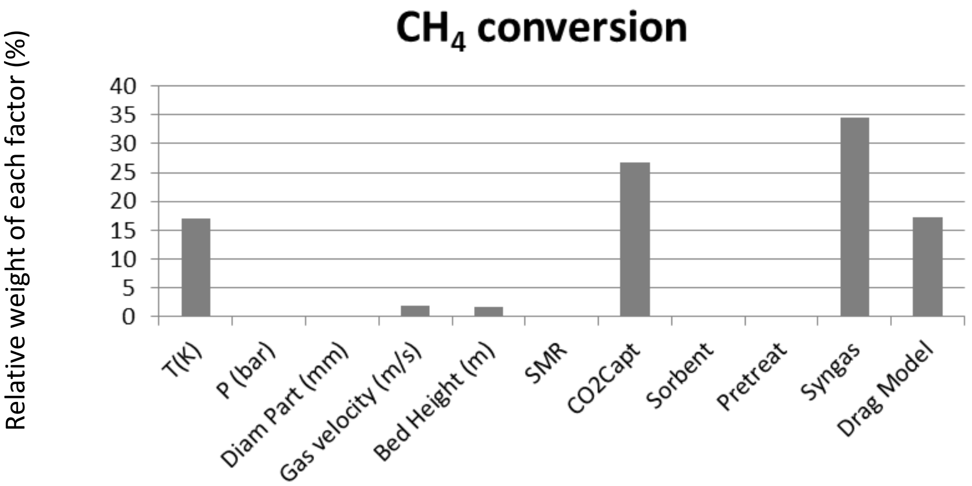

Figure 4. 22 – Influence of operational parameters in methane conversion

By normalizing the influence of the response to all experiments except the gasification SMR cases (3,7,12), the response is modified. As shown in Figure 4. 23(denoted as “Only SE-SMR”), the conversion of methane mainly depends on the presence of catalyst. The presence of sorbent and syngas composition are not influential due to the normalization of the cases.

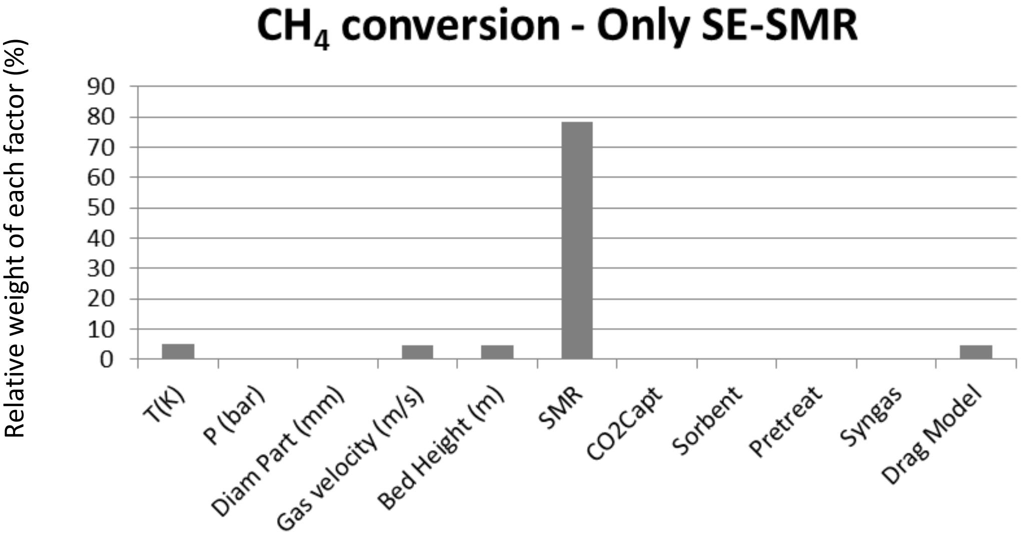

Figure 4. 23 – Influence of operational parameters in methane conversion, normalized for only SE-SMR experiments

This response study is a good example of the sensitivity of the Taguchi model to the experiments realized. In a larger campaign the experiments rejected should have a lower weight, and, in global terms, the variation of methane specie is lower than 2%. Thus, the effect of this error can be considered negligible on the global response of the system and on the other responses studied. Moreover, it is necessary that the user is experimented with the case study in order to evaluate the validity of results.

In any case, it is worth to note as, for both analysis (with and without low concentration CH_4 SMR cases) Methane conversion increases with temperature, Modified Wang drag model, gas velocity and bed height. The effect of residence time (that depends on gas velocity and bed height) and the mixing of the bed (as noted in section 4.2.2) are observed in any case.

However, due to the limitations of application of Taguchi method to the results obtained, a complementary campaign should be carried out in order to evaluate with more precision the optimal operation range, in terms of temperature and minimum methane concentration in gases.

4.5.3 CO and CO_2 concentration

Steam methane reforming reactions (to CO and CO_2, R.1-Eq. 4.3 and R.2-4.4) are competitive, as explained in the section 4.2.2. CO and CO_2 concentrations mainly depends on the presence of catalyst and sorbent. SMR-ON and CO_2-capture-ON parameters increase the conversion to hydrogen, reducing the presence of CO and CO_2.

CO concentration depends on the kinetics of SMR reaction. Thus, the presence of catalyst and the concentration of CO in the syngas affect the reaction rate. In the cases of steam gasification and hydrogasification syngases, the concentration of CO varies strongly from 30 to 8.5% and CH_4 from 2 to 12.4%. Hence, it is possible to understand the influence of syngas in the formation of carbon oxides. Moreover, the presence of CO_2 sorbent directly affects the concentration of CO_2. Thus, the relative weight of main operational parameters presents a reasonable trend (Figure 4. 24).

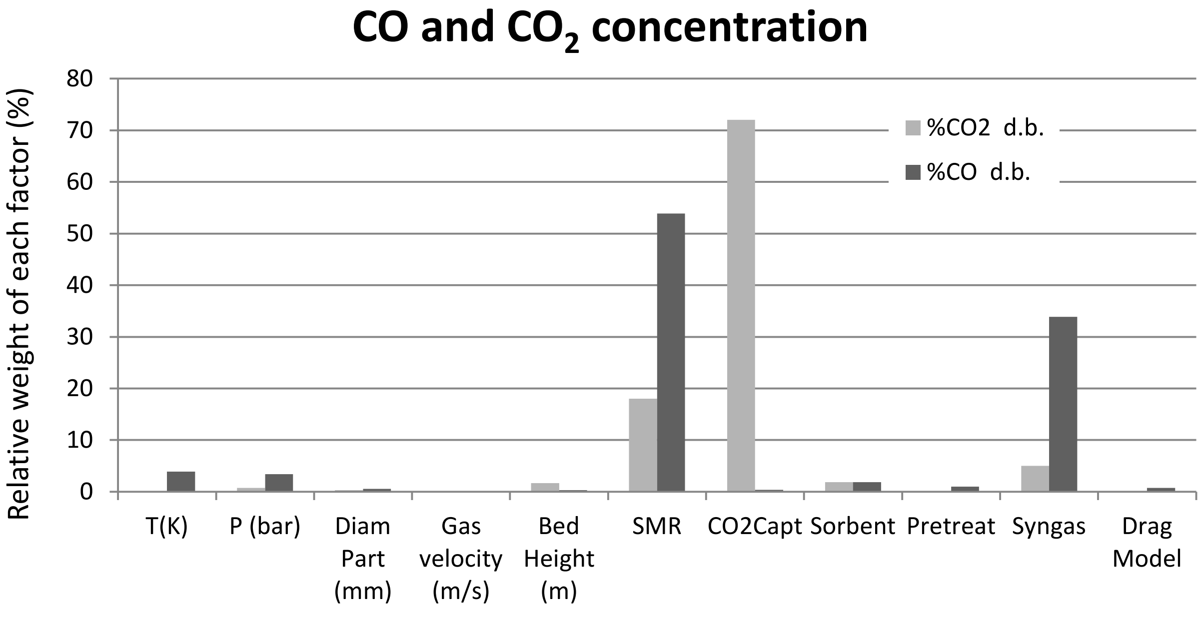

Figure 4. 24 – Influence of operational parameters in CO and CO_2 concentration

Figure 4. 25 summarizes the effect of less influential parameters. It is worth to note as temperature and pressure affects to SMR reaction, and consequently, to the CO concentration a higher degree than CO_2 concentration. CO_2 capture kinetics depends on the nature of sorbent and equilibrium pressure. Thus these two parameters have a greater influence than the other less relevant ones.

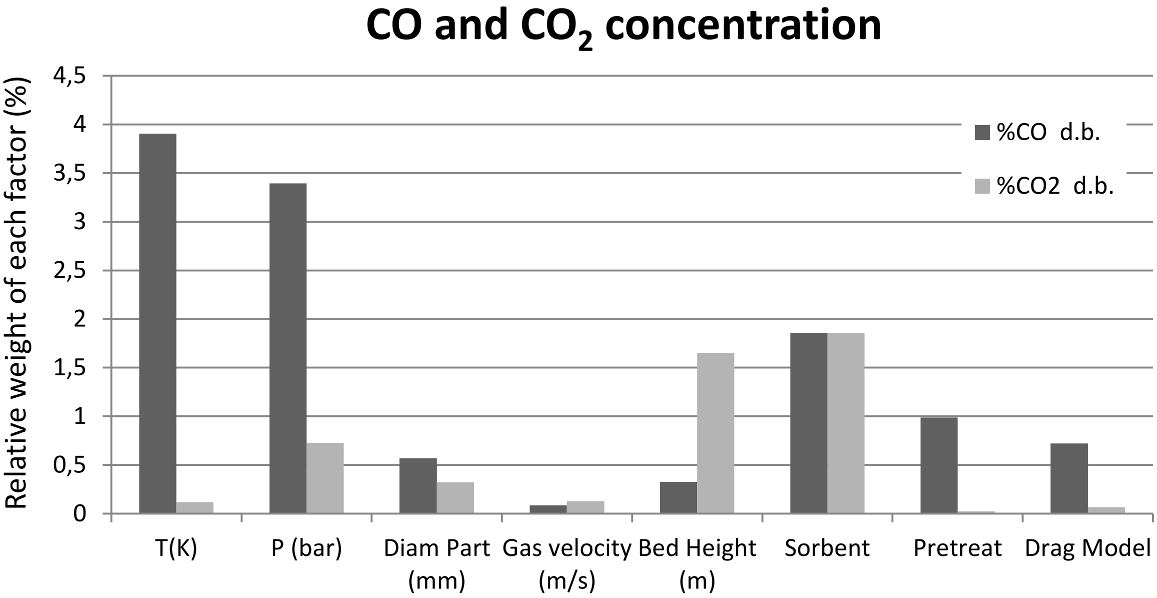

Figure 4. 25 – Influence of less influential parameters in CO and CO_2 concentration

4.5.4 CO_2 capture rate

The most influential parameter in CO_2 capture rate is, obviously, the presence of sorbent (Figure 4. 26). Thus the relative weight of this parameter is higher compared with the other. However, CO_2 capture rate have been averaged for the entire reactor, independently of the bed behavior. For this reason, the low relative value of weight of sorbent presence suggests some interaction with hydrodynamic parameter, characterized by the large weight of drag model.

The other parameters affecting CO_2 capture rate are both, kinetic and hydrodynamic. Hydrodynamics affects carbonation reaction more than kinetics, as demonstrated the high relative weight of drag model and particle diameter. These two parameters, with gas velocity, define the mixing regime in the bed. Kinetic parameters influence carbonation reaction rate in two ways. On one hand reaction rate is function of CO_2 (which depends on pressure and SMR/syngas composition). On the other hand, reaction rate increases if sorbent is pre-treated.

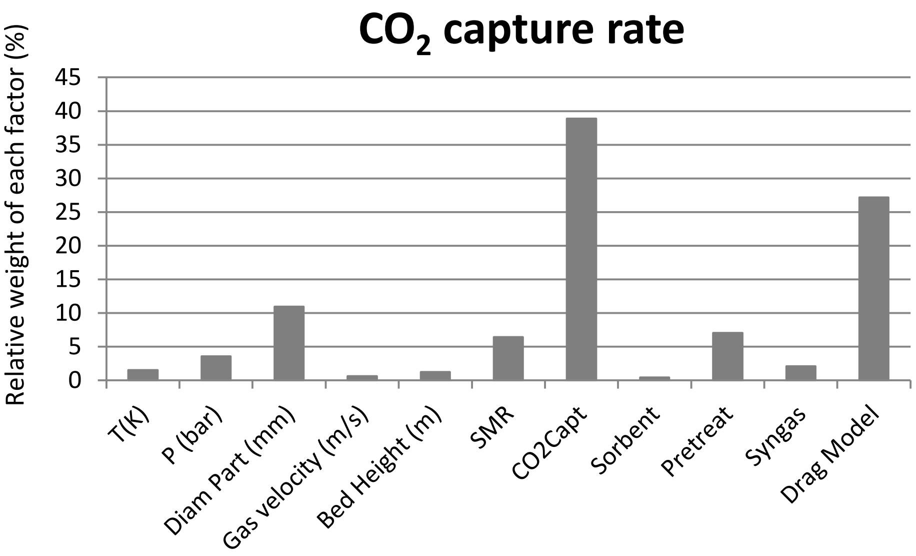

Figure 4. 26 – Influence of operational parameters in CO_2 capture rate.

4.5.5 Bed porosity, bed expansion and pressure drop

Bed porosity, bed expansion and pressure drop are the key parameters that define globally the bed hydrodynamics. Pressure drop mainly depends on the initial bed height. Pressure drop increases linearly with dense bed height. Simulations corroborate this fact. In the case of initial bed height of 0.25 m pressure drop is ~2200 Pa. When bed height is doubled (h=0.5m), and all the other conditions remains fixed, pressure drop is also doubled (~4400 Pa). The relative weight of the initial static bed height contributes for the 95% to the variation of the response, surpassing the contribution of all the other parameters, almost negligible. Thus, this fact also evidences the sensitivity of Taguchi method to the magnitude order of the response parameter compared with the zero/reference cases included in the orthogonal array.

Bed expansion and porosity are intrinsically correlated [234, 308], and, according with Ergun equation mainly depends on particle diameter and gas velocity. This dependence is observed in the simulations and corroborated in the parameter influence plot (Figure 4. 27).

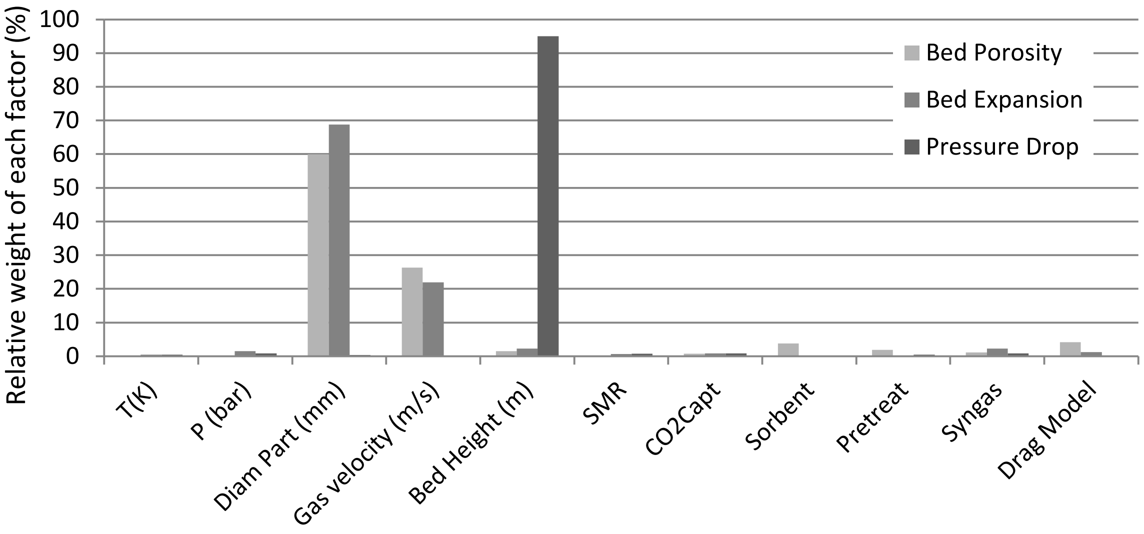

Figure 4. 27 – Influence of operational parameters in bed porosity, bed expansion and pressure drop

Density of gas depends on the composition of the gas, as well as on the temperature. Sorbent density varies when carbonation reaction takes place. Due to the reaction rate is different for dolomite and mayenite, the change in density is also different. This change in density of gas and solid affects bed porosity, bed expansion and pressure drop, as shown in Figure 4. 28. Moreover, the effect of drag model in the bed mixing mainly affects to the bed porosity, than to the other bed hydrodynamics responses.

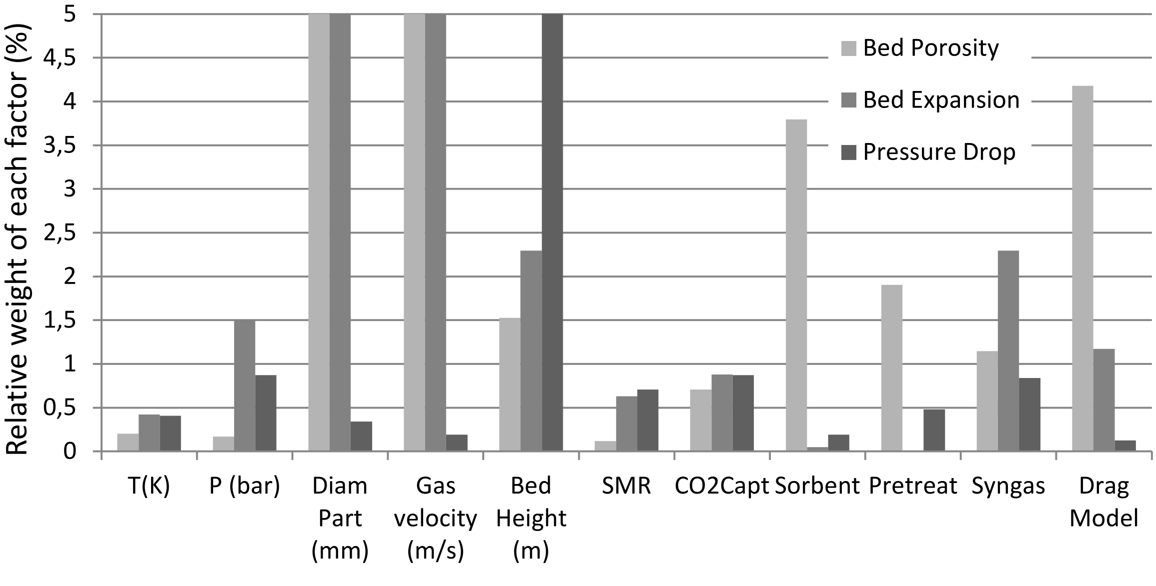

Figure 4. 28 – Influence of less influential operational parameters in bed porosity, bed expansion and pressure drop

4.5.6 Summary of influence of parameters

Figure 4. 29 summarizes the effect of each parameter in the response of the system. Positive values represent an increase in the response compared with the other level of the same factor. And negative, a decrease compared with the other level. For example, at 900K there is an increase in the concentration of hydrogen and a decrease in the pressure drop, with respect to the 800K case. However, the relative weight of each factor in the response is very different, as explained in previous sections. It is worth to note that the percentage is not a relative increase or decrease of the response, but it is the relative influence with respect to the other factors in the response.

Therefore, with a look to previous sections and to the Figure 4. 29, it is possible to find the trends of optimum operational conditions. For example, a higher H_2 concentration is obtained at 900K, P=1atm, particle diameter = 0.25mm, gas velocity =0.2m/s, static bed height = 0.5m, with catalyst and sorbent (SMR and CO_2Capt – ON), with no-pretreated dolomite, using hydrogasification syngas; compared with the other level factors. However, the most important parameters are the presence of catalyst and sorbent, in a long bed at 900K. Hence, if it is more convenient to operate a higher particle diameter with pretreated mayenite, in order to obtain a high CO_2 capture, the effect of these factors in hydrogen production will be very low.

Taguchi method serves to discriminate the factors of importance, as a framework for a subsequent optimization.

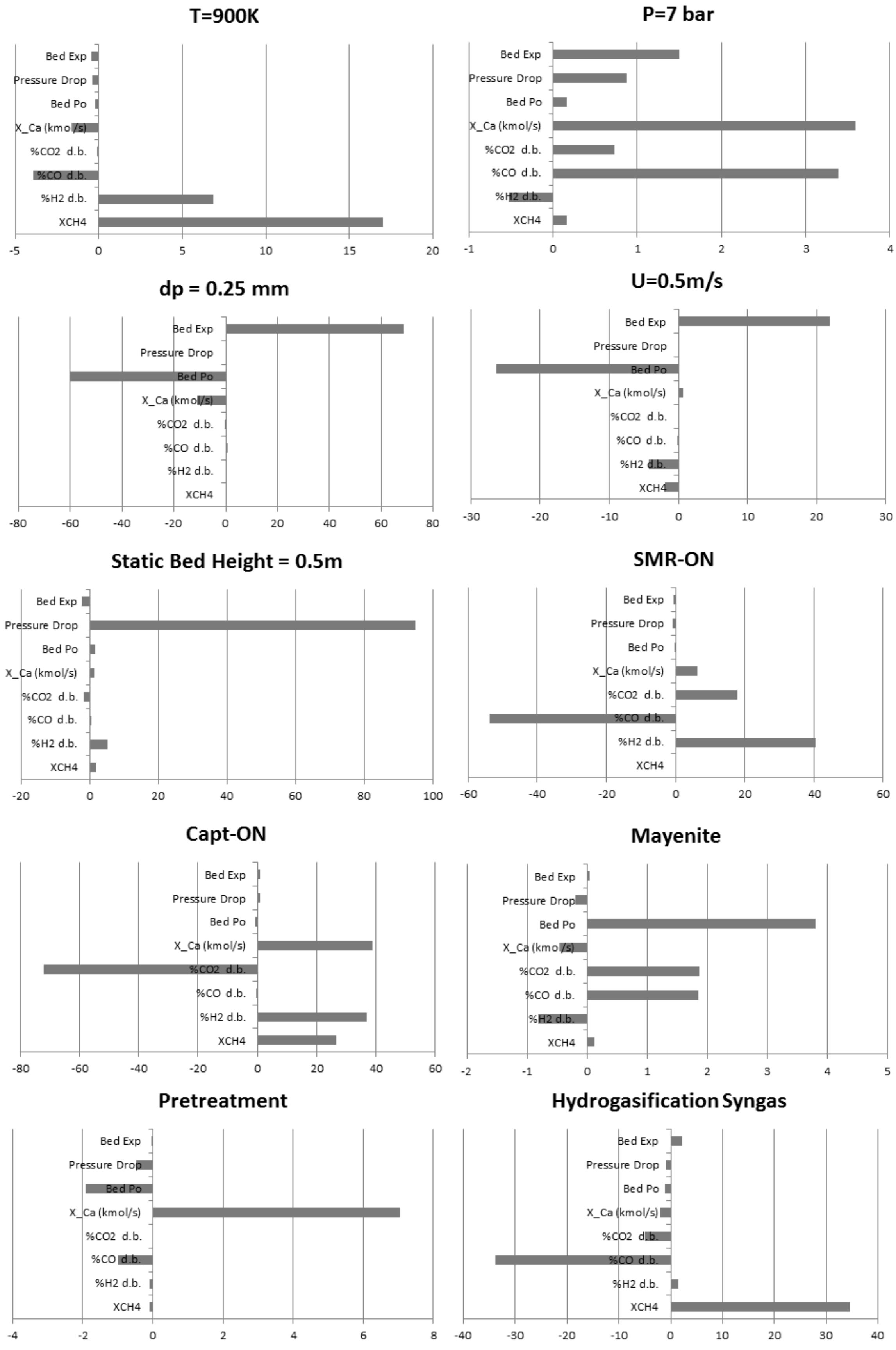

Figure 4. 29 – Summary of influence of operational parameters. Scale is relative weight in response (-)

4.6 Summary and conclusions

This chapter is focused on the simulation of the SE-SMR reactor at semi-industrial scale. The model developed in the previous chapters has been implemented in a coarse grid case, in order to obtain accurate results, with the lowest computational cost possible. The simulations have been validated with literature data under SE-SMR conditions, and subsequently a CFD-Taguchi approach has been adopted in order to validate the ZECOMIX reactor under real conditions.

CFD simulations have been used successfully to scale-up Geldart B bubbling fluidized beds. In this work, we have realized the scale-up to a 1m diameter BFB, with a coarse grid. Firstly we realized grid-independence and time-step-independence studies, obtaining a good performance with a 4000 cells and a 0.01s time step.

Subsequently, a study of sensitivity of the model has been carried out. The behaviour of the system has been evaluated taking into account the presence of sorbent and catalyst (SE-SMR) and the reaction of steam methane reforming without capture (SMR). The trends observed are consequent with literature data, and very close to equilibrium conditions. Moreover, we have corroborated the competence between reforming reactions as a function of temperature and in presence of sorbent.

Additionally, the simulations have demonstrated to be very sensitive to the drag model. At laboratory scale, no strong differences were observed between the Fluent-default Symalal-O’Brien and the Modified-Wang drag models. At semi-industrial scale, similar behaviours have been obtained in the averaged parameters of fluidization with both models. However, increasing the cell-size, very important differences have been observed in the transient pressure fluctuations. On one hand, the Modified-Wang model presents a realistic pseudo-periodic pattern with pressure amplitude according with multiple bubble regime. On the other hand, the Syamal-O’Brien model predicts a periodic pattern, which corresponds to an unrealistic little amplitude single bubble regime.

The ZECOMIX project has undergone several changes from their concept stage to the experimental phase. In order to simulate the ZECOMIX reactor, under realistic conditions, and predict the different stages of the project, a Robust Design of Experiments have been carried out, according to the Taguchi method.

This method provides gathered extensive information about uncertainties of the process, with a minimum number of experiments and the correct statistic treatment of the data. Thus, instead of the limitations of the model, a map of operational windows has been obtained, with particular interest in the influence of each factor in the response of the system. CH_4 conversion, H_2 concentration, CO concentration, CO_2 concentration, CO_2 capture reaction rate, solid fraction, bed expansion and pressure drop have been studied as function of temperature, pressure, particle diameter, gas velocity, static bed height, presence of catalyst, presence of sorbent (dolomite and mayenite, pretreated and no-pretreated), different syngas composition and drag model. Results obtained are reasonable with theory and the effect of the parameters was well predicted.

5 SUMMARY AND CONCLUSIONS

Numerical simulations of a semi-industrial bubbling fluidized bed SE-SMR reactor have been successfully carried out. CFD simulations have been completed applying an Eulerian-Eulerian approach, also known as two fluid modeling both phases are treated as inter-penetrating continua. The solid phase stresses are modeled using kinetic theory of granular flow (KTGF).

The complete CFD model includes three sub-models in order to increase the accuracy of the solution. Firstly, a kinetic scheme and the corresponding rate models of catalytic heterogeneous steam methane reforming. Secondly, a CO_2 capture grain model for carbonation reaction with CaO-based solid sorbents. Thirdly, sub-grid drag model for coarse grid simulations. These models allow to obtain detailed simulations of semi-industrial BFB, with a relative computational low cost.

An extensive experimental campaign in TGA has been carried out in order to characterize two CaO-based CO_2 sorbents at high temperature. A natural sorbent (Dolomite) and a synthetic (CaO - $Ca_{12}Al_{14}O_{33}$) sorbent have been characterized, and their chemical behavior modeled.

The complete model has been implemented in a commercial CFD code. Laboratory scale SE-SMR simulations have been compared with literature data with good agreement. Subsequently, the system has been scaled up to a semi-industrial system.

Finally, a multi-criteria analysis (based in a robust Design of Experiments) has been developed in order to evaluate the effect of several operative parameters in the operation of an experimental 400 kW_{th} syngas SE-SMR plant.

5.1 Solid sorbents for high temperature CO_2 capture

The most suitable solids sorbents for CO_2 at high temperature (600ºC) are based in CaO. In this work two different sorbents have been evaluated.

On one hand a natural sorbent was tested. Natural sorbents (Dolomite) show suitable properties, are broadly available and have low cost. However, they suffer a decay in the CO_2 carrying capacity along cycles. In order to offset the activity losses of dolomite with cycling a novel calcination method is proposed.

The “triggered calcination” consists in a two-step calcination. From room temperature to 900ºC and in a subsequent isothermal treatment for few minutes at 900ºC, the sorbent is exposed at a high concentrated CO_2 atmosphere. These conditions inhibit the calcination of the sorbent. After isothermal treatment, atmosphere concentration is switched to pure N_2, producing a kind of flash calcination. This process produces a stable internal structure, which increases carrying capacity (until 44% for 150 cycles) of the sorbent. This pre-treatment can be easily implemented in a CO_2 capture plant, and is less energy intensive than other pre-treatments.

On the other hand, a manufactured sorbent (CaO - $Ca_{12}Al_{14}O_{33}$, mayenite) has been synthetized and tested. This type of sorbents presents a higher stability than natural ones, and, a higher cost. A modification to the “classical” synthesis route is proposed in this work. During the synthesis process, an intermediate water precursor has been added, improving the stability of the sorbent. Two different concentrations of CaO have been studied in this work (75 and 85%).

Unexpected results have been obtained. The sorbent with a lower quantity of CaO (75%) presents a higher carrying capacity than the other with 85% CaO, under industrial conditions. Moreover, a continuous increase in the carrying capacity has been obtained with cycling (called “self-activation”) if sorbent is exposed a thermal treatment at high temperature for the first calcination.

In addition, a method for estimating kinetic parameters and specific surface area has been developed. By means of TGA experiments, the variation of reaction rate with cycling has been obtained and correlated with specific surface of the particles. The method proves to be a very powerful tool to predict the internal structure of the particle.

5.2 CFD modeling of a Sorption Enhanced - Steam Methane Reforming reactor

A CFD Eulerian-Eulerian model with KTGF for the closure of solid gas has been adopted to simulate the hydrodynamic behaviour of a BFB. An extensive simulation campaign has been carried out in order to characterize the submodels that predict more accurately the fluid-dynamical patterns of a lab scale BFB reactor.

Some improvements have been implemented in a commercial CFD code in order to predict realistically the reactions involved in the SE-SMR process. Two main reactions are involved simultaneously in this process: Steam Methane Reforming and CO_2 capture.

On the one hand, the widely used Xu and Froment [286] kinetic scheme have been chosen for SMR reaction. On the other hand, the Stendardo and Foscolo [138] grain model has been modified to predict the CO_2 capture reaction for different sorbents and pretreatments. Initially, the model was developed for calcined dolomite. With the changes proposed this model has been extended for dolomite calcined with the triggered method, as well to mayenite untreated and pre-teated. In addition the model is able to predict multicycling behavior of sorbents. The modified model has been validated with experimental data.

In addition, the choice of a correct drag model has been proved crucial for the hydrodynamic behavior of the BFB. Hence, a new sub-grid drag model has been implemented in order to improve the resolution of the model in coarse grids, appropriate for simulation of large-scale equipment.

The global model has been used to simulate under different operational conditions, a laboratory scale SE-SMR case. The results present good agreement with literature data. Numerical simulations demonstrated that CO_2 capture is the kinetic limiting step of the SE-SMR reaction. Moreover, the presence of fast bubbles in the bed reduces the performance of the reactor, compared with more homogenous beds. In addition, the detailed simulation of perforated plate distributor improves significantly the hydrodynamic behavior patterns.

5.3 Numerical simulation of the SE-SMR reactor in ZECOMIX plant

Zero Emission Coal MIXed (ZECOMIX) project is a $100kW_e$ ENEA's pilot plant designed in order to testing experimentally a novel CO_2 pre-combustion method. The aim of the project is to demonstrate at semi-industrial size the production of hydrogen and electricity from coal.

CFD simulations have been used to simulate the semi-industrial SE-SMR reactor of ZECOMIX plant. In order to reduce the computational cost, a coarse-grid has been selected to simulate the reactor. A grid-independence and a time-step-independence studies have been carried out to obtain independent results in a coarse grid. An optimum cell size of 5x5 cm has been obtained, with a relative very low computational cost. With this grid size, the predicted values appear to be satisfactory considering the complexity of the simulations.

A sensitivity analysis of the model has been completed. Temperature has been proved the key parameter in the SE-SMR chemical process at large scale. Moreover, the presence of sorbent increases the production of hydrogen, obtaining a decarbonized syngas with a 97% (dry basis) of hydrogen.

Some important results of this sensitivity analysis have been observed. Under the studied SMR and SE-SMR conditions, reactor achieves equilibrium. Species concentration distribution across the bed presents two different slopes correspondent to different dominant reactions. When methane concentration is high, SMR reaction dominates. This reaction is faster than CO_2 capture, which dominates the second part of the reaction. Thus, slope of species distribution is steeper in the SMR dominant zone, than in carbonation-dominanted zone. In addition, the two reforming reactions have been demonstrated to be competitive. R2 (reforming to CO_2) is enhanced by carbonation reaction, producing a strong reduction in the R1 (reforming to CO) reaction rate. Moreover, R1 is most sensitive to temperature than R2.

In addition, the patterns obtained with different drag models have been compared. Very important differences have been observed in the transient pressure fluctuations. The Modified-Wang model presents a realistic pseudo-periodic pattern with pressure amplitude according with multiple-bubble regime. Meanwhile, the Syamal-O'Brien model predicts a periodic pattern, which corresponds to an unrealistic low amplitude single bubble regime. This improvement in the simulations is crucial for the correct predictions of mixing pattern in fluidized beds.

Some modifications of original ZECOMIX project have been realized during the projection and erection of the pilot plant. In order to evaluate the effect of these modifications in the system response, a Robust Design of Experiments, proposed by Taguchi, has been carried out.

Taguchi method is a very powerful in order to evaluate simultaneously the effect of multiple variables in the response of the system. This method has been combined with CFD simulation in order to obtain a multi-criteria analysis of the real ZECOMIX carbonator reactor.

The highlights observed with this method are:

- The presence of a sorbent is required to obtain a rich-hydrogen decarbonized syngas. Without sorbent presence, hydrogen concentration in equilibrium is lower, other undesired species are produced, and isothermicity of the process is not achieved.

- The system response is practically independent of the type sorbent. Thus the synthetic sorbent, in spite of their slower kinetics, presents a good behavior. Hence, its use is recommended due to its better multi-cycling regenerability than dolomite.

- Temperature operation must be close to 900K. At lower temperatures reforming reaction rate decays, and in the case of SMR, without sorbents the methane conversion is unacceptable.

- High concentrations of CH_4 are required. If methane concentration in the syngas is very low, undesired reverse reaction could take place, particularly at low temperatures and if sorbent is not presented.

- Drag model influences strongly hydrodynamics. The new model produces a more realistic pseudo-periodic pattern which improves gas-solid mixing, with an increase in the reactivity of the system.

The other hydrodynamic and chemical responses studied are compatible with theoretical predictions.

5.4 Sulcis coal hydrogasification

The detailed characterization of hydrogasification of Sulcis coal is out of the main aims of this thesis. However, some improvements in the understanding of kinetics of devolatilization of the coal have been achieved.

In order to model devolatilization step, some global models have been applied to thermogravimetric (TGA) tests in order to characterize kinetics of Sulcis coal devolatilization. Due to the important influence of secondary pyrolysis in this coal, there is not a global model capable to reproduce very accurately the complete devolatilization process.

Thus, a novel 2-Distributed Activation Energy Model (2-DAEM) has been developed in order to model the coal devolatilization. This model presents very good predictions for Sulcis coal and it has been successful tested for different coal and biomasses.

5.5 Perspectives for future work

The objectives of the research have been satisfactory accomplished, but several issues for further investigations remain open. Some of them are related to the experimental limitations of the case-study facilities, but others are also concerning the modelling considerations.

Solid sorbents for high temperature CO2 capture

Solids sorbents and pre-treatments have been evaluated in TGA conditions. Therfore, experiments in fluidized bed must be carried out in order to study the behaviour of sorbents under real conditions. Particularly, mechanical studies must be carried out in order to evaluate the effect of treatments in the resistance to the attrition. Moreover, intra- and extra-particle mass transfer effects are different in the TGA experiments and in BFB.

CFD modeling of SE-SMR reactor

The model presents some assumptions that can be improved in further works. Kinetic model of SMR is based in literature data, but in the experimental case, the catalyst must be different. Thus a detailed model of SMR should be applied for the specific catalyst. Diffusional effect has been neglected in the CO_2 capture model, and could be implemented.

CFD Two Fluid Model is very powerful to simulate the BFB. However, it is recommended for further work to include two different phases for catalyst and sorbents. Moreover, an attrition model and a particle size distribution function would increase the accuracy of the solutions.

An analogous numerical campaign should be very interesting in order to cover the complete CFD approaches. This campaign should include 3D simulations, detailed distributor simulations, and other CFD approaches, such as Discrete Element Model simulations.

A refined Taguchi method should include interactions, signal/noise external effects and optimization studies, to optimize the system.

In any case, the most important further work is to validate with experimental data the semi-industrial simulations. Depending of the results of the ZECOMIX plant (when it will be operated), the model surely will need modifications.

6 CONCLUSIONES

En esta tesis se ha llevado a cabo una extensa campaña de simulaciones numéricas para la caracterización de un reactor semi-industrial de reformado de metano mejorado con adsorción (SE-SMR). Las simulaciones CFD han sido desarrolladas aplicando una aproximación Euleriana-Euleriana (E-E) para las fases gaseosa y sólida considerándolas como dos fluidos miscibles. Las propiedades de la fase sólida se calcularon mediante la Teoría Cinética de Flujo Granular (KTGF).

Al modelo CFD se han incorporado tres submodelos con el objetico de aumentar la precisión de las simulaciones. En primer lugar, se ha implementado un modelo de catálisis heterogénea, y su correspondiente esquema cinético, para el reformado de metano. En segundo lugar, para la captura de CO_2, un modelo a grano ha sido modificado para incluir diferentes sorbentes y pretratamientos. Finalmente, se ha desarrollado un modelo de arrastre de partículas para mallas gruesas. La incorporación de estos submodelos permite la simulación del reactor en lecho fluido burbujeante (LFB) a escala semi-industrial, con un alto grado de precisión y bajo coste computacional respecto a los métodos de simulación actuales.

Se ha llevado a cabo una extensa campaña experimental en termobalanza (TGA) con el objetivo de analizar dos sorbentes a base de CaO. Un sorbente natural (Dolomita) y uno sintético (CaO- $Ca_{12}Al_{14}O_{33}$) han sido caracterizados, y su comportamiento químico ha sido modelado.

El modelo completo ha sido implementado en un código CFD comercial. Se han llevado a cabo una serie exhaustiva de simulaciones a escala de laboratorio para evaluar el comportamiento del sistema y validar el modelo. Las simulaciones han presentado una buena concordancia con datos de literatura.

Una vez validado el modelo a escala de laboratorio se ha procedido a un escalado a talla semi-industrial. Un Diseño de Experimentos robusto ha sido combinado con las simulaciones CFD para proceder a un análisis multicriterio del comportamiento de un reactor experimental de 400 kW_t, para el reformado de gas de síntesis mediante SE-SMR.

6.1 Sorbentes sólidos para la captura de CO_2 a alta temperatura

Los sorbentes sólidos basados en óxido de calcio (CaO) son considerados los más adecuados para la captura de CO_2 a alta temperatura (600ºC). En este trabajo se han estudiado dos sorbentes.

Inicialmente se estudió un tipo de dolomita, como ejemplo de sorbente natural. Los sorbentes naturales presenta unas propiedades adecuadas para la captura, son ampliamente disponibles y tienen un coste bajo. Sin embargo, sufren una notable pérdida de capacidad de sorción con el paso de los ciclos de carbonatación/calcinación. Para paliar esta reducción en el rendimiento de captura, se ha desarrollado un nuevo pretratamiento de la dolomita.

Este tratamiento llamado "triggered calcination" consiste en una calcinación del sorbente en dos etapas. Durante la primera etapa, las partículas son calentadas desde temperatura ambiente hasta 900ºC en un atmosfera rica en CO_2. La presencia de altas concentraciones de dióxido de carbono inhibe la reacción de calcinación. Después de someter a un proceso isotermo a 900ºC bajo esta atmosfera de CO_2, súbitamente se cambia la concentración del gas a nitrógeno. Este cambio produce una calcinación instantánea del carbonato de calcio. Este proceso produce una estructura con una alta estabilidad y una apropiada porosidad y superficie especifica, que permite al sorbente aumentar sensiblemente su capacidad de captura (hasta en un 44% en experimentos de 150 ciclos). Además este tratamiento presenta las ventajas de ser fácilmente implementable en una planta industrial, y de ser menos intensivo energéticamente que otros pretratamientos propuestos en literatura.

En contraposición a los sorbentes naturales, un sorbente artificial (CaO- $Ca_{12}Al_{14}O_{33,}$ óxido de calcio soportado sobre mayenita) se ha sintetizado y caracterizado en TGA. Este tipo de materiales presenta un coste mayor que los naturales, pero una mayor estabilidad química y mecánica. Una modificación a la ruta de síntesis se ha propuesto en este trabajo. Durante el proceso de síntesis, se ha añadido una etapa intermedia de hidratación. La posterior evaporación de la humedad añadida mejora sensiblemente la estabilidad estructural en el interior de la partícula. Dos cantidades diferentes de CaO han sido estudiadas en este sorbente (75 y 85% de CaO).

Durante la campaña de caracterización del sorbente se han observado varios resultados inesperados. Por una parte, el sorbente con una menor cantidad de CaO (75%) presenta una mayor capacidad de captura que aquel con 85%, bajo condiciones industriales de carbonatación/calcinación. Este efecto es debido a que, al tener una mayor cantidad de soporte (Ca12Al14O33), se previene el bloqueo de los poros por la sinterización entre granos de CaCO3 durante la carbonatación. Por otra parte, se ha observado un aumento continuo en la capacidad de captura con el aumento de los ciclos si el sorbente se expone a un tratamiento térmico a alta temperatura durante la primera calcinación. Este proceso, recibe el nombre de "autoactivación" (o "self-activation" en inglés).

Finalmente, se ha desarrollado un método para la estimación de parámetros cinéticos y del área superficial de los sorbentes. A partir de los datos de TGA es posible estimar la variación de la velocidad de carbonatación (durante la fase en que los efectos difusionales son despreciables) con el avance de los ciclos, y correlacionar los parámetros cinéticos con la superficie específica de las partículas. Este método ha demostrado ser una herramienta muy útil para predecir la estructura interna de las partículas.

6.2 Modelado CFD del reactor de reformado de metano mejorado con sorción

Un modelo E-E con KTGF para el cierre de las ecuaciones de continuidad de la fase sólida ha sido utilizado para simulara la hidrodinámica de un LFB. Una exhaustiva campaña de simulaciones ha sido llevada a cabo para definir los submodelos que predicen con mayor precisión los patrones fluidodinámicos de un LFB a escala de laboratorio.

Varias mejoras han sido implementadas en un código CFD comercial para predecir de modo realista las reacciones involucradas en el proceso de SE-SMR. Fundamentalmente dos tipos de reaccione heterogéneas tienen lugar simultáneamente: reformado de metano y captura de CO_2.

El reformado de metano con vapor es una reacción catalítica heterogénea ampliamente estudiada por su interés industrial. El esquema cinético propuesto por Xu y Froment [286] ha sido seleccionado en este trabajo ya que ha sido ampliamente aceptado a nivel internacional. Por otro lado, el modelo a grano propuesto por Stendardo y Foscolo [138] ha sido elegido para modelar la reacción de captura de CO_2. Este modelo fue desarrollado originalmente para predecir la respuesta de la dolomita, calcinada en condiciones estándar, durante la carbonatación y a lo largo de los ciclos. Varias modificaciones en los parámetros del modelo han sido propuestas para extender la validez del mismo a diferentes sorbentes (dolomita y mayenita) y tratamientos de activación (“triggered calcination” o “self-activation”). Este modelo modificado ha sido correctamente validado con datos experimentales.

Mediante los análisis hidrodinámicos preliminares, la elección de un correcto modelo de arrastre se ha mostrado crucial para la correcta simulación del LFB. Por lo tanto se ha modificado e implementado un modelo propuesto en literatura [279]. Este modelo permite la mejora de las predicciones del comportamiento fluidodinámico en los casos de utilizar mallas gruesas. El uso de mallas gruesas genera una pérdida de detalle en las simulaciones, pero está justificado para reducir los esfuerzos computacionales en simulaciones de equipos a escalas mayores que las de laboratorio.

El modelo completo ha sido utilizado para simular un reactor de SE-SMR a escala de laboratorio, bajo diversas condiciones operativas. Los resultados obtenidos concuerdan correctamente con valores de literatura. Las simulaciones demostraron que la reacción limitante en el proceso de SE-SMR es la captura de CO_2. Por otra parte, las simulaciones corroboraron que la presencia de burbujas veloces reduce la eficiencia del reactor, comparada con condiciones de fluidización más homogéneas. Además, se ha observado que incluir los detalles del distribuidor (una placa perforada en este caso) aumenta sensiblemente la predicción de los patrones hidrodinámicos del sistema.

6.3 Simulación numérica del reactor de SE- SMR en la planta piloto ZECOMIX

ZECOMIX (acrónimo de Zero Emission Coal MIXed) es un proyecto del ENEA (Agencia Nacional Italiana para las Nuevas Tecnologías, la Energía y el Desarrollo Económico Sostenible) que tiene como objetivo la demostración experimental de una nueva tecnología de captura de CO_2 en precombustión. El proyecto cuenta con una planta piloto de $100kW_e$ para la producción de electricidad e hidrógeno a partir de carbón, con captura in situ de CO_2 mediante lechos fluidos.

El reactor semi-industrial de SE-SMR de ZECOMIX ha sido simulado mediante el modelo CFD, previamente validado a escala de laboratorio. Una malla gruesa ha sido aplicada con el objetivo de simular el reactor con el menor coste computacional. Se ha realizado un estudio detallado de independencia de los resultados con respecto al tamaño de celda y paso temporal; obteniendo un tamaño óptimo de celda de 5x5 cm con un muy bajo coste computacional. Utilizando este tamaño de malla, los valores obtenidos en las simulaciones pueden considerarse satisfactorios considerando la complejidad de los casos estudiados.

Adicionalmente se ha llevado a cabo un estudio de sensibilidad del modelo completo, usando únicamente vapor de agua y metano como reactivos gaseosos. Se ha observado que la temperatura es el parámetro clave en el proceso de SE-SMR a gran escala. Además, la presencia de sorbente aumenta la producción de hidrógeno, obteniendo un syngas con un contenido de hidrógeno del 97% (en base seca).

Otros importantes resultados se han derivado de este estudio de sensibilidad. Bajo las condiciones estudiadas, tanto la reacción de SE-SMR como la de reformado de metano (SMR) alcanzan el equilibrio. La concentración de especies a lo largo del lecho presenta una distribución con dos pendientes bien diferenciadas, que corresponden a la reacción dominante en cada zona. En la parte inferior del lecho, donde la concentración de metano es elevada, la reacción dominante es SMR. Esta reacción es sensiblemente más rápida que la reacción de captura, que domina en la segunda zona del lecho. Por lo tanto, la variación de la concentración especies es más pronunciada en la zona dominada por SMR que en la dominada por la carbonatación. Adicionalmente se ha observado que las reacciones de reformado presentes en el mecanismo de SE-SMR son competitivas. La velocidad de la reacción de reformado a CO_2 (R2) aumenta notablemente con la presencia de la reacción de captura, reduciendo sensiblemente la velocidad de reacción de reformado a CO (R1). Además se ha observado que R1 es mucha más sensible a la temperatura que R2.

Adicionalmente, se han comparado los patrones hidrodinámicos con dos modelos de arrastre (el modelo de Syamlal-O’Brien, definido por defecto en FLUENT, y nuestro modelo modificado). Se han observado importantes diferencias en las fluctuaciones transitorias de presión. El modelo de Wang modificado presenta un patrón pseudoperiódico con una amplitud en la señal correspondiente a un régimen multiburbuja realista. En cambio, el modelo Syamlal-O’Brien presenta una señal periódica, que corresponde a un régimen no realista de burbuja individual con un bajo rango de amplitud. Esta mejora en las simulaciones es crucial para la correcta predicción de los patrones de mezcla en lechos fluidos.

El proyecto ZECOMIX ha sufrido múltiples modificaciones desde su fase de diseño conceptual hasta su construcción. Para poder evaluar el efecto de estos cambios en la respuesta del sistema, se ha propuesto un Diseño de Experimentos robusto propuesto por Taguchi.

El método de Taguchi es una herramienta muy útil para evaluar simultáneamente el efecto de múltiples variables en la respuesta de un sistema. Este método se ha combinado con las simulaciones CFD para realizar un análisis multicriterio de la respuesta del reactor de SE-SMR de ZECOMIX, a diferentes variaciones operativas.

Las conclusiones más destacadas obtenidas de este estudio son:

- La presencia de un sorbente es necesaria para obtener un gas de síntesis con una alta concentración en hidrógeno, y bajo contenido de carbono. Sin la presencia del sorbente, la concentración de equilibrio del hidrógeno es mucho menor, otras especies no deseadas son producidas y el proceso necesita un aporte externo de calor.

- La respuesta del sistema es prácticamente independiente del tipo de sorbente utilizado. Por lo tanto, se recomienda el uso del sorbente sintético. A pesar de tener una velocidad de reacción menor, presenta un correcto comportamiento cinético, y mejores propiedades de regeneración y mecánicas que la dolomita.

- La temperatura de operación debe ser cercana a los 900K. A temperaturas menores la velocidad de reacción de SMR disminuye, y en los casos en los que no hay presencia de sorbentes, la conversión de metano es inaceptable.

- Se requiere una alta concentración de metano en el syngas de alimentación del reactor. Si la concentración de metano es muy baja, pueden tener lugar indeseables reacciones inversas. La incidencia de este hecho es mayor a bajas temperaturas y si el sorbente no está presente.

- El modelo de arrastre de partículas condiciona fuertemente las predicciones hidrodinámicas del lecho. El nuevo modelo produce un patrón pseudoperiódico en la respuesta del sistema que mejora la mezcla de gas y solidos, con un incremento en la reactividad del sistema.

El resto de los resultados obtenidos, químicos e hidrodinámicos, están en línea con predicciones teóricas.

6.4 Hidrogasificación de carbón del Sulcis

La caracterización detallada del proceso de gasificación con hidrógeno de carbón del Sulcis está fuera del alcance de esta tesis. Sin embargo, se han conseguido algunas mejoras en la comprensión de la cinética del proceso de devolatilización de este carbón sub-bituminoso.

Varios modelos cinéticos globales de literatura, se han aplicado a una serie de experimentos realizados en TGA, para poder caracterizar el proceso de devolatilización del carbón del Sulcis, y extrapolar sus parámetros cinéticos a condiciones industriales. Debido a la alta influencia de la pirolisis secundaria en este carbón, no existe un modelo global capaz de reproducir muy detalladamente el proceso completo de devolatilización.

Por lo tanto, se ha desarrollado un nuevo modelo de devolatilización llamado 2-DAEM (Double Distributed Activation Energy Model). Este modelo presenta muy buenas predicciones de la pirolisis de carbón del Sulcis, y también ha sido testado con éxito para diferentes carbones y biomasas.

6.5 Perspectivas para el trabajo futuro

Los objetivos de este trabajo de investigación se han cumplido satisfactoriamente, sin embargo varios aspectos permanecen abiertos para futuros trabajos. Algunos de ellos están relacionados con las limitaciones experimentales encontradas durante el estudio, mientras que otras son inherentes a las hipótesis realizadas durante el proceso de modelado.

Sorbentes sólidos para la captura de CO_2 a alta temperatura

Tanto los diferentes sorbentes, como los pretratamientos desarrollados han sido testados en termobalanza. Por lo tanto, deben realizarse pruebas en lecho fluido para estudiar el comportamiento de los sorbentes, bajo condiciones de operación real. Particularmente, se deben llevar a cabo ensayos mecánicos para evaluar el efecto de los pretratamientos en la resistencia a la fricción de los sorbentes. Además, diferentes respuestas en los modelos se pueden esperar debido a que los mecanismos de transferencia de masa (intra y extra-particulares) son muy diferentes en TGA que en LF.

Modelo CFD del reactor de SE-SMR

El modelo presenta una serie de hipótesis que pueden ser mejoradas en trabajos futuros. El modelo cinético de SMR ha sido tomado de literatura para un catalizador de NiO genérico, pero en el caso experimental es probable que sea diferente. Por lo tanto un modelo detallado de la reacción de SMR debe utilizarse para el catalizador especifico de la planta pilot. Otra simplificación respecto al modelo cinético ha sido despreciar los efectos difusionales en la reacción de captura de CO_2, que puede incluirse en futuros desarrollos.

El modelo E-E es una herramienta muy útil para simular LFB. Sin embargo sería recomendable continuar trabajando en refinar el modelo para simular separadamente las fases de sorbente y catalizador. Por otra parte, debido a su importancia durante la operación real de los LF, sería un avance interesante incluir modelos de fragmentación por fricción y la distribución de tamaños de partícula, para incrementar la precisión de las simulaciones.

Una campaña de simulaciones numéricas análoga a esta sería recomendable para cubrir un espectro más amplio de aproximaciones CFD multifásicas. Esta campaña debería incluir simulaciones en 3D, detalles de los distribuidores de gas, y otros modelos fundamentales como puede ser el Modelo de Elementos Discretos (DEM) en el que se realiza un rastreo individual de las partículas del lecho.

La configuración del método de Taguchi utilizado puede ser refinado para incluir interacciones entre factores, efectos externos de señal/ruido, y un estudio de optimización completo del sistema.

En cualquier caso, el más importante de los trabajos a realizar es la validación con datos experimentales, de las simulaciones semi-industriales. En función de los resultados de las pruebas que se realizarán en la planta piloto de ZECOMIX, el modelo seguramente necesitará las oportunas modificaciones.

A1 - Kinetics of Sulcis coal devolatilization

Worldwide power generation from coal is approximately 40%, and in the last decades has continuously risen reaching about the half of the global energy demand increase [395]. The increasing demand of coal (particularly in China) and fuel transport costs affect the price of fuel, promoting the use of autochthonous resources.

In Italy, most of the coal reserves are located in the Sulcis basin (South-West zone of Sardinia Island). The ASTM rank classification characterizes coal from Sulcis area as a sub-bituminous type with high sulphur content (6-7 %m. as received [113, 396]).

In this work the behavior of the Sulcis sub-bituminous coal during pyrolysis was studied in order to evaluate the global kinetics of the devolatilization step, being well-known that combustion and gasification are strongly dependent on this step [397-401]. Furthermore, Sulcis coal is characterized by a high volatile content (approximately 40% m. as received) [112], principally formed via decomposition of carboxylic and phenolic groups which lead to the production of species having high calorific value [402]. Moreover, during the devolatilization process, particles are disintegrated forming ultra-fine coal particles with high porosity and an increased reactivity. However, this enhanced reactivity implies a lower heating value with respect to less reactive coals with higher rank (i.e. anthracite) [402].

The chemistry of coal devolatilization is very complex. The individual functional groups of the coal macromolecule decompose producing low-molecular mass gaseous species; macro-molecular network contained in the coal lattice decomposes in smaller fragments which can evolve to tar vapors, by means of a complex combination of bridge breaking, crosslinking, hydrogen transfer, substitution reactions and concerted reactions [403-405]. Despite this complexity, it is possible to obtain global models able to reproduce the process from a limited number of experiments.

Typically, the overall process of pyrolysis is characterized by three zones [406]. At low temperature, below 350-400 ºC, several processes as disruption of hydrogen bonds, vaporization and transport of the non-covalently bonded molecular phase occur. Between 400-700ºC the primary devolatilization takes place. In this phase, the weakest bridges may break to produce molecular fragments that can recombine producing tars (condensing at room pressure and temperature), or can be released as light volatile compounds (mainly CH_4, C_2H_4, CO_2, and, depending on coal sulphur content, COS and SO_2) [407]. For temperatures above 700 °C the condensation of the carbon lattice with evolution of CO and H_2 takes place to produce char during the secondary pyrolysis [408].

Scope of this work is to evaluate different global methods approaches to extrapolate the application of the respective models, based on kinetic parameters fitted from thermogravimetric data, to industrially relevant combustion conditions [409, 410]. The results obtained from experimental tests based on thermal analysis technique (TG) are very sensitive to the adopted heating rates [411-413]. In particular, the kinetic compensation effect (KCE) is a linear relationship between the magnitudes of Arrhenius kinetic parameters, *ln(A)* and *E*, calculated for each of a series of related or comparable rate processes [414, 415]. Thus, KCE depends of the thermal history of each experiment. Therefore, in obtaining the kinetic parameters it is required to reduce the KCE by means of multiple heating rate techniques [416]. This is the reason why it is necessary to perform a number of experiments at different heating rate [417].

The first model studied was the single rate (or one-step) model, which correlates measured mass loss data with temperature by means of the Arrhenius law [408, 418, 419]. This model is widely used due to its simplicity but proves to be of limited practical application because it does not take into consideration many important aspects of the pyrolysis process. First of all, this model does not distinguish the number of reactions occurring at different temperature ranges and strongly depends on the thermal history of the experimental tests. Moreover, the reaction order cannot be assumed but has to be estimated fitting the experimental data [420]. Hence, in this work the model-free Kissinger method [421] is applied in order to obtain the one-step kinetic parameters, decoupling the intrinsic kinetics of the reaction from the thermal history of the tests.

Anyway, the Kissinger method presents other limitations which need other more complex models to obtain an accurate modeling of pyrolysis process [416, 422]. To avoid this complex procedure and obtain at the same time robust models, the distributed activation energy model (DAEM) is proposed to fit the experimental data. The DAEM is a powerful method that takes into account multiple parallel reactions assuming for the pyrolysis process a single frequency factor and a Gaussian distribution of activation energies [109]. Four resolutions of DAEM are studied: a numerical single method, a numerical 2-DAEM, and two approximate methods specifically developed for coal pyrolysis. The first approximation due to Braun and Burnham allows the evaluation of kinetic parameters with few TG analyses [423], while the second one proposed by Miura does not assume a predefined activation energy distribution and supposes a non-constant frequency factor [424]. These approaches are utilized in processing the TG mass loss experimental data and allow to obtain kinetic parameters valid in both laboratory and industrial conditions.

The experimental data are finally interpreted with a structural model to obtain information about species evolution. In this work, the CPD model [425] is used to simulate the devolatilization process under conditions equivalent to experimental tests, and the calculated results are compared with experimental data by means the Kissinger method and the Miura approximation of DAEM.

A1. 1 Coal Characterization

The investigated coal was grounded in an agave mortar to obtain fine powder, used in thermal analysis without further treatments. Ultimate analysis of coal shown in Table A1. 1 was estimated via Thermoquest model EA 1110 CHNS-O.

Proximate analysis has been realized in TG instrument (Mettler Toledo TG/DSC 1 Star System) at atmospheric pressure according to the standard test methods ASTM D5142/02 and it is summarized in Table A1. 2.

Table A1. 1 – Proximate and ultimate analysis of Sulcis coal

PROXIMATE ANALYSIS	/ m. %	ULTIMATE ANALYSIS	/ m. % [a]
Moisture	5,25	Carbon C	71,12
Volatile	40,73	Hydrogen H	5,09
C Fixed	40,23	Nitrogen N	1,94
Ash	13,79	Sulphur S	7,34
LOW HEATING VALUE / kJ kg^{-1}	21000	Oxygen (by difference)	14,51

[a] D.A.F. Dry ash-free basis

Table A1. 2 – Experimental method implemented in TG to obtain proximate analysis

T / °C	Heating rate / C min^{-1}	Atmosphere gas: N_2 Flow rate / ml min^{-1}	Atmosphere gas: Air Flow rate / ml min^{-1}
25-105	10	150	-
105	Isotherm (15 min)	150	-
105-950	40	150	-
950	Isotherm (7 min)	150	-
950-600	-40	150	-
600-700	10	-	150
700	Isotherm (15 min)	-	150
700-950	25	-	150
950	10	-	150

A1. 2 Coal Pyrolysis Experimental Tests

Pyrolysis experiments were performed in the TG analyzer at atmospheric pressure with a differential scanning calorimetry (DSC) module, under a nitrogen flow (60 ml min^{-1}), with a recording period of 1 second. The maximum particle diameter was fixed at 100 µm to neglect intraparticle diffusion effects. Sample mass was fixed at 3 mg, in order to obtain a monolayer of coal in the crucible and avoid diffusional effects across the bed. More other values of the mass sample were studied to obtain less noise signals. However, by visual inspection non-reacted zones were detected in the center of the particles for mass samples larger than 8 mg, fixing the mass sample at 3 mg.

Due to the heterogeneity of coal samples, a set of three reproducible experiments were performed at four different heating rates (5, 50, 75, 100ºC min^{-1}) from 105ºC up to 950 ºC, being the maximum temperature and heating rate limited by TG characteristics. The effects of moisture on devolatilization, if any, were deleted with a low heating of the samples from room temperature up to 105ºC, followed by a 5 min isothermal step. As part of the experimental procedure, blank runs were conducted with an empty crucible to record and subtract the disturbances in the mass change and reaction heat readings during the experiments.

To better understand mass variation TG derivative was used (DTG). However, because in DTG curves the experimental errors are emphasized, to reduce the signal noise a Savitzky-Golay filter [426] was applied [427]. According with this digital filter, TG data were fitted by a polynomial of degree *p* = 5 and a 25-point smooth.

A1. 3 Comparison of global models

The mass loss (TG) curves as function of temperature are reported in Figure 1 for each applied heating rate.

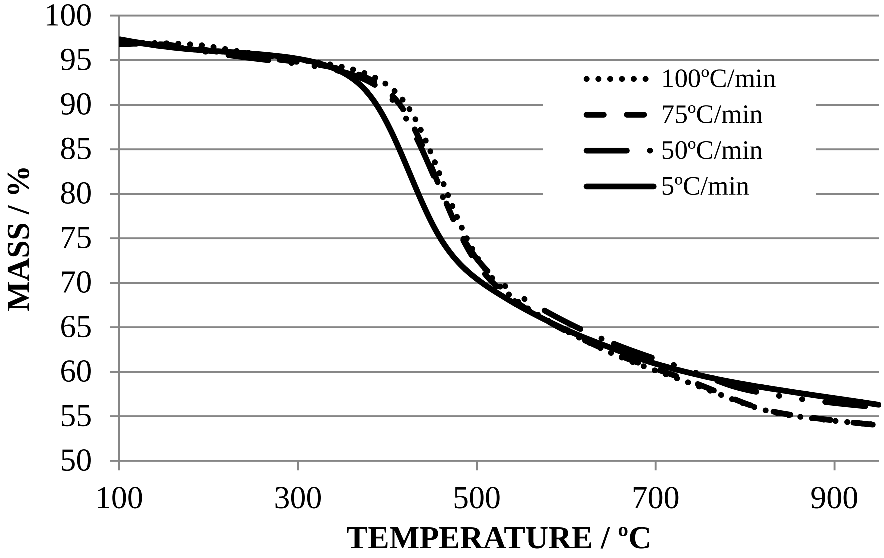

Figure A1. 1– Experimental TG data of mass loss against temperature for different heating rates

DTG curves, reported in Figure 2, show, as expected, that the mass loss rate increases significantly with heating rate. Furthermore, the temperature corresponding to the maximum devolatilization rate increases with heating rate (Table 3) [421]. In Figure 2 three zones can be located, each representing different pyrolysis behavior with temperature: under 300°C, between 300-550 °C, and over 550°C. The overall devolatilization occurs between 350°C and 800°C, with two different slopes which correspond to primary (350 – 550ºC) and secondary pyrolysis (550-800ºC). It is worth to note that a secondary devolatilization takes place at low temperatures [406], since Sulcis is a low rank coal with a high volatile content and thus with a high reactivity.

In the following sections the analysis of the pyrolysis behavior of the Sulcis coal applying different kinetic models is reported.

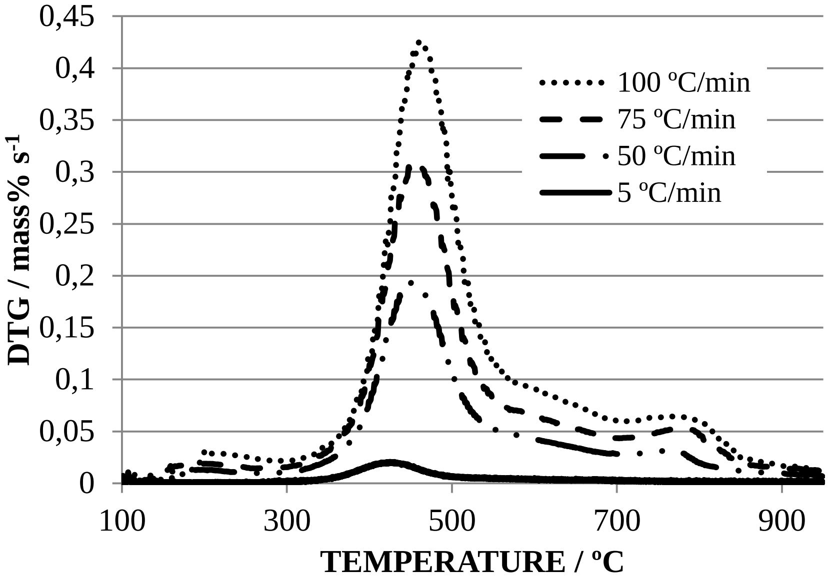

Figure A1. 2 – Mass loss rate against temperature for different heating rates

A1.3.1 Single Kinetic Rate Model – Kissinger Method

The Single Kinetic Rate Model assumes that the overall devolatilization process occurs in one step [418]. This simple approach is very useful to obtain a general overview of the behavior of coal during pyrolysis. This model assumes that during the devolatilization two products are obtained, char and volatiles according the reaction:

$$Coal \overset{k_1}{\rightarrow} X\,(volatiles) + (1 - X)(char) \qquad \text{(A1. 2)}$$

where X is the volatile fraction and k_1 is the rate constant, defined by the Arrhenius law. The time variation of the volatile fraction is described according the relationship:

$$\frac{dX}{dt} = A\ e^{\left(-\frac{E_a}{RT}\right)} f(X) \qquad \text{(A1. 3)}$$

where *f(X)* is the dependence on the extent of conversion described by the reaction model, A the frequency factor (s^{-1}), E_a the activation energy ($J\ mol^{-1}$), R the gas constant ($J\ kmol^{-1}$) and T the absolute temperature (K).

The reaction order and the functional form of *f(X)* were discussed in several works, lacking, however, a general consensus. Furthermore, the reaction order can not be assumed but has to be estimated fitting the experimental data, according with several authors (i.e. [408] and [420]). A common approach is to assume that devolatilization is a first order reaction [418, 428-430]; in that case the volatile evolution rate can be represented by the equation:

$$\frac{dX}{dt} = A\ e^{\left(-\frac{E_a}{RT}\right)}\left(X^* - X\right) \tag{A1. 4}$$

where X^* is the amount of volatiles released at complete pyrolysis. For non isothermal TG experiments (with linear heating rates $\alpha = dT/dt$), Equation A1.3 can be written as:

$$\frac{dX}{dt} = \frac{A}{\alpha}\ e^{\left(-\frac{E_a}{RT}\right)}\left(X^* - X\right) \tag{A1. 5}$$

This equation allows obtaining kinetic parameters values A and E_a which prove to be independent of the thermal history of the experiments. The methods used to calculate the kinetic parameters are called model-free non-isothermal methods, among which the more extensively used is the Kissinger method [421]. In this case, the fundamental equation can be derived assuming a first-order from Equation A1.4, under the condition of maximum heating rate:

$$\frac{d^2X}{dt^2} = \left[\frac{E_a\alpha}{RT_{max}^2} - A^{\left(-\frac{E_a}{RT_{max}}\right)}\right]\left(\frac{dX}{dt}\right)_{max} = 0 \tag{A1. 6}$$

where subscript *max* denotes the maximum value of reaction rate, corresponding to the peak of DTG curve for each heating rate in Figure A1. 2. After simple rearrangements, equation A1.5 is transformed into the Kissinger equation:

$$\ln\left(\frac{\alpha}{T_{max,i}^2}\right) = \ln\left(\frac{AR}{E_a}\right) - \frac{E_a}{RT_{max,i}} \tag{A1. 7}$$

By applying this simple method to the TG data, the agreement is very good ($R^2 = 0.99$). The obtained kinetic parameters are shown in the Table A1. 3 and are in good agreement with kinetic parameters calculated for other similar low rank coals [431].

Table A1. 3 – Characteristic maximum devolatilization temperatures obtained in the TG at different heating rates and kinetic parameters obtained with Kissinger method.

Heating Rate / ºC min^{-1}	5	50	75	100	E_a / kJ mol^{-1}	220.4
T max / ºC	406.7	450.6	452.4	459.8	A / s^{-1}	4.06×10^{11}

However, this method should be carefully applied due to its intrinsic limitations. When the reaction model, *f(X),* can not be considered as first-order, a systematic error in E would be produced, which is reduced if a distributed reactivity model is applied [423]. Moreover, the Kissinger method provides a single value of activation energy independently of the kinetic complexity. Thus the application of global models to the complete devolatilization process assures accurate results if applied to higher rank coals, where secondary pyrolysis has a lower influence [432]. Instead, in the case of Sulcis coal different models which include multi-step kinetics should be considered to confirm the significance of the kinetic parameters obtained with the Kissinger method.

A1.3.2 Distributed Activation Energy Model

It is well known that during the devolatilization process several reactions in series and in parallel occur. To account for this more complex mechanism, a commonly accepted approach is the use of the distributed activation energy model (DAEM). This model assumes that the overall process occurs through several parallel first order reactions, sharing the same frequency factor with a generic distribution of activation energies. The model assumes that the volatile release can be modeled by the relationship:

$$1 - \frac{X}{X^*} = \int_0^\infty \exp(-A \int_0^t e^{-E/RT} dt)\, f(E) dE \qquad \text{(A1. 8)}$$

where *f(E)* is the distribution of the activation energies which satisfies the condition:

$$\int_0^\infty f(E) dE = 1 \qquad \text{(A1. 9)}$$

In the literature, different forms of the activation energy distribution can be found: Gaussian [109], Weibull [433] or Gamma [434] distributions.

The frequency factor is difficult to characterize experimentally. Moreover, the evidence arises that this parameter is highly correlated with the activation energy and consequently difficult to evaluate [435]. Hence, the value of the frequency factor has to be fixed in some way.

The main advantage of this model is the reduction of kinetic parameters necessary to characterize the devolatilization process. For each temperature range, a dominant reaction is considered and then a statistical distribution is assumed. This model has been extensively used with success in modeling coal pyrolysis. However, in the practical application of this method the simplifications introduced as functional approximation of the *f*(*E*) term are considered by some authors too rough, inducing significant errors in the calculation results [33].

A1.3.2.1 Single DAEM Numerical Solution

In this work, in the framework of DAEM the Gaussian distribution was investigated. The distribution function *f(E)* can thus be described as:

$$f(E) = \frac{1}{\sigma_E\sqrt{2\pi}}\exp\left(\frac{-(E-E_a)^2}{2\sigma_E^2}\right) \tag{A1. 10}$$

where E_a and σ_E are respectively the mean activation energy of the process and the standard deviation.

The kinetic parameters to be estimated using this model are the frequency factor *A*, the mean activation energy E_a and the standard deviation σ_E. The DAEM equation was integrated numerically with the method of Gaussian quadrature, without using any functional approximation of the DAEM equation, a way already followed by many authors [435, 436]. The experimental data were fitted with a C++ program run into the ROOT environment (an object oriented framework for large scale data analysis developed at CERN) using the routine MINUIT for the minimization of the fitting function [437]:

$$\chi^2 = \sum_{i=1}^{N}\left(y_i^s - y(T_i)\right)^2 \tag{A1. 11}$$

where *N* is the number of data points, y_i^s and $y(T_i)$ are the experimental and the calculated data, respectively.

As already reported, the evaluation of three parameters from the same fit is a difficult task since *A* and E_a are highly correlated. When the three kinetic parameters were fitted together, a multiplicity of solution arise. In fact, data are well reproduced by values of *A* ranging from 10^{10} e 10^{22} s^{-1}. The correlation coefficient between *A* and E_a parameters assumes a value of 0.971, which means that it is not possible, using the available experimental data, to obtain a unique solutions. Thus one of the kinetic parameters must be fixed to calculate the other ones with statistical significance.

In order to obtain values of kinetic parameters comparable with the values found in the literature and with the parameters calculated from the other selected models in this work, the *A* parameter was fixed at a value characteristic of a sub bituminous coal (Wardoan) similar to Sulcis coal, i.e. $A = 8 \cdot 10^{12}$ s^{-1} [400].

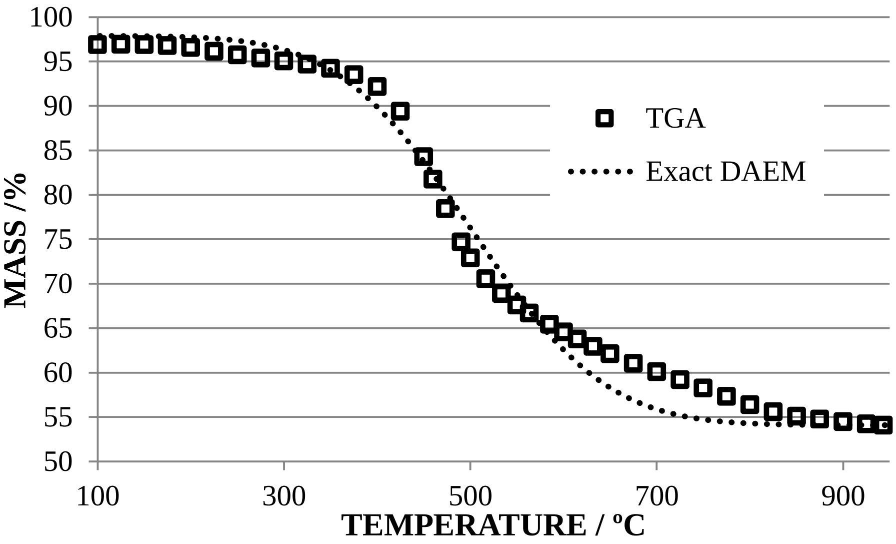

Figure A1. 3 – Experimental values of mass loss during coal devolatilization at 100 ºC min^{-1} and the predicted one assuming DAEM analytical solution by the direct simultaneous fit.

The results of the fit are reported in Figure A1. 3 for a heating rate of 100 ºC min^{-1}. It can be easily noticed that the model reproduces quite well the global devolatilization behavior of the Sulcis coal. Nevertheless, the experimental curves present two different slopes which the model is not able to reproduce.

Table A1. 4 – Kinetic parameters obtained for the DAEM analytical solution at different heating rates.

Heating Rate / ºC min^{-1}	Frequency factor A / s^{-1}	Activation energy , E_a / kJ mol^{-1}	Distribution parameter σ / kJ mol^{-1}
5	8×10^{12}	220	34.3
50	8×10^{12}	213.6	32.6
75	8×10^{12}	212.8	32.3
100	8×10^{12}	212	30.7

To make the solution independent from the heating rate in order to obtain a unique value of the kinetic parameters for all the curves, a simultaneous fit of the data recorded at different heating rates, ranging from 5 to 100 ºC min^{-1}, was performed and the results are reported in Table A1. 4. It can be seen that the kinetic parameters are in accordance with those obtained with the single fit.

In spite of the efforts to obtain global kinetic parameters independent of the heating rate, it is not possible to analytically get an exact solution with the DAEM without any approximation, in this case the Gaussian distribution for *f(E)*, and the need to fix one among the kinetic parameter, in the present case *A*. Hence other energy distributed approaches were studied in this work.

Table A1. 5 – Kinetic parameters obtained for DAEM by means of analytical solution by the direct simultaneous fit and applying Braun-Burnham's correlation.

	DAEM	Braun-Burnham
Frequency factor , A / s^{-1}	8×10^{12}	2.268×10^{20}
Activation energy , E_a / kJ mol^{-1}	214.7	302.5
Distribution parameter, σ / kJ mol^{-1}	33.3	28.4

A1.3.2.2 2-DAEM approach

A 2-Gaussians model was developed assuming that the pyrolysis process occurs in two steps with different kinetic behaviors. The pyrolysis process is divided into two steps: the tar and light hydrocarbon gas formation during the primary pyrolysis and the char condensation, cross-linking reactions and a further gas production during the secondary pyrolysis. Serio et al. [438] proposed a model, that is an extension of a model originally developed by Chermin and van Krevelen [439], in which the pyrolysis is divided into three steps. The first corresponds to the breakage of light bonds and the released of some guest molecules by breakage of very weak bonds, the second is the primary pyrolysis and the third is the secondary pyrolysis. In this work only two stages are taken into account, considering the first and the second steps described by Serio et al. [438] having the same activation energy. Two sets of parallel reactions occur, sharing the same frequency factor but not the same distributed activation energy. The 2-DAEM equation can be written as:

$$1-\frac{v}{v^*}=\int_0^\infty exp\left(-\frac{k_0}{\alpha}\int_0^T exp\left(-\frac{E}{RT}\right)dT\right)\left(\gamma f_1(E)+(1-\beta)f_2(E)\right)dE \qquad \text{(A1. 12)}$$

where $f_i(E)$'s are Gaussian functions of the form:

$$f_i(E)=\frac{1}{\sqrt{2\pi\sigma_{Ei}}}exp\left(\frac{-(E-E_{0i})^2}{2\sigma_{Ei}^2}\right) \qquad \text{(A1. 13)}$$

and γ is a parameter which weighs the two reaction classes, varying from 0 to 1. This parameter describes how many volatiles are released during the primary or during the secondary pyrolysis. The value of γ would be 0 if all the volatiles were produced during the secondary pyrolysis and 1 if they were released during the secondary one.

In this case, the parameters to be estimated are five, two mean activation energies E_{01} and E_{02}, two standard deviations σ_{E1} and σ_{E2}, and γ.

The results of the fitting procedure are reported in Figure A1. 4 where it can be noticed that the model reproduces very well the experimental data.

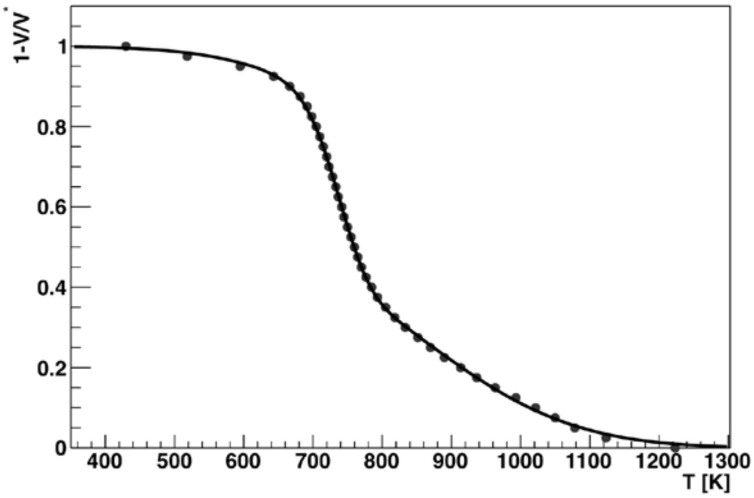

Figure A1. 4 – Comparison between the experimental data (points) and 2-DAEM fitting (line) for a heating rate of 100K/min.

Table A1. 6 – Kinetic parameters of the 2-DAEM for a heating rate of 100 K/min.

	Sulcis coal
k_0 (1/s) fixed	$8\cdot10^{12}$
E_{01} (kJ/mol)	200
σ_{E1}(kJ/mol)	7.33
E_{02} (kJ/mol)	233
σ_{E2}(kJ/mol)	49
γ	0.442

In Table A1. 6, the kinetic parameters obtained from the fit are reported. It can be noticed that for the Sulcis coal the mean activation energy values are quite similar. This behavior is more evident looking at the plots showed in Figure A1. 5 where *f(E)* function vs. activation energy for 1-DAEM and 2-DAEM are reported. The volatile production can be attributed to primary and secondary pyrolysis for the same amount (γ =0.442).

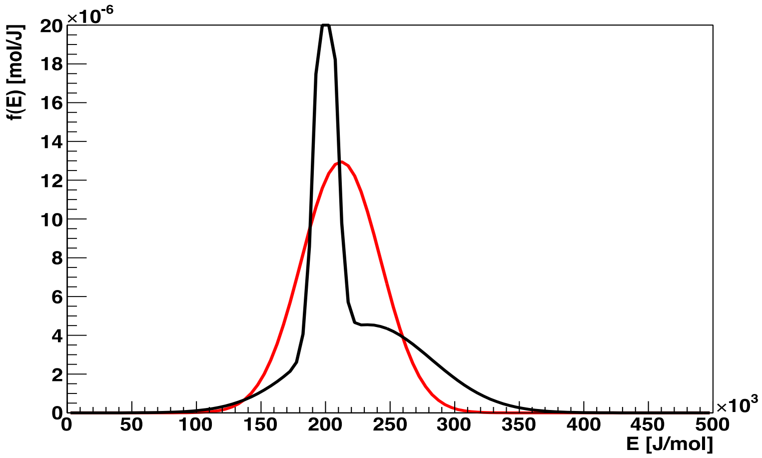

Figure A1. 5 – The distribution activation energy curves as a function of activation energy, in red the curve for 1-DAEM in black for 2-DAEM.

From Figure A1. 5, it can be noticed that Sulcis primary pyrolysis occurs in a small interval of activation energy (σ_{E1}=7.33 kJ/mol) and therefore is confined in a narrow temperature range (650-750K); this process is fast and the energy required to break both functional group and aliphatic bonds is similar. The secondary pyrolysis stage, where the dehydrogenation of the hydroaromatic clusters and aliphatic groups, and the char condensation and cross-linking take place is slower and requires more energy to be accomplished. The two gaussians are partly superimposed as the cross-linking reactions and char condensation begin at the same time of the primary pyrolysis. The high amount of volatiles released instantaneously makes the particle very porous and the coal very reactive, and the char condensation mechanism begins in the particle zone where the first volatiles are released. However the first Gaussian is predominant in the primary pyrolysis and the second, whose the peak is at 950K, in the secondary pyrolysis. The hydrogen extraction from the hydroaromatic clusters occurring during the char condensation takes place with higher activation energy than that needed for Sulcis coal where hydrogen is extracted from the aliphatic less energy bonds either.

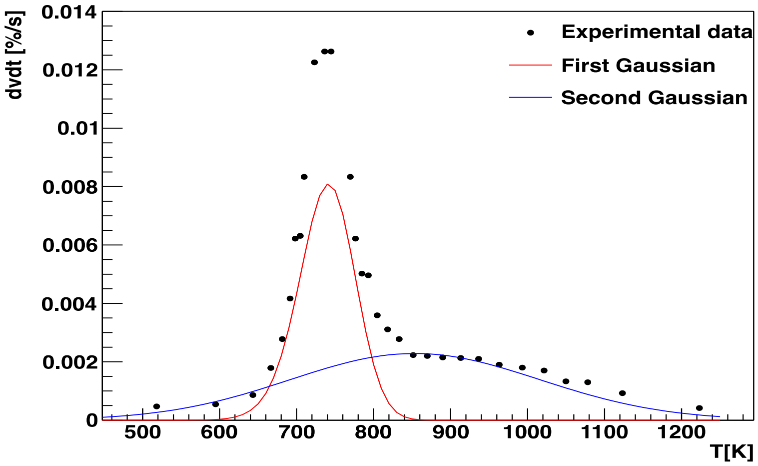

Figure A1. 6 – Comparison between experimental reaction rates and reaction rates obtained with the 2-DAEM kinetic parameters for a heating rate of 100K/min.

In Figure A1. 6, the reaction rates obtained from experimental data are compared with the reaction rate due to the two gaussians. Each curve represents the contribute of one of the two Gaussians distributions in the whole process. It can be noticed the fast primary pyrolysis reactions for the Sulcis coal and the superimposition of the two steps.

One problem of the 2-DAEM is the correlation between the kinetics parameters. The correlation coefficients have a mean value of 0.42. Above all, the γ parameter presents a correlation with the mean activation energy as high as 0.67. To decorrelate the parameters, it was tried to fit simultaneously sets of data taken at different heating rates [440]. The experimental data obtained at heating rates ranging from 5 to 100 K/min are reported in Figure A1. 7. In the analysis code, a function like that reported in Eq. A1.10 was created for each set of data, fixing the heating rate to the proper value. The minimization algorithm was then configured to find the model parameters which, at the same time, better reproduced the different sets of data.

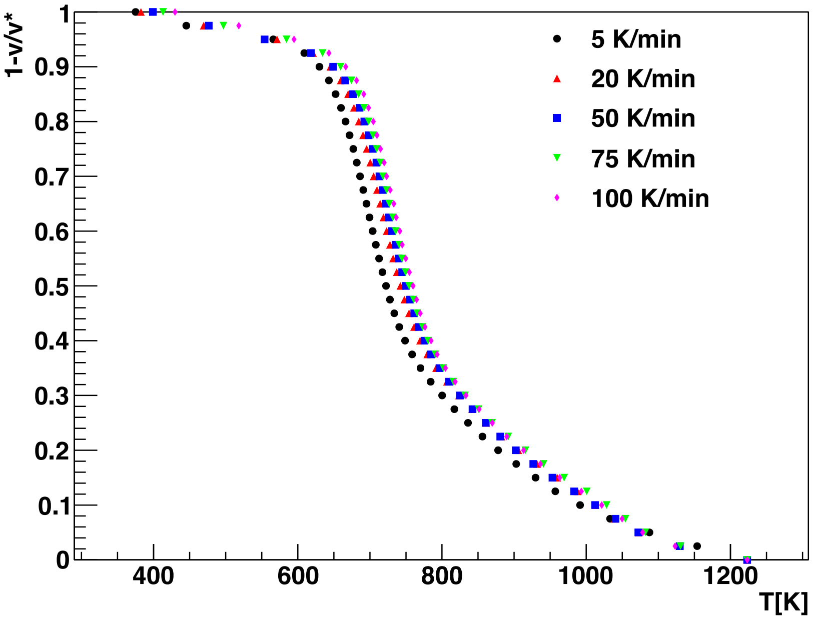

Figure A1. 7 – 1-v/v* for Sulcis coal varying the heating rate from 5 to 100K/min.

With the simultaneous fit, the correlation between the parameters is lowered to a mean value of 0.34. The improvement is not impressive but it seems that performing a simultaneous fit with data taken at different heating rates makes the solution more independent. Therefore spanning the heating rate over a wider range would make it possible to further decorrelate the parameters. Unfortunately our experimental apparatus does not permit to increase the heating rate by more than 100 K/min. As reports in Table A1. 7 the kinetics parameters calculated with the simultaneous fit do not vary significantly from the values reported in Table A1. 6.

Table A1. 7 – Kinetic parameters of the 2-DAEM obtained using the simultaneous fit.

	Sulcis coal
k_0 (1/s) fixed	$8 \cdot 10^{12}$
E_{01} (kJ/mol)	202
σ_{E1}(kJ/mol)	7.33
E_{02} (kJ/mol)	237
σ_{E2}(kJ/mol)	52
γ	0.442

The improvement in the representation of the pyrolysis process using the 2-DAEM is evident. Table A1. 8 gives the residual sum of squares for the two models and the relative improvement of the 2-DAEM.

Table A1. 8 – Summary for the residual sums of squares for the two models.

	Sulcis coal
1-Gaussian	$3.16 \cdot 10^{-3}$
2-Gaussians	$1.41 \cdot 10^{-5}$
χ^2(1-DAEM)/χ^2(2-DAEM)	244

A1.3.2.3 Braun-Burham’s Approach

Although DAEM shows a good performance in regressing the experimental results, the value of the effective activation energy obtained processing the TG data is systematically lower at the high heating rates. To overcome this kind of circumstance, Braun and Burnham [32] developed a procedure to extrapolate with a good agreement the global kinetics got at lower heating rates (TG experiments) over a wide heating rate range using a minimum of two sets of data. The approximate procedure proposed by Burnham et al. [47] rests on a linear regression between heating rate (α), temperature of maximum devolatilization rate (T_{max}), activation energy (E_a) and frequency factor (A), in the form:

$$ln\left(\frac{\alpha}{T_{max}^2}\right) = \frac{-E_a}{RT_{max}} + \ln\left(\frac{AR}{E_a}\right) \tag{A1. 14}$$

The model assumes a Gaussian distribution of activation energies whose distribution parameter σ is then obtained as:

$$\sigma = \frac{1.1}{\rho^3} - \frac{0.66}{\rho^{30}} + 2.88\,\rho - 1.12 \tag{A1. 15}$$

with:

$$\rho = \left(\frac{52.4}{E_a}\right)^{0.5}\left(\frac{\Delta T_\sigma}{\Delta T_0}\right) \tag{A1. 16}$$

where ΔT_σ is the experimental profile width at half-maximum, and ΔT_0 is the Gaussian profile width calculated by using A and E_a from Equation A1.13. Finally A_0 is modified to include the effects of σ.

Experimental data recorded at the four considered heating rates were regressed with this model with an excellent agreement (R^2 of Equation A1.13 = 0.99), achieving the kinetic parameters reported in Table A1. 5.

This model takes into account the effects of high heating rates with a good agreement with literature data. However, it presents two disadvantages such as the divergence with low temperature experimental data, mainly in the primary pyrolysis step, and, as suggested by the authors, a bad correlation for low rank coal over 600ºC due to the evolution of hydrogen in the secondary pyrolysis step. Hence, the kinetic parameters obtained by this method are overestimated respect to literature data of similar coals [400, 431].

A1.3.2.4 Miura's Approach

As already reported, it is not possible to estimate the frequency factor and the activation energy assuring at the meantime a significant statistics without fixing one of the two parameters. Furthermore it is necessary to assume a functional form for the *f(E)* term, in this case a Gaussian distribution. This last hypothesis does not lie on a rigorous theoretical justification, but is supported by very good empirical results [409].

Miura developed a simple method to estimate both *f(E)* and *A(E)* without assuming any functional form for *f(E)* [424], using a minimum of three sets of experimental data performed at different heating rates.

In the application of the method a simplification must be done: only a single reaction whose activation energy is E_S is occurring at a given temperature T. Then Equation A1.7 is simplified to:

$$1-\frac{X}{X^{*}}=\int_{Es}^{\infty} f(E)dE \tag{A1. 17}$$

with E_S satisfying the following condition:

$$\frac{0.545\alpha E_S}{A\,R\,T^2}=e^{-\frac{E_S}{RT}} \tag{A1. 18}$$

The method estimates the activation energy for several X/X^* profiles at different heating rates by means of the Arrhenius law. The procedure arranged in 5 steps allows to obtain the kinetic parameters as a function of temperature, assuming that only one reaction occurs at each temperature.

As shown in Figure A1. 8, the estimated distribution of *f(E)* cannot be assumed as a single Gaussian function. The maximum value of *f(E)* is obtained approximately at E_a=170 kJ mol^{-1} and spreads over 40 and 350 kJ mol^{-1}. Furthermore, Figure A1. 9 shows that the frequency factor increases exponentially with the increase of activation energy. Hence, the application of this method demonstrates that considering the value of *A* as a constant is a strong approximation which can introduce errors in the pyrolysis kinetics.

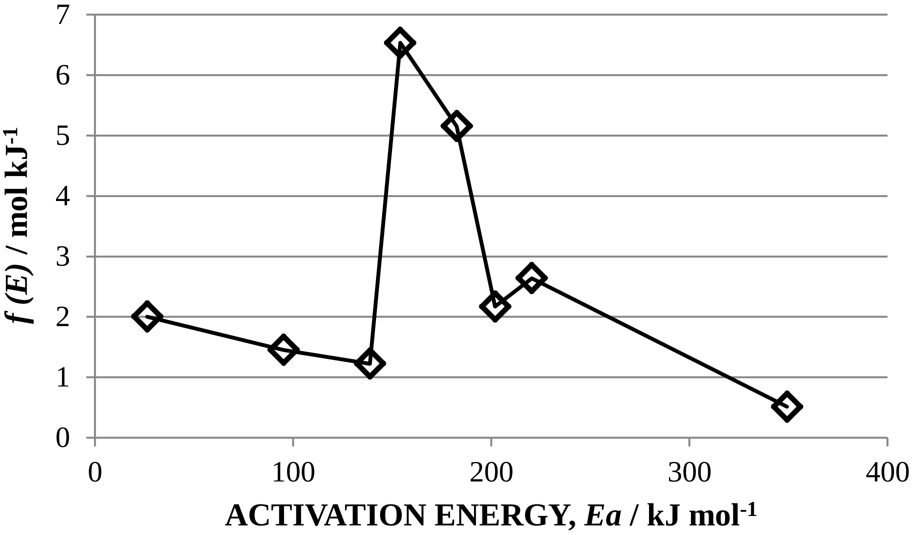

Figure A1. 8 – Estimated distribution curve *f(E)* by Miura’s method.

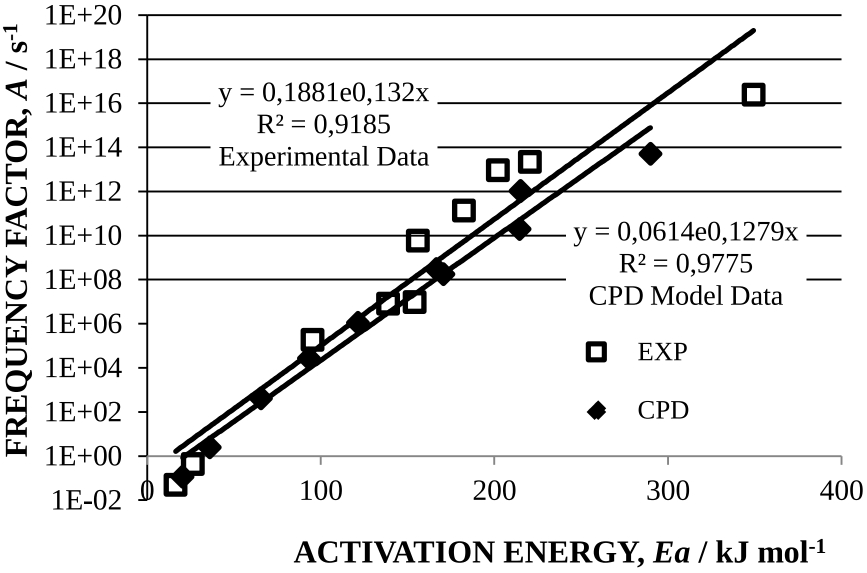

Figure A1. 9 – Estimated frequency factors for experimental and CPD simulated data applying Miura’s method.

The values of the activation energy calculated by the previous described methods are included in the distribution obtained by the Miura’s method application, and the estimated frequency factors present good agreement with the single kinetic rate model. However there are important discrepancies between the frequency factor estimated by this method and by the Braun-Burnham’s method. Firstly, it is evident that the curves shown in Figure A1. 9 can not be approximated to a single Gaussian distribution. Secondly, the tails in the Gaussian distribution underestimate the kinetic rate at low and high temperature which are, on the contrary, very important in the low rank coals devolatilization as is the case of Sulcis [441]. These approximations and the assumption of a single frequency factor explain the difference between the frequency factor values obtained by both the methods. In any case, Miura’s method can be used to estimate the kinetic parameters of the DAEM, without making strong hypothesis and with few sets of experimental data, in an accurate and robust way.

A1.3.3 CPD Model

In contrast with the models previous presented, whose application is based on empirical data, the Chemical Percolation Model for Devolatilization (CPD) was used in this work to simulate the behavior of coal during pyrolysis, so that the calculated data allow to evaluate the kinetic parameters with a more accurate model. The results were then compared with those obtained with empirical models.

CPD model describes the devolatilization occurring at high heating rates [425, 442, 443]. The behavior of coal depends on its composition, and the prediction of the evolution of the single species is based on the coal chemical and physical structure. The main advantage of this model is that only data pertaining to ultimate and proximate analysis are needed to study the overall devolatilization process. As a result, the CPD model provides information about the nature of volatiles released.

During the devolatilization process, the aromatic clusters into the coal lattice initially evolve in two main types of fragments. The low molecular mass and high vapor pressure species leave the lattice as light gas species. Whereas the high molecular mass fragments, which form the tar gas precursors and remain for longer time inside the particle, evolve as tar or are recombined within the coal lattice. The CPD model combines the two effects, explicitly considering the vapor-liquid equilibrium and the crosslinking mechanism.

This model has been selected due to the important information which is able to produce about volatiles composition coupled with mass loss evolution during pyrolysis. CPD model has been validated with several coals under different combustion conditions with very accurate results. However, due to the structure of the mathematical formulation, the model has not been validated under TG conditions. In the present work, three simulations of Sulcis coal devolatilization were carried out with CPD model at three different heating rates (5-50-100 ºC min^{-1}), starting with the coal input parameters reported in Table A1. 9. The Kissinger method were applied to the simulated data obtaining values very similar to those regressed from the experimental data (A(CPD)=2.74·10^{11}s^{-1}, A(TG)=4.06·10^{11}s^{-1}; E_a (CPD)=219.9 kJ mol^{-1}, E_a (TG)=220.4 kJ mol^{-1}), with a quite good agreement, as shown in Figure A1. 10. Moreover, Miura's method was applied to the devolatilization simulated data (the results are shown in Figure A1. 9) presenting again a good correlation with experimental data. Furthermore, it is worth to note that the simulated data are in a good agreement with the experimental ones.

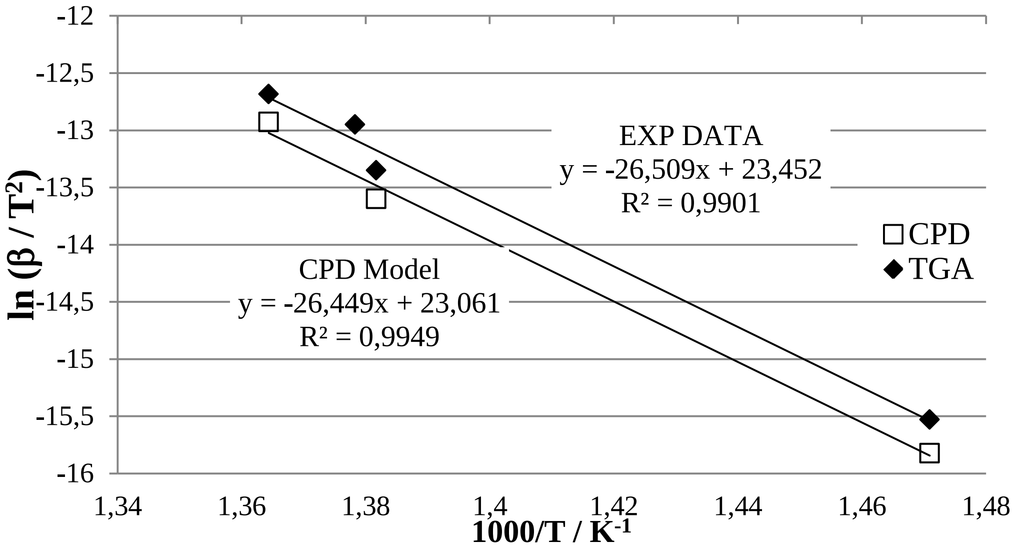

Figure A1. 10 – Kissinger plot for experimental and CPD simulated data.

Table A1. 9 – Input data in CPD simulation for Sulcis coal.

Description	Parameter	Value
[b] Side chain molecular mass / g mol^{-1}	$M\sigma$	48.5
[b] Molecular mass per cluster / g mol^{-1}	$Mclus$	416.8
[b] Initial population of intact bridges / on a per bridge basis, -	$p0$	0.49
[b] Coordination number / number of attachments per cluster, -	$Sig+1$	4.86
[b] Population of char bridges / on a per bridge basis, -	$c0$	0.028
[c] Bridge scission activation energy / kJ mol^{-1}	Eb	231.9
[c] Bridge scission frequency factor / s^{-1}	Ab	2.6×10^{15}
[c] Standard deviation for *Eb* / kJ mol^{-1}	σb	7.5
[c] Gas release activation energy / kJ mol^{-1}	Eg	288.9
[c] Gas release frequency factor / s^{-1}	Ag	3×10^{15}
[c] Standard deviation for *Eg* / kJ mol^{-1}	σg	33.9
[c] Composite rate constant $k\delta/kc$	ρ	0.9
[c] Activation energy for crosslinking rate / kJ mol^{-1}	$Ecross$	272.1
[c] Frequency factor for crosslinking rate / s^{-1}	$Across$	3×10^{15}

[b] Values calculated obtained from [444] based on coal composition (Table A1.1)

[c] Constant values from [443]

However, some discrepancies between the coal mass loss behaviors in both cases can be observed. In CPD model devolatilization is divided into two distinct steps, while the experimental curves do not present the same behavior (Figure A1. 11). The first peak corresponds to the light gas devolatilization and the second one to the tar formation and crosslinking effects. These divergences are due to the formulation of CPD model, which separates the two devolatilization steps as a function of the composition of coal, extrapolating the actual behavior from a database build up by different coals. At higher heating rate only a peak is obtained by simulations, while at lower heating rates, characteristic of the TG conditions, the overlapping between primary and secondary pyrolysis is not present and two peaks are generated.

In any case, the data obtained with the CPD model show a qualitatively similar behavior, and the model can be easily implemented as a subroutine in codes as chemical process simulator or CFD codes [445-447]. The main advantage of this model is the quantitative assessment of the light gas, tar and char (and some particular species) evolution for a wide operational range of temperature and pressures, conditions which are sometimes difficult to reproduce in laboratory.

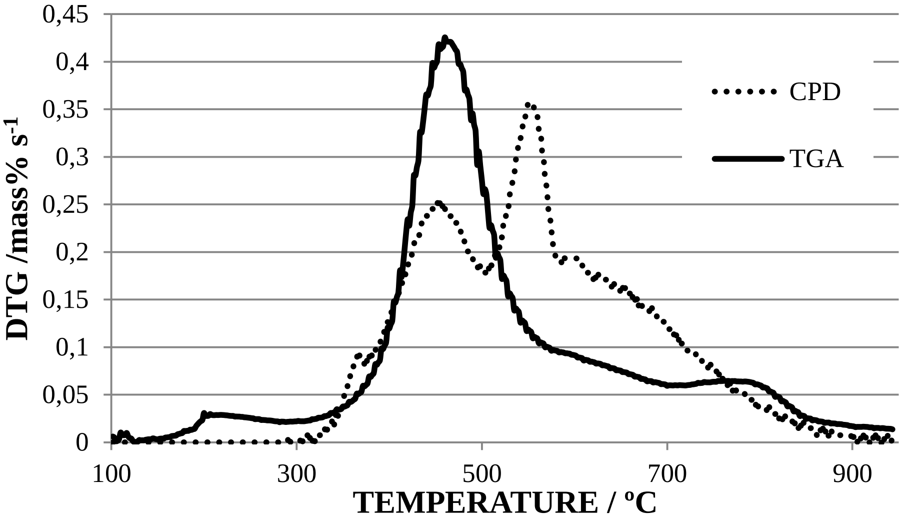

Figure A1. 11 – Comparison of mass loss rate of empirical TG data and simulated CPD model data for a heating rate of 100ºC min^{-1}

A1.3.4 Comparison among the different approaches

In Figure A1. 12 the comparison between the experimental mass loss curve and the fitted data obtained with the studied kinetic models is reported. It can be noticed that all the tested models, except single-rate first-order model based in Kissinger method, present a quite good agreement with experimental data. However, due to the strong effect of secondary devolatilization which characterizes this coal, some discrepancies have been observed, reducing the accuracy of the global methods in reproducing the behavior of this low rank coal. The primary pyrolysis is well represented with both the DAEM approaches and the CPD model. However, for the secondary pyrolysis zone the agreement is lower (except in the case of 2-DAEM model), due mainly to the definition of a global model, where the mass of primary pyrolysis is more important than in the secondary step. The numerical solution of the DAEM presents a good correlation with experimental data. A good agreement is obtained also using the Braun and Burnham’s method. The curve calculated with the kinetic parameters obtained from the CPD simulated data presents a similar trend respect to the experimental curves but some discrepancies in the DTG are notable.

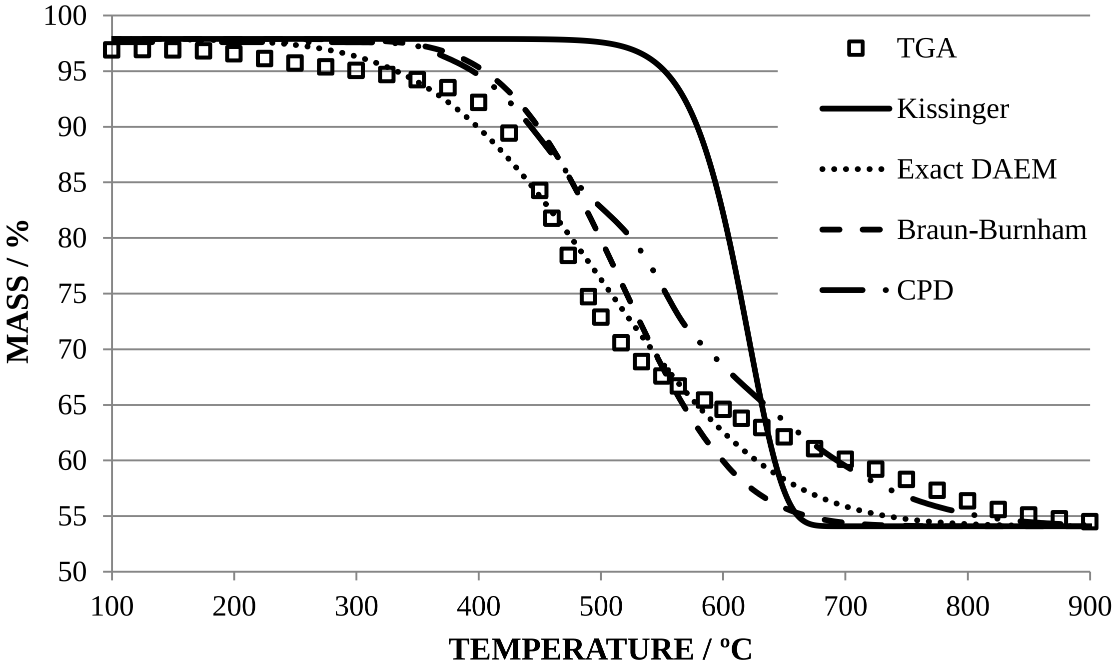

Figure A1. 12 – Experimental values of mass loss during coal devolatilization at 100 K min^{-1} and the predicted ones assuming first order single rate kinetic model, Braun-Burnham's method, analytical DAEM multifit solution and CPD.

A1. 4 Conclusions

In this section a review of different devolatilization model applied to a particular sub-bituminous coal is reported. The kinetics of Sulcis coal devolatilization has been studied using different global models. In general the agreement between different models is acceptable. However, due to the formulation of each model and the strong effect of secondary pyrolysis step in Sulcis coal some discrepancies have been observed.

The kinetic parameters obtained with Kissinger method presents a good agreement with literature data and with the results from other methods. Anyway, instead of the single rate model provides useful qualitative information in order to evaluate the pyrolysis behavior, its application is only valid under restricted hypothesis.

The numerical solutions of the DAEM allow obtaining kinetic parameters which can be extended to high heating rate application. However, this single DAE model presents the problem that kinetic parameters are highly correlated, thus it is necessary to fix one of them (the frequency factor in this work) in order to obtain for the others significant values. In order to increase the accuracy a 2-DAEM has been proposed with very goos results and a lower correlation between parameters. However, a notable increase on the complexity of the model is needed.

The Braun-Burnham's model, which has no need to set any kinetic parameter, represents properly the behavior of the Sulcis coal during pyrolysis, but the calculated kinetic parameters are higher when compared to the values obtained by other methods. However this method produces the better results with the lower quantity of experiments, instead of the losses of accuracy due to the intrinsic approximations of the model. Miura's model does not assume any functional forms of *f(E)* and *A(E)* in the DAEM. The parameters obtained applying this model shows that the hypothesis of Gaussian distribution and constant value of *A* are not strictly accurate for the Sulcis coal.

Kinetic parameters obtained from simulated data produced by the CPD model show value comparable to the kinetic set derived from the experimental data, but significant differences have been observed in DTG curves between simulated and experimental data. These divergences can be attributed to the formulation of CPD model, which separates the two pyrolysis steps as function of the composition of coal, extrapolating the coal actual behavior from a database build up by different coals and moreover at higher temperature rate than TG experiments, producing an overlap between primary and secondary steps. However, CPD model is a powerful tool in order to simulate coal devolatilization under combustion conditions and providing information about species evolution.

In conclusion, the approach based on a distribution of the activation energy seems to be the best option to model globally the pyrolysis process, despite some hypotheses necessary in its formulation which introduce inaccuracies in the results. The CPD model offers additional benefits, because it simulates well the devolatilization process, provides information about species evolution, and is open-source code easy to use, being however more accurate for high than low heating rates. Hence the choice of the specific modeling approach depends on the particularly aim of the study.

NOMENCLATURE

A_i	1/s	Frequency factor of reaction i
C_j	kmol/m^3	molar concentration of species j
C_D	-	drag function
d	m	diameter
d_p^*	-	dimensionless particle diameter
DEN	-	dimensionless value
D_{PL}	m^2/s	coefficient of diffusion thorough the product layer
e_{ss}	-	restitution coefficient
E_i	kJ/mol	Activation energy of reaction i
f_m	-	fractional loss of the conversion due to microporosity losses
f_w	-	net loss of total porosity in the particle
G_s	kg/m^{2}s	average solids feed rate per unit area
k	m/s	carbonation reaction constant
k_i	var.	kinetic constant of reaction i
k_s	m^4/ kmol s	intrinsic rate constant of CaO-CO$_2$ reaction
k'_s	m^4/ kmol s	effective intrinsic rate constant of CaO-CO$_2$ reaction
K_i	var.	equilibrium constant of SMR reaction i
K_j	var.	adsorption constant for species j
n	-	Reaction order

N	-	Number of cycle
N_{Ca}	kmol/m^3	number of moles of calcium carbonate per unit of volume of sorbent particle
P	Pa	pressure
P_j	Pa	partial pressure of species j
r	var.	reaction rate
r_0	1/s	CO_2 capture reaction rate, at the very beginning
r_i	kmol/s	Reaction rate of reaction i
r_i^*	1/s	effective reaction rate of SMR reaction i
S	m^2/g	specific surface
t	s	time
T	K	temperature
U	m/s	velocity
U^*	-	dimensionless superficial gas velocity
V_{CaO}	m^3/ kmol	CaO molar volume
X	-	CaO conversion
X_{CH4}	-	methane conversion
X_{CO2}	-	CO_2 carrying capacity ($gCO_2/g_{sorbent}$)
X_N	-	maximum carbonation conversion in the N cycle
Z	-	dimensionless molar volume ratio of calcium carbonate to calcium oxide

Greek letters

α	ºC / s	heating rate
α_k	-	volume fraction of phase k
β	kg/m^3 s	interphase momentum exchange coefficient
γ	-	Devolatilization dimensionless parameter
δ_{CaO}	m	average diameter of CaO grains in the sorbent
ΔH^0_{298}	kJ/mol	standard enthalpy of reaction
Δm_N	g	mass augment of the solid specimen at each single N
Δt	s	Time step
Δx	m	cell size
ε	-	voidage
η_i	-	effectiveness factors of SMR reaction i
Θ_s	m^2/s^2	granular temperature
ρ	kg/m^3	density
ϕ	-	particle sphericity
ϕ	º	angle of internal friction
σ_{CaO}	1/m	specific active surface of CaO grains

Subscripts

0	beginning of carbonation reaction
c	catalyst
eq	equilibrium
g	gas
mf	minimum fluidization

N	cycle N
p	particle
s	solid
t	terminal

Dimensionless numbers

Archimedes number	$Ar = \frac{\rho_g d_p^3 (\rho_s - \rho_g) g}{\mu_g^2}$
Froude number	$Fr = \left(\frac{u_0^2}{gL}\right)$
Courant number	$N_C = \frac{U_g \, \Delta t}{\Delta x}$
Reynolds number	$Re = \frac{\rho_g u \, L}{\mu_g}$
Particle Reynolds number	$Re_p = \frac{\rho_s d_p (\vec{u}_g - \vec{u}_s)}{\mu_g}$

Acronyms

AAU	Assigned Amount Units in International Emissions Trading
ASU	Air Separation Unit
ATR	Auto-Thermal Reforming
BFB	Bubbling Fluidized Bed
CaL	Calcium Looping
CCS	Carbon Capture and Storage
CDM	Clean Development Mechanism
CER	Certified Emission Reduction
CFB	Circulating Fluidized Bed

CFBC	Circulating Fluidized Bed Combustor
CFD	Computational Fluid Dynamics
CIRCE	Research Center on Energy Resources and Consumption
CLC	Chemical-Looping Combustion
DAEM	Distributed Activation Energy Model
DEM	Discrete Element Model
DNS	Direct Numerical Simulations
DOE	Design of Experiment
DSC	Differential Scanning Calorimetry
ECBM	Enhance Coal Bed Methane
ENEA	Italian National Agency for New Technologies, Energy, and the Sustainable Economic Development
EOR	Enhance Oil Recovery
ERU	Emission Reduction Units
EU	European Union
EU-ETS	European Emission Trading Scheme
FB	Fluidized Bed
FBC	Fluidized Bed Combustion
FCC	Fluid Catalytic Cracking
FFT	Fast Fourier Transform
GDP	Gross Domestic Product
GHG	Greenhouse Gas
HRSG	Heat Recovery Steam Generator
HTC	Hydrotalcite
IEA	International Energy Agency
IGCC	Integrated Gasification Combined Cycle
IL	Ionic Liquids
IPCC	Intergovernmental Panel on Climate Chang
JI	Joint implementation mechanism
KCE	Kinetic Compensation Effect
K-L	Kunii-Levenspiel Two Fluid Model
KTGF	Kinetic Theory of Granular Flow
MDEA	2n-Methyldiethanolamine

MEA	Monoethanolamine
NGCC	Natural Gas Combined Cycle
OECD	Organisation for Economic Co-operation and Development
PC	Pulverized Coal
PP	Power Plant
PSD	Particle Size Distribution
PSD	Pore Size Distribution
PV	Photovoltaic
PZ	Piperazine
RE	Richardson extrapolation
RFG	Recycled Flue Gas
SEM	Scanning Electron Microscope
SE-SMR	Sorption Enhanced Steam Methane Reforming
SMR	Steam Methane Reforming
SOFC	Solid Oxide Fuel Cell
TDH	Transport Disengaging Height
TFM	Two-Fluid Model
TGA	Thermogravimetric Analyzer
UNFCCC	United Nations Framework Convention on Climate Change
URANS	Unsteady-state Reynolds Averaged Navier-Stokes equations
USC	Ultra-supercritical
WGS	Water-Gas Shift
ZECOMIX	Zero Emission Coal MIXed

BIBLIOGRAPHY

[1] I.P.C.C., Climate Change 2007: Synthesis Report. Contribution of Working Groups I, II and III to the Fourth Assessment Report of the Intergovernmental Panel on Climate Change IPPC, 2007.

[2] S. Arrhenius, XXXI. On the influence of carbonic acid in the air upon the temperature of the ground, The London, Edinburgh, and Dublin Philosophical Magazine and Journal of Science, 41 (1896) 237-276.

[3] D. Etheridge, L. Steele, R. Langenfelds, R. Francey, Historical CO2 records from the Law Dome DE08, DE08-2, and DSS ice cores, in: A Compendium of Data on Global Change., Carbon Dioxide Information Analysis Center, Oak Ridge National Laboratory, U.S. Department of Energy, Oak Ridge, U.S.A., 1998.

[4] A. Neftel, H. Friedli, E. Moor, H. Lötscher, H. Oeschger, U. Siegenthaler, B. Stauffer, Historical carbon dioxide record from the Siple Station ice core, in: Trends: a compendium of data on global ghange, Carbon Dioxide Information Analysis Center, Oak Ridge National Laboratory, US Department of Energy, Oak Ridge,U.S.A., 1994.

[5] C. Keeling, T. Whorf, Atmospheric carbon dioxide record from Mauna Loa, in: Trends: A Compendium of Data on Global Change, Carbon Dioxide Information Analysis Center, Oak Ridge National Laboratory, U.S. Department of Energy, Oak Ridge,U.S.A., 2005.

[6] E. Monnin, E.J. Steig, U. Siegenthaler, K. Kawamura, J. Schwander, B. Stauffer, T.F. Stocker, D.L. Morse, J.-M. Barnola, B. Bellier, D. Raynaud, H. Fischer, Evidence for substantial accumulation rate variability in Antarctica during the Holocene, through synchronization of CO2 in the Taylor Dome, Dome C and DML ice cores, Earth and Planetary Science Letters, 224 (2004) 45-54.

[7] H. Fischer, M. Wahlen, J. Smith, D. Mastroianni, B. Deck, Ice Core Records of Atmospheric CO2 Around the Last Three Glacial Terminations, Science, 283 (1999) 1712-1714.

[8] N.N.H. Stern, The economics of climate change: the Stern review, Cambridge University Press, 2007.

[9] U.N.F.C.C.C., Kyoto Protocol to The United Nations Framework Convention on Climate Change United Nations, 1998.

[10] I.E.A., Redrawing Energy Climate Map., IEA/OECD, Paris, 2013.

[11] W.D. Nordhaus, A Review of the" Stern Review on the Economics of Climate Change", Journal of Economic Literature, (2007) 686-702.

[12] J.D. Sachs, Moving beyond Kyoto, Scientific American, 296 (2007) 30-30.

[13] J.E. Stiglitz, A Cool Calculus of Global Warming, Project Syndicate. http://www.project-syndicate.org/commentary/a-cool-calculus-of-global-warming, (2006).

[14] K.J. Arrow, Global climate change: a challenge to policy, The Economists' Voice, 4 (2007).

[15] M.L. Weitzman, A Review of The Stern Review on the Economics of Climate Change, Journal of Economic Literature, 45 (2007) 703-724.

[16] G.W. Yohe, R.S.J. Tol, The Stern Review: Implications for Climate Change, Environment: Science and Policy for Sustainable Development, 49 (2007) 36-43.

[17] N.M. Caminiti, Post Kyoto e cambiamenti climatici, ENEA, 2008.

[18] U. Springer, The market for tradable GHG permits under the Kyoto Protocol: a survey of model studies, Energy Economics, 25 (2003) 527-551.

[19] L.M. Abadie, J.M. Chamorro, European CO2 prices and carbon capture investments, Energy Economics, 30 (2008) 2992-3015.

[20] I.E.A., Technology Roadmap: Carbon Capture and Storage 2013, IEA/OECD, Paris, 2013.

[21] I.E.A., Energy Technology Perspectives 2012 - Pathways to a Clean Energy System, IEA/OECD, Paris, 2012.

[22] Z.E.P., CO2 Capture and Storage (CCS) - Creating a secure environment for investment in Europe, European Technology Platform for Zero Emission Fossil Fuel Power Plants, 2012.

[23] I.E.A., World Energy Outlook: 2009, IEA/OECD, Paris, 2009.

[24] I.E.A., World Energy Outlook: 2011, IEA/OECD, Paris, 2011.

[25] E.C.F., Roadmap 2050 - Technical & Economic Analysis - Full Report, European Climate Foundation, The Hague, 2010.

[26] B.P., BP Statistical Review of World Energy, British Pretroleum, London, 2010.

[27] W.E.C., World Energy Resources: 2013 Survey, World Energy Council, London, 2013.

[28] M.K. Hubbert, Nuclear energy and the fossil fuel, Drilling and production practice, (1956).

[29] M.I.T., The Future of Coal Massachusetts Institute of Technology, Cambridge, U.S.A., 2007.

[30] E.W.G., Coal: Resources and Future Production, Energy Watch Group, Munich, 2007.

[31] B. Kavalov, S.D. Peteves, The Future of Coal, EUR 22744 EN – DG JRC – Institute for Energy, Luxembourg, 2007.

[32] Eurostat, Coal consumption statistics, in: http://epp.eurostat.ec.europa.eu/statistics_explained/index.php/Coal_consumption_statistics, Statistical Office of the European Communities, Luxembourg, 2013.

[33] W.N.A., Nuclear Power in Italy. http://www.world-nuclear.org/info/Country-Profiles/Countries-G-N/Italy/, World Nuclear Association, 2013.

[34] TERNA, Dati statistici sull’energia elettrica in Italia - 2012, Terna S.p.A. - Rete Elettrica Nazionale, Rome, 2012.

[35] E. Macchi, A dieci anni dal Protocollo di Kyoto: politiche e scenari per il futuro, Seminari Pianeta 3000. Politecnico di Milano - Milano, (18 December 2007).

[36] R.E.E., El sistema eléctrico español, Red Eléctrica de España, Madrid, 2012.

[37] Assocarboni, Le Centrali a carbone in Italia, Associazione Generale Operatori Carboni, Rome, 2012.

[38] Carbunion, Memoria 2012, Federación Nacional de Empresarios de Minas de Carbón, Madrid, 2013.

[39] ENEL, Porto Tolle Project in: http://www.portotolleproject.com/, 2013.

[40] Assocarboni, L'Italia che va a carbone Il sole 24 ore, (2012).

[41] ELCOGAS, ELCOGAS IGCC plant: Clean coal technology. Experience and Future, in: http://www.elcogas.es/images/stories/7-noticias-documentos/2-documentos/3-presentaciones/general_2013_eng.pdf, 2013.

[42] F. García-Peña, Puertollano IGCC: Pilot plant for CO2 capture and H2 production, ELCOGAS - First Sharing Event in 2011 of the European CCS Demo Project Network. Compostilla, 9 June 2011.

[43] B. Arias, M.E. Diego, J.C. Abanades, M. Lorenzo, L. Diaz, D. Martínez, J. Alvarez, A. Sánchez-Biezma, Demonstration of steady state CO2 capture in a 1.7MWth calcium looping pilot, International Journal of Greenhouse Gas Control, 18 (2013) 237-245.

[44] M. Lupion, R. Diego, L. Loubeau, B. Navarrete, CIUDEN CCS Project: Status of the CO2 capture technology development plant in power generation, Energy Procedia, 4 (2011) 5639-5646.

[45] M. Lupion, B. Navarrete, P. Otero, V.J. Cortés, Experimental programme in CIUDEN's CO2 capture technology development plant for power generation, Chemical Engineering Research and Design, 89 (2011) 1494-1500.

[46] M. Lupion, I. Alvarez, P. Otero, R. Kuivalainen, J. Lantto, A. Hotta, H. Hack, 30 MWth CIUDEN Oxy-cfb Boiler - First Experiences, Energy Procedia, 37 (2013) 6179-6188.

[47] R.E.E., Mapa del sistema eléctrico, in: http://www.ree.es/sites/default/files/01_ACTIVIDADES/Documentos/Mapas-de-red/mapa_transporte_iberico_2013.pdf, Red Eléctrica de España, Madrid, 2013.

[48] M.I.E.E., Las centrales termoeléctricas. Consumos marginales, consumos medios y costes de arranque. Grupos de carbón., Delegación del Gobierno en la Explotación del Sistema Eléctrico. Ministerio de Industria y Energía, Madrid, 1988.

[49] I.P.C.C., IPCC Special Report on Carbon Dioxide Capture and Storage. Prepared by Working Group III of the Intergovernmental Panel on Climate Change [Metz, B., O. Davidson, H. C. de Coninck, M. Loos, and L. A. Meyer (eds.)], Cambridge University Press, 2005.

[50] I.E.A., CO2 Capture and storage: A key carbon abatement option, IEA/OECD, Paris, 2008.

[51] L.M. Romeo, L.I. Díez, M.P. Lisbona, A. González, I. Guedea, C. Lupiáñez, A. Martínez, Y. Lara, I. Bolea, Captura y almacenamiento de CO2, Prensas Universitarias de Zaragoza, 2010.

[52] M.E. Boot-Handford, J.C. Abanades, E.J. Anthony, M.J. Blunt, S. Brandani, N. Mac Dowell, J.R. Fernandez, M.-C. Ferrari, R. Gross, J.P. Hallett, R.S. Haszeldine, P. Heptonstall, A. Lyngfelt, Z. Makuch, E. Mangano, R.T.J. Porter, M. Pourkashanian, G.T. Rochelle, N. Shah, J.G. Yao, P.S. Fennell, Carbon capture and storage update, Energy & Environmental Science, 7 (2014) 130-189.

[53] T.A. Napp, A. Gambhir, T.P. Hills, N. Florin, P.S. Fennell, A review of the technologies, economics and policy instruments for decarbonising energy-intensive manufacturing industries, Renewable and Sustainable Energy Reviews, 30 (2014) 616-640.

[54] M. FInkenrath, Cost and Performance of Carbon Dioxide Capture from Power Generation, IEA/OECD, Paris, 2012.

[55] I.E.A., Projected Costs of Generating Electricity, IEA/NEA/OECD, Paris, 2010.

[56] I.E.A., Medium-Term Coal Market Report 2012, IEA/OECD, Paris, 2012.

[57] G. Göttlicher, R. Pruschek, Comparison of CO2 removal systems for fossil-fuelled power plant processes, Energy Conversion and Management, 38 (1997) S173-S178.

[58] A.B. Rao, E.S. Rubin, A Technical, Economic, and Environmental Assessment of Amine-Based CO2 Capture Technology for Power Plant Greenhouse Gas Control, Environmental Science & Technology, 36 (2002) 4467-4475.

[59] G.T. Rochelle, Amine Scrubbing for CO2 Capture, Science, 325 (2009) 1652-1654.

[60] G. Puxty, R. Rowland, A. Allport, Q. Yang, M. Bown, R. Burns, M. Maeder, M. Attalla, Carbon Dioxide Postcombustion Capture: A Novel Screening Study of the Carbon Dioxide Absorption Performance of 76 Amines, Environmental Science & Technology, 43 (2009) 6427-6433.

[61] H. Herzog, J. Meldon, A. Hatton, Advanced Post-Combustion CO2 Capture M.I.T. http://sequestration.mit.edu/pdf/Advanced_Post_Combustion_CO2_Capture.pdf, 2009.

[62] G. Rochelle, E. Chen, S. Freeman, D. Van Wagener, Q. Xu, A. Voice, Aqueous piperazine as the new standard for CO2 capture technology, Chemical Engineering Journal, 171 (2011) 725-733.

[63] E.D. Bates, R.D. Mayton, I. Ntai, J.H. Davis, CO2 Capture by a Task-Specific Ionic Liquid, Journal of the American Chemical Society, 124 (2002) 926-927.

[64] J.F. Brennecke, B.E. Gurkan, Ionic Liquids for CO2 Capture and Emission Reduction, The Journal of Physical Chemistry Letters, 1 (2010) 3459-3464.

[65] F. Karadas, M. Atilhan, S. Aparicio, Review on the Use of Ionic Liquids (ILs) as Alternative Fluids for CO2 Capture and Natural Gas Sweetening, Energy & Fuels, 24 (2010) 5817-5828.

[66] A. Basile, F. Gallucci, P. Morrone, A. Iulianelli, Development of advanced CO2-separation technology, in: M.M. Maroto-Valer (Ed.) Developments and innovation on CCS technology, Woodhead Publishing, 2010.

[67] P. Luis, T. Van Gerven, B. Van der Bruggen, Recent developments in membrane-based technologies for CO2 capture, Progress in Energy and Combustion Science, 38 (2012) 419-448.

[68] T.C. Merkel, H. Lin, X. Wei, R. Baker, Power plant post-combustion carbon dioxide capture: An opportunity for membranes, Journal of Membrane Science, 359 (2010) 126-139.

[69] J. Blamey, E.J. Anthony, J. Wang, P.S. Fennell, The calcium looping cycle for large-scale CO2 capture, Progress in Energy and Combustion Science, 36 (2010) 260-279.

[70] Q. Wang, J. Luo, Z. Zhong, A. Borgna, CO2 capture by solid adsorbents and their applications: current status and new trends, Energy & Environmental Science, 4 (2011) 42-55.

[71] J.C. Abanades, E.S. Rubin, E.J. Anthony, Sorbent Cost and Performance in CO2 Capture Systems, Industrial & Engineering Chemistry Research, 43 (2004) 3462-3466.

[72] C.C. Dean, J. Blamey, N.H. Florin, M.J. Al-Jeboori, P.S. Fennell, The calcium looping cycle for CO2 capture from power generation, cement manufacture and hydrogen production, Chemical Engineering Research and Design, 89 (2011) 836-855.

[73] B.J.P. Buhre, L.K. Elliott, C.D. Sheng, R.P. Gupta, T.F. Wall, Oxy-fuel combustion technology for coal-fired power generation, Progress in Energy and Combustion Science, 31 (2005) 283-307.

[74] T.F. Wall, Combustion processes for carbon capture, Proceedings of the Combustion Institute, 31 (2007) 31-47.

[75] L. Chen, S.Z. Yong, A.F. Ghoniem, Oxy-fuel combustion of pulverized coal: Characterization, fundamentals, stabilization and CFD modeling, Progress in Energy and Combustion Science, 38 (2012) 156-214.

[76] G. Scheffknecht, L. Al-Makhadmeh, U. Schnell, J. Maier, Oxy-fuel coal combustion—A review of the current state-of-the-art, International Journal of Greenhouse Gas Control, 5, Supplement 1 (2011) S16-S35.

[77] M.B. Toftegaard, J. Brix, P.A. Jensen, P. Glarborg, A.D. Jensen, Oxy-fuel combustion of solid fuels, Progress in Energy and Combustion Science, 36 (2010) 581-625.

[78] H. Jericha, E. Göttlich, W. Sanz, F. Heitmeir, Design Optimization of the Graz Cycle Prototype Plant, Journal of Engineering for Gas Turbines and Power, 126 (2004) 733-740.

[79] H.M. Kvamsdal, K. Jordal, O. Bolland, A quantitative comparison of gas turbine cycles with capture, Energy, 32 (2007) 10-24.

[80] P. Mathieu, Towards the hydrogen era using near-zero CO2 emissions energy systems, Energy, 29 (2004) 1993-2002.

[81] A. Lyngfelt, Chemical-looping combustion of solid fuels – Status of development, Applied Energy, 113 (2014) 1869-1873.

[82] J. Adanez, A. Abad, F. Garcia-Labiano, P. Gayan, L.F. de Diego, Progress in Chemical-Looping Combustion and Reforming technologies, Progress in Energy and Combustion Science, 38 (2012) 215-282.

[83] M.M. Hossain, H.I. de Lasa, Chemical-looping combustion (CLC) for inherent separations—a review, Chemical Engineering Science, 63 (2008) 4433-4451.

[84] L.M. Romeo, P. Lisbona, C. Lupiáñez, M. Gil, A. González, I. Guedea, A. Rezeau, I. Bolea, C. Bartolomé, J. Meza, G. Mazuque, J.A. Ramírez, Análisis de ciclos de cero emisiones, Energia, 33 (2007) 66-75.

[85] M. Kanniche, R. Gros-Bonnivard, P. Jaud, J. Valle-Marcos, J.-M. Amann, C. Bouallou, Pre-combustion, post-combustion and oxy-combustion in thermal power plant for CO2 capture, Applied Thermal Engineering, 30 (2010) 53-62.

[86] K. Damen, M. van Troost, A. Faaij, W. Turkenburg, A comparison of electricity and hydrogen production systems with CO2 capture and storage—Part B: Chain analysis of promising CCS options, Progress in Energy and Combustion Science, 33 (2007) 580-609.

[87] R. Steeneveldt, B. Berger, T.A. Torp, CO2 Capture and Storage: Closing the Knowing–Doing Gap, Chemical Engineering Research and Design, 84 (2006) 739-763.

[88] D.P. Harrison, Sorption-Enhanced Hydrogen Production: A Review, Industrial & Engineering Chemistry Research, 47 (2008) 6486-6501.

[89] K. Damen, M.v. Troost, A. Faaij, W. Turkenburg, A comparison of electricity and hydrogen production systems with CO2 capture and storage. Part A: Review and selection of promising conversion and capture technologies, Progress in Energy and Combustion Science, 32 (2006) 215-246.

[90] L. Barelli, G. Bidini, F. Gallorini, S. Servili, Hydrogen production through sorption-enhanced steam methane reforming and membrane technology: A review, Energy, 33 (2008) 554-570.

[91] J. Meyer, J. Mastin, T.-K. Bjørnebøle, T. Ryberg, N. Eldrup, Techno-economical study of the Zero Emission Gas power concept, Energy Procedia, 4 (2011) 1949-1956.

[92] S.-Y. Lin, Y. Suzuki, H. Hatano, M. Harada, Developing an innovative method, HyPr-RING, to produce hydrogen from hydrocarbons, Energy Conversion and Management, 43 (2002) 1283-1290.

[93] T. Weimer, R. Berger, C. Hawthorne, J.C. Abanades, Lime enhanced gasification of solid fuels: Examination of a process for simultaneous hydrogen production and CO2 capture, Fuel, 87 (2008) 1678-1686.

[94] S. Ramkumar, M.V. Iyer, L.-S. Fan, Calcium Looping Process for Enhanced Catalytic Hydrogen Production with Integrated Carbon Dioxide and Sulfur Capture, Industrial & Engineering Chemistry Research, 50 (2010) 1716-1729.

[95] T. Pröll, C. Aichernig, R. Rauch, H. Hofbauer, Fluidized bed steam gasification of solid biomass - Performance characteristics of an 8 MWth combined heat and power plant, International Journal of Chemical Reactor Engineering, 5 (2007).

[96] I.E.A., Resources to Reserves: Oil and Gas Technologies for the Energy Markets of the Future, IEA/OECD, Paris, 2005.

[97] S. Bachu, Screening and ranking of sedimentary basins for sequestration of CO2 in geological media in response to climate change, Env Geol, 44 (2003) 277-289.

[98] J.K. Eccles, L. Pratson, R.G. Newell, R.B. Jackson, Physical and Economic Potential of Geological CO2 Storage in Saline Aquifers, Environmental Science & Technology, 43 (2009) 1962-1969.

[99] J. Gale, Geological storage of CO2: What do we know, where are the gaps and what more needs to be done?, Energy, 29 (2004) 1329-1338.

[100] J.D. Figueroa, T. Fout, S. Plasynski, H. McIlvried, R.D. Srivastava, Advances in CO2 capture technology—The U.S. Department of Energy's Carbon Sequestration Program, International Journal of Greenhouse Gas Control, 2 (2008) 9-20.

[101] D. Civile, M. Zecchin, E. Forlin, F. Donda, V. Volpi, B. Merson, S. Persoglia, CO2 geological storage in the Italian carbonate successions, International Journal of Greenhouse Gas Control, 19 (2013) 101-116.

[102] R. Martínez, I. Suárez, M.A. Zapatero, B. Saftic, I. Kolenkovic, M. Car, S. Persoglia, F. Donda, The EU Geocapacity Project—Saline aquifers storage capacity in Group South countries, Energy Procedia, 1 (2009) 2733-2740.

[103] J. Ruby, A.A. Johnson, H. Ziock, Gasification for carbon capture and zero emission, in, 2004, pp. 961-968.

[104] H. Ziock, K. Lackner, D. Harrison, Zero emission coal power, a new concept, in: First National Conference on Carbon Sequestration, 2001.

[105] A. Calabrò, P. Deiana, P. Fiorini, G. Girardi, S. Stendardo, Possible optimal configurations for the ZECOMIX high efficiency zero emission hydrogen and power plant, Energy, 33 (2008) 952-962.

[106] G. Galeno, G. Spazzafumo, ZECOMIX: Performance of alternative lay-outs, International Journal of Hydrogen Energy, 35 (2010) 9845-9850.

[107] M.C. Romano, G.G. Lozza, Long-term coal gasification-based power plants with near-zero emissions. Part A: Zecomix cycle, International Journal of Greenhouse Gas Control, 4 (2010) 459-468.

[108] P. Chiesa, L. Mazzocchi, G. Lozza, Using Hydrogen as Gas Turbine Fuel, Journal of Engineering for Gas Turbines and Power, 127 (2005) 73-80.

[109] D.B. Anthony, J.B. Howard, Coal devolatilization and hydrogastification, AIChE Journal, 22 (1976) 625-656.

[110] A. Tomita, O.P. Mahajan, P.L. Walker Jr, Reactivity of heat-treated coals in hydrogen, Fuel, 56 (1977) 137-144.

[111] M.E. Toomajian, M.G. Lussier, D.J. Miller, Effect of oxidation and other treatments on hydrogasification rate of coal char, Fuel, 71 (1992) 1055-1061.

[112] V. Calemma, L.R. Radovic, On the gasification reactivity of Italian Sulcis coal, Fuel, 70 (1991) 1027-1030.

[113] A. D'Alessio, P. Vergamini, E. Benedetti, FT-IR investigation of the structural changes of Sulcis and South Africa coals under progressive heating in vacuum, Fuel, 79 (2000) 1215-1220.

[114] A. Del Bianco, E. Girardi, F. Stroppa, Liquefaction of Sulcis subbituminous coal in a CO/water/base system, Fuel, 69 (1990) 240-244.

[115] L. Conti, R. Rausa, Flash pyrolysis of an Italian low rank coal, Fuel Processing Technology, 17 (1987) 107-115.

[116] S. Scaccia, A. Calabrò, R. Mecozzi, Investigation of the evolved gases from Sulcis coal during pyrolysis under N2 and H2 atmospheres, Journal of Analytical and Applied Pyrolysis, 98 (2012) 45-50.

[117] S. Scaccia, Reattività di gassificazione di residuo di pirolisi del carbone Sulcis per produzione di gas, in, Report ENEA, RDS/2012/180, 2012.

[118] S. Scaccia, A. Calabrò, Idrogassificazione del carbone Sulcis per la produzione di metano. Studi preliminari, in, Report ENEA, RDS/2010/43, 2010.

[119] S. Scaccia, TG–FTIR and kinetics of devolatilization of Sulcis coal, Journal of Analytical and Applied Pyrolysis, 104 (2013) 95-102.

[120] A. D'Alessio, A.M. Raspolli-Galletti, D. Licursi, M. Martinelli, FT-IR Investigation of the Structural Changes of Sulcis and South Africa Coals under Progressive Heating in Vacuum: Correlation with Volatile Matter, Journal of Combustion, 2013 (2013) 14.

[121] A. Lallai, A. Pistis, E. Fois, Kinetics of sulcis coal chemical cleaning process, Chemical Engineering Transactions, 29 (2012) 943-948.

[122] A. Pettinau, F. Ferrara, C. Amorino, Techno-economic comparison between different technologies for a CCS power generation plant integrated with a sub-bituminous coal mine in Italy, Applied Energy, 99 (2012) 32-39.

[123] A. Pettinau, F. Ferrara, C. Amorino, Combustion vs. gasification for a demonstration CCS (carbon capture and storage) project in Italy: A techno-economic analysis, Energy, 50 (2013) 160-169.

[124] A. Pettinau, A. Orsini, G. Calì, F. Ferrara, The Sotacarbo coal gasification experimental plant for a CO2-free hydrogen production, International Journal of Hydrogen Energy, 35 (2010) 9836-9844.

[125] Chemstations, ChemCad 5.2 User's manual, Chemstations, Inc., (2000).

[126] A. Calabrò, C. Herce, E. Veca, Analisi parametrico del processo di idrogassificazione di carbone In un reattore a letto fisso, in, Unpublished Report ENEA, COMSO/2010/004/IP, 2010.

[127] G.S. Grasa, J.C. Abanades, CO2 Capture Capacity of CaO in Long Series of Carbonation/Calcination Cycles, Industrial & Engineering Chemistry Research, 45 (2006) 8846-8851.

[128] J.C. Abanades, E.J. Anthony, D.Y. Lu, C. Salvador, D. Alvarez, Capture of CO2 from combustion gases in a fluidized bed of CaO, AIChE Journal, 50 (2004) 1614-1622.

[129] K. Gallucci, S. Stendardo, P.U. Foscolo, CO2 capture by means of dolomite in hydrogen production from syn gas, International Journal of Hydrogen Energy, 33 (2008) 3049-3055.

[130] J. Delgado, M.P. Aznar, J. Corella, Calcined dolomite, magnesite, and calcite for cleaning hot gas from a fluidized bed biomass gasifier with steam: Life and usefulness, Industrial and Engineering Chemistry Research, 35 (1996) 3637-3643.

[131] J. Wang, V. Manovic, Y. Wu, E.J. Anthony, A study on the activity of CaO-based sorbents for capturing CO2 in clean energy processes, Applied Energy, 87 (2010) 1453-1458.

[132] Z.S. Li, N.S. Cai, Y.Y. Huang, H.J. Han, Synthesis, experimental studies, and analysis of a new calcium-based carbon dioxide absorbent, Energy and Fuels, 19 (2005) 1447-1452.

[133] Z.S. Li, N.S. Cai, Y.Y. Huang, Effect of preparation temperature on cyclic CO2 capture and multiple carbonation-calcination cycles for a new Ca-based CO2 sorbent, Industrial and Engineering Chemistry Research, 45 (2006) 1911-1917.

[134] R. Pacciani, C.R. Müller, J.F. Davidson, J.S. Dennis, A.N. Hayhurst, Synthetic Ca-based solid sorbents suitable for capturing CO2 in a fluiqized bed, Canadian Journal of Chemical Engineering, 86 (2008) 356-366.

[135] V. Manovic, E.J. Anthony, CaO-based pellets supported by calcium aluminate cements for high-temperature CO2 capture, Environmental Science and Technology, 43 (2009) 7117-7122.

[136] H. Gupta, L.S. Fan, Carbonation-calcination cycle using high reactivity calcium oxide for carbon dioxide separation from flue gas, Industrial and Engineering Chemistry Research, 41 (2002) 4035-4042.

[137] B.R. Stanmore, P. Gilot, Review—calcination and carbonation of limestone during thermal cycling for CO2 sequestration, Fuel Processing Technology, 86 (2005) 1707-1743.

[138] S. Stendardo, P.U. Foscolo, Carbon dioxide capture with dolomite: A model for gas–solid reaction within the grains of a particulate sorbent, Chemical Engineering Science, 64 (2009) 2343-2352.

[139] Z. Chen, H.S. Song, M. Portillo, C.J. Lim, J.R. Grace, E.J. Anthony, Long-Term Calcination/Carbonation Cycling and Thermal Pretreatment for CO2 Capture by Limestone and Dolomite, Energy & Fuels, 23 (2009) 1437-1444.

[140] C.S. Martavaltzi, A.A. Lemonidou, Parametric study of the CaO-Ca12Al14O33 synthesis with respect to high CO2 sorption capacity and stability on multicycle operation, Industrial and Engineering Chemistry Research, 47 (2008) 9537-9543.

[141] J.S. Dennis, R. Pacciani, The rate and extent of uptake of CO2 by a synthetic, CaO-containing sorbent, Chemical Engineering Science, 64 (2009) 2147-2157.

[142] N.H. Florin, J. Blamey, P.S. Fennell, Synthetic CaO-based sorbent for CO2 capture from large-point sources, Energy and Fuels, 24 (2010) 4598-4604.

[143] V. Manovic, E.J. Anthony, Thermal Activation of CaO-Based Sorbent and Self-Reactivation during CO2 Capture Looping Cycles, Environmental Science & Technology, 42 (2008) 4170-4174.

[144] A.I. Lysikov, A.N. Salanov, A.G. Okunev, Change of CO2 Carrying Capacity of CaO in Isothermal Recarbonation−Decomposition Cycles, Industrial & Engineering Chemistry Research, 46 (2007) 4633-4638.

[145] V. Manovic, E.J. Anthony, Lime-Based Sorbents for High-Temperature CO2 Capture—A Review of Sorbent Modification Methods, International Journal of Environmental Research and Public Health, 7 (2010) 3129-3140.

[146] A. Silaban, D.P. Harrison, High temperature capture of carbon dioxide: characteristics of the reversible reaction between CaO(s) and CO2(g), Chemical Engineering Communications, 137 (1995) 177-190.

[147] J. Blamey, N.P.M. Paterson, D.R. Dugwell, P. Stevenson, P.S. Fennell, Reactivation of a CaO-based sorbent for CO2 capture from stationary sources, Proceedings of the Combustion Institute, 33 (2011) 2673-2681.

[148] V. Manovic, E.J. Anthony, Steam Reactivation of Spent CaO-Based Sorbent for Multiple CO2 Capture Cycles, Environmental Science & Technology, 41 (2007) 1420-1425.

[149] H.K. Rusten, E. Ochoa-Fernández, H. Lindborg, D. Chen, H.A. Jakobsen, Hydrogen production by sorption-enhanced steam methane reforming using lithium oxides as CO2-acceptor, Industrial and Engineering Chemistry Research, 46 (2007) 8729-8737.

[150] J.C. Abanades, R. Murillo, J.R. Fernandez, G. Grasa, I. Martínez, New CO2 capture process for hydrogen production combining Ca and Cu chemical loops, Environmental Science and Technology, 44 (2010) 6901-6904.

[151] Q. Wang, Z. Wu, H.H. Tay, L. Chen, Y. Liu, J. Chang, Z. Zhong, J. Luo, A. Borgna, High temperature adsorption of CO2 on Mg-Al hydrotalcite: Effect of the charge compensating anions and the synthesis pH, Catalysis Today, 164 (2011) 198-203.

[152] R.H. Borgwardt, Calcium oxide sintering in atmospheres containing water and carbon dioxide, Ind. Eng. Chem. Res., 28 (1989) 493-500.

[153] D. Beruto, L. Barco, A.W. Searcy, CO2–catalyzed surface area and porosity changes in high-surface area CaO aggregates, J. Am. Cer. Soc., 67 (1984) 512–515.

[154] J. Ewing, L. Beruto, A.W. Searcy, The nature of CaO produced by calcite powder decomposition in vacuum and in CO2, J. Am. Cer. Soc., 62 (1975) 580–584.

[155] T. Shimizu, T. Hirama, H. Hosoda, K. Kitano, M. Inagaki, K. Tejima, A Twin Fluid-Bed Reactor for Removal of CO2 from Combustion Processes, Chemical Engineering Research and Design, 77 (1999) 62-68.

[156] R.A.W. Haul, L.H. Stein, J.W.L. De Villiers, Exchange of Carbon-13 Dioxide between Calcite Crystals and Gaseous Carbon Dioxide, Nature, 171 (1953) 619-620.

[157] A.J. Dedman, A.J. Owen, Calcium cyanamide synthesis. Part 4.-The reaction CaO + CO2= CaCo3, Transactions of the Faraday Society, 58 (1962) 2027-2035.

[158] T.F. Anderson, Self-diffusion of carbon and oxygen in calcite by isotope exchange with carbon dioxide, Journal of Geophysical Research, 74 (1969) 3918-3932.

[159] R. Barker, The reversibility of the reaction CaCO3 ⇄ CaO+CO2, Journal of Applied Chemistry and Biotechnology, 23 (1973) 733-742.

[160] J.C. Abanades, D. Alvarez, Conversion Limits in the Reaction of CO2 with Lime, Energy & Fuels, 17 (2003) 308-315.

[161] P. Sun, J.R. Grace, C.J. Lim, E.J. Anthony, The effect of CaO sintering on cyclic CO2 capture in energy systems, AIChE Journal, 53 (2007) 2432-2442.

[162] P. Sun, C.J. Lim, J.R. Grace, Cyclic CO2 capture by limestone-derived sorbent during prolonged calcination/carbonation cycling, AIChE Journal, 54 (2008) 1668-1677.

[163] K. Chrissafis, C. Dagounaki, K.M. Paraskevopoulos, The effects of procedural variables on the maximum capture efficiency of CO2 using a carbonation/calcination cycle of carbonate rocks, Thermochimica Acta, 428 (2005) 193-198.

[164] M. Alonso, M. Lorenzo, B. González, J.C. Abanades, Precalcination of CaCO3 as a Method to Stabilize CaO Performance for CO2 Capture from Combustion Gases, Energy & Fuels, 25 (2011) 5521-5527.

[165] V. Manovic, E.J. Anthony, Screening of Binders for Pelletization of CaO-Based Sorbents for CO2 Capture†, Energy & Fuels, 23 (2009) 4797-4804.

[166] V. Manovic, E.J. Anthony, D. Loncarevic, CO2 looping cycles with CaO-based sorbent pretreated in CO2 at high temperature, Chemical Engineering Science, 64 (2009) 3236-3245.

[167] D.C. Ozcan, B.H. Shanks, T.D. Wheelock, Improving the stability of a CaO-based sorbent for CO 2 by thermal pretreatment, Industrial and Engineering Chemistry Research, 50 (2011) 6933-6942.

[168] B. Arias, G.S. Grasa, M. Alonso, J.C. Abanades, Post-combustion calcium looping process with a highly stable sorbent activity by recarbonation, Energy & Environmental Science, 5 (2012) 7353-7359.

[169] J.M. Valverde, Ca-based synthetic materials with enhanced CO2 capture efficiency, Journal of Materials Chemistry A, 1 (2013) 447-468.

[170] S. Choi, J.H. Drese, C.W. Jones, Adsorbent Materials for Carbon Dioxide Capture from Large Anthropogenic Point Sources, ChemSusChem, 2 (2009) 796-854.

[171] Y. Ding, E. Alpay, Equilibria and kinetics of CO2 adsorption on hydrotalcite adsorbent, Chemical Engineering Science, 55 (2000) 3461-3474.

[172] J.R. Hufton, S. Mayorga, S. Sircar, Sorption-enhanced reaction process for hydrogen production, AIChE Journal, 45 (1999) 248-256.

[173] H.T.J. Reijers, S.E.A. Valster-Schiermeier, P.D. Cobden, R.W. van den Brink, Hydrotalcite as CO2 Sorbent for Sorption-Enhanced Steam Reforming of Methane, Industrial & Engineering Chemistry Research, 45 (2005) 2522-2530.

[174] N.N.A.H. Meis, J.H. Bitter, K.P. de Jong, Support and Size Effects of Activated Hydrotalcites for Precombustion CO2 Capture, Industrial & Engineering Chemistry Research, 49 (2009) 1229-1235.

[175] E.L.G. Oliveira, C.A. Grande, A.E. Rodrigues, CO2 sorption on hydrotalcite and alkali-modified (K and Cs) hydrotalcites at high temperatures, Separation and Purification Technology, 62 (2008) 137-147.

[176] K. Nakagawa, T. Ohashi, A novel method of CO 2 capture from high temperature gases, Journal of the Electrochemical Society, 145 (1998) 1344-1346.

[177] M. Kato, S. Yoshikawa, K. Nakagawa, Carbon dioxide absorption by lithium orthosilicate in a wide range of temperature and carbon dioxide concentrations, Journal of Materials Science Letters, 21 (2002) 485-487.

[178] J.-i. Ida, R. Xiong, Y.S. Lin, Synthesis and CO2 sorption properties of pure and modified lithium zirconate, Separation and Purification Technology, 36 (2004) 41-51.

[179] D.J. Fauth, E.A. Frommell, J.S. Hoffman, R.P. Reasbeck, H.W. Pennline, Eutectic salt promoted lithium zirconate: Novel high temperature sorbent for CO2 capture, Fuel Processing Technology, 86 (2005) 1503-1521.

[180] E. Ochoa-Fernández, M. Rønning, T. Grande, D. Chen, Synthesis and CO2 Capture Properties of Nanocrystalline Lithium Zirconate, Chemistry of Materials, 18 (2006) 6037-6046.

[181] F.-C. Yu, N. Phalak, Z. Sun, L.-S. Fan, Activation Strategies for Calcium-Based Sorbents for CO2 Capture: A Perspective, Industrial & Engineering Chemistry Research, 51 (2011) 2133-2142.

[182] W. Liu, N.W.L. Low, B. Feng, G. Wang, J.C. Diniz da Costa, Calcium Precursors for the Production of CaO Sorbents for Multicycle CO2 Capture, Environmental Science & Technology, 44 (2009) 841-847.

[183] Y.-j. Li, C.-s. Zhao, L.-b. Duan, C. Liang, Q.-z. Li, W. Zhou, H.-c. Chen, Cyclic calcination/carbonation looping of dolomite modified with acetic acid for CO2 capture, Fuel Processing Technology, 89 (2008) 1461-1469.

[184] Y.J. Li, C.S. Zhao, C.R. Qu, L.B. Duan, Q.Z. Li, C. Liang, CO2 Capture Using CaO Modified with Ethanol/Water Solution during Cyclic Calcination/Carbonation, Chemical Engineering & Technology, 31 (2008) 237-244.

[185] G. Grasa, B. González, M. Alonso, J.C. Abanades, Comparison of CaO-based synthetic CO2 sorbents under realistic calcination conditions, Energy and Fuels, 21 (2007) 3560-3562.

[186] J.A. Shearer, I. Johnson, C.B. Turner, Effects of sodium chloride on limestone calcination and sulfation in fluidized-bed combustion, Environmental Science & Technology, 13 (1979) 1113-1118.

[187] C. Salvador, D. Lu, E.J. Anthony, J.C. Abanades, Enhancement of CaO for CO2 capture in an FBC environment, Chemical Engineering Journal, 96 (2003) 187-195.

[188] E.P. Reddy, P.G. Smirniotis, High-Temperature Sorbents for CO2 Made of Alkali Metals Doped on CaO Supports, The Journal of Physical Chemistry B, 108 (2004) 7794-7800.

[189] H. Lu, A. Khan, S.E. Pratsinis, P.G. Smirniotis, Flame-Made Durable Doped-CaO Nanosorbents for CO2 Capture, Energy & Fuels, 23 (2008) 1093-1100.

[190] R. Barker, The reactivity of calcium oxide towards carbon dioxide and its use for energy storage, Journal of Applied Chemistry and Biotechnology, 24 (1974) 221-227.

[191] N.H. Florin, A.T. Harris, Reactivity of CaO derived from nano-sized CaCO3 particles through multiple CO2 capture-and-release cycles, Chemical Engineering Science, 64 (2009) 187-191.

[192] M. Wang, C.-G. Lee, C.-K. Ryu, CO2 sorption and desorption efficiency of Ca2SiO4, International Journal of Hydrogen Energy, 33 (2008) 6368-6372.

[193] L. Li, D.L. King, Z. Nie, C. Howard, Magnesia-Stabilized Calcium Oxide Absorbents with Improved Durability for High Temperature CO2 Capture, Industrial & Engineering Chemistry Research, 48 (2009) 10604-10613.

[194] M. Aihara, T. Nagai, J. Matsushita, Y. Negishi, H. Ohya, Development of porous solid reactant for thermal-energy storage and temperature upgrade using carbonation/decarbonation reaction, Applied Energy, 69 (2001) 225-238.

[195] C.S. Martavaltzi, A.A. Lemonidou, Development of new CaO based sorbent materials for CO2 removal at high temperature, Microporous and Mesoporous Materials, 110 (2008) 119-127.

[196] C.S. Martavaltzi, A.A. Lemonidou, Hydrogen production via sorption enhanced reforming of methane: Development of a novel hybrid material—reforming catalyst and CO2 sorbent, Chemical Engineering Science, 65 (2010) 4134-4140.

[197] K.R. Rout, H.A. Jakobsen, A numerical study of pellets having both catalytic- and capture properties for SE-SMR process: Kinetic- and product layer diffusion controlled regimes, Fuel Processing Technology, 106 (2013) 231-246.

[198] J.S. Dennis, A.N. Hayhurst, the effect of CO2 on the kinetics and extent of calcination of limestone and dolomite particles in fluidised beds, Chemical Engineering Science, 42 (1987) 2361-2372.

[199] F. García-Labiano, A. Abad, L.F. de Diego, P. Gayán, J. Adánez, Calcination of calcium-based sorbents at pressure in a broad range of CO2 concentrations, Chemical Engineering Science, 57 (2002) 2381-2393.

[200] A. Abad, H2S removal from gasification derived syngas in pressurized moving fixed bed (in Spanish), in: Instituto de Carboquimica – CSIC, 2003.

[201] S.K. Bhatia, D.D. Perlmutter, Effect of the product layer on the kinetics of the CO2-lime reaction, AIChE Journal, 29 (1983) 79-86.

[202] B. Arias, G.S. Grasa, J.C. Abanades, Effect of sorbent hydration on the average activity of CaO in a Ca-looping system, Chemical Engineering Journal, 163 (2010) 324-330.

[203] P. Lisbona, A. Martínez, Y. Lara, L.M. Romeo, Integration of Carbonate CO2 Capture Cycle and Coal-Fired Power Plants. A Comparative Study for Different Sorbents, Energy & Fuels, 24 (2009) 728-736.

[204] A. Silaban, M. Narcida, D.P. Harrison, Characteristics of the reversible reaction between CO2(g) and calcined dolomite, Chemical Engineering Communications, 146 (1996) 149-162.

[205] L.A. Stanciu, V.Y. Kodash, J.R. Groza, Effects of Heating Rate on Densification and Grain Growth during Field-Assisted Sintering of -Al2O3 and MoSi2 Powders, Metallurgical and Materials Transactions A, 32 (2001) 2633-2638.

[206] C.-F. Yan, J.R. Grace, C.J. Lim, Effects of rapid calcination on properties of calcium-based sorbents, Fuel Processing Technology, 91 (2010) 1678-1686.

[207] R.M. German, Sintering Theory and Practice, John Wiley and Sons, New York, 1996.

[208] D. Alvarez, J.C. Abanades, Determination of the Critical Product Layer Thickness in the Reaction of CaO with CO2, Industrial & Engineering Chemistry Research, 44 (2005) 5608-5615.

[209] A.B. Fuertes, D. Alvarez, F. Rubiera, J.J. Pis, G. MarbÁN, J.M. Palacos, Surface area and pore size changes during sintering of calcium oxide particles, Chemical Engineering Communications, 109 (1991) 73-88.

[210] V. Manovic, E.J. Anthony, Parametric Study on the CO2 Capture Capacity of CaO-Based Sorbents in Looping Cycles, Energy & Fuels, 22 (2008) 1851-1857.

[211] G. Grasa, J.C. Abanades, E.J. Anthony, Effect of Partial Carbonation on the Cyclic CaO Carbonation Reaction, Industrial & Engineering Chemistry Research, 48 (2009) 9090-9096.

[212] D. Mess, A.F. Sarofim, J.P. Longwell, Product Layer Diffusion during the Reaction of Calcium Oxide with Carbon Dioxide, Energy & Fuels, 13 (1999) 999-1005.

[213] J. Szekely, J.W. Evans, H.Y. Sohn, Gas Solid Reactions, Academic Press, London, 1976.

[214] P. Sun, J.R. Grace, C.J. Lim, E.J. Anthony, Determination of intrinsic rate constants of the CaO–CO2 reaction, Chemical Engineering Science, 63 (2008) 47-56.

[215] S. Stendardo, L.K. Andersen, C. Herce, Self-activation and effect of regeneration conditions in CO2–carbonate looping with CaO–Ca12Al14O33 sorbent, Chemical Engineering Journal, 220 (2013) 383-394.

[216] J. Kozeny, Ueber kapillare Leitung des Wassers im Boden, Sitzungsber Akad. Wiss., 136 (1927) 271-306.

[217] P. Guo, Dependency of Tortuosity and Permeability of Porous Media on Directional Distribution of Pore Voids, Transp Porous Med, 95 (2012) 285-303.

[218] M. Matyka, A. Khalili, Z. Koza, Tortuosity-porosity relation in porous media flow, Physical Review E, 78 (2008) 026306.

[219] A. Koponen, M. Kataja, J. Timonen, Permeability and effective porosity of porous media, Physical Review E, 56 (1997) 3319-3325.

[220] F. Rubiera, A.B. Fuertes, J.J. Pis, V. Artos, G. Marbàn, Changes in textural properties of limestone and dolomite during calcination, Thermochimica Acta, 179 (1991) 125-134.

[221] S. Scaccia, A. Calabrò, R. Mecozzi, R. Scipioni, Studio del processo di desolforazione e decarbonatazione del gas di sintesi in sorbenti solidi a base di Ca, in, Report ENEA, RDS/2010/42, 2010.

[222] V. Manovic, E.J. Anthony, G. Grasa, J.C. Abanades, CO2 Looping Cycle Performance of a High-Purity Limestone after Thermal Activation/Doping, Energy & Fuels, 22 (2008) 3258-3264.

[223] W. Liu, H. An, C. Qin, J. Yin, G. Wang, B. Feng, M. Xu, Performance Enhancement of Calcium Oxide Sorbents for Cyclic CO2 Capture—A Review, Energy & Fuels, 26 (2012) 2751-2767.

[224] J. Adánez, A. Cuadrat, A. Abad, P. Gayán, L.F. de Diego, F. García-Labiano, Ilmenite Activation during Consecutive Redox Cycles in Chemical-Looping Combustion, Energy & Fuels, 24 (2010) 1402-1413.

[225] S. Brunauer, P.H. Emmett, E. Teller, Adsorption of Gases in Multimolecular Layers, Journal of the American Chemical Society, 60 (1938) 309-319.

[226] E.P. Barrett, L.G. Joyner, P.P. Halenda, The Determination of Pore Volume and Area Distributions in Porous Substances. I. Computations from Nitrogen Isotherms, Journal of the American Chemical Society, 73 (1951) 373-380.

[227] D. Alvarez, J.C. Abanades, Pore-size and shape effects on the recarbonation performance of calcium oxide submitted to repeated calcination/recarbonation cycles, Energy and Fuels, 19 (2005) 270-278.

[228] D. Kunii, O. Levenspiel, Fluidization Engineering, 2nd ed., Butterworth-Heinemann, 1991.

[229] W.C. Yang (Ed.), Handbook of Fluidization and Fluid-Particle Systems, Marcel-Dekker, 2003.

[230] J.F. Davidson, R. Clift, D. Harrison (Eds.), Fluidization. 2nd Ed., Academic Press, 1985.

[231] L.G. Gibilaro, Fluidization Dynamics, Butterworth-Heinemann, 2001.

[232] S. Ergun, Fluid flow through packed columns, Chem. Eng. Prog., 48 (1952) 89-94.

[233] J.R. Grace, Contacting modes and behaviour classification of gas—solid and other two-phase suspensions, The Canadian Journal of Chemical Engineering, 64 (1986) 353-363.

[234] D. Geldart, Types of gas fluidization, Powder Technology, 7 (1973) 285-292.

[235] J.M. Valverde, Fluidization of Fine Powders, Springer Netherlands, 2013.

[236] H.T. Bi, J.R. Grace, Flow regime diagrams for gas-solid fluidization and upward transport, International Journal of Multiphase Flow, 21 (1995) 1229-1236.

[237] J.G. Yates, Fundamentals of fluidized-bed chemical processes, Butterworths, 1983.

[238] F.A. Zenz, The Fluid Mechanics of Bubbling Beds, Fibonacci Quarterly 16 (1978) 171–183.

[239] J.F. Davidson, Symposium on Fluidization—Discussion, Trans. Inst. Chem. Eng., 39 (1961) 230-232.

[240] P.N. Rowe, Gas-solid reaction in a fluidized bed, Chem. Eng. Prog., 60 (1964) 75.

[241] R.M. Davies, G. Taylor, The Mechanics of Large Bubbles Rising through Extended Liquids and through Liquids in Tubes, Proceedings of the Royal Society of London. Series A. Mathematical and Physical Sciences, 200 (1950) 375-390.

[242] G. Yasui, L.N. Johanson, Characteristics of gas pockets in fluidized beds, AIChE Journal, 4 (1958) 445-452.

[243] S. Mori, C.Y. Wen, Estimation of bubble diameter in gaseous fluidized beds, AIChE Journal, 21 (1975) 109-115.

[244] R.C. Darton, R.D. LaNauze, J.F. Davidson, D. Harrison, Bubble Growth due to Coalescence in Fluidised Beds, Trans Inst Chem Eng, 55 (1977) 274-280.

[245] J. Solsvik, R.A. Sánchez, Z. Chao, H.A. Jakobsen, Simulations of Steam Methane Reforming/Sorption-Enhanced Steam Methane Reforming Bubbling Fluidized Bed Reactors by a Dynamic One-Dimensional Two-Fluid Model: Implementation Issues and Model Validation, Industrial & Engineering Chemistry Research, 52 (2013) 4202-4220.

[246] I. Guedea, L.I. Díez, J. Pallarés, L.M. Romeo, On the modeling of oxy-coal combustion in a fluidized bed, Chemical Engineering Journal, 228 (2013) 179-191.

[247] D. Gidaspow, J. Jung, R.K. Singh, Hydrodynamics of fluidization using kinetic theory: an emerging paradigm: 2002 Flour-Daniel lecture, Powder Technology, 148 (2004) 123-141.

[248] J.A.M. Kuipers, Lecture notes of "9th Course on Computational Fluid Dynamics of Multiphase Flow", University of Twente, Enschede, The Netherlands, (2009).

[249] M.A. van der Hoef, M. van Sint Annaland, N.G. Deen, J.A.M. Kuipers, Numerical Simulation of Dense Gas-Solid Fluidized Beds: A Multiscale Modeling Strategy, Annual Review of Fluid Mechanics, 40 (2008) 47-70.

[250] G.A. Bokkers, J.A. Laverman, M. van Sint Annaland, J.A.M. Kuipers, Modelling of large-scale dense gas–solid bubbling fluidised beds using a novel discrete bubble model, Chemical Engineering Science, 61 (2006) 5590-5602.

[251] S. Movahedirad, A. Molaei Dehkordi, N.G. Deen, M. van Sint Annaland, J.A.M. Kuipers, Novel phenomenological discrete bubble model of freely bubbling dense gas–solid fluidized beds: Application to two-dimensional beds, AIChE Journal, 58 (2012) 3306-3317.

[252] M.A. van der Hoef, M. Ye, M. van Sint Annaland, A.T. Andrews, S. Sundaresan, J.A.M. Kuipers, Multiscale Modeling of Gas-Fluidized Beds, in: B.M. Guy (Ed.) Advances in Chemical Engineering, Academic Press, 2006, pp. 65-149.

[253] A.J.C. Ladd, R. Verberg, Lattice-Boltzmann Simulations of Particle-Fluid Suspensions, Journal of Statistical Physics, 104 (2001) 1191-1251.

[254] K.D. Kafui, C. Thornton, M.J. Adams, Discrete particle-continuum fluid modelling of gas–solid fluidised beds, Chemical Engineering Science, 57 (2002) 2395-2410.

[255] N.G. Deen, M. Van Sint Annaland, M.A. Van der Hoef, J.A.M. Kuipers, Review of discrete particle modeling of fluidized beds, Chemical Engineering Science, 62 (2007) 28-44.

[256] M. Sommerfeld, B. van Wachem, R. Oliemans, Best Practice Guidelines for Computational Fluid Dynamics of Dispersed Multi-Phase Flows, ERCOFTAC (European Research Community on Flow, Turbulence and Combustion) 2008.

[257] J. Wang, M.A. van der Hoef, J.A.M. Kuipers, Comparison of Two-Fluid and Discrete Particle Modeling of Dense Gas-Particle Flows in Gas-Fluidized Beds, Chemie Ingenieur Technik, 85 (2013) 290-298.

[258] E. Loth, Numerical approaches for motion of dispersed particles, droplets and bubbles, Progress in Energy and Combustion Science, 26 (2000) 161-223.

[259] D. Gera, M. Gautam, Y. Tsuji, T. Kawaguchi, T. Tanaka, Computer simulation of bubbles in large-particle fluidized beds, Powder Technology, 98 (1998) 38-47.

[260] M. Chiesa, V. Mathiesen, J.A. Melheim, B. Halvorsen, Numerical simulation of particulate flow by the Eulerian–Lagrangian and the Eulerian–Eulerian approach with application to a fluidized bed, Computers & Chemical Engineering, 29 (2005) 291-304.

[261] P.J. O'Rourke, P. Zhao, D. Snider, A model for collisional exchange in gas/liquid/solid fluidized beds, Chemical Engineering Science, 64 (2009) 1784-1797.

[262] D. Gidaspow, Multiphase Flow and Fluidization: Continuum and Kinetic Theory Description, Academic Press, New York, 1994.

[263] M. Syamlal, W. Rogers, T.J. O'Brien, MFIX documentation: Theory guide, Technical Note, DOE/METC-94/1004, NTIS/DE94000087, National Technical Information Service, Springfield, VA, (1993).

[264] N.E.T.L. (NETL), Multiphase Flow with Interphase eXchange - MFIX - Release 2013-2, in, https://mfix.netl.doe.gov/, 2013.

[265] K. Agrawal, P.N. Loezos, M. Syamlal, S. Sundaresan, The role of meso-scale structures in rapid gas-solid flows, Journal of Fluid Mechanics, 445 (2001) 151-185.

[266] A. Fluent, Fluent 6.3 Documentation, Fluent Inc., Lebanon, NH, (2006).

[267] C.K.K. Lun, S.B. Savage, D.J. Jeffrey, N. Chepurniy, Kinetic theories for granular flow: inelastic particles in Couette flow and slightly inelastic particles in a general flowfield, Journal of Fluid Mechanics, 140 (1984) 223-256.

[268] D.G. Schaeffer, Instability in the evolution equations describing incompressible granular flow, Journal of Differential Equations, 66 (1987) 19-50.

[269] S. Dartevelle, Numerical and granulometric approaches to geophysical granular flows, Ph.D. thesis., Michigan Technological University, Department of Geological and Mining Engineering, Houghton, Mi, U.S., 2003.

[270] S. Ogawa, A. Umemura, N. Oshima, On the equations of fully fluidized granular materials, Journal of Applied Mathematics and Physics (ZAMP), 31 (1980) 483-493.

[271] K. Sankaranarayanan, X. Shan, I.G. Kevrekidis, S. Sundaresan, Analysis of drag and virtual mass forces in bubbly suspensions using an implicit formulation of the lattice Boltzmann method, Journal of Fluid Mechanics, 452 (2002) 61-96.

[272] K. Sankaranarayanan, S. Sundaresan, Lift force in bubbly suspensions, Chemical Engineering Science, 57 (2002) 3521-3542.

[273] H.A. Jakobsen, S. Grevskott, H.F. Svendsen, Modeling of Vertical Bubble-Driven Flows, Industrial & Engineering Chemistry Research, 36 (1997) 4052-4074.

[274] B.G.M. van Wachem, J.C. Schouten, C.M. van den Bleek, R. Krishna, J.L. Sinclair, Comparative analysis of CFD models of dense gas–solid systems, AIChE Journal, 47 (2001) 1035-1051.

[275] M. Syamlal, T.J. O'Brien, Computer simulation of bubbles in a fluidized bed, in AIChE Symposium Series, 1989, pp. 22-31.

[276] C.Y. Wen, Y.H. Yu, A generalized method for predicting the minimum fluidization velocity, AIChE Journal, 12 (1966) 610-612.

[277] N. Herzog, M. Schreiber, C. Egbers, H.J. Krautz, A comparative study of different CFD-codes for numerical simulation of gas–solid fluidized bed hydrodynamics, Computers & Chemical Engineering, 39 (2012) 41-46.

[278] S. Schneiderbauer, S. Puttinger, S. Pirker, Comparative analysis of subgrid drag modifications for dense gas-particle flows in bubbling fluidized beds, AIChE Journal, 59 (2013) 4077-4099.

[279] J. Wang, M.A. van der Hoef, J.A.M. Kuipers, Coarse grid simulation of bed expansion characteristics of industrial-scale gas–solid bubbling fluidized beds, Chemical Engineering Science, 65 (2010) 2125-2131.

[280] R. Beetstra, M.A. van der Hoef, J.A.M. Kuipers, Drag force of intermediate Reynolds number flow past mono- and bidisperse arrays of spheres, AIChE Journal, 53 (2007) 489-501.

[281] J. Adanez, P. Gayán, G. Grasa, L.F. de Diego, L. Armesto, A. Cabanillas, Circulating fluidized bed combustion in the turbulent regime: modelling of carbon combustion efficiency and sulphur retention, Fuel, 80 (2001) 1405-1414.

[282] J. Werther, J. Wein, Expansion behavior of gas fluidized beds in the turbulent regime, AIChE Symp. Ser., 90 (1994) 31-44.

[283] D. Pallarès, F. Johnsson, Macroscopic modelling of fluid dynamics in large-scale circulating fluidized beds, Progress in Energy and Combustion Science, 32 (2006) 539-569.

[284] J.F. Richardson, W.N. Zaki, Sedimentation and fluidisation. Part I., Transactions of the Institution of Chemical Engineers, 32 (1954) 35–53.

[285] O. Levenspiel, G/S reactor models—packed beds, bubbling fluidized beds, turbulent fluidized beds and circulating (fast) fluidized beds, Powder Technology, 122 (2002) 1-9.

[286] J. Xu, G.F. Froment, Methane steam reforming, methanation and water-gas shift: I. Intrinsic kinetics, AIChE Journal, 35 (1989) 88-96.

[287] M.I. Temkin, The Kinetics of Some Industrial Heterogeneous Catalytic Reactions, in: H.P. D.D. Eley, B.W. Paul (Eds.) Advances in Catalysis, Academic Press, 1979, pp. 173-291.

[288] J.R. Rostrup-Nielsen, Catalytic Steam Reforming, Catalysis: Science and Technology, 5 (1984) 1-117.

[289] G.W. Crabtree, M.S. Dresselhaus, M.V. Buchanan, The hydrogen economy, Physics Today, 57 (2004) 39-44.

[290] K. Hou, R. Hughes, The kinetics of methane steam reforming over a Ni/α-Al2O catalyst, Chemical Engineering Journal, 82 (2001) 311-328.

[291] M. Zeppieri, P.L. Villa, N. Verdone, M. Scarsella, P. De Filippis, Kinetic of methane steam reforming reaction over nickel- and rhodium-based catalysts, Applied Catalysis A: General, 387 (2010) 147-154.

[292] L.M. Aparicio, Transient Isotopic Studies and Microkinetic Modeling of Methane Reforming over Nickel Catalysts, Journal of Catalysis, 165 (1997) 262-274.

[293] M.A. Soliman, A.M. Adris, A.S. Al-Ubaid, S.S.E. El-Nashaie, Intrinsic kinetics of Nickel/Calcium aluminate catalyst for methane steam reforming, Journal of Chemical Technology and Biotechnology, 55 (1992) 131-138.

[294] J.R. Rostrup-Nielsen, New aspects of syngas production and use, Catalysis Today, 63 (2000) 159-164.

[295] J. Xu, G.F. Froment, Methane steam reforming: II. Diffusional limitations and reactor simulation, AIChE Journal, 35 (1989) 97-103.

[296] A. Di Carlo, E. Bocci, F. Zuccari, A. Dell'Era, Numerical Investigation of Sorption Enhanced Steam Methane Reforming Process Using Computational Fluid Dynamics Eulerian−Eulerian Code, Industrial & Engineering Chemistry Research, 49 (2010) 1561-1576.

[297] S. Stendardo, A. Calabrò, G. Girardi, P.U. Foscolo, C. Herce, A Study of a chemical looping carbon capture for high-hydrogen content syngas, Proceedings 1st International Conference on Chemical Looping - Lyon (France), (17-19 March 2010).

[298] I. Guedea, L.I. Díez, J. Pallarés, L.M. Romeo, Influence of O2/CO2 mixtures on the fluid-dynamics of an oxy-fired fluidized bed reactor, Chemical Engineering Journal, 178 (2011) 129-137.

[299] L.M. Romeo, L.I. Díez, I. Guedea, I. Bolea, C. Lupiáñez, A. González, J. Pallarés, E. Teruel, Design and operation assessment of an oxyfuel fluidized bed combustor, Experimental Thermal and Fluid Science, 35 (2011) 477-484.

[300] C. Herce, Y. Li, Q. Wang, I. Guedea, L.I. Díez, C. Cortés, CFD simulation of a 90 kWth oxy-fuel combustion bubbling fluidized bed reactor Proceedings of "International Conference on Power Engineering-13 (ICOPE 2013)" - Wuhan (China), (24-27 October 2013).

[301] C. Herce, A. Calabrò, S. Stendardo, Numerical simulation of a high temperature CO2 capture fluidized bed, Proceedings of "International Conference on Processes and Technologies for a Sustainable Energy" - Ischia (Italy), (27-30 June 2010).

[302] C. Herce, A. Calabrò, S. Stendardo, Modelizzazione CFD del letto fluido bollente di reforming de metano con cattura di CO2 dell'impianto ZECOMIX. Simulazione numerica del campo di velocità del carbonatatore ZECOMIX., in: A. Dattola (Ed.) Fossil Fuels and Carbon

Capture and Storage. Joint Research Program MSE/ENEA – Research on National Electric System., ENEA, Frascati (It.), 2012.

[303] Q. Wang, Numerical simulation and validation of fluid dynamics on an oxy-fired bed reactor. Cold tests. MsC thesis., in: ICARE - China- EU Institute for Clean And Renewable Energy, 2012.

[304] Y. Li, CFD simulation of an oxyfuel fluidized bed. Sensitivity analysis of operating conditions. MsC Thesis in: ICARE - China- EU Institute for Clean And Renewable Energy, 2012.

[305] S. Cooper, C.J. Coronella, CFD simulations of particle mixing in a binary fluidized bed, Powder Technology, 151 (2005) 27-36.

[306] S.A. Vasquez, V.A. Ivanov, A phase coupled method for solving multiphase problems on unstructured meshes, American Society of Mechanical Engineers, Fluids Engineering Division (Publication) FED, 251 (2000) 743-748.

[307] M.J.V. Goldschmidt, J.A.M. Kuipers, W.P.M. van Swaaij, Hydrodynamic modelling of dense gas-fluidised beds using the kinetic theory of granular flow: effect of coefficient of restitution on bed dynamics, Chemical Engineering Science, 56 (2001) 571-578.

[308] D. Geldart, Expansion of Gas Fluidized Beds, Industrial & Engineering Chemistry Research, 43 (2004) 5802-5809.

[309] J.A. Almendros-Ibáñez, D. Pallarès, F. Johnsson, D. Santana, Voidage distribution around bubbles in a fluidized bed: Influence on throughflow, Powder Technology, 197 (2010) 73-82.

[310] P.U. Foscolo, A. Germanà, N. Jand, Specifiche Impianto ZECOMIX, in: Report TEPSI-UNIVAQ-2006, 2006.

[311] L. Huilin, H. Yurong, L. Wentie, J. Ding, D. Gidaspow, J. Bouillard, Computer simulations of gas–solid flow in spouted beds using kinetic–frictional stress model of granular flow, Chemical Engineering Science, 59 (2004) 865-878.

[312] J.T. Cornelissen, F. Taghipour, R. Escudié, N. Ellis, J.R. Grace, CFD modelling of a liquid–solid fluidized bed, Chemical Engineering Science, 62 (2007) 6334-6348.

[313] J. Ding, D. Gidaspow, A bubbling fluidization model using kinetic theory of granular flow, AIChE Journal, 36 (1990) 523-538.

[314] F. Taghipour, N. Ellis, C. Wong, Experimental and computational study of gas–solid fluidized bed hydrodynamics, Chemical Engineering Science, 60 (2005) 6857-6867.

[315] D. Gera, M. Syamlal, T.J. O'Brien, Hydrodynamics of particle segregation in fluidized beds, International Journal of Multiphase Flow, 30 (2004) 419-428.

[316] X. Gao, C. Wu, Y.-w. Cheng, L.-j. Wang, X. Li, Experimental and numerical investigation of solid behavior in a gas–solid turbulent fluidized bed, Powder Technology, 228 (2012) 1-13.

[317] S.D. Sharma, Numerical Simulation of Catalytic Partial Oxidation of Methane to Synthesis Gas in a Bubbling Fluidized Bed Reactor Proceedings "6th international symposium on Catalysis in Multiphase Reactors" - Pune (India), (14-17 January 2007).

[318] S.H. Hosseini, G. Ahmadi, M. Olazar, CFD simulation of cylindrical spouted beds by the kinetic theory of granular flow, Powder Technology, 246 (2013) 303-316.

[319] G.K. Khoe, Mechanics of Spouted Beds, University Press, 1980.

[320] A.R. Brun-Tsekhovoi, A.N. Zadorin, Y.R. Katsobashvili, S.S. Kourdyumov, The process of catalytic steam reforming of hydrocarbons in the presence of carbon dioxide acceptor, in: Hydrogen Energy Progress VII: Proceedings of the 7th World Hydrogen Energy Conference 1988, pp. 885-900.

[321] C. Han, D.P. Harrison, Simultaneous shift reaction and carbon dioxide separation for the direct production of hydrogen, Chemical Engineering Science, 49 (1994) 5875-5883.

[322] B. Balasubramanian, A. Lopez Ortiz, S. Kaytakoglu, D.P. Harrison, Hydrogen from methane in a single-step process, Chemical Engineering Science, 54 (1999) 3543-3552.

[323] A. Lopez Ortiz, D.P. Harrison, Hydrogen Production Using Sorption-Enhanced Reaction, Industrial & Engineering Chemistry Research, 40 (2001) 5102-5109.

[324] Z.-s. Li, N.-s. Cai, J.-b. Yang, Continuous Production of Hydrogen from Sorption-Enhanced Steam Methane Reforming in Two Parallel Fixed-Bed Reactors Operated in a Cyclic Manner, Industrial & Engineering Chemistry Research, 45 (2006) 8788-8793.

[325] Y. Ding, E. Alpay, Adsorption-enhanced steam–methane reforming, Chemical Engineering Science, 55 (2000) 3929-3940.

[326] D.K. Lee, I.H. Baek, W.L. Yoon, Modeling and simulation for the methane steam reforming enhanced by in situ CO2 removal utilizing the CaO carbonation for H2 production, Chemical Engineering Science, 59 (2004) 931-942.

[327] M. Broda, V. Manovic, Q. Imtiaz, A.M. Kierzkowska, E.J. Anthony, C.R. Müller, High-Purity Hydrogen via the Sorption-Enhanced Steam Methane Reforming Reaction over a Synthetic CaO-Based Sorbent and a Ni Catalyst, Environmental Science & Technology, 47 (2013) 6007-6014.

[328] K. Johnsen, H.J. Ryu, J.R. Grace, C.J. Lim, Sorption-enhanced steam reforming of methane in a fluidized bed reactor with dolomite as -acceptor, Chemical Engineering Science, 61 (2006) 1195-1202.

[329] Y. Chen, Y. Zhao, C. Zheng, J. Zhang, Numerical study of hydrogen production via sorption-enhanced steam methane reforming in a fluidized bed reactor at relatively low temperature, Chemical Engineering Science, 92 (2013) 67-80.

[330] G.-h. Xiu, P. Li, A. E. Rodrigues, Sorption-enhanced reaction process with reactive regeneration, Chemical Engineering Science, 57 (2002) 3893-3908.

[331] Y.-N. Wang, A.E. Rodrigues, Hydrogen production from steam methane reforming coupled with in situ CO2 capture: Conceptual parametric study, Fuel, 84 (2005) 1778-1789.

[332] K. Johnsen, J.R. Grace, S.S.E.H. Elnashaie, L. Kolbeinsen, D. Eriksen, Modeling of Sorption-Enhanced Steam Reforming in a Dual Fluidized Bubbling Bed Reactor, Industrial & Engineering Chemistry Research, 45 (2006) 4133-4144.

[333] G.C. Koumpouras, E. Alpay, F. Stepanek, Mathematical modelling of low-temperature hydrogen production with in situ CO2 capture, Chemical Engineering Science, 62 (2007) 2833-2841.

[334] S. Stendardo, P.U. Foscolo, Modelling of a multi-particle reactor for carbon dioxide capture and hydrogen production, Proceedings "5th Conference on Clean Coal Technologies " - Zaragoza (Spain), (8-12 May 2011).

[335] H. Lindborg, H.A. Jakobsen, Sorption Enhanced Steam Methane Reforming Process Performance and Bubbling Fluidized Bed Reactor Design Analysis by Use of a Two-Fluid Model, Industrial & Engineering Chemistry Research, 48 (2008) 1332-1342.

[336] Y. Wang, Z. Chao, H.A. Jakobsen, CFD modelling of CO2 capture in the SE-SMR process in the fluidized bed reactors, Chemical Engineering Transactions 21 (2010) 601-606.

[337] Y. Wang, Z. Chao, H.A. Jakobsen, 3D Simulation of bubbling fluidized bed reactors for sorption enhanced steam methane reforming processes, Journal of Natural Gas Science and Engineering, 2 (2010) 105-113.

[338] Y. Wang, Z. Chao, H.A. Jakobsen, Effects of Gas–Solid Hydrodynamic Behavior on the Reactions of the Sorption Enhanced Steam Methane Reforming Process in Bubbling Fluidized Bed Reactors, Industrial & Engineering Chemistry Research, 50 (2011) 8430-8437.

[339] O. Levenspiel, Difficulties in Trying To Model and Scale-Up the Bubbling Fluidized Bed (BFB) Reactor, Industrial & Engineering Chemistry Research, 47 (2007) 273-277.

[340] V.V. Kelkar, K.M. Ng, Development of fluidized catalytic reactors: Screening and scale-up, AIChE Journal, 48 (2002) 1498-1518.

[341] F.M. White, Fluid Mechanics, McGraw-Hill, 2003.

[342] L.R. Glicksman, M.R. Hyre, P.A. Farrell, Dynamic similarity in fluidization, International Journal of Multiphase Flow, 20, Supplement 1 (1994) 331-386.

[343] E. Buckingham, On Physically Similar Systems; Illustrations of the Use of Dimensional Equations, Physical Review, 4 (1914) 345-376.

[344] M. Rüdisüli, T.J. Schildhauer, S.M.A. Biollaz, J.R. van Ommen, Scale-up of bubbling fluidized bed reactors — A review, Powder Technology, 217 (2012) 21-38.

[345] J.B. Romero, L.N. Johanson, Factors affecting fluidized bed quality, Chem. Eng. Prog. Symp. Ser. , 58 (1962) 28-37.

[346] T.E. Broadhurst, H.A. Becker, The application of the theory of dimensions to fluidized bed, (1973) 10-27.

[347] T.J. Fitzgerald, S.D. Crane, Cold fluidized bed modeling, Proceedings of 6th International Conference on Fluidized Bed Combustion (Atlanta), III (1980) 815-820.

[348] L.R. Glicksman, Scaling relationships for fluidized beds, Chemical Engineering Science, 39 (1984) 1373-1379.

[349] T.B. Anderson, R. Jackson, Fluid Mechanical Description of Fluidized Beds. Equations of Motion, Industrial & Engineering Chemistry Fundamentals, 6 (1967) 527-539.

[350] L.R. Glicksman, M. Hyre, K. Woloshun, Simplified scaling relationships for fluidized beds, Powder Technology, 77 (1993) 177-199.

[351] J. Werther, Scale-up modeling for fluidized bed reactors, Chemical Engineering Science, 47 (1992) 2457-2462.

[352] P.U. Foscolo, R. Di Felice, L.G. Gibilaro, L. Pistone, V. Piccolo, Scaling relationships for fluidisation: the generalised particle bed model, Chemical Engineering Science, 45 (1990) 1647-1651.

[353] M. Horio, A. Nonaka, Y. Sawa, I. Muchi, New Similarity Rule for Fluidized Bed Scale-Up, AIChE Journal, 32 (1986) 1466-1482.

[354] C.M. Van Den Bleek, J.C. Schouten, Can deterministic chaos create order in fluidized-bed scale-up?, Chemical Engineering Science, 48 (1993) 2367-2373.

[355] B. Leckner, P. Szentannai, F. Winter, Scale-up of fluidized-bed combustion – A review, Fuel, 90 (2011) 2951-2964.

[356] B.G.M. van Wachem, J.C. Schouten, R. Krishna, C.M. van den Bleek, Validation of the Eulerian simulated dynamic behaviour of gas–solid fluidised beds, Chemical Engineering Science, 54 (1999) 2141-2149.

[357] R. Krishna, J.M. van Baten, Using CFD for scaling up gas–solid bubbling fluidised bed reactors with Geldart A powders, Chemical Engineering Journal, 82 (2001) 247-257.

[358] J. Wang, M.A. van der Hoef, J.A.M. Kuipers, Why the two-fluid model fails to predict the bed expansion characteristics of Geldart A particles in gas-fluidized beds: A tentative answer, Chemical Engineering Science, 64 (2009) 622-625.

[359] Y.P. Tsuo, D. Gidaspow, Computation of flow patterns in circulating fluidized beds, AIChE Journal, 36 (1990) 885-896.

[360] B. Chalermsinsuwan, P. Piumsomboon, D. Gidaspow, A computational fluid dynamics design of a carbon dioxide sorption circulating fluidized bed, AIChE Journal, 56 (2010) 2805-2824.

[361] P. Khongprom, D. Gidaspow, Compact fluidized bed sorber for CO2 capture, Particuology, 8 (2010) 531-535.

[362] A. Almuttahar, F. Taghipour, Computational fluid dynamics of high density circulating fluidized bed riser: Study of modeling parameters, Powder Technology, 185 (2008) 11-23.

[363] J. Li, M. Kwauk, Particle-fluid two-phase flow: the energy-minimization multi-scale method, Metallurgical Industry Press, 1994.

[364] Z. Shi, W. Wang, J. Li, A bubble-based EMMS model for gas–solid bubbling fluidization, Chemical Engineering Science, 66 (2011) 5541-5555.

[365] B. Lu, N. Zhang, W. Wang, J. Li, J.H. Chiu, S.G. Kang, 3-D full-loop simulation of an industrial-scale circulating fluidized-bed boiler, AIChE Journal, 59 (2013) 1108-1117.

[366] Y. Zhao, H. Li, M. Ye, Z. Liu, 3D Numerical Simulation of a Large Scale MTO Fluidized Bed Reactor, Industrial & Engineering Chemistry Research, 52 (2013) 11354-11364.

[367] A. Srivastava, S. Sundaresan, Analysis of a frictional–kinetic model for gas–particle flow, Powder Technology, 129 (2003) 72-85.

[368] Y. Igci, A.T. Andrews, S. Sundaresan, S. Pannala, T. O'Brien, Filtered two-fluid models for fluidized gas-particle suspensions, AIChE Journal, 54 (2008) 1431-1448.

[369] A. Gobin, H. Neau, O. Simonin, J.-R. Llinas, V. Reiling, J.-L.c. Sélo, Fluid dynamic numerical simulation of a gas phase polymerization reactor, International Journal for Numerical Methods in Fluids, 43 (2003) 1199-1220.

[370] J.-F. Parmentier, O. Simonin, O. Delsart, A functional subgrid drift velocity model for filtered drag prediction in dense fluidized bed, AIChE Journal, 58 (2012) 1084-1098.

[371] A. Ozel, P. Fede, O. Simonin, Development of filtered Euler–Euler two-phase model for circulating fluidised bed: High resolution simulation, formulation and a priori analyses, International Journal of Multiphase Flow, 55 (2013) 43-63.

[372] J.R. van Ommen, M. Teuling, J. Nijenhuis, B.G.M. van Wachem, Computational validation of the scaling rules for fluidized beds, Powder Technology, 163 (2006) 32-40.

[373] F.P. Di Maio, A. Di Renzo, Verification of scaling criteria for bubbling fluidized beds by DEM–CFD simulation, Powder Technology, 248 (2013) 161-171.

[374] A. Calabrò, Precombustion CO2 capture in coal power plants: research activities at ENEA, "CO2 Capture & Storage: Towards a UK-Italy Common Strategy within a Global Framework." Erice (Italy), (1-7 November 2007).

[375] S. Stendardo, P. Deiana, A. Calabrò, Short-cut dynamic model of a catalytic reactor for the CO2 capture by means of dolomite., in: Technical report RSE/2009/21, ENEA, Rome, 2009.

[376] L.F. Richardson, The Approximate Arithmetical Solution by Finite Differences of Physical Problems Involving Differential Equations, with an Application to the Stresses in a Masonry Dam, Philosophical Transactions of the Royal Society of London. Series A, Containing Papers of a Mathematical or Physical Character, 210 (1911) 307-357.

[377] L.F. Richardson, J.A. Gaunt, The Deferred Approach to the Limit. Part I. Single Lattice. Part II. Interpenetrating Lattices, Philosophical Transactions of the Royal Society of London. Series A, Containing Papers of a Mathematical or Physical Character, 226 (1927) 299-361.

[378] I.B. Celik, U. Ghia, P.J. Roache, C.J. Freitas, H. Coleman, P.E. Raad, Procedure for Estimation and Reporting of Uncertainty Due to Discretization in CFD Applications, Journal of Fluids Engineering, 130 (2008) 078001-078001.

[379] ASME, Standard for Verification and Validation in Computational Fluid Dynamics and Heat Transfer in, 2009.

[380] J.R. Grace, F. Taghipour, Verification and validation of CFD models and dynamic similarity for fluidized beds, Powder Technology, 139 (2004) 99-110.

[381] H. Lindborg, M. Lysberg, H.A. Jakobsen, Practical validation of the two-fluid model applied to dense gas–solid flows in fluidized beds, Chemical Engineering Science, 62 (2007) 5854-5869.

[382] R. Courant, K. Friedrichs, H. Lewy, Über die partiellen Differenzengleichungen der mathematischen Physik, Math. Ann., 100 (1928) 32-74.

[383] A. Gel, R. Garg, C. Tong, M. Shahnam, C. Guenther, Applying uncertainty quantification to multiphase flow computational fluid dynamics, Powder Technology, 242 (2013) 27-39.

[384] S. Sasic, B. Leckner, F. Johnsson, Characterization of fluid dynamics of fluidized beds by analysis of pressure fluctuations, Progress in Energy and Combustion Science, 33 (2007) 453-496.

[385] F. Johnsson, R.C. Zijerveld, J.C. Schouten, C.M. van den Bleek, B. Leckner, Characterization of fluidization regimes by time-series analysis of pressure fluctuations, International Journal of Multiphase Flow, 26 (2000) 663-715.

[386] R.A. Fisher, The design of experiments, Oliver and Boyd, 1935.

[387] D.R. Cox, N. Reid, The Theory of the Design of Experiments, Taylor & Francis, 2000.

[388] D.C. Montgomery, Design and Analysis of Experiments, John Wiley & Sons, 2008.

[389] G. Taguchi, System of experimental design: engineering methods to optimize quality and minimize costs, UNIPUB/Kraus International Publications, 1987.

[390] R.K. Roy, A Primer on the Taguchi Method, Society of Manufacturing Engineers, 2010.

[391] J.C. Miranda, Design of Experiments using the Taguchi Method, in: Product design: techniques for robustness, reliability and optimization. Class Notes., Instituto Tecnologico y de Estudios Superiores de Monterrey, Toluca (Mexico), 2004.

[392] R. Spence, J. Amaral-Teixeira, A CFD parametric study of geometrical variations on the pressure pulsations and performance characteristics of a centrifugal pump, Computers & Fluids, 38 (2009) 1243-1257.

[393] Q. Chen, M. Zeng, J. Zhang, Q. Wang, Optimal design of bi-layer interconnector for SOFC based on CFD-Taguchi method, International Journal of Hydrogen Energy, 35 (2010) 4292-4300.

[394] J.-M. Wang, H.-J. Yan, J.-M. Zhou, S.-X. Li, G.-C. Gui, Optimization of parameters for an aluminum melting furnace using the Taguchi approach, Applied Thermal Engineering, 33–34 (2012) 33-43.

[395] I.E.A., World Energy Outlook: 2011 - executive summay, IEA/OECD, Paris, 2011.

[396] R. Cyprès, S. Furfari, Hydropyrolysis of a high-sulphur-high-calcite Italian Sulcis coal. 1. Hydropyrolysis yields and catalytic effect of the calcite, Fuel, 61 (1982) 447-452.

[397] P.R. Solomon, T.H. Fletcher, Impact of coal pyrolysis on combustion, Symposium (International) on Combustion, 25 (1994) 463-474.

[398] J. Yu, J.A. Lucas, T.F. Wall, Formation of the structure of chars during devolatilization of pulverized coal and its thermoproperties: A review, Progress in Energy and Combustion Science, 33 (2007) 135-170.

[399] P.R. Solomon, M.A. Serio, E.M. Suuberg, Coal pyrolysis: Experiments, kinetic rates and mechanisms, Progress in Energy and Combustion Science, 18 (1992) 133-220.

[400] S. Niksa, C.-W. Lau, Global rates of devolatilization for various coal types, Combustion and Flame, 94 (1993) 293-307.

[401] T.F. Wall, G.-s. Liu, H.-w. Wu, D.G. Roberts, K.E. Benfell, S. Gupta, J.A. Lucas, D.J. Harris, The effects of pressure on coal reactions during pulverised coal combustion and gasification, Progress in Energy and Combustion Science, 28 (2002) 405-433.

[402] P. Carbini, L. Curreli, M. Ghiani, F. Satta, Desulphurization of europeans coal using molten caustic mixtures, in: Processing and utilization of high sulphur coals III, Markuvzewski, R. Wheelock, T. D., 1990.

[403] R.C. Borah, P. Ghosh, P.G. Rao, A review on devolatilization of coal in fluidized bed, International Journal of Energy Research, 35 (2011) 929-963.

[404] P.R. Solomon, D.G. Hamblen, R.M. Carangelo, M.A. Serio, G.V. Deshpande, General model of coal devolatilization, Energy & Fuels, 2 (1988) 405-422.

[405] A. Sarwar, M. Nasiruddin Khan, K. Azhar, Kinetic studies of pyrolysis and combustion of Thar coal by thermogravimetry and chemometric data analysis, Journal of Thermal Analysis and Calorimetry, 109 (2012) 97-103.

[406] W.R. Ladner, The products of coal pyrolysis: properties, conversion and reactivity, Fuel Processing Technology, 20 (1988) 207-222.

[407] S. Scaccia, A. Calabrò, R. Mecozzi, Investigation of the evolved gases from Sulcis coal during pyrolysis under N2 and H2 atmospheres, Journal of Analytical and Applied Pyrolysis, 98 (2012) 45-50.

[408] A. Arenillas, F. Rubiera, C. Pevida, J.J. Pis, A comparison of different methods for predicting coal devolatilisation kinetics, Journal of Analytical and Applied Pyrolysis, 58–59 (2001) 685-701.

[409] A.K. Burnham, R.L. Braun, Global Kinetic Analysis of Complex Materials, Energy & Fuels, 13 (1998) 1-22.

[410] M.V. Kök, Thermal Analysis Applications In Fossil Fuel Science. Literature survey, Journal of Thermal Analysis and Calorimetry, 68 (2002) 1061-1077.

[411] M.E. Brown, A.K. Galwey, The significance of “compensation effects” appearing in data published in “computational aspects of kinetic analysis”: ICTAC project, 2000, Thermochimica Acta, 387 (2002) 173-183.

[412] M. Maciejewski, Computational aspects of kinetic analysis.: Part B: The ICTAC Kinetics Project — the decomposition kinetics of calcium carbonate revisited, or some tips on survival in the kinetic minefield, Thermochimica Acta, 355 (2000) 145-154.

[413] V. Strezov, J.A. Lucas, T.J. Evans, L. Strezov, Effect of heating rate on the thermal properties and devolatilisation of coal, Journal of Thermal Analysis and Calorimetry, 78 (2004) 385-397.

[414] A.K. Galwey, M.E. Brown, Arrhenius parameters and compensation behaviour in solid-state decompositions, Thermochimica Acta, 300 (1997) 107-115.

[415] A.K. Galwey, Is the science of thermal analysis kinetics based on solid foundations?: A literature appraisal, Thermochimica Acta, 413 (2004) 139-183.

[416] S. Vyazovkin, A.K. Burnham, J.M. Criado, L.A. Pérez-Maqueda, C. Popescu, N. Sbirrazzuoli, ICTAC Kinetics Committee recommendations for performing kinetic computations on thermal analysis data, Thermochimica Acta, 520 (2011) 1-19.

[417] A. Figen, O. İsmail, S. Pişkin, Devolatilization non-isothermal kinetic analysis of agricultural stalks and application of TG-FT/IR analysis, Journal of Thermal Analysis and Calorimetry, 107 (2012) 1177-1189.

[418] S. Badzioch, P.G.W. Hawksley, Kinetics of thermal decomposition of pulverized coal particles, Industrial and Engineering Chemistry: Process Design and Development, 9 (1970) 521-530.

[419] G.H. Ko, D.M. Sanchez, W.A. Peters, J.B. Howard, Application of first-order single-reaction model for coal devolatilization over a wide range of heating rates, Preprints of Papers, American Chemical Society, Division of Fuel Chemistry; (USA), (1988) 112-119.

[420] M.a.-J. Lázaro, R. Moliner, I. Suelves, Non-isothermal versus isothermal technique to evaluate kinetic parameters of coal pyrolysis, Journal of Analytical and Applied Pyrolysis, 47 (1998) 111-125.

[421] H.E. Kissinger, Reaction kinetics in differential thermal analysis, Analytical Chemistry, 29 (1957) 1702-1706.

[422] K. Slopiecka, P. Bartocci, F. Fantozzi, Thermogravimetric analysis and kinetic study of poplar wood pyrolysis, Applied Energy, 97 (2012) 491-497.

[423] R.L. Braun, A.K. Burnham, Analysis of chemical reaction kinetics using a distribution of activation energies and simpler models, Energy & Fuels, 1 (1987) 153-161.

[424] K. Miura, A new and simple method to estimate f(E) and k0(E) in the distributed activation energy model from three sets of experimental data, Energy & Fuels, 9 (1995) 302-307.

[425] D.M. Grant, R.J. Pugmire, T.H. Fletcher, A.R. Kerstein, Chemical model of coal devolatilization using percolation lattice statistics, Energy & Fuels, 3 (1989) 175-186.

[426] A. Savitzky, M.J.E. Golay, Smoothing and Differentiation of Data by Simplified Least Squares Procedures, Analytical Chemistry, 36 (1964) 1627-1639.

[427] J.A. Caballero, J.A. Conesa, Mathematical considerations for nonisothermal kinetics in thermal decomposition, Journal of Analytical and Applied Pyrolysis, 73 (2005) 85-100.

[428] A. Williams, M. Pourkashanian, J.M. Jones, The combustion of coal and some other solid fuels, Proceedings of the Combustion Institute, 28 (2000) 2141-2162.

[429] P.R. Solomon, D.G. Hamblen, Finding order in coal pyrolysis kinetics, Progress in Energy and Combustion Science, 9 (1983) 323-361.

[430] J. Pallarés, I. Arauzo, A. Williams, Integration of CFD codes and advanced combustion models for quantitative burnout determination, Fuel, 86 (2007) 2283-2290.

[431] H.S. Harold, Lignites of North America, in: Coal Science and Technology, Vol. 23, Elsevier, 1995, pp. 202.

[432] M.J.G. Alonso, D. Alvarez, A.G. Borrego, R. Menéndez, G. Marbán, Systematic Effects of Coal Rank and Type on the Kinetics of Coal Pyrolysis, Energy & Fuels, 15 (2001) 413-428.

[433] C.C. Lakshmanan, N. White, A New Distributed Activation Energy Model Using Weibull Distribution for the Representation of Complex Kinetics, Energy & Fuels, 8 (1994) 1158-1167.

[434] T.C. Ho, R. Aris, On apparent second-order kinetics, AIChE Journal, 33 (1987) 1050-1051.

[435] C.C. Lakshmanan, M.L. Bennett, N. White, Implications of multiplicity in kinetic parameters to petroleum exploration: distributed activation energy models, Energy & Fuels, 5 (1991) 110-117.

[436] C.P. Please, M.J. McGuinness, D.L.S. McElwain, Approximations to the distributed activation energy model for the pyrolysis of coal, Combustion and Flame, 133 (2003) 107-117.

[437] R. Brun, F. Rademakers, ROOT - An object oriented data analysis framework, Nuclear Instruments and Methods in Physics Research, Section A: Accelerators, Spectrometers, Detectors and Associated Equipment, 389 (1997) 81-86.

[438] M.A. Serio, D.G. Hamblen, J.R. Markham, P.R. Solomon, Kinetics of volatile product evolution in coal pyrolysis: experiment and theory, Energy & Fuels, 1 (1987) 138-152.

[439] H.A.G. Chermin, D.W. Van Krevelen, Chemical structure and properties of coal XVII - A mathematical model of coal pyrolysis, Fuel, 36 (1957) 85-104.

[440] A.K. Burnham, B.J. Schmidt, R.L. Braun, A test of the parallel reaction model using kinetic measurements on hydrous pyrolysis residues, Organic Geochemistry, 23 (1995) 931-939.

[441] B. de Caprariis, P. De Filippis, C. Herce, N. Verdone, A Double-Gaussian Distributed Activation Energy Model for Coal Devolatilization, Energy & Fuels, 26 (2012) 6153–6159.

[442] T.H. Fletcher, A.R. Kerstein, R.J. Pugmire, D.M. Grant, Chemical percolation model for devolatilization. 2. Temperature and heating rate effects on product yields, Energy & Fuels, 4 (1990) 54-60.

[443] T.H. Fletcher, A.R. Kerstein, R.J. Pugmire, M.S. Solum, D.M. Grant, Chemical percolation model for devolatilization. 3. Direct use of carbon-13 NMR data to predict effects of coal type, Energy & Fuels, 6 (1992) 414-431.

[444] Fletcher TH. 13C NMR parameter calculator. In: Chemical Percolation Devolatilization (CPD) Model. 2006. http://www.et.byu.edu/~tom/cpd/correlation.html. Last accessed 24 Nov 2013.

[445] D. Gera, M. Mathur, M. Freeman, Parametric Sensitivity Study of a CFD-Based Coal Devolatilization Model, Energy & Fuels, 17 (2003) 794-795.

[446] I. Ion, F. Popescu, G. Rolea, A biomass pyrolysis model for CFD application, Journal of Thermal Analysis and Calorimetry, 111 (2013) 1811-1815.

[447] J.O. Pou, Y.E. Alvarez, J.K. Watson, J.P. Mathews, S. Pisupati, Co-primary thermolysis molecular modeling simulation of lignin and subbituminous coal via a reactive coarse-grained simplification, Journal of Analytical and Applied Pyrolysis, 95 (2012) 101-111.